Impacts of genetically encoded acoustic reporters on Escherichia coli physiology

Simon Barral

Université Paris Cité

THESE DE DOCTORAT

Thèse de doctorat - Université Paris Cité
UMR 168 - Physique des Cellules et Cancer, Institut Curie

Impacts of genetically encoded acoustic reporters on *Escherichia coli* physiology

Rapporteurs :

Meriem El Karoui (DR CNRS - Laboratoire de Biologie et Pharmacologie Appliquée - ENS Paris Saclay)

Morgan Delarue (DR CNRS -Laboratory for Analysis and Architecture of Systems - Université de Toulouse)

Examinateurs :

Florence Gazeau (DR CNRS - Laboratoire Matière et Systèmes Complexes - Université Paris Cité)

Pierre Crozet (MCF CNRS - Synthetic and Systems Biology of Microalgae - Sorbonne Université)

Soutenue par
Simon BARRAL
le 27 octobre 2025

Dirigée par
Pascal HERSEN

Ecole Doctoral 474
Frontière de l'Innovation en Recherche et Education (FIRE)

Spécialité
Sciences du vivant appliquées, biotechnologie et ingénierie des biosystèmes moléculaires

institut Curie

LEARNING PLANET INSTITUTE

Table of contents

Abstract

Impacts of genetically encoded acoustic reporters on Escherichia coli physiology

Key words : Sythetic biology, gas vesicle, sonogenetic, metabolic burden, microfluidic, ultrasounds, molecular crowding, *E.coli*, spheroids

Gas vesicles are intracellular, protein-based structures produced by various aquatic bacteria and archaea that have been studied for decades. These hollow, gas-filled organelles consist of a rigid protein shell shaped as cylindrical tubes with conical end caps, typically measuring approximately 150 nanometers in diameter and a few hundred nanometers in length. In their natural context, gas vesicles primarily function is to confer buoyancy, enabling cells to regulate their vertical position in the water column and access more favorable growth conditions.

Over the past decade, gas vesicles have attracted growing interest as versatile tools for biological research. Owing to their unique interactions with ultrasound, gas vesicles exhibit behaviors reminiscent of microbubbles, which have long been used as ultrasound contrast agents. Unlike microbubbles, however, gas vesicles are composed entirely of proteins, are mechanically robust, and can be genetically engineered. These characteristics have enabled their development as multifunctional tools for diverse biotechnological and biomedical applications, most notably as a genetically encoded ultrasound contrast agent. Despite these advances, little attention has been given to how heterologous gas vesicle production affects host cell physiology, even though many applications depend on expressing gas vesicle genes in non-native hosts.

The goal of my thesis was to address this knowledge gap by investigating the physiological impacts of these genetically encoded acoustic reporter in *Escherichia coli*, a host organism of particular relevance for gas vesicle–based applications.

To this end, I quantified the effects of gas vesicle production on cell growth in both homogeneous batch cultures and microcolonies grown within microfluidic devices. My findings demonstrate that gas vesicle production in *E. coli* imposes a measurable burden on host physiology, reducing growth rates and biomass yields, and promoting the emergence of non-producing subpopulations in an induction-dependent manner. Collectively, these results underscore the need for careful optimization and the development of synthetic gene circuits to regulate gas vesicle expression and mitigate their associated burden. Furthermore, I report a strong correlation between the intracellular volume occupied by gas vesicles and increased persistence to antibiotics, likely arising from altered cytoplasmic crowding due to vesicle accumulation.

Résumé

Impacts des rapporteurs acoustiques codés génétiquement sur la physiologie d'Escherichia coli

Mots-clés : Biologie synthétique, vésicule gazeuse, sonogénétique, contrainte métabolique, microfluidique, ultrasons, encombrement moléculaire, *E.coli*, sphéroïdes

Les vésicules de gaz sont des structures intracellulaires constituées de protéines, produites par diverses bactéries et archées aquatiques, étudiées depuis plusieurs décennies. Ces organites creux, remplis de gaz, possèdent une enveloppe rigide en forme de tube cylindrique coiffé de deux extrémités coniques, mesurant généralement environ 150 nanomètres de diamètre et quelques centaines de nanomètres de longueur. Dans leur contexte naturel, leur fonction principale est de conférer de la flottabilité aux cellules, leur permettant de réguler leur position verticale dans la colonne d'eau et d'accéder à des conditions de croissance plus favorables.

Au cours de la dernière décennie, les vésicules de gaz ont suscité un intérêt croissant en tant qu'outils polyvalents pour la recherche biologique. Grâce à leurs interactions uniques avec les ultrasons, elles présentent des comportements analogues à ceux des microbulles, largement utilisées comme agents de contraste échographique. Contrairement aux microbulles, cependant, les vésicules de gaz sont constituées exclusivement de protéines, sont mécaniquement robustes et peuvent être génétiquement modifiées. Ces caractéristiques ont permis leur développement comme outils multifonctionnels pour diverses applications biotechnologiques et biomédicales, notamment en tant qu'agents de contraste échographiques génétiquement encodés. Malgré ces avancées, peu d'attention a été portée à l'impact de la production hétérologue de vésicules de gaz sur la physiologie de l'hôte, alors que de nombreuses applications reposent sur l'expression de leurs gènes dans des organismes non natifs.

L'objectif de ma thèse a été de combler cette lacune en étudiant les impacts physiologiques de ces rapporteurs acoustiques génétiquement encodés chez *Escherichia coli*, un organisme hôte particulièrement pertinent pour les applications basées sur les vésicules de gaz.

À cette fin, j'ai quantifié les effets de la production de vésicules de gaz sur la croissance cellulaire, à la fois dans des cultures homogènes en batch et dans des microcolonies cultivées sur puces microfluidiques. Mes résultats démontrent que la production de vésicules de gaz chez E. coli impose un fardeau significatif à la physiologie de l'hôte, réduisant les taux de croissance et les rendements en biomasse, tout en favorisant l'émergence de sous-populations non productrices en fonction du niveau d'induction. Collectivement, ces résultats soulignent la nécessité d'une optimisation rigoureuse et du développement de circuits de biologie synthétique pour réguler l'expression des vésicules de gaz et limiter le fardeau qu'elles imposent. Enfin, je rapporte une forte corrélation entre le volume intracellulaire occupé par les vésicules de gaz et une persistance accrue aux antibiotiques, probablement liée à des modifications de la compaction du cytoplasme dues à leur accumulation.

Acknowledgement

First of all, I would like to thank my PhD supervisor, Pascal Hersen, for welcoming me into your laboratory and giving me the opportunity to carry out my thesis there. Thank you for your advice, your understanding, the freedom you gave me in conducting my research, as well as for your high standards, which constantly pushed me to improve myself.

My gratitude also goes to the members of my thesis committee, Stéphanie Descroix and Samar Issa, who accompanied me throughout these years with seriousness and kindness.

I am deeply grateful to all the members of the Hersen team, and more broadly to the Institut Curie community, with whom I shared over four years of joys and challenges in everyday research life. Among you, I wish to express my special thanks to:

- Céline Cordier, lab manager and true pillar of the team, upon whom all the logistics and organization of the laboratory relied.
- Sylvain Pouzet and Mathias Lebec, the dynamic yeast duo, who welcomed me into the lab, shared their precious knowledge, and enlivened many meals with scientific debates.
- Alvaro Benderas, for our collaborations, your excellent experimental ideas, and your seemingly limitless knowledge of microbiology.
- Lionel Chiron, for the training in machine learning, the snippets of code I managed to borrow here and there, and your broad general knowledge, which you shared at every opportunity.
- Julie Stoufflet, for your many tips and tricks in microfluidics and microscopy, as well as your always relevant advice and feedback.
- Jessica Riou-Ramon, for starting the tradition of TranTranZai lunch, which allowed me to test the limits of my chili tolerance.
- Margot Le Bot, for your constant and contagious smile.

I am also thankful to Jérôme Bonnet and your team at the Centre de Biochimie Structurale in Montpellier, for our collaborations, your warm welcome, and the training you provided. A very special thank you goes to Habib Hani, who not only trained me in L2, sometimes late into the night, but also made sure I was always well housed, fed, and transported during my stays in Montpellier. And of course, thank you Chloé Sasson, for our joint work and for the fun times we shared during the conference in Los Angeles.

Many thanks also to my family and friends for your unconditional support. To Maman and Papa, who have always been present despite the distance and always curious and enthusiastic about my research. To Thomas and Nico, for the climbing sessions and beers that helped clear my mind after afternoons battling with buggy code or a leaking microfluidic chip. Thanks also to my old friends from my hometown, and to my not-as-old friends from engineering school.

Finally, and above all, thank you Jeanne: you are a solid anchor I can always rely on, no matter what. Your daily support has been essential.

Abbreviations

ARG : Acoustic Reporter Genes

bARGser : ARG for expression in bacteria, with Serratia gas vesicle operon

CFU : Colony Forming Units

DAPI : 4',6-diamidino-2-phenylindole, a blue fluorescent DNA dye

FP : Fluorescent Protein

fUS : functional UltraSound imaging

FUS : Focused Ultrasound

GFP : Green Fluorescent Protein

GV : Gas Vesicle

Gvp : Gas Vesicle Protein

HyperCEST : Hyperpolarized Chemical Exchange Saturation Transfer

ISBUS : International Symposium on Biomolecular Ultrasound & Sonogenetics

mARG : ARG for expression in mammalian cells

$mARG_{Mega}$: Mammalian ARG from Bacillus megaterium

MRI : Magnetic Resonance Imaging

OMVs : Outer Membrane Vesicles

OPD : Optical Path Difference

OVD : Optical Volume Difference

PALM : Photoactivated Localization Microscopy

PBS : Phosphate-Buffered Saline solution

PEG : polyethylene glycol

PRP : Polarity Reversal Point

PSF : Point Spread Function

QPI : Quantitative Phase Imaging

RI : Refractive Index

ROS : Reactive Oxygen Species

SDT : SonoDynamic Therapy

TC : TetraCysteine motif

TNP : TriNitroPhenol

UV : Ultraviolet radiation

VPLs : Virus-Like Particles

Introduction

From marine biology curiosity to major research tool

Serendipity, the phenomenon of making fortunate discoveries by chance, has played a pivotal role in scientific advancements.

"The most exciting phrase to hear in science, the one that heralds new discoveries, is not 'Eureka!' but 'That's funny...'"

possibly Isaac Asimov[1]

Throughout history, numerous accidental discoveries have significantly impacted science and technology. In 1928, Alexander Fleming noticed that a mold contaminating his *Staphylococcus* culture inhibited bacterial growth, leading to the discovery of penicillin, the first widely used antibiotic. Similarly, Wilhelm Conrad Röntgen's observation of unknown rays emanating from a cathode ray tube in 1895 resulted in the discovery of X-rays, revolutionizing medical imaging. Additionally, the invention of the microwave oven stemmed from Percy Spencer's chance observation that radar emissions melted a candy bar in his pocket, leading to the realization that microwaves could cook food. But to me, the coolest serendipity history is that of the Green Fluorescent Protein (GFP).

In 1962, Osamu Shimomura and his colleagues isolated a protein responsible for the green fluorescence observed in the deep-sea jellyfish *Aequorea victoria*. This protein was later named Green Fluorescent Protein. Initially, GFP's potential applications were not evident, and it remained a biochemical curiosity for several decades. In 1989, Martin Chalfie, a geneticist at Columbia University who had never heard of GFP before, happened to attend a seminar where GFP was briefly mentioned[2]. He realized the potential of the protein as a reporter in living cells. After five years of cloning and trial and error, he finally demonstrated that the GFP gene could be expressed and fluorescence obtained in organisms other than jellyfish, such as *Escherichia coli* and *Caenorhabditis elegans*[3].This breakthrough allowed GFP to serve as a fluorescent marker, enabling visualization and tracking of proteins within living cells without the need for additional substrates or cofactors. Roger Tsien[4] further expanded GFP's utility by engineering variants with different fluorescence spectra and improved stability, broadening the scope of GFP-based applications (see examples in Figure 1[a]) .

GFP's versatility led to its integration into a wide array of biological research applications. It facilitated real-time observation of protein localization, movement, and interactions within living cells, revolutionizing the study of protein dynamics. As a reporter gene, GFP enabled visualization and quantification of gene expression patterns across organisms and tissues. Researchers uses GFP to track cell division, differentiation, and migration during development or in response to treatments, enhancing our understanding of developmental biology. Additionally, GFP served as a foundation for developing biosensors that detect changes in cellular conditions, such as pH, ion concentrations, or

[a] Underlined texts in this document are links to other parts of the documents or to websites.

the presence of specific metabolites[5]. Recent techniques like Bimolecular Fluorescence Complementation uses split GFP fragments to study protein-protein interactions within their native cellular environments[6,7].

GFP and other derived fluorescent proteins (FPs) have been instrumental in numerous scientific breakthroughs, a significance recognized by the 2008 Nobel Prize in Chemistry awarded to Osamu Shimomura, Martin Chalfie, and Roger Tsien[8]. In neuroscience, it enables mapping of neural circuits and understanding neuronal connectivity through visualization of specific neurons and their networks[9]. In developmental biology, FPs facilitate elucidation of embryonic development processes by allowing real-time tracking of cell fate and tissue formation. Cancer research benefits from FPs through monitoring tumor growth, metastasis, and angiogenesis in live animal models, leading to insights into cancer progression and potential therapeutic interventions. In drug discovery, GFP facilitates high-throughput screening assays to identify compounds that modulate specific cellular pathways or protein interactions. Moreover, in synthetic biology, FPs enable the construction and visualization of synthetic genetic circuits and pathways within living organisms.

Therefore, in the span of a few decades, this obscure marine protein transformed from a niche biochemical curiosity into an illuminating and indispensable tool across various disciplines, profoundly impacting modern biological research.

In recent years, a new similar phenomenon has emerged. An obscure marine biology discovery, known for decades, has recently gained significant interest as a potential new tool for biologists. **Gas vesicles,** gas-filled structures found in certain aquatic microorganisms, have demonstrated remarkable acoustic properties, making them potential **genetically encoded acoustic reporters**, among other applications. Gas vesicles are central to my research**.** Although numerous proof-of-concept studies over the past few years have demonstrated the use of gas vesicles as genetically encoded acoustic reporters, little attention has been paid to the physiological impact of gas vesicles production on the host cells. During my PhD, I focused on evaluating the cellular burden and potential costs associated with GV expression. This work provides essential insights required to transition gas vesicles from experimental demonstrations to robust and widely applicable imaging tools. To provide context for my work, the following sections will detail the structure, natural functions, biosynthesis, and potential applications of gas vesicles.

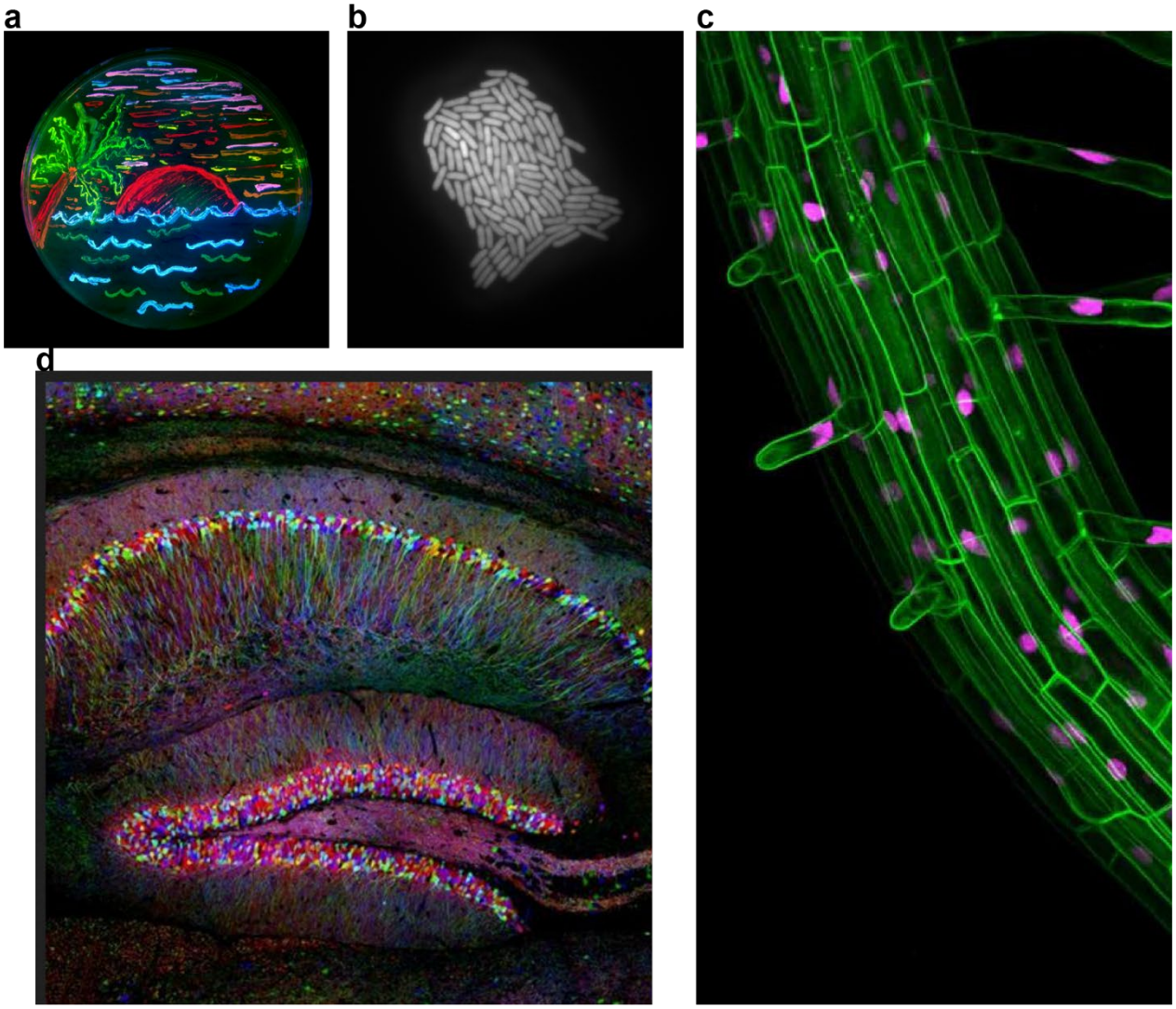

Figure 1 : Diversity and applications of fluorescent proteins : (**a**) Petri dish art featuring *Escherichia coli* expressing a palette of FPs spanning distinct emission spectra, including GFP, BFP, mTFP1, Emerald, Citrine, mOrange, mApple, mCherry, and mGrape. From Nathan Shaner in Roger Tsien lab (link) (**b**) Microcolony of *E. coli* expressing constitutive GFP on an agar pad, enabling single-cell segmentation and lineage tracking, a foundational tool in analyzing time-lapse microscopy of bacterial populations. Image captured by the author. (**c**) Root tissue of *Arabidopsis thaliana* expressing a membrane-targeted GFP and a nuclear RFP fusion, demonstrating multi-channel localization of subcellular structures using spectrally distinct FPs. From Fernan Federici (link). (**d**) Brain section from a "Brainbow" transgenic mouse in which Cre–lox recombination stochastically drives expression of multiple FPs in individual neurons, enabling discrimination of adjacent neurons by unique spectral signatures and facilitating reconstruction of neural circuits[10].

Discovery of gas vesicles

The gas vacuole theory

Water blooms are captivating natural phenomena. Across the globe, in water bodies such as lakes, rivers, ponds, and coastal areas, the color of water can undergo dramatic seasonal changes, turning green, blue, or even an intense, almost apocalyptic red (commonly referred to as "red tides"). In some cases, blooms can create bioluminescent displays, adding an almost magical effect to the aquatic environment (Figure 2a-c).

These blooms result from the rapid proliferation and accumulation of microscopic algae or cyanobacteria (blue-green algae) at the water's surface, sometimes reaching massive proportions (Figure 2c). While such events can occur naturally, human activities frequently exacerbate their occurrence. Factors such as agricultural runoff, sewage discharge, and industrial pollution contribute significantly to the frequency and intensity of these blooms. In the late 19th and early 20th centuries, microbiologists began examining these blooms under the microscope. Among them, the German scientist Robert Lauterborn vividly described the microscopic world revealed by these investigations:

"An unexpected abundance of forms [...] so rich and so beautifully diverse in their adaptations to the crystalline environment that not only dedicated researchers, eager to claim this promising field, have taken interest, but also an ever-growing number of enthusiasts who approach nature purely for aesthetic delight and contemplation." [11]

Among many floating microorganisms, researchers observed intriguing intracellular structures: conspicuous, refractile bodies of varying size and shape (Figure 2d-e). The nature of these structures was initially a topic of debate. In 1894, Richter proposed that these bodies were droplets of sulfur in a soft, oily state[12]. Others, however, hypothesized that these structures were gas-filled vacuoles. The gas vacuole theory was pioneered by two German scientists, Strodtmann and Klebahn. The most famous experimental demonstration of this idea was conducted by Klebahn in 1895[13], who designed the "Hammer, Cork, and Bottle" experiment (Figure 2g). He collected surface water from a nearby lake experiencing a water bloom, sealed it in a sturdy glass bottle with a cork stopper tightly in contact with the suspension, and struck the bottle sharply with a hammer. The experiment yielded three key observations:

- The appearance of the suspension changed immediately, shifting from milky to dark.
- Gas bubbles accumulated under the cork.
- The algal cells gradually sank to the bottom of the bottle.

Furthermore, microscopic examination of the cells revealed that most of the refractile bodies had disappeared (illustrated in Figure 2e-f; note that these are not the original images from Klebahn's work). Klebahn concluded that these vacuoles must have been gas-filled structures that collapsed under the increased pressure caused by the impact.

This experiment, simple and easily reproducible, quite literally hammered in the idea that the refractile bodies visible in floating microorganisms were filled with gas. Over time, various terms were used to describe these structures, including hollow bodies, aerosomes, pseudovacuoles, and flotation bodies. However, the term “gas vacuole”, introduced by Klebahn, ultimately became the standard nomenclature in the field[14,15].

From gas vacuole to gas vesicles

In the decades following Klebahn’s discovery, extensive research was conducted on gas vacuoles, focusing on their presence across different species and the environmental conditions influencing their formation. Researchers also speculated on their functional role within gas-vacuole-producing cells. However, little progress was made in understanding the fundamental nature of gas vacuoles themselves.
This lack of advancement was likely due to, at least in part, technological limitations. Gas vacuoles were simply too small to be observed in detail using light microscopy. As Fogg stated in his 1941 review[12]:

> *“The nature of the vacuole membrane is obscure, although its ready destruction by traces of fat solvents suggests that it may be of a lipide nature.”*

This hypothesis, however, would later be proven incorrect.

Although the first commercial electron microscope became available in 1938, it was not until 1965 that Bowen and Jensen[16] produced the first electron microscopy images of gas vacuoles, finally allowing researchers to take a closer look at gas vacuole structures. In *Aphanizomenon flos-aquae*, researchers observed that gas vacuoles were not, as previously thought, composed of a single membrane. Instead, they were formed by an assembly of arrays of electron-transparent cylindrical vesicles (example shown in Figure 3b). These structures were logically named "gas vesicles." This discovery revitalized interest in the study of gas vacuoles.

In the following chapter, I will review the current state of knowledge on gas vesicles, including their composition and structure, genetic regulation, assembly process, ecological roles, and potential applications as research tools.

Before proceeding, however, I would like to acknowledge Professor Anthony Edward Walsby, a microbiologist who, from the late 1960s to 2006, dedicated much of his research to the study of gas vesicles. His work made a profound impact on the field, and his reviews, most notably his 1994 publication, modestly titled "Gas Vesicles"[17], even though now partially outdated, served as a treasure trove of information and an invaluable resource in shaping my understanding of the subject.

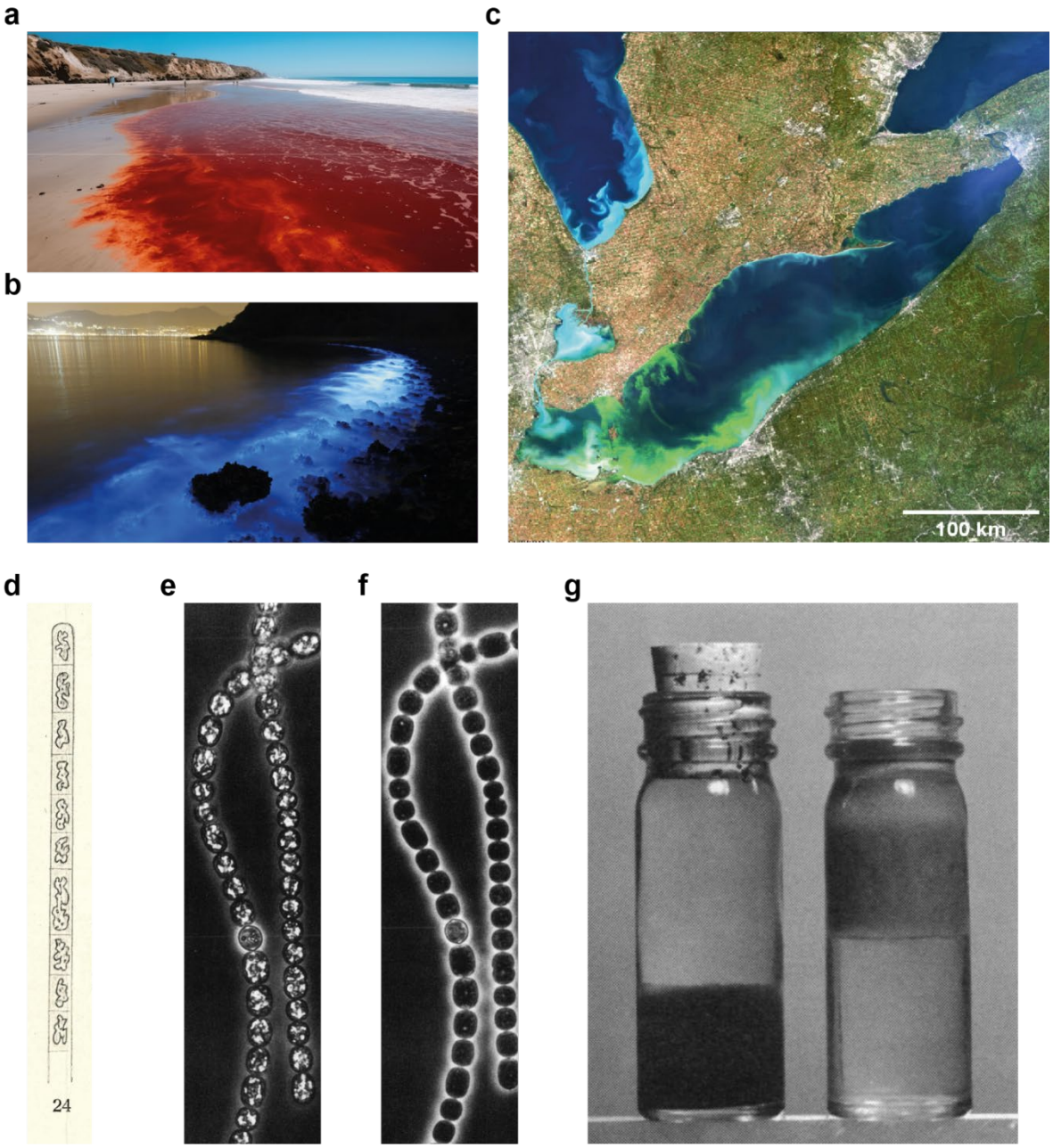

Figure 2 : Water blooms and the discovery of Gas Vacuoles (**a**) "red tide" caused by the blooming of red pigmented dinoflagellate cyanobacteria. Here on San Digeo beach (image from Wyatt Sloan (link)) (**b**) long exposure image a bloom of *Noctiluca scintillans* in Hong Kong (from Kin Cheung for The Atlantic (link)) (**c**) Satellite image of large algae bloom in Lake Erie (from European Space Agency (link)) (**d**) 1901 drawing of *Oscillatoria Lauterbornii* with gas vacuoles visible in individual cells[11] (**e**) Filaments of the cyanobacterium *Anabaena flos-aquae* with gas vacuoles visible as bright white spots within cells[17] (**f**) Same filament after collapse of the vacuoles application of a pressure of 1.0 MPa, where most vacuoles disappeared[17] (**g**) Reproduction of Klebahn's "Hammer, Cork, and Bottle" experiment[14]. On the right, a bottle containing a preserved water bloom sample, with a milky clump of floating cells. On the left, the same sample after being subjected to a sudden pressure increase from a hammer strike. Note that the cells have sunk, and the clump has taken on a much darker appearance.

Gas vesicles in nature: environment, species and functions

In a recent genomic mining experiment run in 2023, Hurt and colleagues reported that genes involved in the production of gas vesicles could be found in hundreds of species and that gas vesicles production had so far been reported in the literature in 253 species[18] (Figure 3a). These species span across eight bacterial phyla and two archaeal phyla[17,18]. Gas vesicle-producing organisms are predominantly aquatic microorganisms, including photosynthetic bacteria, mesophilic haloarchaea, and psychrophilic heterotrophic bacteria[19]. They are found in a wide range of environments[17], like deep freshwater lakes, estuaries, coastal basins, saline lakes but also in more extreme environments like hypersaline brine pools[20] and even in the arctic ices[21,22]. Such environment typically contains stratified water columns (waters with layers of salinity, oxygenation, density and temperature at different depths).

The widespread occurrence of gas vesicles is comparable to that of photosynthesis, raising questions about their evolutionary origin[17]. Given their phylogenetic distribution (Figure 3a), gas vesicles may have originated in an ancestral lineage predating the divergence of bacteria and archaea. Alternatively, their presence across distantly related organisms could be the result of lateral gene transfer. A key to distinguishing between these possibilities lies in the homology of gas vesicle gene sequences across different taxa. If gas vesicles originated from a common ancestor, one would expect sequence homology to decline with increasing phylogenetic distance. Conversely, if their widespread distribution were primarily due to lateral gene transfer, no clear correlation between phylogenetic distance and homology would be expected. Analysis of the GvpA[b] gene, which encodes the main structural protein of gas vesicle walls (see Structural Proteins and the Structure of Gas Vesicle Walls section), supports the hypothesis of vertical inheritance. The lowest homology (54–64% identity) is observed between halobacteria and cyanobacteria, the most phylogenetically distant gas vesicle-producing groups. In contrast, within cyanobacteria, sequence identity ranges from 79–100%, with the highest similarity (98–100% identity) observed among closely related heterocystous genera (*Anabaena, Aphanizomenon*, and *Calothrix* spp.). Similar patterns have been observed in other genes involved in gas vesicle production. These findings support the hypothesis that gas vesicle genes were inherited vertically rather than acquired through lateral gene transfer, suggesting that their origin traces back to an ancestral lineage predating the bacterial and archaeal domains[17,23]. It does not exclude however the possibility of some lateral gene transfers.

What functions do gas vesicles serve? Since the discovery of gas vacuoles, multiple hypotheses have been proposed to explain their ecological and physiological roles:

The primary and most widely accepted function of gas vesicles is buoyancy regulation, enabling microorganisms to adjust their vertical position in aquatic environments. Most of what composes living cells is denser than water: the density of protein is approximately 1330 $kg.m^{-3}$, that of carbohydrate is 1550 $kg\ m^{-3}$, that of nucleic acid is above 1660 $kg\ m^{-3}$, and that of glycolipid is 1050 $kg\ m^{-3}$. This means that most cells should sink in water. Cyanobacteria *Anabaena flos-aquae* for example has a density (without gas vesicles) of roughly 1060 $kg\ m^{-3}$ (compared to 998 $kg.m^{-3}$ for fresh

[b] Gvp stands for Gas Vesicle Protein. Each protein encoded in the gas vesicle operons are referred to as Gvp followed by the a letter (here for example A) indicating specific protein.

water, or 1025 $kg.m^{-3}$ for sea water at 20°C). However, gas vesicles have a much lower density, between 100 and 160 $kg.m^{-3}$ (taking vesicle's wall mass into account). Therefore, accumulating gas vesicles reduces the overall cell density by replacing a certain volume of water by gas, not unlike what submarines does. For *Anabaena flos-aquae,* this means that to reach neutral buoyancy it must have at least 6.2% of its volume occupied by gas vesicles, a value which they can surpass, reaching up to 9.8%[17].

But why is buoyancy so important? Buoyancy control can bring many advantages to cells in aquatic environments. As previously mentioned, many of these organisms are photosynthetic and require sunlight for survival. However, light availability decreases sharply with depth. The ability to float toward the surface ensures access to optimal light conditions. In cyanobacteria such as *Anabaena flos-aquae, Calothrix, Planktothrix*, and *Microcystis*, gas vesicle production has been shown to correlate with light intensity, decreasing light levels trigger increased vesicle formation[19,24]. Interestingly, buoyancy control is not exclusive to photosynthetic organisms. Some non-photosynthetic archaea, such as members of the *Halobacteriaceae*, rely on the membrane-bound light-driven proton pump bacteriorhodopsin, which directly converts light energy into a proton gradient for ATP synthesis. These cells may also benefit from controlled buoyancy to maximize light exposure, and indeed, several species possessing bacteriorhodopsin have been shown to produce gas vesicles[20].

Beyond light acquisition, buoyancy regulation also plays a crucial role in oxygen availability. In stagnant, salt-saturated brine, the high salinity and lack of mixing lead to steep oxygen gradients, with oxygen concentration decreasing with depth. In such conditions, gas vesicle production in *Halobacterium salinarum* can provides a selective advantage by allowing cells to reach the more oxygen-rich upper layers[25]. These are but a few examples of situations where buoyancy control is advantageous, in stratified water, it can also help to reach optimal salt concentration water layers, access to nutrients or even facilitate spreading[17].

Could gas vesicles serve as oxygen reservoirs for aerobic bacteria? This idea was suggested early in the study of gas vacuoles. However, this function is unlikely. As I will explain later in Why is there only gas in gas vesicles? And what gas is it? section, gas molecules diffuse freely across the GV protein shell. Therefore, the internal gas composition of gas vesicles rapidly equilibrates with the surrounding environment, depending on the partial pressures of each gas. In the absence of active transport or selective permeability, gas vesicles cannot maintain elevated concentrations of specific gases such as O_2 and thus cannot function as true storage compartments.

Several authors have hypothesized that gas vesicles may provide light shielding, protecting cells from the harmful effects of excessive UltraViolet (UV) radiation[17]. This idea arises from the fact that gas vesicles scatter light due to the significant difference in refractive index between gas and the surrounding cytoplasm or medium. This scattering effect is also what makes gas vacuoles visible under optical microscopy. However, does this scattering provide meaningful UV protection to cells? Experimental studies investigating cellular responses to increasing UV exposure, with and without gas vesicles, in *Halobacterium salinarum*[26] and *Anabaena flos-aquae*[27] found no significant protective effect against UV-induced damage. Similarly, research on *Microcystis aeruginosa* comparing light-energy absorption of cell suspensions with and without gas vesicles found no correlation, further suggesting that any shielding effect is negligible[28]. To date, no direct or indirect evidence supports the idea of a protective role of gas vesicles against light damage.

In conclusion, the only function of gas vesicles for which we have convincing evidence so far is to adjust cells buoyancy, allowing them to reach more favorable environmental conditions in water with access to light, oxygen or nutrients. However, there are some exceptions for which the function of gas vesicles remains unknown. This is notably the case non-aquatic *Bacillus megaterium*[29] and several species actinomycetes[30], a group of soil bacteria. Considering these organisms don't live in water, they probably don't need to adjust their buoyancy, so their gas vesicle are likely to serve another unknown function.

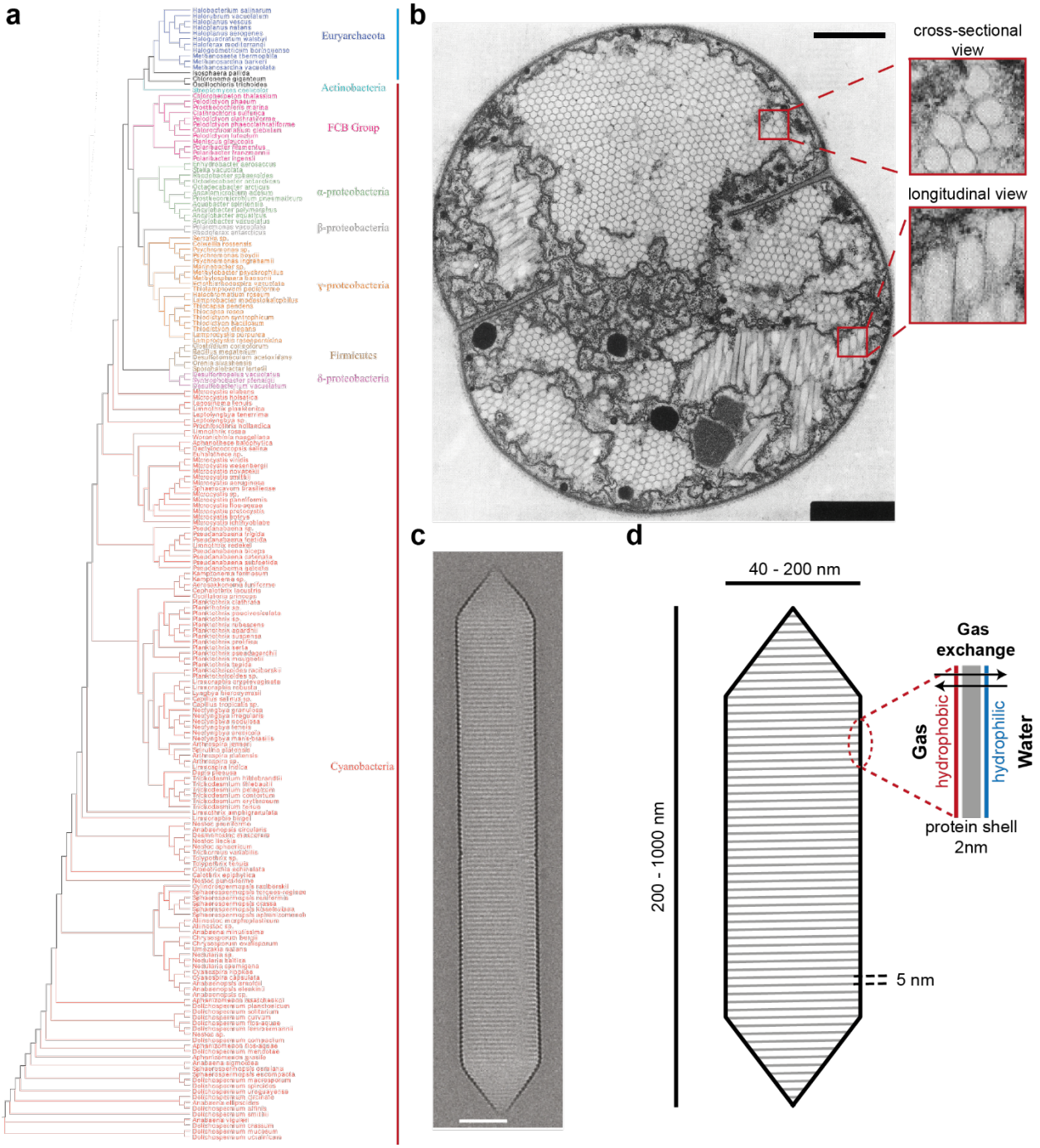

Figure 3 : Morphology of gas vacuoles, single gas vesicles and their phylogeny. (**a**) 16S phylogenic tree of all 253 known gas-vesicles-producing organisms (as of 2024), with color indicating different phyla, red vertical line indicates bacteria, blue vertical line indicates archaea. From Hurt, R. C. *et al.* 2024[18]. A larger version is available in Appendix 1 (**b**) Section of cyanobacteria *Microcystis sp.* with gas vacuoles in transmission electron microscopy. Single gas vesicles are visible in cross sectional view, where their honeycomb organization is clear and in a longitudinal view, where their characteristic spindle shape is visible. Scale bar, in top right corner, represents 1µm. From Walsby, A. E. 1994[17]. (**c**) Longitudinal view of single purified gas vesicles from *Anabaena flos-aquae* in cryo electron microscopy. The scale bar represents

50 nm. From Dutka, P. *et al.* 2022[31] (**d**) Schematic representation of a single gas vesicle with average dimensions ranges annotated.

Gas vesicles general morphology

Gas vesicles are intracellular organelles located within the cytoplasm of the organisms that produce them. While their size and composition vary between species, they share several fundamental structural features, which are introduced below.

General Morphological Characteristics of Gas Vesicles (see Figure 3):

- Most mature gas vesicles have the shape of hollow cylinders with conical end caps.
- Their dimensions range from 200 to 1000 nm in length and 45 to 200 nm in width.
- The central lumen is filled with gas.
- They tend to cluster, forming gas vacuoles.
- The vesicle wall is approximately 2 nm thick.
- Their surface features ribs with a spacing of 4–5 nm.
- They collapse under increased pressure

Among the morphological characteristics, some are highly conserved across all phyla, including overall shape, gas-filled lumen, organization into vacuoles, wall thickness, and rib spacing. In contrast, other traits, such as width, length and collapse pressure, exhibit significant variation between species.

In the following sections on gas vesicle morphology, we will examine these variable traits (width, length, and collapse pressure) in more detail and analyze the potential causes of this variability. We will then take a closer look at the structure of gas vesicles at the molecular scale.

Gas vesicle width and what influence it

The width of gas vesicles can be directly measured using cryo electron microscopy or indirectly derived from widths of flat collapsed and negatively stained vesicles[32,33]. It is relatively uniform within a single species. For instance, Walsby and colleagues demonstrated that in the cyanobacterium *Anabaena flos-aquae*, the diameter of gas vesicles follows a normal distribution centered at 84 nm, with a standard deviation of roughly 5% of the mean[33]. However, substantial variation exists between different species (Table 1), with width varying between 45nm to 200nm[17]. This variability is likely as an adaptive response to specific environmental conditions. Indeed, the production of gas vesicles represents a significant energetic investment; in *Anabaena flos-aquae*, it has been estimated that approximately 3% of the cell's dry weight must be allocated to GvpA synthesis to generate sufficient gas vesicles for neutral buoyancy[34].

To evaluate the cost-effectiveness of gas vesicles across species, one metric is the ratio of internal gas volume (Vi) to wall volume (Vw). A higher Vi/Vw ratio indicates that more gas can be stored per

unit of wall material, enhancing the vesicle's buoyancy efficiency. A 1988 study[33] proposed a mathematical model to estimate this ratio, which is presented in Appendix 2. The ratio *Vi/Vw* for various lengths and widths is also presented in Appendix 2. It shows that vesicle width has the most significant influence on the cost-efficiency of gas vesicles, with larger vesicles exhibiting greater efficiency, while length has little impact. However, some gas vesicles are notably more cost-effective than others. For instance, vesicles from *Dactylococcopsis salina* require 2.44 times less material than those of *Trichodesmium thiebautii* to store the same volume of gas. This difference likely arises from variations in environmental constraints affecting the gas vesicles.

One such factor is the pressure to which gas vesicles are exposed. As previously mentioned, increasing pressure can cause gas vesicles to suddenly and irreversible collapse, leading to gas loss and a reduction in buoyancy. This represents a net loss for the cell, as the buoyancy gained through this significant investment is entirely lost. In natural environments, the total pressure exerted on gas vesicles (*Pn*) is the sum of atmospheric pressure (*Pf*, approximately 0.1 MPa), hydrostatic pressure (*Ph*, which increases by roughly 0.01 MPa per meter of water depth), and cell turgor pressure (*Pt*, which varies between 0 and 0.5 MPa depending on the cell type and its environment), minus the internal gas pressure (*Pg*). As I will discuss in a following section, the gas inside the vesicles remains in equilibrium with dissolved gases in the surrounding solution, which, under natural conditions, typically corresponds to atmospheric pressure (*Pf* ≈ 0.1 MPa)[35]. Each vesicle has a maximum pressure threshold, known as the critical pressure (*Pc*), beyond which it collapses (when *Pn*>*Pc*)[17]. *Pc* is measured as the pressure above which more than 50% of the vesicles in a population collapse.

$$Pn = Pf + Ph + Pt - Pg$$

Critical pressure (*Pc*) varies widely among organisms. At one extreme, gas vesicles from the halophilic bacterium *Halobacterium* have a *Pc* of only 0.09 MPa[36]. Conversely, gas vesicles from *Trichodesmium thiebautii* exhibit an exceptionally high critical collapse pressure. In fact, when first investigated by Walsby and colleagues, the available pressure nephelometers were unable to generate sufficient pressure to collapse the vesicles, leaving Pc undetermined. To overcome this limitation (and perhaps seizing an opportunity for fieldwork in the Caribbean Sea) the researchers sealed the cells in a bottle fitted with a serum stopper and submerged it to a depth of 700 meters, where the hydrostatic pressure reaches approximately 7 MPa. Upon recovery, all gas vesicles were found to have collapsed. In subsequent experiments using improved high-pressure nephelometers, the Pc of *Trichodesmium thiebautii* was directly measured at 3.7 MPa[37].

Interestingly an inverse correlation between gas vesicles width and Pc can be noted. Walsby and Bleything investigated this relationship across seven cyanobacterial genera and found the inverse correlation described by the following equation[33,38] :

$$Pc = 275r^{-1.67}$$

where *Pc* is the collapse pressure (MPa) and r is the vesicle radius (nm). (Note that for these experiments, turgor pressure was first brought to 0 by addition of 0.5 M of sucrose to the culture medium, so that *Pn* can be known even for cell with unknown natural turgor pressure.) The inverse dependence of *Pc* on the radius aligns with the engineer's second mode of collapse by instability failure, which dictates that thin-walled cylindrical structures fail at pressures inversely related to their size[39,40].

Therefore, the width of gas vesicles likely reflects a trade-off between cost efficiency (the volume of gas stored relative to the volume of wall material required) and the pressure constraints imposed by the environment. This balance is exemplified by the gas vesicles of *Halobacterium*, which thrive in shallow, hypersaline pools where hydrostatic pressure is minimal, and turgor pressure is nearly absent as consequence of the high salinity. As a result, their vesicles are wide and highly cost-effective. However, this structural advantage comes at the expense of mechanical resilience. If vesicles from *Halobacterium* were subjected to the same high-pressure conditions as those of *Trichodesmium thiebautii* (which inhabits deeper ocean waters where hydrostatic pressure can increase significantly) they would collapse, rendering the cells unable to maintain the buoyancy necessary for survival. This trade-off highlights the evolutionary adaptation of gas vesicle morphology to specific environmental constraints, optimizing both efficiency and structural integrity in different ecological niches. Hypothesis concerning the molecular changes that can lead to tighter or wider gas vesicles will be addressed in the section Structural proteins and the structure of gas vesicles walls.

While vesicle width is undoubtedly a key determinant of collapse pressure, it is not the only factor. The equation proposed by Walsby and Bleything describes an inverse relationship between vesicle radius and collapse pressure across multiple cyanobacterial genera. However, this model does not accurately predict *Pc* for every species. For instance, it significantly underestimates the *Pc* of *Trichodesmium thiebautii* (predicated at 1.52 MPa, compared to the measured value at 3.7 MPa), suggesting that additional factors contribute to vesicle reinforcement. One such factor is the structural protein GvpC, which has been shown to play a crucial role in stabilizing vesicles against collapse. The role of GvpC and its reinforcing mechanisms are explored in more detail in the section Structural proteins and the structure of gas vesicles walls.

Gas vesicles length

Like gas vesicle width, gas vesicle length also varies between species (Table 1), with reported values ranging from 200 nm to 1000 nm in nature[17]. However, within a single species, the length distribution is considerably broader than that of the width. For instance, in *Anabaena flos-aquae*, the average vesicle length is 494 nm, with a standard deviation of approximately 35% of the mean[36]. As shown in Appendix 2, vesicle length has little to no effect on the cost-efficiency of gas vesicles in cells. Moreover, imaging of surviving vesicles subjected to increasing pressure revealed no correlation between vesicle length and mechanical strength. This suggests that the structural integrity of these vesicles is primarily determined by individual ribs which get little support from their neighbors[36]. These findings indicate that gas vesicle length does not require as stringent a regulation as the width.

Vesicle length appears to be age-dependent, with older vesicles tending to be longer[41]. This observation aligns with current models of gas vesicles assembly (see section Gas Vesicle Assembly). To date, it is not clear what stops the elongation of a gas vesicle or whether anything stops it at all. It is possible that gas vesicles continue elongating until they break due to mechanical constraints, such as pushing against the cell membrane or other intracellular structures. This hypothesis is supported by experimental observations: in *Anabaena flos-aquae*, gas vesicles can reach lengths of up to 800 nm. However, when the *Anabaena flos-aquae* gas vesicle operon is expressed in human epithelial

cells, which have a much larger volume and therefore provide more space for elongation, some gas vesicles were observed to reach lengths exceeding 3500 nm[18].

Species	Average width (nm)	Average length (nm)	Environment	Average Pc (MPa)	Ratio Vi/Vw*	Reference
Trichodesmium thiebautii	45	450	Tropical oceans (up to 200 m deep)	3.7	4.9445	[37,42]
Oscillatoria agardhi	62	337	Freshwater lake (Lake Gjersjøen, up to 70m deep)	0.99 +- 0.13	6.9144	[17,33]
Anabaena flos-aquae	84	494	Surface layer of freshwater Lake (up to 5m)	0.61 +- 0.10	9.7034	[33]
Dactylococcopsis salina	109	292	Shallow salted lake (up to 2.5m deep)	0.33 +- 0.11	12.0697	[33,43]
Halobacterium sp.	133	216	Shallow saturated brines (less than a meter deep)	0.09	13.9532	[36]

Table 1 : Examples illustrating the variety in gas vesicles size and stiffness in different environments (* calculated from model described in Appendix 2)

Gas vesicles operons and proteins

Early studies on gas vesicles revealed that, unlike other organelles, they are composed exclusively of proteins and contain no lipids[44,45]. Structurally, gas vesicles consist of two primary constituent proteins, though their assembly requires the involvement of additional accessory proteins. Gas vesicle proteins, whether structural or accessory, are designated “Gvp” (Gas Vesicle Protein), followed by a letter indicating the specific protein. The genes necessary for gas vesicle formation and assembly are always clustered in operons, the composition of which varies between organisms (Table 2), with roughly 10 genes. Not each gene is unique in a cluster, some cluster can contain several identical copies of the same gene, there are for example reports of *Anabaena flos aquae* cluster containing 7 identical copies of the GvpA gene[46]. There are also clusters that contains several variants of a single genes, and cells that have several independent gas vesicles gene clusters[47]. Furthermore,

not all genes in the gvp operons seems to be necessary to produce functional gas vesicles. In the gas vesicle operon from *Halobacterium salinarum* (Table 2), only 8 out 14 genes were shown to be necessary, although deletions could lead to changes in vesicles dimensions and strength[48]. Stoichiometry also seems to play an important role, as suggested by the various number of copies in different organisms. Experiments also showed that overexpression[49] or underproduction[48] of various genes can alter gas vesicle shape, strength or even prevent their formation.

Species	gvp Gene Cluster(s)
Halobacterium salinarum	gvpACNO + gvpDEFGHIJKLM
Haloquadratum walsbyi	gvpACNO / gvpFGHIJKLM
Anabaena flos aquae	gvpAAAAAAACNJKFGVW
Bacillus megaterium	gvpAPQBRNFGLSKJTU
Methanosarcina barkeri	gvpAAA – NOFG – JHKLM
Serratia sp. ATCC39006	gvpA1CNVF1GWA2KXA3Y / gvpAHZF2F3BC

Table 2 : Gas vesicles gene clusters of various archea and bacteria, illustrating the number of genes involved and the wide variety of their organization between species. (+) indicates that genes or gene clusters are arranged in opposite directions and (−) that gvp genes are separated by unrelated genes not involved in gas vesicle formation; (/) describes two consecutive operons. Adapted from Pfeifer, F. 2022[47].

Decades of research have elucidated the roles and regulation of several of these genes, particularly those encoding structural proteins. However, given the large number of genes potentially involved, their organization into multiple operons, and marked variation among species, our understanding of the gas vesicle operon's overall functioning remains incomplete. In the sections that follow, we examine the proteins required for gas vesicle production, beginning with the principal structural components GvpA and GvpC, and then discuss current knowledge of the accessory proteins and their potential interactions.

Structural proteins and the structure of gas vesicles walls

The primary structural proteins of gas vesicles are GvpA and GvpC. While both are frequently present in gas vesicles, only GvpA is essential for gas vesicle formation. **GvpA constitutes the main component of the gas vesicle wall**[17,19,50]. In *Anabaena flos-aquae*, GvpA accounts for approximately 90–95% of the total gas vesicle mass, while GvpC contributes 5–10%, yielding a GvpA-to-GvpC ratio of 25:1[51].

GvpA is a small protein (~7 kDa) composed of approximately 70 amino acid residues. It adopts a coil-α-β-β-α-coil fold (Figure 4a) with distinct hydrophilic and hydrophobic faces (Figure 4a-b)[31,52]. It is the main component of the gas vesicles wall.

In gas vesicles, GvpA monomers are primarily connected laterally through an extensive hydrogen-bonding network between the β-strand backbones of adjacent monomers. These lateral connections

are further reinforced by a network of salt bridges, specifically involving Glu43-Arg31 between two monomers, leading to the formation of GvpA ribs. As a rib extend, it curves and forms a continuous helix. At each helica turn, the ribs are then interconnected primarily through the N-terminal region of GvpA. The N-terminus extends perpendicularly to helix α1 and folds across the β-hairpin of the adjacent rib, where it forms stabilizing interactions with several residues in the β-hairpin and helix α2. These connections provide the structural integrity needed to form a strong shell from such a continuous helix (Figure 4c-f). This organization results in a structure with walls of one to two GvpA thickness, where helix α1 forms bridges between GvpA ribs, creating empty spaces on each side, which may serve as pores allowing gas diffusion in and out of the vesicle (Figure 4e). Furthermore, the inner surface of the vesicle is predominantly hydrophobic, while the outer surface is largely hydrophilic. This structural model was recently confirmed in two separated studies using high-resolution cryo-electron microscopy (Figure 4c-f) for *Bacillus megaterium*[52] and *Anabaena flos-aquae*[31] gas vesicles.

The GvpA sequence is highly conserved across all phyla, despite significant phylogenetic divergence[17,23]. This conservation suggests that the fundamental assembly mechanism of GvpA is structurally similar across species, a hypothesis supported by computational predictions using AlphaFold2, which have revealed strikingly similar structural models for evolutionarily distant GvpA homologs[52]. However, comparative sequence analyses indicate that the N-terminal, C-terminal, and helix α2 regions exhibit the highest degree of sequence variability[31,31]. These regions, which are critical for rib-to-rib connections, undergo more frequent mutations compared to the relatively conserved core of the protein (Figure 4g). They play a key role in stabilizing interactions between GvpA monomers, and variations in their amino acid composition influence the mechanical strength and diameter of gas vesicles[31,53]. What these mutations specifically change in the structure of GvpA polymers is still unclear, but we can speculate that differences in these regions could affect the curvature and spacing of the assembled ribs, thereby modifying the helical twist between GvpA monomers and ultimately determining the final vesicle diameter. There is some experimental evidence supporting this hypothesis. For example in a 2002 study[53], Beard and colleagues noted that changing the 7th residue in the N-terminal region of *Halobacterium salinarum* GvpA from Gly to Ser led to the production of much narrower gas vesicles.

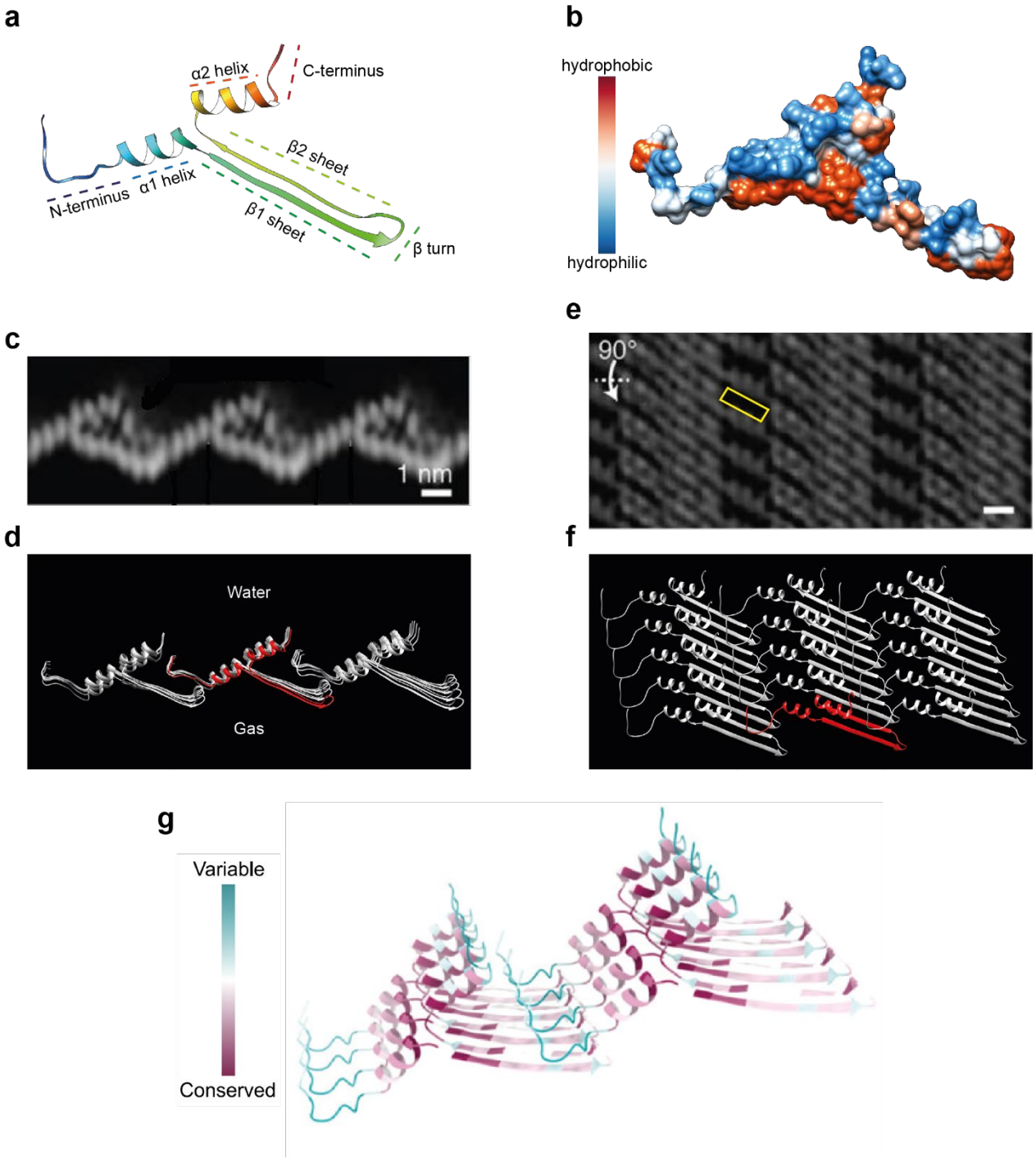

Figure 4 : GvpA protein and its organization in gas vesicle's wall. (**a**) Ribbon diagram of individual GvpA monomer, with domains indicated. Model from Huber *et al*. 2023[52] (**b**) Hydrophobicity of GvpA monomer, note the strong hydrophilic face above the α1 and α2 helix and strong hydrophobic face under α1 helix and β sheets. (**c**) 2D-projected side view of *Bacillus megaterium* gas vesicle wall in 3.2 A˚cryo-EM. Here water is above the structure and gas below it. Adapted from Huber *et al*. 2023[52] (**d**) Side view of a ribbon diagram of a 3*5 array of GvpA assembled into a wall section. In red is indicated a single GvpA monomer. (**e**) 2D-projected Top view of *Bacillus megaterium* gas vesicle wall in 3.2 A˚cryo-EM. A single pore, between adjacent α1 helixes is indicated in yellow. Scale bar represents 1nm. Adapted from Huber *et al*. 2023[52] (**f**) Top view

of a ribbon diagram of a 3*5 array of GvpA assembled into a wall section. In red is indicated a single GvpA monomer. (**g**) Conservation analysis of GvpA across different sequences highlighting the conserved and variable regions of GvpA. Adapted from Dutka, P. *et al.* 2022[31]. Models used for (a), (b), (d) and (f) came from Huber *et al*. 2023[52].

The second structural protein of gas vesicles is GvpC. As previously mentioned, GvpC is not essential for vesicle formation, and some species lack this protein entirely. However, in species where it is present, GvpC serves to reinforce the vesicle structure, enhancing its mechanical stability[17,54]. Removal of GvpC, either chemically or through genetic engineering, has demonstrated that its primary role is to reinforce the vesicle wall, allowing it to withstand higher pressures without collapsing. The most compelling evidence of GvpC's stabilizing function was demonstrated by Walsby and colleagues in 1993. In native *Anabaena flos-aquae* gas vesicles, which naturally contain GvpC, the collapse pressure was measured at approximately 0.60 MPa. However, when GvpC was removed via urea treatment of purified gas vesicles, the collapse pressure dropped significantly to 0.19 MPa. Furthermore, native collapse pressure was almost fully restored when the stripped vesicles were re-exposed to recombinant GvpC, confirming that GvpC directly enhances vesicle robustness[55].

GvpC is an amphipathic protein, larger than GvpA, with a molecular weight ranging from 20 to 42 kDa, depending on the species. The primary structural feature of GvpC is a series of repeating 33-amino-acid motifs (or 32–38 amino acid repeats in haloarchaea), which form a long α-helical structure (Figure 5d). GvpC binds to the outer surface of the gas vesicle shell, interacting with multiple GvpA monomers. The number of repeats determines the binding span, with one repeat covering four GvpA monomers[31,52] (Figure 5b-c). For instance, in *Anabaena flos-aquae* GvpC consists of 5 such repeats, plus short N- and C-termini, therefore covering 20 GvpA. Studies with recombinant GvpC with various numbers of repeats showed that the more repeats per GvpC there is, the stronger the vesicle will be[56]. Similarly, it has been showed that increasing the number of GvpC attached to a vesicle, until saturation, also increases the critical pressure it can withstand[55]. Notably, GvpC does not interact with isolated GvpA monomers, but only with the assembled vesicle wall[57]. Recent cryo-electron microscopy and electron tomography studies suggest that GvpC binds specifically with the surface-exposed α2 helix of GvpA (Figure 5a), aligning along the ribs of the vesicle and not across several ribs as it had been speculated in the past[31,52]. Furthermore, crosslink identifications by mass spectrometry reveled potential GvpC-GvpC crosslinks near the N and C terminus of the protein, suggesting potential tail-to-tail interactions that would reinforce the structure even more[31]. The exact mechanism by which GvpC binding along GvpA ribs increases the collapse pressure of a gas vesicle is not fully understood. However, a plausible explanation is that GvpC attachment increases the overall thickness of the vesicle's wall from approximately 3 nm to 4 nm at the binding sites. Since the buckling pressure of thin-walled cylinders is proportional to the cube of the wall thickness[58], this would result in a higher collapse pressure.

By reinforcing the vesicle shell, GvpC enables bacteria to produce stronger vesicles without reducing their diameter, thereby maintaining buoyancy cost-efficiency (see Gas vesicle width and what influence it section). While narrower vesicles are more resistant to pressure-induced collapse, the presence of GvpC provides the cell an alternative strategy for enhancing vesicle strength without sacrificing flotation efficiency.

Unlike GvpA, the GvpC sequence varies widely between organisms. However, sequence homology analysis of 91 GvpC repeat sequences revealed that nine residues are conserved in more than 90%

of them. These residues are all clustered on the same face of the helix. Furthermore, any modification of these conserved residues was shown to abolish the stabilization of gas vesicles by GvpC. This strongly suggests that these residues play a crucial role in the binding of GvpC to the vesicle shell[52].

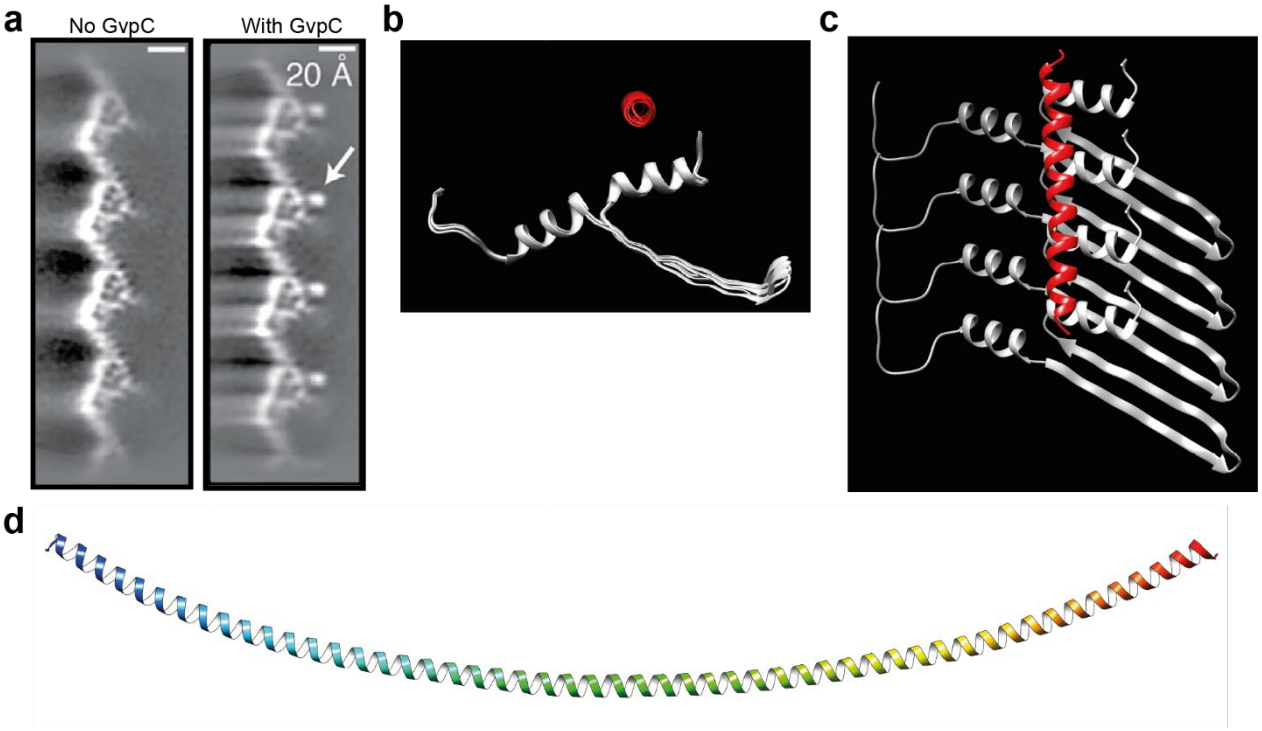

Figure 5 : GvpC and its binding to GvpA shell. (**a**) 2D-projected side view of *Anabaena flos-aquae* gas vesicle wall in 3.2 A˚ cryo-EM without (left) and with (right) GvpC bonded. GvpC are visible as dots, like the one indicated by the arrow. Adapted from Huber *et al*. 2023[52]. (**b**) Side view of a ribbon diagram of a single GvpC repeat attached to a wall section of 4 GvpA monomers. The GvpC repeat is shown in red. (**c**) Top view of (b). (**d**) AlphaFold2 prediction of a full *Anabaena flos-aquae* GvpC[59]. Models used for (b) and (c) came from Huber *et al*. 2023[52].

Accessory proteins

In this section, the term "*accessory proteins"* refers to proteins that are not incorporated into the final purified structure of mature gas vesicles. These proteins are encoded within the same gene clusters as the structural components and are notable for their number and functional diversity. While many of their precise roles remain unresolved, they are generally thought to contribute to transcriptional regulation or serve as chaperones during gas vesicle biogenesis. Although the specific composition of accessory proteins varies among gas vesicle-producing microorganisms, a core set of conserved proteins has been identified as essential for gas vesicle formation. In the archaeon *Halobacterium salinarum*, seven such proteins (excluding GvpA) have been shown to be required: GvpO, GvpF, GvpG, GvpJ, GvpK, GvpL, and GvpM[48]. Homologues of these proteins are also found in gas vesicle-producing bacteria, albeit sometimes under different names[19].

In 2020, Völkner and colleagues[57] used split-GFP analysis to investigate protein–protein interactions among these components, concluding that they likely function as chaperones during the early stages of gas vesicle assembly. They proposed that GvpL serves as a scaffold for a nucleation complex that includes GvpF, GvpG, GvpM, GvpK, GvpH, GvpI and GvpJ. The exact temporal sequence of these interactions remains unclear. This complex is hypothesized to facilitate the initiation of gas vesicle formation, possibly by shielding the hydrophobic inner surfaces of the GvpA-formed ribs before the structure is fully closed. The role of GvpO, the only essential protein that does not participate in this nucleation complex, is still uncertain, though it has been shown to bind directly to GvpA[60].

While not strictly necessary for gas vesicle formation, several other accessory proteins contribute important auxiliary functions. GvpD and GvpE, for example, are involved in transcriptional regulation in archaea[61]. GvpN, an AAA-ATPase, is believed to supply energy for the elongation of the initial bicone-shaped gas vesicle. Mutants lacking GvpN produce only small vesicles that fail to elongate into the characteristic cylindrical shape[62,63] (Figure 6a). GvpU appears to mediate interactions between individual gas vesicles, promoting the formation of organized clusters, likely through binding to the C-terminal region of GvpA. Deletion of GvpU results in disorganized vesicles, which fail to form the typical honeycomb-like arrangements[64]. The function of GvpI remains unclear, though ΔI mutants exhibit longer gas vesicles than wild-type strains[48]. GvpI, GvpH, and GvpA have been shown to interact, and mutants lacking GvpH produce gas vesicles that are mechanically weaker than those of the wild type[48].

Finally, the relative expression levels of accessory proteins in comparison to GvpA are critical not only for efficient gas vesicle production, but also for overall cellular health. An imbalance in expression can severely disrupt cell physiology. In one extreme case, overexpression of GvpG in *Serratia* led to complete growth arrest and a marked reduction in viability[49].

Assembly molecular mechanisms

Despite significant progress in recent years, the exact mechanisms of gas vesicle assembly remain poorly understood. Electron microscopy of gas vesicles in cells shows that they begin as small bicones that grow until reaching a specific width, after which they elongate from the center with a constant diameter, forming the cylindrical central portion of the structure. The precise mechanisms by which the original bicones form remain unknown, but they likely involve a complex of chaperone proteins mentioned in the previous section. Similarly, the mechanism underlying the transition from bicone to cylinder is also unclear. However, recent work using high-resolution cryo-electron microscopy and structural modeling has provided insights into the elongation mechanism of the cylindrical portion[52]. These studies established that the gas vesicle shell is composed of two helical half-shells with opposite GvpA orientations, joined along a central seam. It remains uncertain whether the bicone represents the initial structure of the gas vesicle or results from the fusion of two independently formed nuclei assembling in opposing orientations[50]. In some cases, the two half-shells differ slightly in width, making the seam more visually apparent (Figure 6b and c). Since GvpA orientation is opposed between the two half-shells, the seam features two GvpA subunits in an inverted arrangement, a unique “polarity reversal point” (PRP) where the helical orientation of the

lattice is reversed. Structural modeling predicts that this junction is intrinsically weaker, with only six hydrogen bonds forming between oppositely oriented GvpA monomers, compared to eleven between monomers of the same orientation. This reduced bonding makes the PRP energetically more favorable for transient opening. Such an opening could allow the insertion of a single GvpA monomer, which may stochastically adopt either orientation and continue lattice extension. If this hypothesis is correct, it implies that the seam is not necessarily centered along the longitudinal axis of the gas vesicle, as growth of the two half-shells may be asymmetric. Indeed, such asymmetry in shell dimensions has been independently observed in multiple studies[31,52].

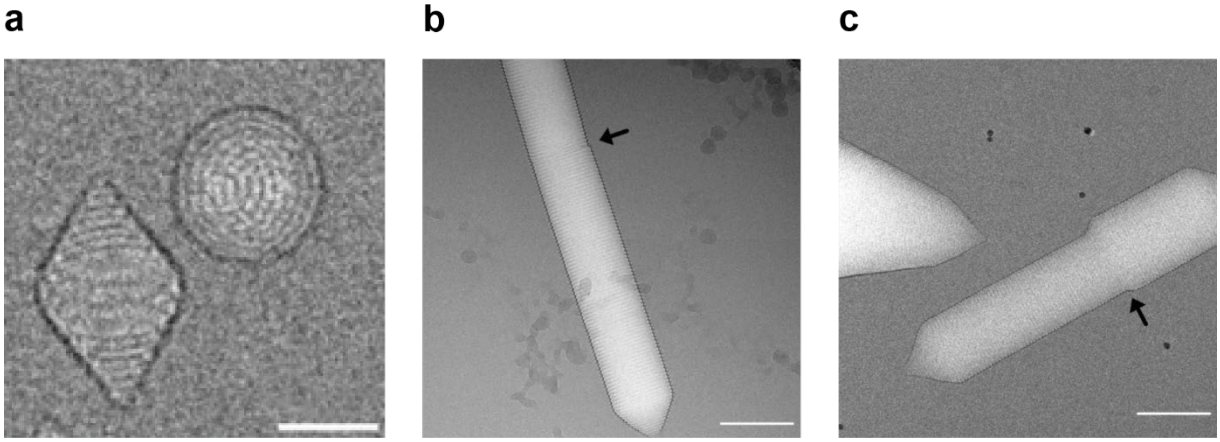

Figure 6 : Gas vesicles shape alterations illustrating the functions of Accessory proteins and the assembly mechanisms (**a**) Gas vesicles without GvpN stay stuck in small bicone shape. Scale bar represents 25nm. From Ling *et al.* 2024[63]. (**b**)(**c**) Gas vesicles seam made clearly visible by width difference between half-shells (**b**) in *Anabaena flos-aquae gas* vesicle (**c**) in *Halobacterium salinarum* gas vesicle. Scale bar represents 100nm. Arrows indicate the seam localization. (b) and (c) from Dutka *et al.* 2023[31].

Why is there only gas in gas vesicles? And what gas is it?

What gas do gas vesicles contain? This is an important question, and although I have already touched on it in the section Structural Proteins and the Structure of Gas Vesicle Walls, I would like to clarify it further here.

Gas vesicles often evoke comparisons to bubbles or balloons, but these analogies are misleading. Unlike bubbles, gas vesicles are rigid structures, their volume remains mostly fixed, with only slight changes (up to approximately 8%) under increased pressure[65]. Their shape is not maintained by internal gas pressure but by the structural integrity of their protein shell. As mentioned earlier, gas vesicle walls contain pores. Cryo-electron microscopy analysis determined that the average pore diameter in *B. megaterium* gas vesicles is approximately 0.38 nm[52], a value likely similar in other gas vesicles, given the highly conserved structure of the GvpA protein. Because of their small size, the pressure required for bulk water to penetrate the gas vesicle as a liquid, as predicted by the Young–Laplace equation (where Δp is inversely proportional to the pore radius), reaches several hundred

MPa. This far exceeds any pressure experienced in natural environments and is well beyond the mechanical tolerance of gas vesicle shells. While individual water molecules, in the form of vapor, can diffuse through the gas vesicles pores, condensation inside the vesicle is prevented by the hydrophobic inner surface, which provides no nucleation sites for water molecules to accumulate and form liquid droplets[66]. As a result, water remains in vapor form inside the vesicles, maintaining a stable gas-filled compartment. **Experimental evidences have shown that H_2, N_2, O_2, CO_2, CO, CH_4, Ar and Xe[67] can freely enter and leave gas vesicles. The only factor limiting gas diffusion appears to be molecular size[68].**

Interestingly, perfluorocyclobutane (C_4F_8), can also enter gas vesicles[69], despite having a collision diameter of 0.63 nm, larger than the average pore size. This phenomenon may be attributed to structural flexibility, leading to transient variations in pore size that allow it to pass through at specific moments. This hypothesis is consistent with previous observations that the diffusion rate of perfluorocyclobutane into the gas vesicle is slower than that of smaller gases, suggesting that its entry occurs through temporary pore expansions[17,52].

Since gases can freely diffuse in and out of gas vesicles, the internal gas composition equilibrates with the surrounding environment. But how long does this process take?

In a 1984 publication, Walsby *et al*.[35] reported measuring it. To do so, they placed dried *Anabaena flos-aquae* gas vesicles in a chamber connected to an O_2 gas tank, with the pressure in the gas tank (p') being higher than the initial pressure in the chamber (p0). The exponential rate at which gas flowed from the tank to the chamber (λ) could be controlled with the gas valve opening, and p0 was monitored with a transducer. When the valve opened, p0 rose and, in turn, the pressure inside gas vesicles (p) rose as well, although lagging behind p0. Eventually, p', p0, and p equilibrate; however, for a brief moment, there is a pressure difference between p0 and p. The maximum pressure difference (Δpm) depends on how fast p0 increases (i.e., λ) and how fast p0 and pp can equilibrate (that is, how fast gas can cross the gas vesicle wall, the exponential gas diffusion rate: α). If a rate of pressure rise λ is found that causes the gas vesicles in such a chamber to collapse, it is then known that Δpm=pc. In that case, because Δpm varies with λ, which is known, and α, it is possible to calculate α and, from it, the exponential filling time (te). In their work, the authors reported that even with the fastest pressure rise they could test (0 to 4.6 MPa in 2 ms), gas vesicles did not collapse, from which they estimated a lower limit of the exponential gas diffusion rate at $22\times10^3 s^{-1}$, and the exponential filling time was at most 46 μs, meaning that gas pressure could equilibrate between a gas vesicle and its surroundings in no more than a few hundred microseconds. **These findings reveal that gas vesicles equilibrate on microsecond timescales, rendering gas exchange effectively instantaneous relative to most biological processes.**

While no measurements of the diffusion rates of other gases have been reported, the orders of magnitude involved are likely similar to those of O_2. Essentially, any fluctuation in dissolved gas composition in the environment is reflected almost instantaneously inside the gas vesicles. Therefore, the gas content of gas vesicles is not fixed but is instead determined by the gas composition of the surrounding cytoplasm, which in turn depends on both external environmental conditions and the cell's metabolism.

Potential applications of gas vesicles

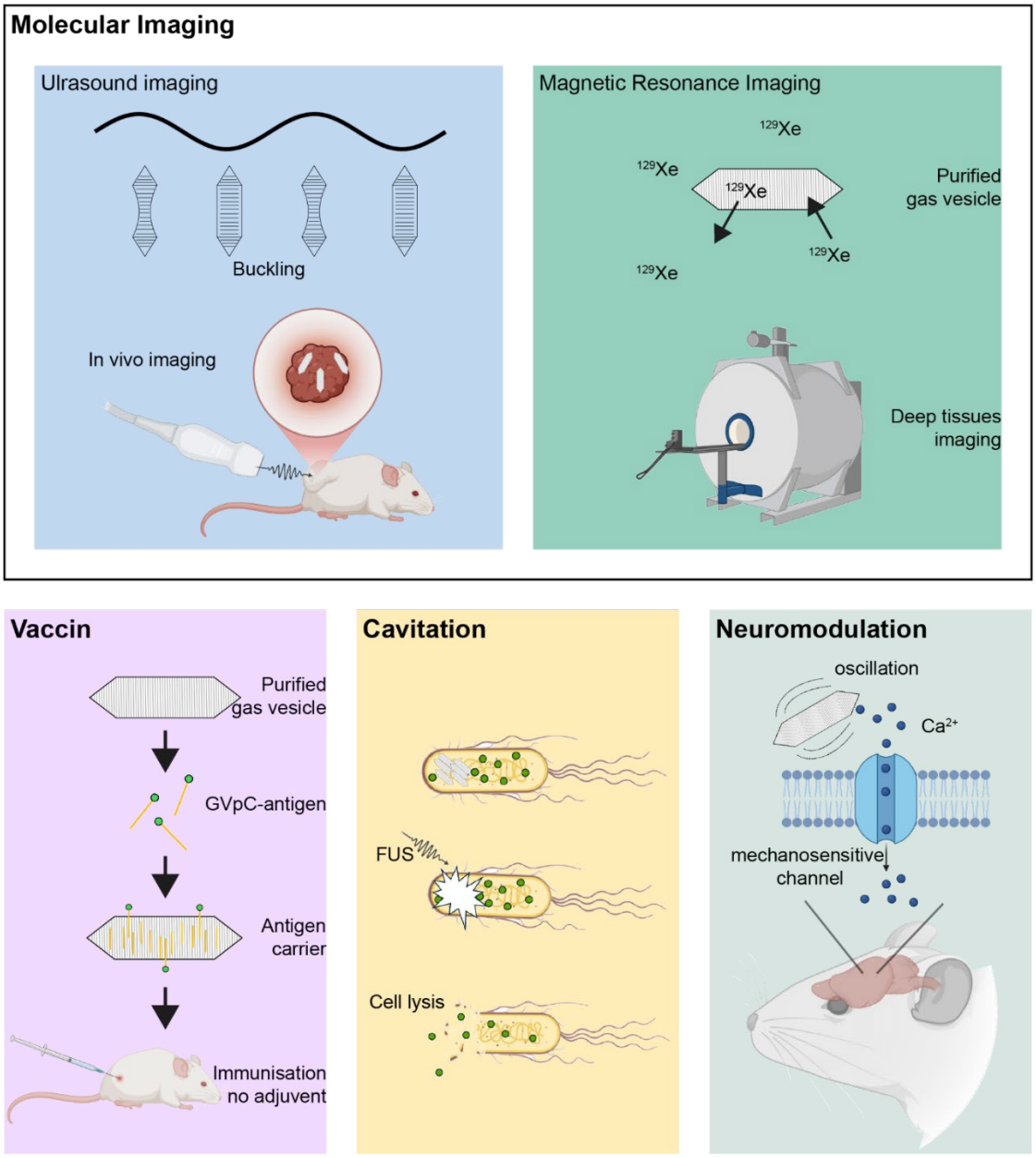

Figure 7 : Overview of potential gas vesicle applications. In molecular imaging (**two top panels**), gas vesicles can be used as a new contrast agent for ultrasound imaging, similarly to what is currently done with microbubbles, and for Magnetic Resonance Imaging. However, contrary to other existing contrast agents, gas vesicles can be genetically encoded and can therefore serve as genetic reporters for acoustic imaging, like an acoustic counterpart to FPs. They can also serve as an adaptable alternative to existing antigen carriers for vaccination, simultaneously acting as an adjuvant (**bottom left panel**). Focused ultrasound (FUS) can be used to induce cavitation of gas vesicles present in cells, leading to openings in the cell membrane (and potentially cell lysis), making gas vesicles an attractive tool for targeted payload delivery or transient cell membrane opening *in vivo* (**bottom center panel**). Due to their acoustic responsiveness, gas vesicles exposed to ultrasound can activate mechanosensitive ion channels in adjacent neurons, offering a non-invasive tool for ultrasound-mediated neuromodulation (**bottom right panel**).

Gas vesicles are remarkable marine biological structures that, for decades, have primarily intrigued scientists as subjects of fundamental study. Initially valued for the insights they offered into microbial buoyancy and adaptation, they were long regarded as a biological curiosity. In recent years, however, interest in these nanostructures has extended far beyond basic biology, following a trajectory reminiscent of GFP. Through human ingenuity and advances in bioengineering, gas vesicles have emerged as versatile tools with a wide array of applications, as summarized in Figure 7.

Owing to their unique protein-based shell and their gas-filled interior, gas vesicles exhibit pronounced interactions with ultrasound. They scatter, reflect, and resonate in response to acoustic waves, generating harmonic signals. These behaviors parallel those of microbubbles, long used as ultrasound contrast agents to achieve high-resolution imaging. However, unlike microbubbles, gas vesicles are genetically encoded, proteinaceous, mechanically robust, and readily engineered, offering superior stability and tunability. These properties underpin a diverse set of applications that exploit their acoustic responses, ranging from enhanced biomedical imaging to localized cavitation and even the activation of mechanosensitive ion channels for neuromodulation. Beyond ultrasound, their gas content also makes them promising candidates as MRI contrast agents. Finally, the modular nature of their protein shell enables functionalization, such as antigen display for vaccine development. These emerging applications, illustrated in Figure 7, will be examined in greater detail in the sections that follow.

Before delving into the breadth of applications, it is worth briefly acknowledging the origins of this field. Most of the advances discussed here stem from the recognition that gas vesicles interact strongly with ultrasound, a connection that, while seemingly obvious today, was far from apparent at the time. Medical imaging and marine microbiology, after all, are disciplines that seldom intersect. The breakthrough came in 2014, when Mikhail Shapiro, then a postdoctoral researcher at Caltech, first identified this link. His insight not only reframed how these nanostructures could be perceived but also catalyzed the surge of interest in their translational potential. Since that discovery, a significant portion of the work exploring gas vesicle-based technologies has been driven by Shapiro and his group at Caltech, whose efforts have laid much of the groundwork for the applications now emerging.

Molecular imaging

Molecular imaging is a field of bioimaging that focuses on imaging molecules within living subjects. This approach enables the visualization of cellular functions and the monitoring of molecular processes *in vivo*, with a direct relevance for medical applications. Its applications are critically important for diagnosing diseases such as cancer, as well as neurological and cardiovascular disorders, allowing for earlier and more precise detection and treatment. A significant aspect of molecular imaging relies on genetically encoded reporters for visualizing specific biological processes. Commonly used reporters include fluorescent proteins and bioluminescent systems like luciferase[70,71]. These tools have profoundly impacted the field over the past decades; however, they share a common limitation, already noted in 2003 by Roger Tsien[72] (see From marine biology curiosity to major research tool section) : their reliance on light for readout. Light has limited tissue penetration

capabilities, which restricts the depth in living animals at which these reporters can effectively function. Fluorescent proteins typically have a readable depth range of up to a few millimeters in tissue, while luciferase-based bioluminescence imaging can penetrate slightly deeper, up to a centimeter depending on tissue properties and wavelength of emitted light. Considering the human body is usually much larger than that, it makes visualization in deep organs challenging. However, other imaging modalities, allowing for deeper visualization, exist. Magnetic Resonance Imaging (MRI) allows for images across the whole body, albeit it has a relatively low spatial resolution, typically in the range of 0.1 to 1 mm for clinical scans. Ultrasounds allow for images to a depth of several centimeters, typically up to 20–30 cm in soft tissues, in certain conditions, with new techniques allowing a spatial resolution of as low as 10 µm in high-frequency modes[73]. Reporters for molecular imaging in these techniques would therefore greatly benefit the field. There are some existing MRI reporters that could reveal molecular mechanisms, gene expression and dynamics. However, their low signal yield constitutes a barrier for their clinical usage[74,75]. So how could we visualize molecular mechanisms using these modalities?

In 2014, Shapiro and colleagues introduced the innovative concept of utilizing gas vesicles as genetically encoded reporters for ultrasound imaging[76] and, to a lesser extent, for MRI[67]. This groundbreaking approach has since catalyzed extensive research aimed at characterizing, enhancing, and broadening the application of gas vesicles in molecular imaging. Notably, the ultrasound imaging capabilities of gas vesicles have garnered significant attention, leading to substantial advancements in this area. In the subsequent sections, we will explore the current state of gas vesicles as molecular imaging reporters, focusing initially on their role in ultrasound imaging and subsequently addressing their application in MRI.

Ultrasound imaging

Ultrasound refers to mechanical longitudinal waves characterized by oscillations in pressure and particle displacement. The primary distinction between audible sound and ultrasound lies in frequency: ultrasound encompasses frequencies exceeding the upper limit of human hearing, specifically above 20 kHz. In clinical settings, ultrasound frequencies typically range from 2 MHz to 10 MHz. As an ultrasound beam propagates through a medium, several interactions occur. A crucial property of each material is its acoustic impedance (Z, typically expressed as kg/(sec·m^2)), calculated as:

$$Z = \rho \times v$$

where ρ represents the material's density, and v denotes the speed of sound within the material. When ultrasound waves transition between materials with differing acoustic impedances, a portion of the wave is reflected, while the remainder is transmitted. The reflection coefficient (R), indicating the fraction of the wave's intensity that is reflected, is determined by the equation:

$$R = \left(\frac{Z2 - Z1}{Z2 + Z1}\right)^2$$

Here, Z1 and Z2 are the acoustic impedances of the respective materials. This reflection phenomenon, producing echoes (the reflected sound waves), is fundamental to diagnostic imaging, as ultrasound devices detect these echoes to construct images of internal structures. The magnitude of the reflection (and thus the echo's amplitude) is directly proportional to the disparity in acoustic impedance between the two media. For instance, at a fat-muscle interface, where the difference in acoustic impedance is approximately 0.3×10^6 kg/(sec·m^2)[c] the reflection coefficient is about 0.011, resulting in an echo with 1.1% of the incident beam's amplitude. Conversely, at a soft tissue-air boundary, with an acoustic impedance difference of approximately 1.63×10^6 kg/(sec·m^2), the reflection coefficient approaches 0.99, yielding an echo with 99% of the initial beam's amplitude[77,78]. When a beam is sent to such interface, its reflection is sent at an angle given by Snell's law (which relates the angle of refraction to the speed of sound in that tissue), and some heat is generated. However, if the waves encounter an object that is small in comparison to the wavelength, echoes are scattered in many directions.

Ideally, for imaging purposes, if you were to build an acoustic reporter, you would need something with a significant acoustic impedance mismatch with most tissues, allowing for high detection sensitivity, and a size small enough to both generate scattering, enabling detection from all directions. Gas vesicles meet both criteria. As you may know by now, gas vesicles are filled with gas, and while the impedance of the gas varies with its composition, it is generally on the order of 10^2 to 10^3 kg/(sec·m^2)[79], whereas water, blood, and soft tissues have an impedance on the order of 10^6 kg/(sec·m^2)[77]. In terms of reflection, this mismatch is extremely high, meaning that gas vesicle detection with ultrasound can potentially be highly sensitive. Furthermore, as mentioned in the section Gas Vesicle Width and What Influences it, gas vesicle diameters range between 45 and 200 nm, which is much smaller than the wavelength of typical ultrasound waves used in medical imaging (ranging roughly from 100 to 1000 μm in soft tissues[78]). This means that gas vesicles, whether individual or clustered, will always scatter such waves. Therefore, gas vesicles can potentially constitute effective contrast agents for ultrasound imaging.

As mentioned earlier, the idea of using gas vesicles as acoustic contrast agents was first tested in 2014[76]. There, gas vesicles from *Anabaena flos-aquae* and *Halobacterium salinarum NRC-1* were shown to produce ultrasound contrast in their purified form, inside cells, and even after injection in mouse of gas vesicle filled cells, opening the door to their development as biomolecular reporters for ultrasound molecular imaging. This initial study provided a glimpse of the potential of gas vesicles to serve as background-subtracted imaging agents based on their ability to collapse at specific acoustic pressures, the ability to distinguish multiple gas vesicle types for multiplexing, and their production of nonlinear acoustic signals. Since then, considerable progress has been made in understanding and engineering the acoustic properties of gas vesicles, enhancing the ability of ultrasound imaging to detect them, and developing them as acoustic reporter genes.

[c] Impendence is 1.38×10^6 kg/(sec·m^2) for fat and 1.69×10^6 kg/(sec·m^2) for muscle

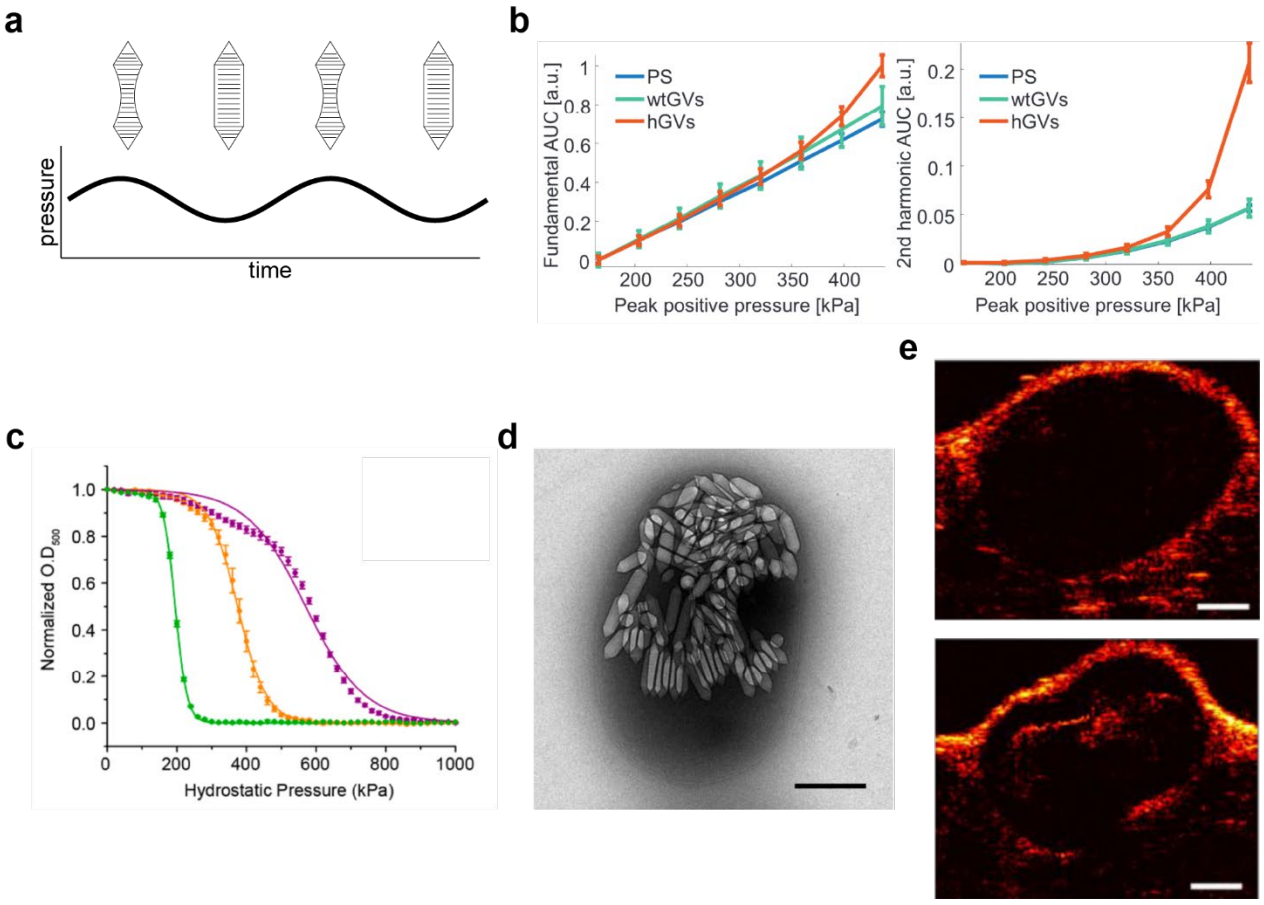

Figure 8 : Ultrasound imaging of gas vesicles. (**a**) Diagram of the buckling of gas vesicles. In an ultrasound wave, at positive peak pressure, the vesicle is contracted and relaxes at negative pressure. This buckling causes the production of harmonics, and the non-linearity used for gas vesicles imaging with ultrasounds. (**b**) Nonlinearity of *Anabaena flos-aquae* gas vesicles for fundamental (left) and 2nd harmonic (right). The Y axis shows the area under the curve (AUC) of the backscattering spectra of gas vesicles in the fundamental (9.5 MHz to 13 MHz) and second harmonic (19 MHz to 26 MHz) bands. PS = PolyStyrene bead, a control for linear response, wtGVs = wild type gas vesicle, with maximum GVpC load, hGVs = gas vesicle stripped of GVpC. From Maresca *et al*. 2017[80]. (**c**) Altering or removing GVpC provides a way to modify the pressure tolerances of the gas vesicle and is one of the main way to engineer them to change their acoustic properties. Here this is illustrated by the change in hydrostatic collapse pressure of *Anabaena flos-aquae* gas vesicles. Purple = wild type vesicles, Orange = truncated form of GvpC without its N- and C-terminal regions, Green = no GVpC. The y axis represents the optical density of a purified gas vesicles suspension, which drops when gas vesicles collapse. From Lakshmanan *et al*. 2016[81]. (**d**) Gas vesicles can be expressed in *E.coli* to serve as acoustic reporters. Here is an *E.coli* cell in electron microscopy containing gas vesicles produced with bARGser, the second generation of Acoustic Reporter Genes. From Hurt *et al.* 2023[82]. Scale bar represents 500 nm. (**e**) ultrasounds AM images of *E.coli* microcolonies with bARGser within a mouse tumor, illustrating the possibility to image bacteria colonizing a tumor with ultrasounds. Top image shows the colonized tumor before expression of bARGser, bottom image shows the same tumor after 24h of expression. From Hurt *et al.* 2023[82]. The scale bar represents 2mm.

Ultrasound imaging technics for gas vesicles

One standard modality for acoustic imaging is called B-mode. A short ultrasound pulse is transmitted from a transducer at a specified frequency, and echoes are collected by the same transducer over a bandwidth centered on that frequency. The time delay between the transmitted pulse and the received echo gives the distance of the echo source to the transducer, while the echo amplitude determines the pixel intensity of the constructed image. Although gas vesicles can be visualized in B-mode *in vitro* using a uniform phantom gel, *in vivo* imaging is complicated by multiple backscattering sources that elevate background noise and obscure the vesicles. Gas vesicles can be localized by subtracting images acquired before and after their collapse by acoustic pressure[76]. More recently, another destructive imaging method called BURST contrast has been developed to enhance the sensitivity of gas vesicle detection[83]. This technique exploits the unique temporal signal pattern generated by gas vesicles as high acoustic pressure waves are sent to collapse them, releasing their gas into the surrounding liquid environment. To date, BURST contrast is likely the most sensitive method for detecting gas vesicle-expressing cells, as it has been reported to detect single gas vesicle-producing bacteria[83]. However, this method inherently requires the destruction of gas vesicles, which prevents its use for imaging dynamic biological processes and leads to some reduction in gas-vesicles-containing-cell viability. The development of a nondestructive approach for specifically detecting gas vesicles *in vivo*, even against complex anatomical backgrounds, is therefore crucial for their successful use as ultrasound reporters[76].

This difficulty is not unique to gas vesicles, as it was encountered with microbubbles decades ago[84]. A solution is to construct images not from the backscattered waves around the transmitted fundamental frequency, but from waves around harmonic frequencies. Indeed, harmonic backscatter arise from oscillations in microbubble radius in response to incident pressure waves[85]. Studies showed that a similar phenomenon happened when gas vesicles are subjected to ultrasounds[76]. Therefore, harmonic imaging offers a better solution to image gas vesicles in noisy environments. Shapiro and colleagues showed that *Halobacterium salinarum NRC-1* gas vesicles signal to noisy ratio of the second and third harmonics relative to the fundamental scatterer respectively showed a 3.7-fold and 4.6-fold signal increase[76].

Later studies[80] revealed that gas vesicles produce harmonics through pressure-dependent nonlinear deformations under ultrasound. Above a critical buckling pressure (Pb), which is lower to but correlated with the vesicle's collapse pressure, gas vesicles begin to buckle (Figure 8a), contracting and relaxing with the acoustic wave. This behavior not only generates harmonics but also causes the backscattered signal to scale nonlinearly with increasing wave amplitude, in contrast to most soft tissues, which tend to exhibit more linear scaling[86,87] (Figure 8b). Exploiting this property allows gas vesicles to be imaged using an alternative modality known as amplitude modulation (AM) [80]. In AM, differential backscattering is detected by transmitting pulses at multiple amplitudes: specifically, two half-amplitude transmissions are digitally subtracted from a third, full-amplitude transmission. The full-amplitude pulse induces pressures above the buckling threshold, triggering harmonic scattering, whereas the half-amplitude pulses remain below threshold, producing linear scattering. After subtraction, the distinct scattering response from gas vesicles persists, whereas linear echoes from surrounding tissue, merely scaling in amplitude, are canceled. In the first demonstration of AM for gas vesicle imaging, this approach achieved a signal-to-noise ratio of up to 15.6 relative to linear tissue[80]. Beyond improving the signal-to-noise ratio, this technique also enables non-destructive multiplex

imaging of different vesicle populations, since the buckling pressure, like the collapse pressure, depends on both the presence and the quantity of GvpC[80,81] on the vesicle.

However, *in vivo* use of AM can be confounded by the distortion of high-pressure ultrasound waves as they propagate through tissue, generating false signals downstream of gas vesicle inclusions. This issue reduces specificity because soft tissue may erroneously appear as a gas vesicle signal. To overcome this limitation, Maresca and colleagues[86] introduced an improved modality, xAM, to mitigate AM artifacts *in vivo*. Rather than using a single collinear wave, xAM employs two angled ultrasound waves that intersect, creating a localized amplitude modulation. This localized modulation surpasses the buckling pressure of gas vesicles while suppressing tissue-related nonlinear artifacts. Consequently, xAM substantially enhances contrast-to-artifact ratios, enabling clearer and more specific gas vesicle imaging, especially in deep tissue.

Since 2014, methods for *in vivo* visualization of gas vesicles via ultrasound have advanced significantly and continue to evolve. A recent preprint[88] describes an enhancement of xAM, termed HxAM (with H for Harmonic), which harnesses harmonic frequencies to boost the signal-to-background ratio, allowing gas vesicles to be detected 20% deeper in tissue compared to xAM. Another work, to which I contributed (see Chapter III: Side projects)[89] introduces Nonlinear Singular Value Decomposition (SVD) Beamforming, an ultrafast nonlinear imaging technique designed to improve gas vesicle detection by separating nonlinear signals from tissue background noise via SVD-based post-processing. This approach not only provides a superior signal-to-background ratio relative to xAM but also requires 4.8 times fewer pulse transmissions and offers greater flexibility in selecting acoustic pressure amplitudes. Collectively, these advances underscore the rapid evolution of gas vesicle imaging methodologies and their growing potential for biomedical applications. But imaging technology has not been the only thing that improved. Since gas vesicles are genetically encoded, they are also genetically engineerable.

Engineering gas vesicles for ultrasound imaging

To engineer gas vesicles for ultrasound imaging, one key parameter you can play with is the stiffness of gas vesicles. As explained earlier, gas vesicles can be made more or less stiff by changing sequences of their constituent proteins GvpA and GvpC, which results in changes in the collapse pressure under hydrostatic pressure for the vesicle (Figure 8c). While hydrostatic pressure and acoustic pressure[d] are two different phenomena (mainly, one is constant, the other fluctuates with the wave frequency), both can, above a critical threshold, cause the collapse of the vesicle. Their values have been shown to be correlated: altering the critical hydrostatic collapse pressure (Pc_h) also affects the acoustic collapse pressure (Pc_a)[81]. Typically, Pc_a exceeds Pc_h, likely due to the transient nature of the pressure waves used in acoustic imaging. Why ? At the frequencies used for acoustic imaging, peak pressures persist for only a few nanoseconds, whereas, as discussed in Why is there only gas in gas vesicles? And what gas is it?, gas exchange in the vesicle occurs on the timescale of microseconds. Consequently, during peak pressure, the gas does not have sufficient time to escape; instead, it transiently compresses, reinforcing the structural integrity of the shell[81]. Furthermore, the buckling pressure (Pb), the acoustic pressure at which gas vesicles start to buckle and produce harmonics as well as exhibiting a nonlinear behavior, is also connected to the Pc_h, happening at a

[d] For the sake of simplicity, we will referrer to the peak pressure caused by the ultrasound wave as “acoustic pressure”.

lower acoustic pressure that Pc_a[80]. For example, *Anabaena flos-aquae* gas vesicles stripped of GvpC have a Pc_h of 195 kPa, a Pc_a of 571 kPa[81] and a Pb of 320 kPa[80]. Therefore, genetic changes that were identified to affect the Pc_h of gas vesicles can be used to tune their acoustic properties. Having a library of vesicles that collapse and/or buckle at different amplitude could allow multiplex imaging in the same way that different fluorescent proteins with different excitation and emission spectrum can be used.

There are several proteins that can be modified for that purpose. Most of the work so far has focused on GvpC however. Indeed it has several advantages: it can be readily removed and added back to the shell, allowing control of the quantity of GvpC per shell for purified vesicles[81]. Possible modifications of its sequence leading to changes in its strengthening effect are already well identified (see Structural proteins and the structure of gas vesicles walls section). For example, removing the terminal regions, likely involved in the GvpC-GvpC interactions, causes a reduction in Pc_h[81]. Same thing for the number of repeats in the sequence[90]. Considering that the gas vesicle width changes the Pc_h of vesicles and that the GvpA sequence affects their width, GvpA could also constitute a good target to change the acoustic properties of a gas vesicle. However, GvpA is harder to engineer, most of its sequence is highly conserved and cannot be changed without altering the production of gas vesicles (see Structural proteins and the structure of gas vesicles walls section), and for the parts that can be modified it is not clear how changes could affect the dimensions of the vesicles. This doesn't mean that GvpA cannot be used to engineer gas vesicles acoustic properties. GvpA from one species can be inserted into the operon of another one, changing the acoustic properties. This strategy has already been successfully employed[91]. More recently, directed evolution of GvpA protein also showed to be successful in changing the acoustic contrast produced from gas vesicles[92]. Another strategy could be to change the clustering of gas vesicles instead of changing the vesicles themselves. Clustered and uncluttered purified gas vesicles were shown to be distinguishable with acoustic imaging and usable for multiplex imaging[93]. While this was achieved by using different purification process, recent work[64] clearly established the role of GvpU protein in the clustering of the vesicles in cells, opening the door for genetic engineering of the clustering of gas vesicles for ultrasound imaging. Combining all these different approaches enables the creation of a library of gas vesicles or gas vacuoles with different acoustic properties, similarly to what was done with fluorescent proteins before.

Gas vesicle as genetically encoded acoustic reporter in live bacteria

Concomitant with progress in imaging techniques and the engineering of gas vesicles, the application of gas vesicles as genetically encoded acoustic reporters in live bacteria has also advanced in recent years. *Escherichia coli* serves as the workhorse of bacterial synthetic biology, owing to the availability of genetic engineering tools, a well-characterized metabolic framework, and its widespread use in medicine, industry, and environmental applications. Therefore, a crucial first step in establishing gas vesicles as a viable synthetic biology tool has been their heterologous expression in *E. coli*, which does not naturally produce gas vesicles. This milestone was first achieved in 1998 by Canon et al. [29], who expressed *Bacillus megaterium* gas vesicles under the *lacZ* promoter in *E. coli*, predating the discovery of the acoustic properties of gas vesicles.

In 2018, Bourdeau et al.[91] expanded upon this foundational work, optimizing gas vesicle production in *E. coli* to enhance ultrasound contrast *in cellulo*. This was accomplished by assembling two gene

clusters derived from *Bacillus megaterium* and *Anabaena flos-aquae*, with varying copy numbers of gvpA and gvpC genes. Each variant exhibited distinct collapse and buckling pressures, enabling multiplex imaging. These first-generation live acoustic reporter gene clusters, termed ARG1 and ARG2 (for Acoustic Reporter Genes, gene clusters containing the required genes to produce gas vesicle used as acoustic reporters), were placed under IPTG-inducible control, demonstrating ultrasound contrast proportional to induction strength. When introduced into the murine colon, bacteria previously filled with these gas vesicles were detectable using B-mode ultrasound with collapse-subtract imaging.

Despite the promise of this first generation of ARGs, a major limitation emerged : gas vesicle production was robust at 30°C but significantly diminished at 37°C, the optimal growth temperature for *E. coli* and a physiologically relevant condition for *in vivo* applications. This temperature dependency posed a significant barrier to the use of ARGs in biomedical settings, particularly for bacterial cancer therapy and microbiome engineering.

To address this limitation, a second-generation ARG system was developed in 2023, optimized for gas vesicle production at 37°C[82] (Figure 8d). The authors employed a genomic mining approach, selecting and screening a diverse panel of gas vesicle gene clusters from phylogenetically distinct organisms. The gene cluster from *Serratia* sp. 39006 was identified as optimal, yielding a ninefold increase in nonlinear ultrasound contrast relative to first-generation ARGs at 37°C. Further optimization involved the removal of non-essential genes, resulting in a 17-kb operon, named bARGser. This cluster was subsequently inserted into a pBAD plasmid under an arabinose-inducible promoter, allowing controlled expression in *E. coli* microcolonies within tumors in mice. *In situ* expression of bARGser resulted in a strong acoustic signal even at 37°C, making this system the closest equivalent to GFP in ultrasound-based reporter gene technology (Figure 8e).

This second-generation ARG system represents a major step toward genetically encoded ultrasound reporters, as it can be expressed in *E. coli*, its expression is controllable, it functions at application-relevant temperatures, and its gene cluster, though relatively, large remains cloneable into other plasmids. Moreover, it provides a strong ultrasound signal even in bacteria deep inside animals. ARGs could serve as a powerful tool for tracking therapeutic bacteria as they home to and proliferate within tumors or other target organs, enabling real-time assessment of therapeutic efficacy. Additionally, mapping their spatial distribution could inform and enhance tumor-targeted interventions. Beyond oncology, ARGs hold promise for microbiome research and the tracking of engineered probiotics designed for diagnostic applications. However, challenges remain before widespread adoption. In particular, the impact of heterologous ARG expression on bacterial physiology and population dynamics remains poorly characterized. Since bacterial cancer therapy relies on maintaining a stable bacterial population within the tumor microenvironment for a long time, further investigation is required to assess potential metabolic burdens and fitness costs associated with ARG expression. A deeper understanding of these factors will be critical for advancing ARG technology toward clinical and synthetic biology applications.

Gas vesicles can also be engineered as acoustic biosensors by dynamically modulating their ultrasound contrast in response to their environmental cues. This is achieved by inserting specific protease cleavage sequences into the GvpC protein. Because the length and number of repeats in GvpC influence the stiffness of the gas vesicle shell, splitting it with proteolytic cleavage alters the

vesicle mechanical properties (specifically the susceptibility to buckling). Using this approach, Lakshmanan and colleagues designed gas vesicles that change their nonlinear acoustic response in the presence of protease activity. They showed the effectiveness of this approach with three distinct enzymes, each targeting unique cleavage sequences: the tobacco etch virus (TEV) endopeptidase, the calcium-dependent mammalian protease calpain, and the bacterial protease ClpXP. These biosensors were validated both *in vitro* and *in vivo* in the mouse gastrointestinal tract[94]. The authors suggest that this strategy could be extended to sense a broad range of other enzymatic activities. Building on the same concept of dynamically modulating gas vesicle stiffness for biosensing, a recent study (currently under review) has described and tested gas vesicles engineered to act as intracellular pH reporters[95], expending even more the available tools for *in cellulo* acoustic molecular imaging.

Gas vesicle as genetically encoded acoustic reporter in eucaryote cells

Producing genetically encoded acoustic reporters in eukaryotic cells represents another crucial step toward their broader adoption in biomedical research and clinical applications. For instance, the expression of gas vesicles in mammalian tumor cells could facilitate the tracking of tumor progression and metastasis in whole-animal models or enable the visualization of localized variations in gene expression. Similarly, ARGs could serve as tools for studying immune system dynamics and organismal development. Moreover, the expression of ARGs in mammalian cells could allow real-time tracking and targeted sampling of therapeutic cells, such as CAR-T cells or stem cells, enhancing their potential for monitoring and optimizing cell-based therapies.

However, introducing this prokaryotic organelle into eukaryotic cells presents significant challenges. One hurdle is the difference in codon usage between distantly related organisms, necessitating codon optimization for efficient translation. Additionally, unlike prokaryotes, eukaryotic gene expression requires that genes within a single operon be linked by sequences such as P2A to ensure coordinated expression and the production of separate proteins[96]. Furthermore, physiological differences between prokaryotic and eukaryotic cellular environments may affect the stoichiometry of gas vesicle proteins, meaning that expression levels optimized for bacterial systems may not function as effectively in eukaryotic cells.

A first-generation mammalian ARG was developed in 2019[97] and named $mARG_{Mega}$ (*Mammalian ARG from Bacillus megaterium*). As the name suggests, genes from the gas vesicle operon of *Bacillus megaterium* were used. Following codon optimization, systematic screening of various operon compositions, and fine-tuning of gene stoichiometry, a three-plasmid system enabling gas vesicle production in HEK 293 cells was established. This system could be used transiently or integrated into the host cell genome for stable expression. Upon induction, gas vesicles became detectable by acoustic imaging after three days of induction, both *in vitro* and *in vivo* in mouse tumor models. However, the construct resulted in a low number of vesicles per cell, limiting its potential for non-destructive imaging. As a result, detection was only possible using BURST contrast imaging[82]. In a concomitant but independent work, another team also reported the production of gas vesicles, from *Planktothrix rubescens* this time, into human cancer cells[98]. However, no acoustic imaging was attempted for this construct.

In 2023, a second-generation mARG was developed to overcome these limitations[82]. In this approach, codon-optimized genes from *Anabaena flos-aquae* were distributed across two plasmids: one encoding all accessory proteins and another containing only GvpA, allowing precise control over the

stoichiometry of GvpA relative to the other proteins. Notably, the GvpC gene was excluded from both plasmids. By increasing the GvpA/accessory protein ratio, the authors successfully generated a second-generation mARG, named $mARG_{Ana}$, which exhibited a 38.8-fold improvement in signal for non-destructive xAM imaging compared to the first-generation $mARG_{Mega}$ *in vitro*. *In vivo*, in chimeric tumors composed of a mixture of gas vesicle-producing and non-producing cells, clusters of gas vesicle-producing cells were successfully detected and distinguished using xAM imaging, potentially enabling real-time ultrasound-guided biopsy.

While these mARGs proved to be working as acoustic reporters, building stable cell lines that can produce it remained costly and time consuming, due to their integration system that requires fluorescence-activated cell sorting followed by single-cell cloning to isolate the cells that have been properly transfected via random integration[99]. To facilitate this, a drug-selectable version of the mARGs have been developed to streamline the selection of successfully transfected cells, facilitating even more the availability of the technology[99].

mARGs open a wide range of potential applications for gas vesicles as acoustic reporters, and recent advances have made them more easily detectable and more convenient to work with. However, as with ARGs in bacteria, further research is needed to determine if and how they impact cellular physiology. Their use has so far been limited to a small number of fast-growing laboratory strains, and it remains unclear whether they can be effectively implemented in more sensitive cell types. Moreover, only a single type of gas vesicle has been engineered for the second generation of mARGs, limiting their potential for multiplex imaging.

Purified Gas vesicles as nanoscale ultrasound contrast agents

For decades, bubbles have been used as injectable contrast agents for ultrasound imaging, benefiting from nonlinear detection methods similar to gas vesicles. Once introduced into the bloodstream, they can be tracked in real time. Several FDA-approved lipid-based microbubbles (1–10 µm in diameter) are currently available and widely used in clinical diagnostics, including cardiac and vascular imaging, as well as cancer and inflammatory disease detection. Beyond these established applications, research is actively expanding the use of microbubbles for targeted drug delivery, blood-brain barrier opening, and antibacterial effect (sonobactericide)[100]. Additionally, advances in ultrafast ultrasound imaging now allow for high-resolution imaging of cerebral blood flow at the micrometer scale. This breakthrough has enabled ultrasound-based functional brain imaging, using subtle blood volume changes as a proxy for neural activity, a technic sometimes referred to as functional UltraSound imaging (fUS[e])[101,102]. However, a key limitation of microbubbles is their large size, which prevents them from crossing blood vessel walls into non-vascular tissues, particularly restricting their use in tumor therapy[103]. To address this issue, small nanobubbles where more recently used, with a diameter between 100 and 500nm[100]. While this reduced size allow them to leak through defective vasculature of tumors and accumulate into tumors, nanobubbles face stability challenges, including gas leakage and collapse, which might limit their clinical translation[103].

[e] Not to be confused with FUS (Focused UtraSounds), where focus ultrasound beams are converged to a target, resulting in a localized strong acoustic pressure, a completely different thing. How do you make the distinction between fUS and FUS in oral presentation ? Good question.

Purified gas vesicles have been explored as an alternative injectable contrast agent. Their diameter is comparable to that of nanobubbles, and they offer key advantages, including ease of production, purification, and a naturally uniform width (unlike synthetic bubbles). Due to their unique shell structure, gas vesicles are highly stable, and as discussed in the section Engineering Gas Vesicles for Ultrasound Imaging, they can be engineered to fine-tune their acoustic properties. These characteristics make purified gas vesicles promising candidates for molecular ultrasound imaging.

Following intravenous injection in mice, purified gas vesicles have been detected in the inferior vena cava and liver using ultrasound imaging[76]. Their biodistribution in healthy animals typically mirrors that of other nanoparticles, with accumulation primarily in the liver, spleen, and lungs[104]. Gas vesicles are cleared from the bloodstream and organs by the reticuloendothelial system within tens of minutes to a few hours[104]. However, coating gas vesicles with polyethylene glycol (PEG) or hyaluronic acid significantly extends their stability in organisms. Wang and colleagues demonstrated that PEG-coated gas vesicles remained detectable in tumors via ultrasound imaging for up to 48 hours[103], a major improvement over nanobubbles, which typically dissipate within minutes[105]. Additionally, PEG-coated gas vesicles showed reduced liver accumulation, leading to a prolonged presence in the bloodstream, which enhances their utility for vascular imaging[103]. Similarly, gas vesicles injected directly into the mouse brain remained detectable via ultrasound for up to 12 days[106], demonstrating their potential for long-term brain imaging applications. Such coated gas vesicles can also be used in combination with ultrafast ultrasound and fUS to visualize brain activity with ultrasounds. Compared to previously used microbubbles, they provided increased contrast, likely due to the longer circulation time of gas vesicles[107]. All these findings support the idea that purified gas vesicles can be used for imaging in vivo similarly to micro and nanobubbles, with the advantage of a longer stability, resulting in enhanced circulation time in the blood stream and extended stability in organs and tumors.

Magnetic resonance imaging

Magnetic Resonance Imaging (MRI) is an imaging technique capable of visualizing structures deep within tissues (tens of centimeters) with a spatial resolution up to 100 µm[108]. It operates by detecting the relaxation time of hydrogen nuclei (^{1}H), primarily from water molecules, after their alignment with a strong magnetic field is disrupted by a radiofrequency pulse. While MRI is widely utilized in both clinical and research settings for high-resolution anatomical imaging and functional studies, there remains no fully satisfactory method for imaging dynamic cellular processes, such as those tracked with genetically encoded reporters which are readily accessible using optical techniques like GFP.

Over the past two decades, several strategies have been explored to address this limitation. Some approaches rely on controlling cellular uptake or availability of contrast agents, such as gadolinium or metal ions. Others seek to alter the MRI signal of endogenous ^{1}H nuclei, thereby eliminating the need for external contrast agents. These techniques have been recently reviewed by Brindle K.M.[109]. However, all current strategies suffer from low molecular sensitivity, with practical detection limits in the micromolar range[74,75].

In 2014, Shapiro and colleagues[67] introduced an alternative approach utilizing gas vesicles in combination with HyperCEST MRI[f] to enable the specific detection of hyperpolarized xenon (^{129}Xe). When water containing gas vesicles is infused with xenon, ^{129}Xe atoms can freely exchange between the gaseous phase inside the vesicles and the surrounding aqueous environment. The distinct chemical environment of this compartment results in a specific chemical shift of the ^{129}Xe magnetic resonance frequency. By applying a selective saturation pulse at the resonance frequency of xenon inside the gas vesicles, Shapiro *et al*. successfully visualized gas vesicles with high sensitivity using ^{129}Xe HyperCEST MRI. Their study demonstrated that gas vesicles could be detected at low concentrations, representing a substantial improvement over previously developed genetically encoded MRI reporters.

Additionally, the size and morphology of gas vesicles were found to influence their MRI properties, enabling the differentiation of gas vesicles from *Microcystis* sp., *Bacillus megaterium*[111], and *Halobacteria* sp. NRC-1 based on their respective resonance frequencies[67] . This means that it is possible to perform multiplexed imaging of gas vesicles analogous to multicolor fluorescent protein microscopy. More recently, it was shown that heterologously expressed gas vesicles in mammalian cells could also be detected using a similar approach[98].

All these findings suggest that gas vesicles have significant potential as a tool for live MRI imaging of gene expression, offering high sensitivity and multiplexing capabilities. Given that MRI enables deep tissue penetration, this approach could theoretically allow whole-body imaging in humans.

However, further development is required before gas vesicle-based MRI can be practically implemented. Despite the promising results initially reported by Shapiro *et al*. more than a decade ago[67], to my knowledge, only two subsequent studies have replicated these findings one in *Bacillus megaterium*[111] and another in human cells[98]. Both studies were conducted *in vitro*, and although pharmacokinetic modeling suggests that *in vivo* applications are feasible[67], this has yet to be experimentally demonstrated. The relatively slow progress in this field is likely due to the greater attention given to gas vesicles for acoustic imaging, which has seen much broader adoption over the past decade. Both MRI and ultrasound imaging could serve similar roles in molecular and cellular imaging; however, MRI suffers from lower spatial resolution and, unlike acoustic imaging, would requires for *in vivo* use repeated inhalation of hyperpolarized ^{129}Xe. Additionally, MRI-based detection of gas vesicles relies on specialized, costly instrumentation, which is less accessible to research teams working in synthetic biology and molecular imaging.

[f] HyperCEST stands for “Hyperpolarized Chemical Exchange Saturation Transfer” and combines two techniques. First, hyperpolarization (usually of xenon-129 gas) dramatically boosts the MRI signal by aligning more atomic nuclei in the same magnetic state. Second, CEST (Chemical Exchange Saturation Transfer) creates image contrast by selectively targeting molecules that can exchange atoms, such as protons, with their surroundings. This indirect detection enables highly sensitive imaging, even at very low concentrations[110].

Gas vesicles for vaccines

Antigen carriers are critical components of vaccine formulations, particularly for so called subunit vaccines. Subunit vaccines are vaccines containing only a portion of the infectious agent. These avoid the risk of accidental infection or reversion to an active, infectious state. But to do so, antigens are rarely injected alone in their soluble form. Indeed, free-floating antigens tend to be rapidly degraded and have limited immunogenicity, which leads to the antigen being often not recognized effectively by the immune system. A solution to this problem is to use antigen carriers. Antigen carriers are biological or synthetic scaffolds to which the antigen is bonded and that help deliver it to antigen-presenting cells, enhance immune responses, and provide structural stability to otherwise fragile antigenic molecules.

Some of the currently used antigen carriers include virus-like particles (VLPs), conjugate carriers (toxoid-protein conjugates), or bacterial outer membrane vesicles (OMVs). Each of these carriers has been widely employed in licensed vaccines but is not without limitations. VLPs and conjugate carriers are expensive to produce and purify at scale and usually require to be stored at 2-8°C to maintain efficacy and OMVs suffer from heterogeneity issues that limit standardization. More stable, cheaper and standardized carriers would therefore be welcome.

Therefore, in the quest to find new antigen carriers that overcome some of these limitations, gas vesicles have been proposed for the first time in 2001 by Stuart *et al.*[112]. Indeed, gas vesicles have several advantageous traits as antigen carriers. First, they are very stable, at room temperature and higher, they can stay intact for months. This facilitates storage compared to other existing solutions. Second, they have a comparable size to existing carriers such as VLPs. Third, their structural proteins are identified and are available for genetic manipulation which ultimately would allow the expression of unique epitopes as an integral part of the vesicle structure. Finally, they are easily purified from and likely amenable to industrial production on a large scale.

Several studies have shown the potential of engineered gas vesicles as an antigen carrier[113,114]. Stuart *et al.*[112] showed that *Halobacterium NRC-1* gas vesicles could be conjugated with a classical hapten, the trinitrophenol (TNP) and injection of such vesicles in mice lead to immune response by the mice directed specifically towards the TNP. Furthermore, they showed that wild-type gas vesicles stimulated an immune response but had no negative impact in terms of mouse survival, or any obvious indications of toxicity for the doses used for vaccination. Then, to show the potential genetic manipulation of vesicles, an 18 base pair sequence coding for mevinolin, was inserted in the C-terminus of the GvpC gene. These recombinant vesicles not only were not altered by the insertion, but they also immunized mice toward the antigen. A later study[115], using the same recombination strategies to several sites in GvpC, showed that similar results could be achieved with much bigger antigens, going up to a 705 bp insertion of a simian immunodeficiency virus antigen. Since then, using the similar approaches, immunization against human pathogens *Salmonella enterica*[116], *Chlamydia trachomatis*[117] and malaria responsable pathogen *Plasmodium falciparum*[118] was achieved in mice. Additionally, it was also shown that the wild-type gas vesicles itself is immunogenic, meaning that in gas vesicle based vaccines, no additional immunogenic adjuvant are necessary, reducing the final cost of the vaccine[112,119]. Studies have also demonstrated that multiple engineered GvpC proteins can

be incorporated into a single vesicle, allowing the creation of vesicles carrying a mix of antigens, which could enhance the development of multivalent protective vaccines[120].

The use of gas vesicle as antigen carrier is promising, offering a modulable, easily engineerable, and potentially cheap alternative to existing solutions. However, it has limitations too. Suitable antigens for it are limited to protein and peptide antigens. Furthermore, if post-translational modifications of proteins or peptides, such as glycosylation, are critical for the induction of protective immunity, it will be challenging to generate them in bacteria, therefore requiring more expensive bioproduction in mammalian systems. Therefore, the gas vesicle-based vaccines may be most suited for bacterial protein antigens, and only to a limited extent for viral, eucaryotic and cancer antigens.

Gas vesicle-based vaccines are still in the early stages of development, requiring further research. While their self-adjuvating properties are well established, comprehensive studies on their immunogenicity remain limited. Additionally, the stability of gas vesicles in animal models and their effectiveness across different delivery methods have not been thoroughly evaluated. Although current studies indicate an immune response to the antigen, definitive evidence of long-term protective immunity against pathogens has yet to be demonstrated[119]. Finally, so far, all *in vivo* experiments were only led in mice and not humans[121]. For better translational research, moving toward humanized models will be necessary step.

Gas vesicles as cavitation nuclei

Acoustic cavitation arises when gas bubbles are exposed to an oscillating pressure field, such as that generated by ultrasound. These bubbles undergo cyclic phases of compression (high pressure) and rarefaction (low pressure). During rarefaction, the surrounding pressure drops, enabling the bubble to expand through rectified diffusion of dissolved gases and, in some cases, through coalescence with neighboring bubbles. Upon compression, the bubble may either contract and re-expand in subsequent cycles, maintaining a stable oscillatory behavior known as “stable cavitation”, or collapse violently. In the latter case, termed “inertial cavitation”, the implosion can generate intense local effects, including heat, shock waves, microjets, and even light emission (sometimes referred to as “sonoluminescence”). The transition between these cavitation regimes is governed by the soundwave parameters: low-frequency, high-amplitude ultrasound tends to favor inertial cavitation, whereas high-frequency, low-pressure waves promote stable cavitation[122,123]. But for this to happen, you first need a bubble. That first bubble that is going to expend and collapse with the sound wave is called a “cavitation nucleus”. Such nuclei can arise spontaneously if the peak negative pressure falls below the threshold for vapor bubble formation. Alternatively, pre-existing bubbles or gas-filled structures can act as nuclei, dramatically lowering the cavitation threshold and facilitating the onset of inertial cavitation.

Inertial cavitation has been extensively harnessed in therapeutic applications, most notably in high-intensity focused ultrasound, where the heat and shockwaves generated by collapsing bubbles are used to ablate targeted tissues or vascular occlusion. Beyond ablation, cavitation can also transiently permeabilize cell membranes through the formation of nanoscale pores, a process known as “sonoporation”. This non-lethal effect facilitates intracellular delivery of therapeutic agents such as

small molecules, DNA, or antibodies, both *in vitro* and *in vivo*[124]. The use of focused ultrasound (FUS) in conjunction with exogenous cavitation nuclei (typically microbubbles administered systemically) significantly lowers the acoustic threshold required to elicit bioeffects. This strategy has been successfully applied to achieve reversible opening of the blood–brain barrier, enhancing the delivery of drugs to the brain[125].

Building on the use of exogenous cavitation nuclei, gas vesicles have emerged as a novel class of genetically encodable nanostructures capable of mediating inertial cavitation. In 2021, Bar-Zion *et al*. demonstrated that purified gas vesicles derived from *Anabaena flos-aquae* can serve as effective cavitation seeds when exposed to focused ultrasound at an acoustic pressures exceeding their collapse threshold and at sub-megahertz frequencies (0.67 MHz), significantly lower than the frequencies typically used for GV imaging[126]. Upon collapse, gas vesicles release nanoscale gas pockets into their environment, which can then act as cavitation nuclei, initiating inertial cavitation under suitable acoustic conditions. The same study showed that gas vesicle engineered to bind specifically to cancer cells could then be used to destroy it by harnessing their ultrasound induced internal cavitation.

The same mechanism was shown to work with gas vesicles contained in cells. In this context, *E. coli* engineered to produce GVs could be selectively lysed via inertial cavitation, enabling the release of intracellular content[126]. This approach holds promise for bacterial cancer therapies, where therapeutic agents synthesized *in situ* could be released on demand. Subsequent studies also extended the use gas vesicle mediated cavitation to gene delivery, showing that DNA-bound gas vesicles could facilitate the transfection of mammalian cells both *in vitro*[127] and *in vivo*[128] via sonoporation, offering a non-viral, spatially targeted gene transfer platform. Furthermore, gas vesicles have been employed to transiently open the blood–brain barrier in mice[129], paralleling strategies previously developed with microbubbles, and highlighting their potential for targeted central nervous system drug delivery.

Beyond gene delivery and blood–brain barrier modulation, gas vesicle–mediated cavitation has also been explored as an enabler of sonodynamic therapy (SDT) for cancer. In SDT, sonosensitizers (small molecules that preferentially accumulate in tumors) are activated by ultrasound to generate cytotoxic effects. One proposed mechanism involves light emission during inertial cavitation events, which may activate certain sonosensitizers, triggering the production of reactive oxygen species (ROS). These ROS induce oxidative stress and apoptosis within cancer cells, offering a non-invasive route to tumor ablation[130,131]. In this context, gas vesicles have been proposed as nanoscale cavitation nuclei for enhancing SDT, owing to their ability to penetrate tumor tissues. An *in vivo* study have demonstrated that the combination of purified gas vesicles with ultrasound exposure significantly increases tumor cell death compared to SDT alone[132]. These findings suggest that gas vesicles can serve to expand the scope of SDT as a spatially controllable, non-invasive cancer treatment.

Gas vesicles for neuromodulation

Neuromodulation, the targeted alteration of neural activity using external stimuli, has become a powerful approach for probing neural circuits and treating neurological disorders. Among the various

modalities, FUS has emerged as a promising non-invasive method capable of activating neurons via mechanosensitive ion channels[133]. FUS has been used to manipulate brain activity across multiple species, including rodents[134], rabbits[135], sheep[136], and non-human primates[137], and is being investigated as a therapeutic strategy for neurological diseases such as Alzheimer's disease[138], Parkinson's disease[139], and depression[140].

However, transcranial ultrasound faces inherent physical constraints. Frequencies low enough to penetrate the intact skull are limited in spatial precision, as beam focus scales inversely with wavelength. In mice, this trade-off restricts targeting resolution to approximately 1–10 mm, complicating the stimulation of small, specific brain regions[141]. A promising solution involves the use of nanoparticle-based acoustic actuators, which locally amplify ultrasound effects in regions where they are injected.

Gas vesicles have recently been studied as one such actuator, owing to their unique acoustic properties and long-term stability in brain tissue. In a 2021 study[142], purified *Anabaena flos-aquae* gas vesicles were shown to be non-cytotoxic and not internalized by neurons *in vitro*. When exposed to low-intensity ultrasound, neurons cultured with gas vesicles exhibited calcium influx, a response absent in control conditions without gas vesicles. Similar effects were observed *in vivo* following sub-millimeter-scale gas vesicle injections into deep brain regions of mice. Subsequent work revealed that this response is primarily mediated by calcium-selective mechanosensitive ion channels, which drive intracellular calcium accumulation and burst firing upon ultrasound stimulation[143].

Expanding on this mechanism, gas vesicle-assisted neuromodulation was shown to modulate behavior in mice[106]. When PEG coated gas vesicles were injected into various motor cortex regions and stimulated transcranially with low-intensity ultrasound, animals exhibited reproducible, intensity-dependent changes in limb movement. The behavioral effects ceased within seconds of ultrasound offset, demonstrating precise temporal control. Importantly, the ultrasound pressure used was insufficient to collapse the vesicles, enabling multiple rounds of stimulation from a single injection. In a depression mouse model, gas vesicle-mediated stimulation of mood-relevant brain regions significantly altered depression-like behaviors, further validating the neuromodulatory potential of this approach.

These findings establish gas vesicles as a minimally invasive tool for spatiotemporally precise neuromodulation, with capabilities approaching those of optogenetics but without the need for genetic modification or implanted optical hardware[106]. Despite their promise, translation to human applications will require careful evaluation of the safety and feasibility of intracerebral gas vesicles delivery.

Objectives

After several decades of fundamental research carried out by a relatively small number of groups worldwide, interest in gas vesicles has grown significantly over the past ten years. This renewed interest was largely driven by the seminal work of Mikhail Shapiro's team at the California Institute of Technology. Although several laboratories in the United States rapidly followed this original line of research, by 2021 (the year I began my PhD) there were, to my knowledge, no research groups in Europe specifically dedicated to the use of gas vesicles as reporters. The sole exception was the newly established group of David Maresca at Delft University of Technology, whose work mainly focused on developing new ultrasound imaging modalities for gas vesicles. But this situation was on the verge of change. In France, three teams decided to join forces to explore and develop this emerging field: our team at Institut Curie, Mickaël Tanter's group at ESPCI (specialized in ultrafast ultrasound imaging), and Jérôme Bonnet's group at the Centre de Biologie Structural in Montpellier (specialized in synthetic biology and the design of microbial sensors and genetic circuits). Our team brought additional expertise at the interface of cancer biology, microbiology, synthetic biology, and microfluidics.
This convergence of complementary expertise provided a unique opportunity to establish and expand this line of research in France. One of the objectives of my PhD was therefore to help set up the experimental and conceptual tools necessary to work with gas vesicles as acoustic reporters, and to contribute to the broader adoption of this innovative technology in France.

But of course the objectives of my PhD don't stop there. While I have no doubt that gas vesicles will become widely used tools in scientific research in the coming decades substantial work remains to fully unlock their potential. The current literature frequently highlights the need to develop increasingly sensitive and specific imaging techniques for gas vesicles, to improve our understanding of their formation mechanisms, and to refine their molecular engineering. Within this abundant flow of ideas and proposals, one particular issue remains, in my opinion, insufficiently addressed. Indeed, for most envisioned applications, gas vesicles are produced heterologously in organisms that do not naturally synthesize them. Yet these vesicles are among the largest intracellular structures in prokaryotes, requiring the coordinated expression of numerous proteins, with dozens of these structures potentially accumulating in just a few hours within the host cell. Taken together, these elements suggest that the production and accumulation of gas vesicles may significantly impact the physiology of host cells. Precisely identifying and quantifying this impact appears essential to bridge the gap from proof-of-concept studies to genuine translational applications. To date, however, these aspects have received relatively little attention in the scientific literature.

It is precisely to this issue that I contributed in addition to helping start the field of sonogenetics in my research team. The impact of heterologous production of gas vesicles on host cells might resemble the effects observed when producing large quantities of other heterologous proteins, namely, a metabolic burden associated with the energetic and resources costs of protein synthesis and potential specific toxicity of certain proteins produced. Futhermore, gas vesicles possess the unique characteristic of occupying a substantial fraction of the cellular volume, which may also significantly affect the integrity and overall physiology of host cells.

Throughout my three-year doctoral research, I chose to address these specific issues by primarily focusing on two aspects: first, the impact of gas vesicle production on bacterial growth; and second, the potential effects of the GV occupied volume in the cytoplasm on the bacterial physiology. These aspects constitute the core of my research.
In parallel, I worked on expanding the methodological toolkit for studying gas vesicles. I conducted preliminary imaging experiments using super-resolution microscopy and collaborated with Mickaël Tanter's group to optimize gas vesicle imaging techniques, which led to the publication of a research article earlier this year.
In the context of therapeutic applications such as anticancer bacterial therapies, I collaborated with Jérôme Bonnet's group from the Centre de Biologie Structural in Montpellier to develop a method for three-dimensional visualization of bacterial colonization within tumor models.
The methods that I developed and implemented during my PhD, now form a technical foundation for gas vesicle research within our team at Institut Curie.

This thesis is structured into three main chapters:

- The first chapter addresses the impact of gas vesicle production on the growth of *Escherichia coli*, both in batch cultures and continuous microfluidic cultures.
- The second chapter explores how the volume occupied by gas vesicles can influence antibiotic tolerance in *Escherichia coli*.
- The third chapter presents complementary work, namely the preliminary observation of gas vesicles through super-resolution microscopy and the three-dimensional imaging of bacterial colonization of in vitro tumor models.

Chapter I : Heterologous production of Gas Vesicles imposes stress and reduces growth in Escherichia coli in batch culture and microcolonies.

Contextual introduction

Our team at Institut Curie has a longstanding interest in synthetic biology across various model organisms. Before starting my PhD, I worked as an assistant engineer in the lab for a year, during which I contributed to several synthetic biology projects in yeast[144,145], while earlier work from the team had focused on bacteria[146,147]. Since relocating to Institut Curie in 2020, the team has also developed a growing interest in cancer research.
It was therefore natural that, when we began exploring the emerging field of acoustic imaging using gas vesicles, one of the most compelling applications that caught our attention was the use of ARGs for monitoring of bacteria in live animals.

Early in my PhD, I gained access to plasmids encoding the first generation of ARGs[91]. Using these, I was able to induce gas vesicle production at 30°C. However, in preliminary experiments, I quickly noticed that induction at 37°C, more relevant for *in vivo* applications, nearly halted bacterial growth. As I began to investigate the possible causes of this effect and how it might be mitigated, a preprint from Mikhail Shapiro's group was released on bioRxiv describing a second-generation ARG, bARGser[82], engineered from a different gene cluster and reportedly functional at 37°C. We reached out to Shapiro's group, who promptly provided us with the new plasmids. With this second-generation system, we confirmed that gas vesicles could indeed be produced at 37°C without such an impact on growth. However, in preliminary experiments, I still observed some noticeable impact on growth, particularly a reduced final cell density in overnight cultures, an effect that was not addressed in the preprint at the time.

That same year, I attended the first International Symposium on Biomolecular Ultrasound & Sonogenetics (ISBUS 2022), a relatively small international conference hosted by Shapiro's group at the California Institute of Technology. The conference centered largely (though not exclusively) on gas vesicles as acoustic reporters. There, I presented some of my initial results and discussed with researchers from the still nascent field of biomolecular ultrasound.

While many facets of gas vesicle applications were addressed during the symposium, I was surprised to find that none had investigated the physiological burden imposed by heterologous gas vesicle production. In hindsight, this oversight makes sense, as most published work at that point was still at the proof-of-concept stage. Yet, it seemed (and still seems) to me that this question is fundamental for advancing toward more translational uses of gas vesicles, particularly as genetically encoded reporters in live animals.

This realization led me to want to investigate and address this knowledge gap in the literature myself through a dedicated research article. This is the work that I'll present to you in this first chapter of my thesis. This paper will soon be available as preprint on bioRxiv, and is presented in the following chapter in a layout adapted for this PhD thesis.

Supplementary materials associated with this paper are available in Appendix 3. Please note that, as this chapter is written as a standalone paper, it includes its own bibliography, separate from that of the thesis. Accordingly, the reference numbers in the text of this chapter refer to the paper's bibliography.

Article

Heterologous production of Gas Vesicles imposes stress and reduces growth in Escherichia coli in batch culture and microcolonies.

Simon Barral[1], Chloé Sasson[2], Céline Cordier[1], Jessica Riou-Ramon[1], Benoit Sorre[1], Karine Guevorkian[1], Mickael Tanter[3], Jérôme Bonnet[2] , Pascal Hersen*[,1].

[1] *Physics of Cells and Cancer CNRS UMR168, Sorbonne Université, Institut Curie, 11 Rue Pierre et Marie Curie, 75005 Paris, France.*
[2] *Centre de Biologie Structurale CNRS UMR5048 and INSERM* U1054*, University of Montpellier,* 29 Rue de Navacelles, 34090 Montpellier, *France.*
[3]*Physics for Medicine Paris UMR8063, ESPCI Paris, Paris Science Lettres University (PSL), CNRS, 2-10 rue d'Oradour-sur-Glane, 75015 Paris, France.*

** Correspondence and requests for materials should be addressed to Pascal Hersen (pascal.hersen@curie.fr).*

Keywords:

Gas vesicles, metabolic burden, sonogenetic, E.coli, microfluidic, Acoustic reporter genes, growth, microcolonies

Abstract

Gas vesicles (GVs) are gas-filled protein nanostructures that are naturally produced by some aquatic microorganisms to regulate their buoyancy. Their heterologous expression in bacteria can be used as acoustic reporters of gene expression, an emerging acoustic analogue to fluorescent proteins. Despite the growing interest in GV-based imaging tools, the physiological burden of GV production in engineered hosts remains largely unexplored. Here, we quantitatively assess the impact of heterologous GV expression on *Escherichia coli* physiology under both homogeneous batch culture and heterogeneous structured microcolony conditions obtained in microfluidic devices. We demonstrate that GV production leads to a reduced growth, pronounced reduction in biomass yield, and induction-dependent apparition of GV non-producing populations. Our findings reveal that, while GVs are powerful tools for acoustic imaging, their production imposes a non-negligible burden on host cells. These insights call for careful optimization and new synthetic biology circuits to regulate GV expression and decrease the GV induced burden, particularly in applications requiring sustained viability and stability over time.

Introduction

Gas vacuoles are large, refractile intracellular structures found in various aquatic microorganisms which have been known for more than 130 years[1]. In 1965, Bowen and Jensen provided the first electron microscopy images of such gas vacuoles, revealing that they are composed of smaller, gas-filled vesicles organized in a honeycomb-like arrangement, which they named "Gas Vesicles" (GVs)[2]. Since then, GVs primary biological function to regulate cell buoyancy has been well-established[3,4]. By adjusting their buoyancy, cells containing GVs can adjust their vertical position to reach optimal growth conditions.

Structurally, GVs are rigid, gas-filled cylindrical shells with conical end caps, typically 45 to 200 nm in width and 200 to 1000 nm in length. They are composed of a protein lattice characterized by a hydrophilic outer surface and a hydrophobic inner surface. Nanopores in their structure allow gas to circulate freely between the vesicle's interior and exterior. Comprehensive reviews have previously summarized recent findings about their structure, function, and regulatory mechanisms[3–6].

Interestingly, over the past 15 years, interest in GVs has substantially increased due to their promising utility in biomedical research and medical applications. Gas vesicles have notably been employed as antigen carriers for vaccination[7–9], as cavitation nuclei for the transient permeabilization of cell membranes[10], enabling applications like blood-brain barrier opening[11] and in vivo non-viral gene delivery[12,13], and as tools for neuromodulation via focused ultrasound[14,15].

Another promising and actively explored application area for GVs is deep-tissue imaging. Due to their nonlinear deformation in response to ultrasounds, GVs can be specifically detected and quantified by acoustic imaging[16–19]. This for example enables the use of purified gas vesicles as injectable, tunable nanoscale contrast agent for ultrasound imaging[16,20]. Moreover, following the seminal works of M. Shapiro and colleagues, it is now possible to insert optimized gene coding sequence to use GVs as genetically encoded reporter an acoustic equivalent of green fluorescent protein (GFP). As a matter of fact, engineered GV gene clusters known as Acoustic Reporter Genes (ARGs) have been developed and successfully implemented in bacterial and mammalian cells, showing considerable promise[17,21]. This allows to monitor gene expression and sensing of cellular environments through ultrasounds rather than optical signals. Such an approach is particularly advantageous for contexts where deep-tissue monitoring of cells in humans or animals is required since ultrasound can penetrate way deeper into living materials than what light can. Potential applications include the study of microbiota in vivo or the non invasive monitoring of engineered therapeutic bacteria within tumors. Development of ARGs remains in its early stages, and many improvements are needed to facilitate their use in fundamental research and biotechnological applications

In particular, the cost of producing and accumulating gas vesicles in cells is not known. Indeed, while GVs are mostly made of one protein (GVpA), their assembly requires the expression of a large gene cluster. As an example, the latest optimized generation of ARGs for *E.coli* is composed of 19 essential genes with a total length of more than 16kb[21]. Producing a large amount of such GVs in cells can not only divert resources from growth, but it can also trigger stress responses and metabolism overflow that could significantly alter the overall cell metabolism[22] and physiology. Furthermore, GVs are fairly large structures, occupying an important volume of the intracellular space, and electron microscopy images of recombinant E.coli producing GVs show that dozens of them can accumulate in it, potentially impacting water homeostasis, molecular crowding and cytoplasm dynamics[17,21]. It is

therefore expected that using ARGs could significantly impact on the growth and the metabolism of the host cell. Precisely identifying and quantifying this impact appears essential to bridge the gap from proof-of-concept studies to genuine translational applications. To date, however, these aspects have received relatively little attention in scientific literature.

In this study, we address this knowledge gap by quantitatively assessing the physiological impact of heterologous GV production in *E. coli*. We engineered strains expressing $bARG_{ser}$, the latest ARG for *E.coli* developed by M. Shapiro's team and systematically analyzed their growth dynamics in two relevant contexts : homogeneous liquid batch cultures and spatially structured microcolonies in microfluidic continuous-culture systems. Our findings provide essential insights into the trade-offs between ARG expression and cell growth rate in *E. coli*, guiding future applications and optimization strategies.

Results

Gas vesicles can easily be produced in batch culture.

We transformed an E.coli strain unable to metabolize arabinose, with a plasmid encoding gas vesicle production under arabinose induction (see Supplementary information for strains and plasmid lists), allowing us to keep a constant level of induction in batch culture experiments, and another plasmid encoding constitutive sfGFP production. To confirm gas vesicle production, we imaged the cells using light microscopy and Transmission Electron Microscopy (TEM) (Figure 1a-d) under 0.1% arabinose induction. Bright-field microscopy revealed clusters of gas vesicles within cells, appearing as bright spots, consistent with reports in the literature and the expected light scattering[3] produced by GVs. Interestingly, in fluorescent microscopy, these clusters appeared as darker regions where cytoplasmic volume exclusion caused by gas vesicle accumulation displaced GFP fluorescence. TEM imaging confirmed the presence of several gas vesicles (Figure 1b-d) that formed larger clusters within the cells.

GVs affect the optical density of bacterial cultures.

To quantify the impact of GVs on bacterial growth rate, we monitored the optical density (at 600 nm) of the bPH_669 strain in batch culture with various induction strengths (arabinose concentrations). However, since GVs are known to scatter light[3], we first needed to determine the contribution of GVs to the optical density. We first compared OD_{600} measurements of cultures with and without arabinose induction (i.e with or without GVs). As shown in Figure 1e, arabinose-induced cultures exhibited an OD_{600} increase from 0.123 ± 0.009 to 0.231 ± 0.009, despite having the same cell density (cells/ml) as measured independently (see Material and methods). This confirmed that OD_{600} measurements alone are unreliable for estimating cell density and growth rates in gas vesicle-producing bacteria : indeed the contributions of light scattering by GVs in bacteria and of the increase of cell density cannot be distinguished with a simple OD measurements. Therefore, we decided to count directly the number of cells per sample using a Helber counting chamber, allowing us to distinguish and quantify separately cell growth and GVs accumulation.

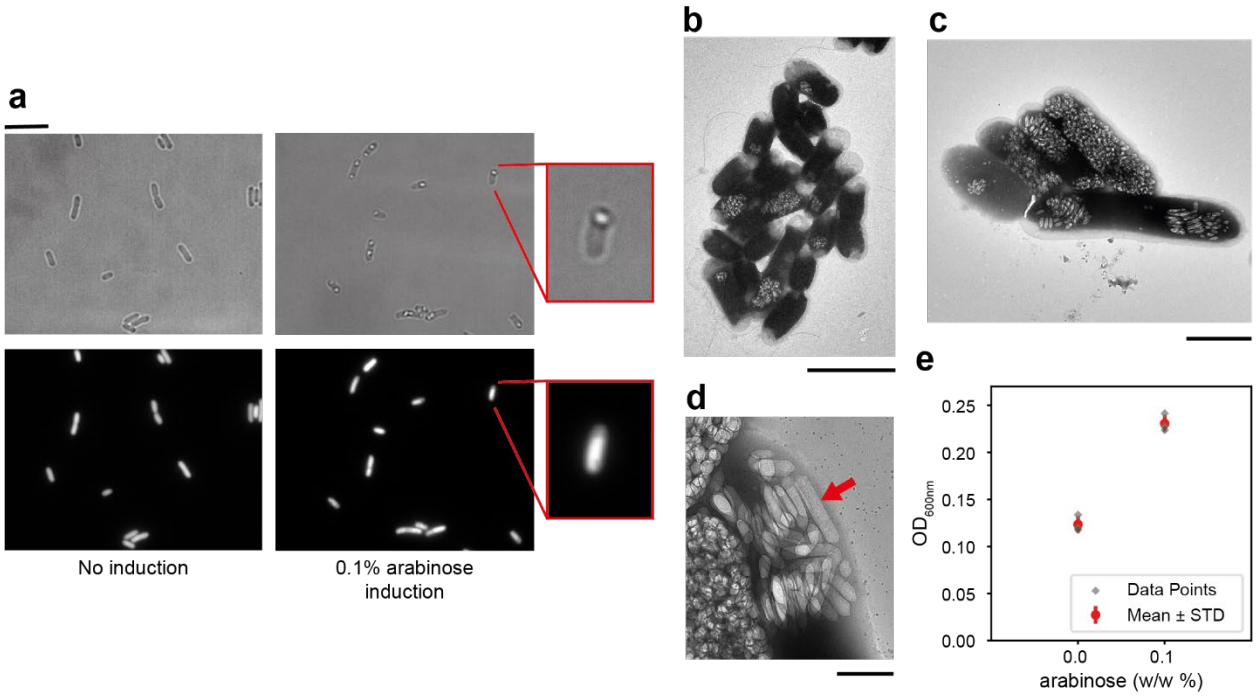

Figure 1 : GVs production in E. coli and its impact on OD. (**a**) Bright-field (top) and fluorescence microscopy (bottom) images of E. coli with (right) and without (left) arabinose induction of GVs production. Inserts show close-up of a single cell containing a GV cluster appearing as a bright spot in bright-field and a darker spot in fluorescence. Scale bar represents 3 µm. (**b-d**) Transmission Electron Microscopy images of E. coli cells containing GVs, at different scales. (**b**) scale bar represents 2.5 µm, GV clusters are visible in some cells as grainy white areas, while some cells do not contain any GVs. (**c**) scale bar represents 1.5 µm, cells with different quantity of GVs in it and GV clustering clearly visible (**d**) scale bar represents 0.5 µm, close-up on a GV cluster, with individual rode shaped GV visible, one of them indicated by the red arrow. Some individual GVs are indicated by red arrows. Scale bar represents 1 µm. (**e**) Difference of Optical Density at 600 nm between samples with and without induction of GV production after 12h of culture. All samples contain the same number of cells per ml, counted in Helber chamber and equilibrated. Red points represent the average of three independent experiments, red bars indicate one standard deviation and grey points show individual datapoints.

GV production leads to a decrease in maximal cell density and induces stress in batch culture.

To quantify the physiological impact of GV production in batch cultures, we estimated *E. coli* growth by manually counting cell number using a Helber chamber, across conditions and time points (Figure 2). These measurements were complemented by bright field microscopy acquisitions to assess GV expression kinetics and cellular morphology. First, we observed that induction of GV expression led to a significant decrease in the maximum cell density, with the effect scaling with the strength of arabinose induction (Figure 2a). Under the highest induction condition (0.1% arabinose), the final cell density reached only 46% of the control experiment with no induction and no detectable GV, with cell counts of $1.3 \times 10^9 \pm 2.1 \times 10^8$ cells/mL versus $2.7 \times 10^9 \pm 7.1 \times 10^8$ cells/mL, respectively. Notably, while the growth rate in the exponential phase (between 2 and 4h datapoints) remained unchanged upon induction, it is diminished (compared to the non-induce condition) for the two strongest induction conditions at the end of the exponentials phase (Supplementary Figure 3) and could indicates earlier entry into the stationary phase. Because cultures were grown in LB medium, where stationary phase is primarily triggered by carbon source depletion[23], we conclude that the premature growth arrest is the trace of increased carbon consumption during the growth phase, a phenomenon likely associated with increased resource consumption associated with the induction of ARG expression[24]. Yet, another contributing factor may be the progressive accumulation of gas vesicles within individual cells over time, as shown in Figure 1.

To better quantify GV production, we analyzed bright intracellular refractile bodies previously confirmed to be GV clusters. From microscopy images, both the cells and their GV clusters were segmented and their surface measured (see Supplementary information).The segmented surface area of GV clusters can serves as a proxy for relative GV abundance. Our analysis revealed a positive correlation between the induction level and the measured GV accumulation (Figure 2b). At 0.1% arabinose (maximum induction), GV abundance was 5.4-fold higher than at 0.001% arabinose (the lowest induction condition), similar to the increase in ultrasound signal-to-background ratios previously reported under similar conditions by Hurt *et al.* at roughly 5.8 fold[21]. This increase resulted from both a steady growth in average cluster size (Figure 2d) and a higher fraction of GV-positive cells (Figure 2c). Indeed, not all cells in a sample, even at the strongest induction, contained visible GV clusters. At ≥ 0.01% arabinose, the vast majority of cells contained detectable GV clusters (95 ± 2% at 0.1% and 91 ± 4% at 0.01% induction), whereas only 34 ± 6% were GV-positive under low induction (0.001%) by the time they reach stationary phase. A possible explanation for that is the limit of detection of GVs clusters. With such low induction, it is possible that most GVs clusters formed could be so small that they go undetected with our method. Moreover, the average size of GV clusters also increases with time, indicating that individual cells accumulate GVs with time.

Induction also impacted cell morphology (Figure 2e, Supplementary Figure 1), with a marked increase in both mean cell length and the fraction of abnormally sized cells, suggestive of stress-associated phenotypes[22].

The relationship between total biomass and GV load is summarized in Figure 2f. Collectively, these results indicate that, on average at the population scale, GV expression imposes a measurable metabolic and physiological burden under homogeneous culture conditions.

While this burden is relevant to scalable GV bioproduction, it may not recapitulate the dynamics in complex *in vivo* environments such as the gut microbiota or solid tumors, where ARGs are most

applicable. In such dense communities, steep gradients in nutrients, oxygen, and metabolites generate pronounced metabolic heterogeneity, which could modulate both GV production and its associated fitness cost[25]. Even in well-mixed liquid cultures, we observed substantial cell-to-cell variation, with a fraction of cells lacking detectable GVs at any given timepoint and induction level. The origins of this heterogeneity, and its consequences for GV production in structured environments, cannot be resolved from the static snapshots of uniformly grown batch cultures used so far; we therefore decided to employ an alternative approach.

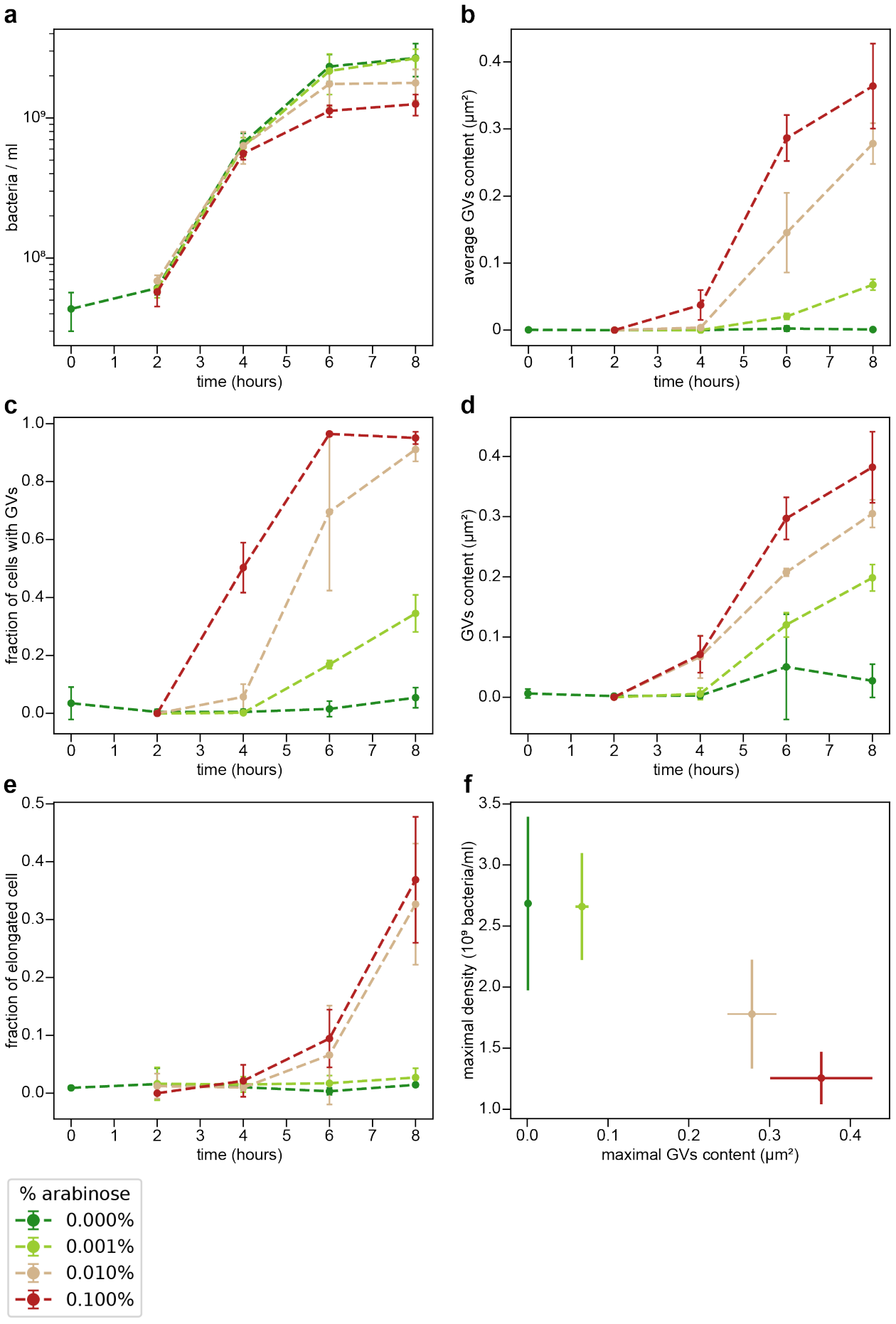
a
bacteria / ml
10^9
10^8
time (hours)
b
average GVs content (µm²)
time (hours)
c
fraction of cells with GVs
time (hours)
d
GVs content (µm²)
time (hours)
e
fraction of elongated cell
time (hours)
f
maximal density (10^9 bacteria/ml)
maximal GVs content (µm²)
% arabinose
0.000%
0.001%
0.010%
0.100%

Figure 2 : In batch culture, arabinose induction leads to GVs production which impacts cell growth, maximal cell density and cell morphology. (**a**) Growth curves upon various arabinose inductions, determined by counting cells in Helber chamber. (**b**) GVs production determined with bright field microscopy, here showing the average surface of refractile bodies per cell in the whole population as a proxy for the overall GVs content of the sample. For more details on determination of these values see Supplementary Information (**c**) Fraction of cells containing detectable GV clusters. (**d**) GVs content measured only in cells that contain GVs as shown in (c), showing increased GV cluster size over time. (**e**) Fraction of elongated cells in the samples, indicating stress response following induction of GVs production. Cells with length above the average value plus 3 standard deviations of the corresponding non induced sample are considered to be elongated. (**f**) Correlation between the maximum cell density and the maximum GVs produced for various arabinose inductions, indicating the cost of GVs production. Established by plotting 8h timepoints bacteria/ml values from (a) vs 8h timepoint of GVs content from (b). See Supplementary Information for the number of cells studied in microscopy in each sample to obtain these curves. Histograms showing the distribution of cell length and GV content for each timepoint and each induction strength are provided in Supplementary Figure 1 and Supplementary Figure 2. For each plot, points represent the average of the mean of three independent experiments; error bars correspond to one standard deviation.

Gradients of bacteria colonies can be replicated in 2D microcolonies in microfluidic chips, enabling assessment of GV effects in structured populations.

To more accurately assess the impact of GVs on bacterial microcolonies, we engineered a microfluidic chip designed to support the growth of two-dimensional bacterial colonies. The device contains chambers measuring 375 µm in length, 30 µm in width, and 1.4 µm in height, perfused from one side (Figure 3). Similar designs have been used previously[26–28] and shown that, in such configurations, cells nearest the inlet rapidly consume available nutrients, creating a steep nutrients concentration decline with increasing distance into the chamber. This gradient establishes a distinct growth profile: cells close to the inlet divide rapidly, whereas those further away, experiencing reduced nutrient availability, slow their growth, alter their metabolism, and eventually enter dormancy. Such spatial structuring produces gene-expression patterns that delineate physiological zones arising primarily from the interplay between nutrient diffusion and cellular consumption[27].

In our experiments, we generated such 2D colonies by inserting cells at the end of the chamber and let them colonize it and establish stable gradient for 24h. We then monitor them for 31 hours experiments, with constant flow of fresh culture medium containing (or not) the arabinose to induce GV production within the colony. We developed a Python pipeline to quantify both bacterial growth and GVs production over time, across the chambers (Figure 3). Kymographs depicting growth rates and GV accumulation over 31 hours are shown in Figure 4 and Figure 5, respectively. In the absence of GV induction, we observed a well-defined and stable growth gradient within the 100 µm region closest to the chamber inlet (Figure 4 a). Our results aligns with previous reports[26–28], indicating the spontaneous generation of nutrient gradient and the resulting metabolic landscape.

Importantly, we verified that despite the possible presence of antibiotic gradients within the colonies, the overall antibiotic concentration remained sufficient to maintain plasmid selection throughout the entire depth of the chamber (Supplementary Figure 4c, Supplementary Information). We also assessed the penetration of arabinose within the colony and demonstrated that it was not a limiting factor for the activation of the *pBAD* promoter driving GV expression (Supplementary Figure 4a and b, Supplementary Information).

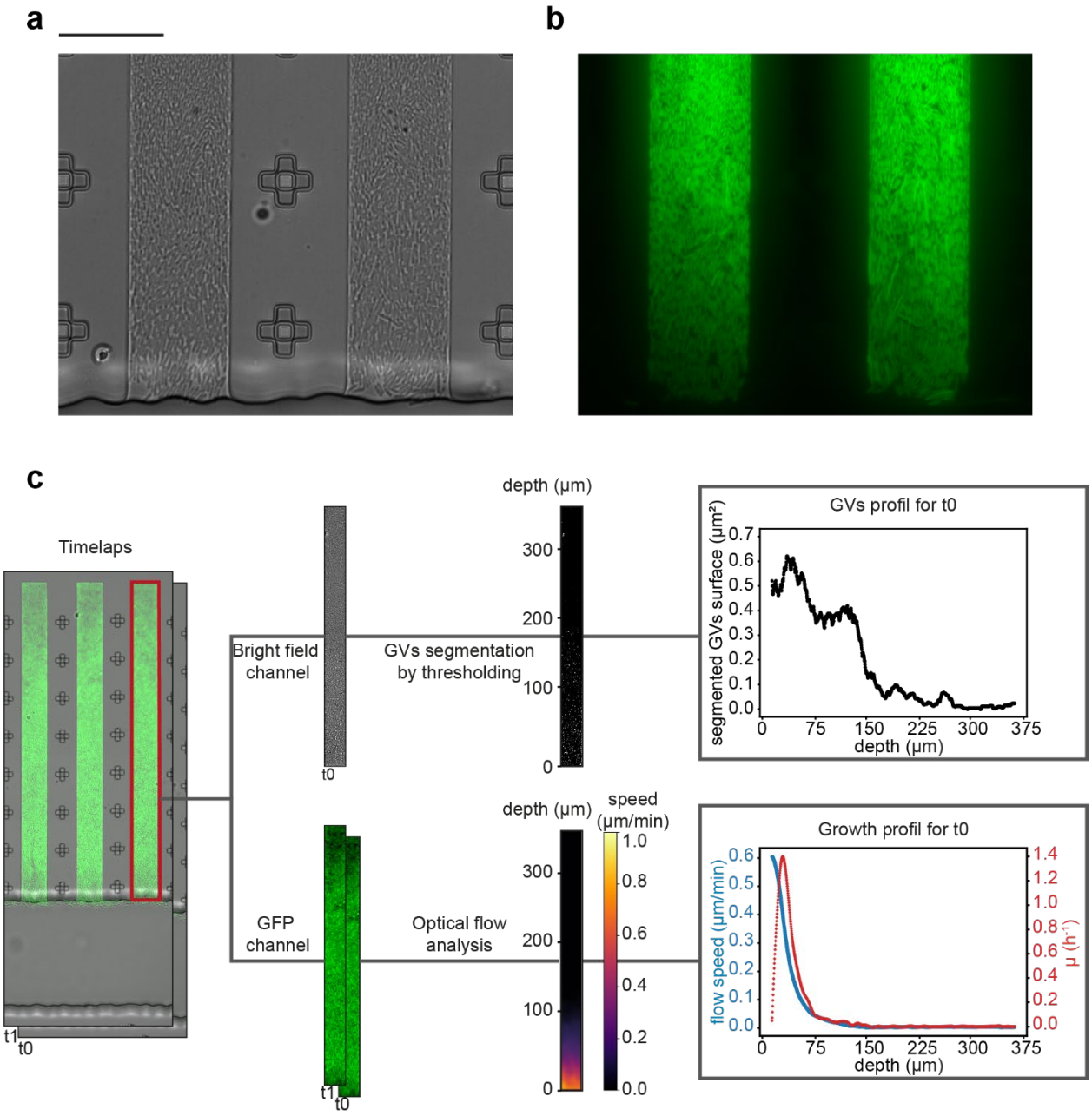

Figure 3 : Microfluidic system and image analysis pipeline for quantifying growth and GVs production in bacterial microcolonies from time-lapse microscopy. (**a-b**) Bright field (a) and fluorescent (b) images of the 100 µm of the chamber closer to the inlet, roughly corresponding to the extent of the growing area of the microcolony. (a) and (b) share the same scale bar representing 30 µm. On both contrast was adjusted for better visualization. (**c**) Diagram of the pipeline for image analysis. The microfluidic chip contains chambers measuring 30 × 375 µm with a height of 1.4 µm, which are seeded with bacteria and supplied with fresh medium from one side only, establishing nutrient gradients across the colony. Bright-field images enable GV detection, with GVs segmented using automatic thresholding; their surface area serves as a proxy for GV content. Optical flow analysis is performed on consecutive frames (t0 and t1) from the GFP channel to estimate bacterial displacement within the chamber. As the bacteria are non-motile, movement reflects colony expansion and arises solely from growth. Therefore, at a given depth, the observed flow is the result of local growth plus the cumulative growth from deeper regions. Thus, the local growth rate along the

chamber can be inferred by computing the spatial derivative of the flow velocity. For GV quantification, the segmented GV surface is calculated at each depth (0.33 μm step size) by summing the segmented GV area within a 16.5 μm-long sliding window, providing a smoothed depth profile of GV abundance. Additional methodological details are available in Supplementary Information.

GV production in microcolonies reduces the spatial extent of the growth region, the maximal growth rate, and consequently, the overall biomass production.

When inducing the production of GV in this setup, we observed several changes in the microcolonies' growth.

First, the boundary separating growing from non-growing areas shifted toward the chamber inlet following induction, with a maximal reduction observed after 13.6 hours at 0.1% arabinose, where the boundary moved from an initial position of 118 ± 14μm to 68 ± 38 μm. Similar phenomenon was observed with the 0.01% arabinose induction, with the boundary moving from 118 ± 13μm to 80 ± 10 μm over the same time. In contrast, for the lowest induction (0.001% arabinose) and in non-induced controls, the boundary remained stable at approximately the initial position (Figure 4; Supplementary Figure 4a) throughout the whole experiment. This shift is consistent with the hypothesis of increased carbon consumption rate upon GV induction that we formulated following batch culture experiments : cells near the nutrient source consume more resources upon induction, steepening the gradient and thereby reducing the spatial extent of the actively growing region of the colony.

Second, following induction, a reduction in maximal growth rate was observed under the strongest induction condition (0.1%). In this case, the maximal growth rate (located in the close proximity to the chamber inlet, where nutrient availability is highest) progressively declined after induction, stabilizing around 9 h post-induction (Figure 4d). Upon stabilization, the maximal growth rate was 81 ± 30% of its pre-induction value (Supplementary Figure 5d). This effect was not observed under weaker induction conditions or in the non-induced control.

Overall, GV production led to a reduction in total biomass production over time. Indeed, the biomass production at each time point (Figure 4) can be estimated by integrating the local growth rate over the chamber length (Supplementary Figure 5b). To quantify steady-state biomass production, these values were further averaged over a stable period from 9 to 19 hours post-induction, yielding a relative biomass production yield for each condition (Supplementary Figure 5c). The results revealed a dose-dependent reduction in biomass yield, with the strongest induction (0.1% arabinose) producing only 53% ± 18% of the biomass observed in non-induced controls, consistent in effect and scale with our earlier findings in batch culture.

In structured environment, kinetics of GV production scale with induction strength

GV clusters were segmented from microscopy images, providing a proxy for relative GV abundance. GV production was reliably detected under medium (0.01%) and strong (0.1%) induction conditions. In contrast, under the weakest induction level (0.001% arabinose), no significant GV signal was observed (Figure 5).

GV production was primarily localized to the growing region of the colony. However, an accumulation of GVs was also detected in a non-growing zone extending up to ~125 μm in depth, close to the pre-induction growth boundary (e.g., 118± 14μm in the 0.1% condition). In this region, GV accumulation

occurred at a slower rate and subsequently stabilized for the remainder of the experiment (Figure 5). Because cells here and in the deeper regions are not growing (and therefore not displaced by colony expansion), the stabilization of signal suggests that GV production in these cells ceases after a few hours.

In conditions where GVs were detectable, GV production followed a logistic-like trajectory. GV levels became detectable after ~1.8 h and ~2.9 h of induction for 0.1% and 0.01% arabinose conditions, respectively. This was followed by a sharp increase: under 0.1% induction, maximal GV levels were reached after 4.5 h, whereas the same level was attained only after 7.3 h at 0.01%. Notably, GV accumulation plateaued after 4.5 h in the strongest induction condition. By contrast, under 0.01% induction, GV levels continued to rise beyond 10 h, albeit at a reduced rate, eventually surpassing those in the 0.1% condition by the end of the experiment (Figure 5; Supplementary Figure 6a). However, this differences almost completely disappeared when accounting for the appearance of non-GV-producing populations in the chamber (discussed in the next paragraph). When chambers containing such populations were excluded from the analysis from the moment of their appearance, the final GV levels were similar for both induction conditions (Supplementary Figure 6)

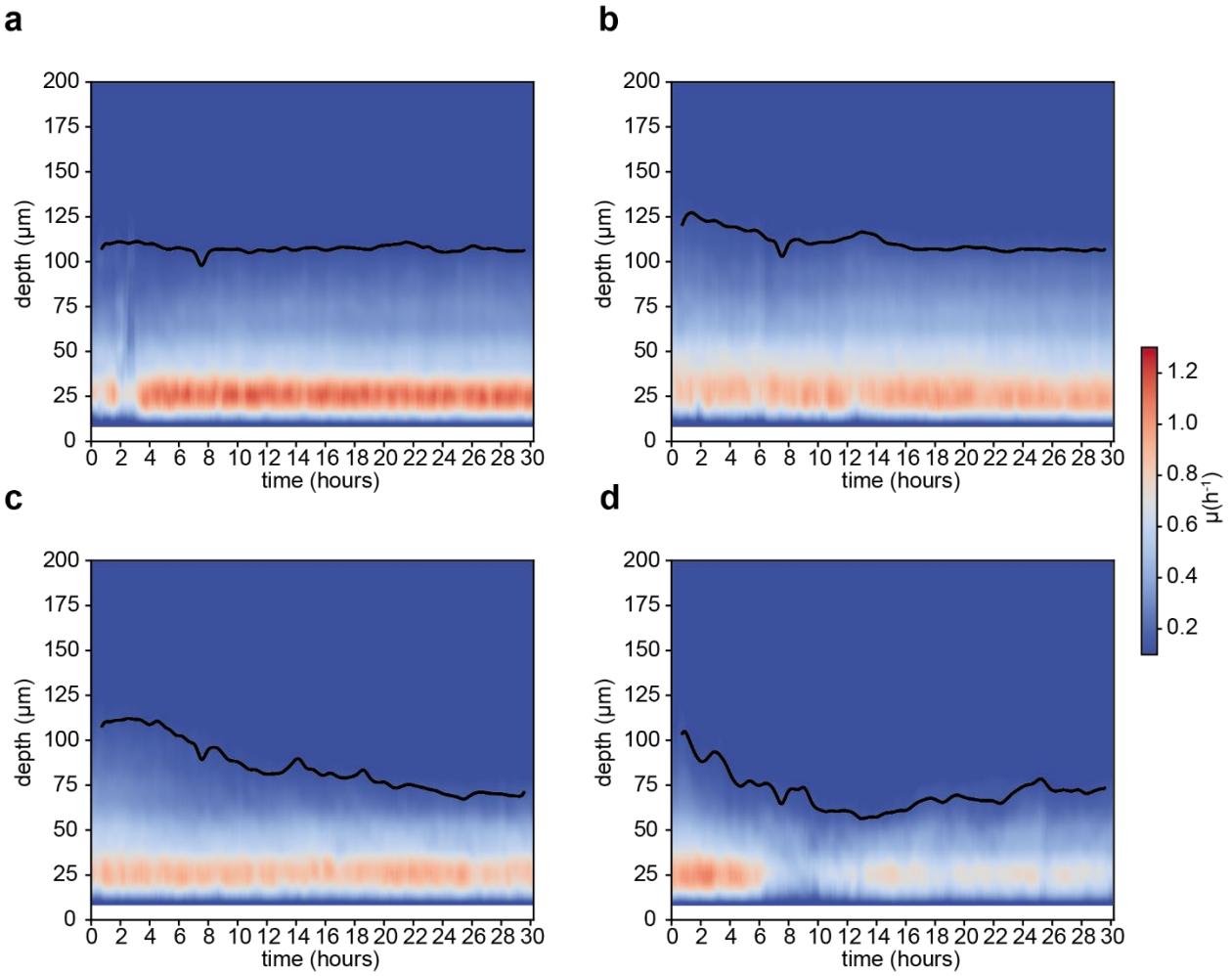

Figure 4 : Spatial and temporal dynamics of growth rate as a function of depth and induction time in bacterial microcolonies. Each kymograph represents the local bacterial growth rate as a function of colony depth and time. Growth rate is encoded by color intensity and reflects the average of 26 to 30 microfluidic chambers combined from three independent experiments. The black line marks the average boundary between actively growing and growth-arrested regions within the microcolonies. As in Fig. 4, kymographs are cropped at 200 µm depth for clarity, as no growth was observed beyond this region. Panels correspond to different levels of arabinose induction: (**a**) no arabinose, (**b**) 0.001% arabinose, (**c**) 0.01% arabinose, and (**d**) 0.1% arabinose. In the induced conditions, arabinose reaches the microcolonies 1 hour after the start of the kymograph, accounting for both a fixed system delay and the time required for medium change in the central channel. Additional methodological details are available in Supplementary Information.

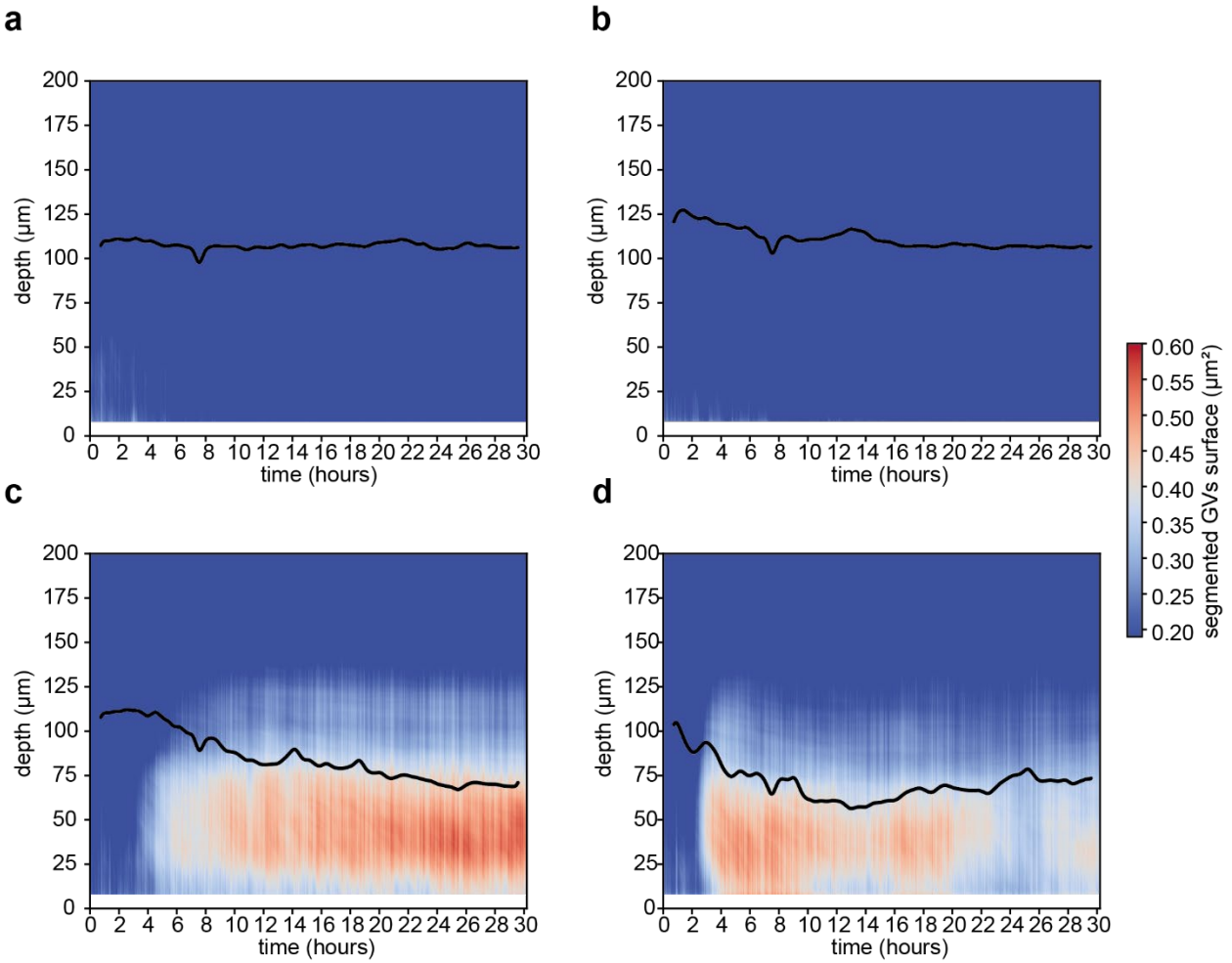

Figure 5 : GVs production as a function of depth and induction time in bacterial microcolonies. Each kymograph displays the segmented GVs surface area across colony depth and over time following induction. GVs abundance, indicated by color intensity, reflects the average of the total segmented surface area from 26 to 30 microfluidic chambers pooled across three independent experiments. The black line marks the average boundary between actively growing and growth-arrested regions within the microcolonies, highlighting the GVs produced in the non-growing regions of the colony. Although the chambers extend to a depth of 300 µm, the kymographs are cropped at 200 µm to enhance visibility, as GVs production was not detected beyond this range. Panels correspond to different induction conditions: (**a**) no arabinose, (**b**) 0.001% arabinose, (**c**) 0.01% arabinose, and (**d**) 0.1% arabinose. In the induced conditions, arabinose reaches the microcolonies 1 hour after the start of the kymograph, accounting for both a fixed system delay and the time required for medium change in the central channel. Additional methodological details are available in Supplementary Information.

Strong arabinose induction promotes the emergence of non-GV-producing subpopulations in microcolonies

Over the 30 microcolonies studied for the 0.1% arabinose condition, in 20 instances we observed the emergence of distinct non-GV-producing subpopulations. These appeared as expanding regions within the colony where no GV clusters could be detected (Figure 6a). A similar phenomenon was observed 5 times under the 0.01% arabinose condition. We estimated the frequency of emergence of cells at the origin of such non-GV-producing subpopulations (see Supplementary information) and found a significant difference between different induction strength, with the strongest induction leading to the highest frequency of non-GV-producing subpopulations (Figure 6d). The depth in the colony at which such subpopulation emerged also differs with the induction strength, but in both conditions, these tend to appear slightly above the boundary between growing and non-growing regions of the colony (Supplementary Figure 7a). However, the timing of onset did not differ significantly between the two conditions (Supplementary Figure 7b). These non-GV-producing subpopulations typically emerged as narrow zones that expanded laterally as they progressed toward the chamber outlet, suggesting a competitive growth advantage over surrounding GV-producing cells. Over the course of the 31-hour experiments, the majority of these non-producing regions remained stably devoid of GV expression for the rest of the experiment. However, we observed in one single instance, under the 0.1% induction condition, a non-GV-producing subpopulation that resumed GVs production around 6 hours after it emerged (Supplementary Figure 8).

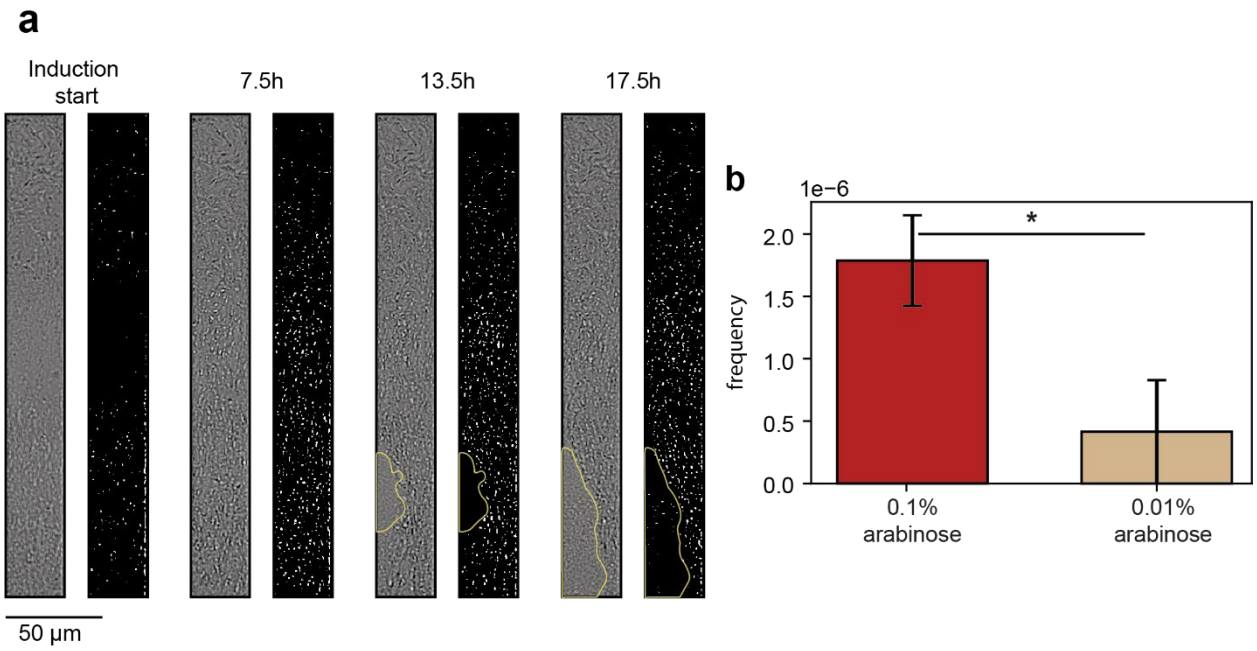

Figure 6 : Emergence of non-GV-producing populations in microcolonies under medium and strong arabinose induction. (**a**) Representative example of the emergence and spatial spread of a non-GV-producing subpopulation within a GV-producing microcolony under 0.1% arabinose induction. Bacteria flow is from top to bottom. Time points correspond to hours post-induction. For each time point, the left panel shows a bright-field image of the colony (cropped to the first 200 µm near the chamber outlet), with contrast enhanced to improve visibility of bright GV clusters. The corresponding right panel displays the segmented GV clusters in white, with yellow outlines highlighting regions devoid of GV signal. (**b**) Frequency of non-GV-producing cell emergence, calculated as the number of non-GV-producing regions detected divided by the estimated total number of divisions in all chambers of the experiment, for each condition, bar height represents the average value across 3 separated experiments, error bars indicate ±1 standard deviation. Here, statistical comparisons between induction conditions were performed using two-tailed t-test (* = $p < 0.05$). More details on methods to calculate these frequencies are available in Supplementary Information.

Discussion

In this study we showed that the production of GVs and GV proteins does impact growth at the population scale, although at different degrees depending on the context. In batch culture, we noted a decrease in the maximal growth rate only at the end of the exponential phase, where GVs really start to accumulate in the cells (Figure 2a-d, Supplementary Figure 3) for the strongest induction tested. In the earlier stage of the induction, however, where GV proteins are being produced but no assembled GVs can be detected, we did not observe any significant effect of the induction on growth rate. This suggests that GV expression remains within the cell's biosynthetic buffer capacity, without creating a bottleneck in proteomic or metabolic resources such as ribosomes, amino acids, or tRNAs. The late reduction of growth observed in this context might therefore be the consequence of several factor : earlier resources exhaustion, accumulation of large number of GVs and buildup of excess GV proteins.

In microfluidic experiments, consistent with batch culture results, we observed a reduction in maximal growth rate under 0.1% arabinose induction after more than 4 hours of induction (Figure 4). By contrast, no reduction was detected at 0.01% induction, despite both conditions ultimately reaching similar GV levels. Because our measurements capture only assembled GVs and not the total pool of GV proteins, these findings indicate that growth rate reduction is not directly caused by GV accumulation itself.

In their natural hosts, the organization of GV operons, the presence of regulatory genes, and differences in protein stability ensure heterogeneous relative abundances of GV proteins and temporally controlled expression[4,5,29]. In ARGs expressed in *E. coli*, however, this regulation is lost: regulatory genes are removed, and all remaining genes are driven by a single promoter. This is likely to create an imbalance in the relative abundance of GV proteins, with some produced faster than they can be used to assembled GVs. Over time, the buildup of such excess proteins could exert toxic effects. This mechanism provides a possible explanation for why gradual reductions in maximal growth rate were observed only under the strongest induction, where GV proteins are produced the fastest. To our knowledge, however, no study has yet directly assessed the toxicity of individual GV proteins when overexpressed in *E. coli*.

We also observed a substantial reduction in biomass yield, defined as the amount of biomass produced per unit of carbon source, upon GV production, with yields reduced by approximately twofold in both batch cultures (Figure 2e) and microcolonies (Supplementary Figure 4). This indicates that a greater proportion of the available carbon source is being diverted toward processes other than biomass synthesis. A likely contributor is the energetic demand associated not only with the synthesis of GV proteins but also with their assembly into functional gas vesicles. Although the ATP cost of GV assembly has not been formally quantified, many GV operons (including the ARG used in this study) encode the ATP-hydrolyzing protein GvpN, which is believed to supply energy for vesicle elongation[5,30], implying that GV formation requires active energy input.

This energetic burden is consistent with our observation that the rate of nutrient consumption increases upon GV induction, likely as a compensatory response to meet elevated ATP demand. In the spatially structured microcolonies, this manifests as a reduced extent of the growing region (Figure 4), reflecting more rapid depletion of diffusible nutrients by GV-producing cells.

Furthermore, reduced biomass yield is a well-known hallmark of overflow metabolism, a physiological state in which cells, despite the presence of sufficient oxygen, shift toward fermentative pathways that generate ATP less efficiently than respiration[31,32]. This metabolic switch results in the excretion of carbon-rich byproducts, most notably acetate, which diverts carbon flux away from biomass production. Overflow metabolism is tightly linked to growth rate[32] and is commonly observed in fast-growing bacterial populations in rich media. For example, acetate production has been reported in chemostat cultures at growth rates as low as 0.35 to 0.48 h^{-1}[34]. This phenomenon has also been observed in cells growing in LB[33], the same medium used in our experiments. Importantly, the threshold growth rate at which acetate begins to be produced is known to decrease following recombinant protein production[31,34,35], likely due to the increased demand for both energy and biosynthetic resources. Taken together, these factors provide a putative explanation for the reduced biomass yield observed in our batch cultures following GV induction.

We also found that GV production, even at moderate induction levels as low as 0.01% arabinose, tenfold lower than the induction used in the original *in vivo* imaging proof-of-concept by *Hurt et al.* [21], elicits clear signs of cellular stress. This was evidenced by increased cell filamentation in batch cultures (Figure 2d). Filamentation can arise from several stress responses[22], including the nutrient starvation response, which has been linked to the induction of mutagenic double-strand break repair pathways[22,36,37]. Consistent with this, our microcolony experiments revealed an induction-dependent increase in the frequency of non-GV-producing cell emergence (Figure 6d), with such cells arising preferentially in regions of slow or arrested growth (Supplementary Figure 7), areas where nutrient limitation is likely to trigger stress responses. These findings indicate that in colonies, GV production associated stress promote genetic instability.

While genetic escape is an anticipated outcome in burdensome synthetic systems, our findings demonstrate that such escape can occur relatively rapidly under strong induction in spatially structured environments. Gas vesicles production relies on the coordinated expression of a large number of genes, making the system particularly susceptible to loss-of-function mutations, as any one of which can eliminate vesicle formation entirely[21]. This inherent fragility increases the likelihood of non GV producing mutants emerging under sustained selective pressure. This observation is relevant for one of the primary envisioned applications of ARGs : long-term, non-invasive imaging of therapeutic bacterial populations within tumors. These applications often depend on the persistence of viable colonies over several days or weeks[38]. Although bacterial growth in the tumor microenvironment would likely be slower than in nutrient-rich laboratory media, potentially delaying the onset of mutant emergence, the sustained selective pressure imposed by continuous ARG induction could still favor the gradual outgrowth of GV-deficient mutants, which would escape ultrasound detection.

However, mutation may not be the only cause of GV-negative cells in the population. As mentioned earlier, in one instance, we observed a temporary cessation of GV production lasting several hours, after which production resumed to its initial level (Supplementary Figure 8). Given its transient nature, this interruption is unlikely to have arisen from a genetic mutation. A possible explanation is the asymmetric inheritance of GV clusters during cell division: if one daughter cell retains all previously synthesized GVs and GV proteins while the other receives none, the latter may gain a transient growth advantage by avoiding GV-associated stress. Such a cell would effectively “restart” GV production from zero, similar to cells not exposed to the inducer at the beginning of the experiment. The observed

time to recover initial GV levels, of ~5.5 h, closely matches the ~4.5 h delay between induction onset and attainment of maximal GV levels at the start of the experiment, supporting this hypothesis. This same mechanism could also account for the presence of a small fraction of GV-negative cells observed in every induced batch culture, even under the strongest induction level, and even after hours after reaching stationary phase of the growth curve.

A potential solution to the limitations imposed by the deleterious effects of GV production on cell growth and health is to implement dynamic control of ARG expression, using short, intermittent pulses of induction timed with imaging needs. The optimal strength and duration of such induction pulses *in vivo* remain to be determined, but our results provide important initial guidance. Specifically, we show that in spatially structured environments, stronger induction leads to faster GV accumulation but does not necessarily result in higher final GV concentrations. There is therefore an optimal combination of induction strength, timing and duration to be found to achieve sufficient ultrasound contrast while minimizing cellular stress and reducing the selective pressure against GV expression. Fine-tuning these parameters in both *in vitro* and relevant *in vivo* contexts will be essential for translating ARGs from proof-of-concept systems to robust, practical tools for microbial imaging. An interesting first step in that direction could be to implement a feedback-controlled microfluidic platform, coupled with recently developed smart-microscopy frameworks[39–41] to empirically identify optimal induction regimes. For example, the system could dynamically adjust inducer levels to maintain a target GV abundance while minimizing overall induction.

Materials and Methods

Strains

E.coli K12 BW25113 ΔfliA Δ(araD-araB), from the Keio collection[42], was used as the parental strain. The Δ(araD-araB) deletion makes it unable to consume arabinose, and the ΔfliA deletion makes it unable to swim. To construct the strain used in all experiments involving GV expression (bPH_669), cells were sequentially transformed with a low-copy number plasmid encoding the ARG operon under control of the arabinose-inducible pBAD promoter (Addgene #192473) and a second plasmid for constitutive sfGFP expression. To assess arabinose diffusion in microcolonies, strain bPH_715 was constructed by transforming the same parental strain with a plasmid expressing sfGFP under the pBAD promoter. The strain used to evaluate the efficacy of selection antibiotics in microcolonies in microfluidic chip, strain bPH_657, was produced by transforming the parental strain only with the plasmid encoding for constitutive sfGFP production. Tables are provided in Supplementary Information detailing the strains and plasmids used in this work.

Cell Culture, GV Induction, and Sampling in Batch Culture

Luria-Bertani (LB) Miller medium was used in this work. It was prepared by adding 10g Bacto™ Tryptone (Gibco) with 10g Sodium Chloride (Sigma Aldrich) and 5g yeast extract (Sigma Aldrich) per liter of miliQ water, mixing and autoclaving it. Overnight cultures were prepared from isolated colonies grown in the homemade LB Miller medium at 37 °C with shaking at 270 rpm. GV production was induced by adding L-arabinose (Thermo Scientific ref 365180250) to final concentrations of

0.1%, 0.01%, or 0.001% (w/w), followed by incubation at 37 °C with shaking at 225 rpm. For experiments shown in Fig. 2, 50 µL samples were collected before induction and every 2 hours over an 8-hour period, then stored at 4 °C prior to analysis.

Sample analysis from batch culture

Cell densities were measured using a Helber counting chamber (Hawksley Z30000). GV clusters were visualized via bright-field and fluorescence microscopy on agar pads using an Olympus IX83 microscope with a UPlanSApo 100×/1.40 objective. Cells were segmented and analyzed using a custom Python script. GV content per cell was quantified by calculating the surface area of bright-field pixels exceeding an adaptive, cell-specific intensity threshold.

Microfluidic chip preparation and loading

Microfluidic molds were designed using CleWin 5 software and fabricated via standard SU-8 (MicroChem) photolithography. Each chip contained 10 growth chambers measuring 375 × 30 × 1.4 µm, aligned along 100 µm-wide, 30 µm-high channels. Chips were cast by pouring a 5:1 mixture of PDMS and curing agent onto the mold, degassed, and cured overnight at 65 °C. After curing, chips were cut, inlet and outlet holes were punched, and devices were bonded to glass coverslips using oxygen plasma treatment followed by a 30-minute bake at 65 °C. For loading, cells were cultured at 37 °C for 5 hours, centrifuged, and concentrated 20-fold in LB supplemented with 5 g/L Pluronic F-127 (Sigma Aldrich). Concentrated suspensions were introduced into the channels via syringe. Following loading, chips were mounted on an Olympus IX83 microscope, and a continuous flow of fresh medium was established. Before the start of the experiment, without recording, cells were incubated under flow for 16 hours at 37 °C to allow full chamber colonization and the establishment of stable nutrient gradients.

Recording of microfluidic experiments

Time-lapse imaging was performed using an Olympus IX83 microscope with a 20× objective (Olympus UplanSApo 20x, Thermo Scientist AMEP4734) and Andor Zyla 4.2 sCMOS camera, capturing all 10 chambers per lane every 3 minutes (similar to the acquisition rate used by others for e.coli in similar contexts[26,28,43]) in bright-field and GFP channels. For GFP channel, excitation filter was 470/40nm, emission filter was 525/50nm (Chroma cube 49002). Chips were maintained at 37 °C under 50 µL/min perfusion with LB medium containing Pluronic F-127 (Sigma Aldrich), antibiotics, and L-arabinose (Thermo Scientific ref 365180250) using a peristatic pump (Ismatec IPC). In every experiment, a 1hour pre-induction phase without arabinose was recorded before medium switching.

Image preprocessing and growth analysis

Bright-field and GFP fluorescence stacks were aligned using the SIFT Linear Stack Alignment algorithm[44] implemented in Fiji to correct for drift. Maximum intensity projections of the GFP channel

were used to segment chambers via thresholding, generating binary masks. Images were rotated to orient chambers vertically, and individual chambers were cropped using a custom Python script. Contrast Limited Adaptive Histogram Equalization[45] was applied with OpenCV to GFP images to normalize fluorescence across the field of view.

Local growth rates along the depth of each chamber were estimated from pixel displacements between consecutive frames using optical flow analysis, as described previously[26,46]. Optical flow was computed with the Farnebäck algorithm[47] (OpenCV), which generates a dense two-dimensional vector field of horizontal (x) and vertical (y) motion from a pair of sequential frames. A 60 × 60 pixel (19.8 µm) interrogation window was used to balance sensitivity to small displacements against noise. The y-component, representing motion toward the chamber opening, was averaged across the chamber width and smoothed with a 10-frame rolling average. Because the cells were non-motile and densely packed, observed motion reflected only growth-driven displacement. In the confined geometry of a single-opening chamber, displacement at a given depth arises both from local cell growth and from cumulative expansion of cells located further inside. The local growth rate at each position was therefore obtained by calculating the spatial derivative of the velocity profile.

Non-growing control colonies, generated by treatment with a non-permissive antibiotic, were used to define a velocity threshold used to distinguish between growing and non-growing areas of the colony. For these colonies, the mean y-flow and its standard deviation were calculated across all chambers and time points 10 hours after beginning exposure to antibiotic. The velocity threshold was set to the control mean velocity plus three standard deviations. The growth boundary of colonies was defined as the furthest distance to the chamber entry at which the y-flow exceeded the velocity threshold.

GV clusters were segmented from bright-field images as bright, highly refractile regions. A chamber-specific intensity threshold was automatically determined from the first five pre-induction frames, where GV production was absent, by identifying the pixel value below which 99% of intensities fell. Pixels exceeding this threshold were classified as GV-positive. To generate a depth-resolved GV content profile, segmented pixels were summed within a 50-pixel (16.5 µm) sliding window across the full chamber width and centered at each depth along the y-axis. This yielded a one-dimensional spatial profile of GV abundance for each time point.

More detailed information about the methods are available in supplementary information.

Supplementary Information

“Supplementary_material.pdf” contains more detailed versions of experimental protocols and image analysis procedures as well as strains and plasmids tables.

Data used to produce every plots and the associated python script are also provided.

References

1. Klebahn, H., 1895 :: AlgaeBase. https://www.algaebase.org/search/bibliography/detail/?biblio_id=32397.
2. Bowen, C. C. & Jensen, T. E. Blue-Green Algae: Fine Structure of the Gas Vacuoles. *Science* **147**, 1460–1462 (1965).
3. Walsby, A. E. Gas Vesicles. *Microbiol. Rev.* **58**, 94–144 (1994).
4. Pfeifer, F. Distribution, formation and regulation of gas vesicles. *Nat. Rev. Microbiol.* **10**, 705–715 (2012).
5. Pfeifer, F. Recent Advances in the Study of Gas Vesicle Proteins and Application of Gas Vesicles in Biomedical Research. *Life* **12**, 1455 (2022).
6. Huber, S. T. & Jakobi, A. J. Structural biology of microbial gas vesicles: historical milestones and current knowledge. *Biochem. Soc. Trans.* **52**, 205–215 (2024).
7. Stuart, E. S., Morshed, F., Sremac, M. & DasSarma, S. Antigen presentation using novel particulate organelles from halophilic archaea. *J. Biotechnol.* **88**, 119–128 (2001).
8. Adamiak, N., Krawczyk, K. T., Locht, C. & Kowalewicz-Kulbat, M. Archaeosomes and Gas Vesicles as Tools for Vaccine Development. *Front. Immunol.* **12**, 746235 (2021).
9. Hill, A. M. & Salmond, G. P. C. Microbial gas vesicles as nanotechnology tools: exploiting intracellular organelles for translational utility in biotechnology, medicine and the environment. *Microbiology* **166**, 501–509 (2020).
10. Bar-Zion, A. *et al.* Acoustically triggered mechanotherapy using genetically encoded gas vesicles. *Nat. Nanotechnol.* **16**, 1403–1412 (2021).
11. Zhang, J. *et al.* Biosynthetic Gas Vesicles Combined with Focused Ultrasound for Blood–Brain Barrier Opening. *Int. J. Nanomedicine* **17**, 6759–6772 (2022).
12. Tayier, B. *et al.* Biosynthetic nanobubbles for targeted gene delivery by focused ultrasound. *Nanoscale* **11**, 14757–14768 (2019).
13. Xie, L., Wang, J., Song, L., Jiang, T. & Yan, F. Cell-cycle dependent nuclear gene delivery enhances the effects of E-cadherin against tumor invasion and metastasis. *Signal Transduct. Target. Ther.* **8**, 1–16 (2023).
14. Hou, X. *et al.* Precise Ultrasound Neuromodulation in a Deep Brain Region Using Nano Gas Vesicles as Actuators. *Adv. Sci. Weinh. Baden-Wurtt. Ger.* **8**, e2101934 (2021).
15. Hou, X. *et al.* Nanobubble-actuated ultrasound neuromodulation for selectively shaping behavior in mice. *Nat. Commun.* **15**, 2253 (2024).
16. Shapiro, M. G. *et al.* Biogenic gas nanostructures as ultrasonic molecular reporters. *Nat. Nanotechnol.* **9**, 311–316 (2014).
17. Bourdeau, R. W. *et al.* Acoustic reporter genes for noninvasive imaging of microorganisms in mammalian hosts. *Nature* **553**, 86–90 (2018).
18. Feng, R., Lan, J., Goh, M. C., Du, M. & Chen, Z. Advances in the application of gas vesicles in medical imaging and disease treatment. *J. Biol. Eng.* **18**, 41 (2024).
19. Maresca, D. *et al.* Nonlinear ultrasound imaging of nanoscale acoustic biomolecules. *Appl Phys Lett* (2017).
20. Wang, G. *et al.* Surface-modified GVs as nanosized contrast agents for molecular ultrasound imaging of tumor. *Biomaterials* **236**, 119803 (2020).

21. Hurt, R. C. *et al.* Genomically mined acoustic reporter genes for real-time in vivo monitoring of tumors and tumor-homing bacteria. *Nat. Biotechnol.* 1–13 (2023) doi:10.1038/s41587-022-01581-y.
22. Snoeck, S., Guidi, C. & De Mey, M. "Metabolic burden" explained: stress symptoms and its related responses induced by (over)expression of (heterologous) proteins in Escherichia coli. *Microb. Cell Factories* **23**, 96 (2024).
23. Sezonov, G., Joseleau-Petit, D. & D'Ari, R. Escherichia coli Physiology in Luria-Bertani Broth. *J. Bacteriol.* **189**, 8746–8749 (2007).
24. Picon, A., Teixeira de Mattos, M. j. & Postma, P. w. Reducing the glucose uptake rate in Escherichia coli affects growth rate but not protein production. *Biotechnol. Bioeng.* **90**, 191–200 (2005).
25. Jo, J., Price-Whelan, A. & Dietrich, L. E. P. Gradients and consequences of heterogeneity in biofilms. *Nat. Rev. Microbiol.* **20**, 593–607 (2022).
26. Stevanovic, M. *et al.* Nutrient Gradients Mediate Complex Colony-Level Antibiotic Responses in Structured Microbial Populations. *Front. Microbiol.* **13**, 740259 (2022).
27. Marinkovic, Z. S. *et al.* A microfluidic device for inferring metabolic landscapes in yeast monolayer colonies. *eLife* **8**, e47951 (2019).
28. Bittihn, P., Didovyk, A., Tsimring, L. S. & Hasty, J. Genetically engineered control of phenotypic structure in microbial colonies. *Nat. Microbiol.* **5**, 697–705 (2020).
29. Völkner, K., Jost, A. & Pfeifer, F. Accessory Gvp Proteins Form a Complex During Gas Vesicle Formation of Haloarchaea. *Front. Microbiol.* **11**, (2020).
30. Cai, K. *et al.* The model cyanobacteria Anabaena sp. PCC 7120 possess an intact but partially degenerated gene cluster encoding gas vesicles. *BMC Microbiol.* **20**, 110 (2020).
31. Basan, M. *et al.* Overflow metabolism in Escherichia coli results from efficient proteome allocation. *Nature* **528**, 99–104 (2015).
32. Vemuri, G. N., Altman, E., Sangurdekar, D. P., Khodursky, A. B. & Eiteman, M. A. Overflow Metabolism in Escherichia coli during Steady-State Growth: Transcriptional Regulation and Effect of the Redox Ratio. *Appl. Environ. Microbiol.* **72**, 3653–3661 (2006).
33. Baev, M. V., Baev, D., Radek, A. J. & Campbell, J. W. Growth of Escherichia coli MG1655 on LB medium: determining metabolic strategy with transcriptional microarrays. *Appl. Microbiol. Biotechnol.* **71**, 323–328 (2006).
34. Eiteman, M. A. & Altman, E. Overcoming acetate in Escherichia coli recombinant protein fermentations. *Trends Biotechnol.* **24**, 530–536 (2006).
35. Åkesson, M., Karlsson, E. N., Hagander, P., Axelsson, J. P. & Tocaj, A. On-line detection of acetate formation in Escherichia coli cultures using dissolved oxygen responses to feed transients. *Biotechnol. Bioeng.* **64**, 590–598 (1999).
36. Ponder, R. G., Fonville, N. C. & Rosenberg, S. M. A switch from high-fidelity to error-prone DNA double-strand break repair underlies stress-induced mutation. *Mol. Cell* **19**, 791–804 (2005).
37. Shee, C., Gibson, J. L., Darrow, M. C., Gonzalez, C. & Rosenberg, S. M. Impact of a stress-inducible switch to mutagenic repair of DNA breaks on mutation in Escherichia coli. *Proc. Natl. Acad. Sci.* **108**, 13659–13664 (2011).
38. Torres, W. *et al.* Bacteria in cancer therapy: beyond immunostimulation. *J. Cancer Metastasis Treat.* **4**, N/A-N/A (2018).

39. Chiron, L. *et al*. CyberSco.Py an open-source software for event-based, conditional microscopy. *Sci. Rep.* **12**, 11579 (2022).
40. Almada, P. *et al*. Automating multimodal microscopy with NanoJ-Fluidics. *Nat. Commun.* **10**, 1223 (2019).
41. Pinkard, H., Stuurman, N., Corbin, K., Vale, R. & Krummel, M. F. Micro-Magellan: open-source, sample-adaptive, acquisition software for optical microscopy. *Nat. Methods* **13**, 807–809 (2016).
42. Baba, T. *et al*. Construction of Escherichia coli K-12 in-frame, single-gene knockout mutants: the Keio collection. *Mol. Syst. Biol.* **2**, 2006.0008 (2006).
43. Bakshi, S. *et al*. Tracking bacterial lineages in complex and dynamic environments with applications for growth control and persistence. *Nat. Microbiol.* **6**, 783–791 (2021).
44. Lowe, D. G. Distinctive Image Features from Scale-Invariant Keypoints. *Int. J. Comput. Vis.* **60**, 91–110 (2004).
45. Zuiderveld, K. VIII.5. - Contrast Limited Adaptive Histogram Equalization. in *Graphics Gems* (ed. Heckbert, P. S.) 474–485 (Academic Press, 1994). doi:10.1016/B978-0-12-336156-1.50061-6.
46. Dal Co, A., van Vliet, S. & Ackermann, M. Emergent microscale gradients give rise to metabolic cross-feeding and antibiotic tolerance in clonal bacterial populations. *Philos. Trans. R. Soc. B Biol. Sci.* **374**, 20190080 (2019).
47. Farnebäck, G. Two-Frame Motion Estimation Based on Polynomial Expansion. in *Image Analysis* (eds. Bigun, J. & Gustavsson, T.) 363–370 (Springer, Berlin, Heidelberg, 2003). doi:10.1007/3-540-45103-X_50.

Supplementary figures

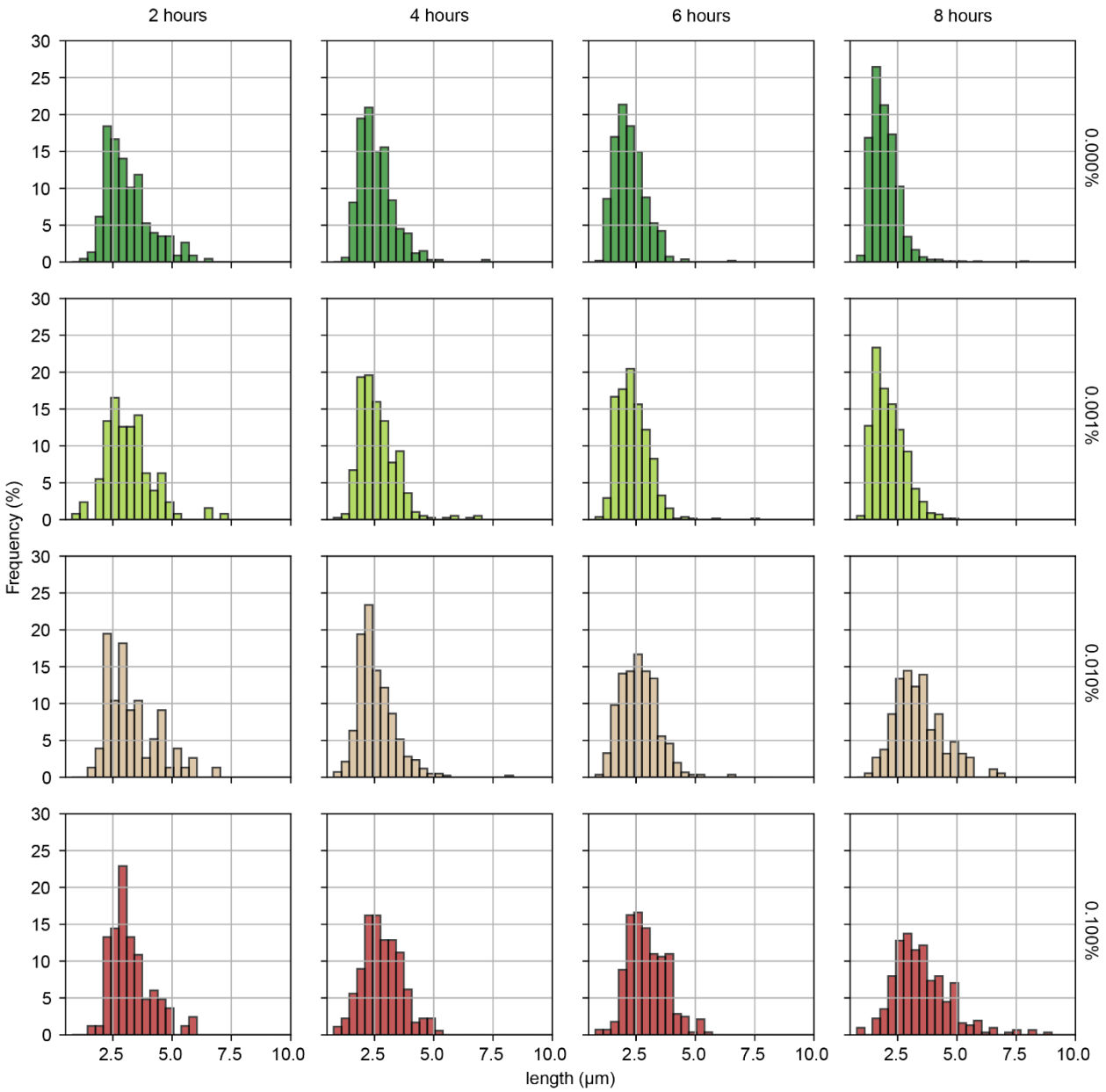

Supplementary Figure 1 : Distribution of cell length in batch culture experiments. Each histogram represents the distribution of the 3 replications of the batch culture experiments pooled together. Histograms are sorted by time (in column) and induction strength (in rows).

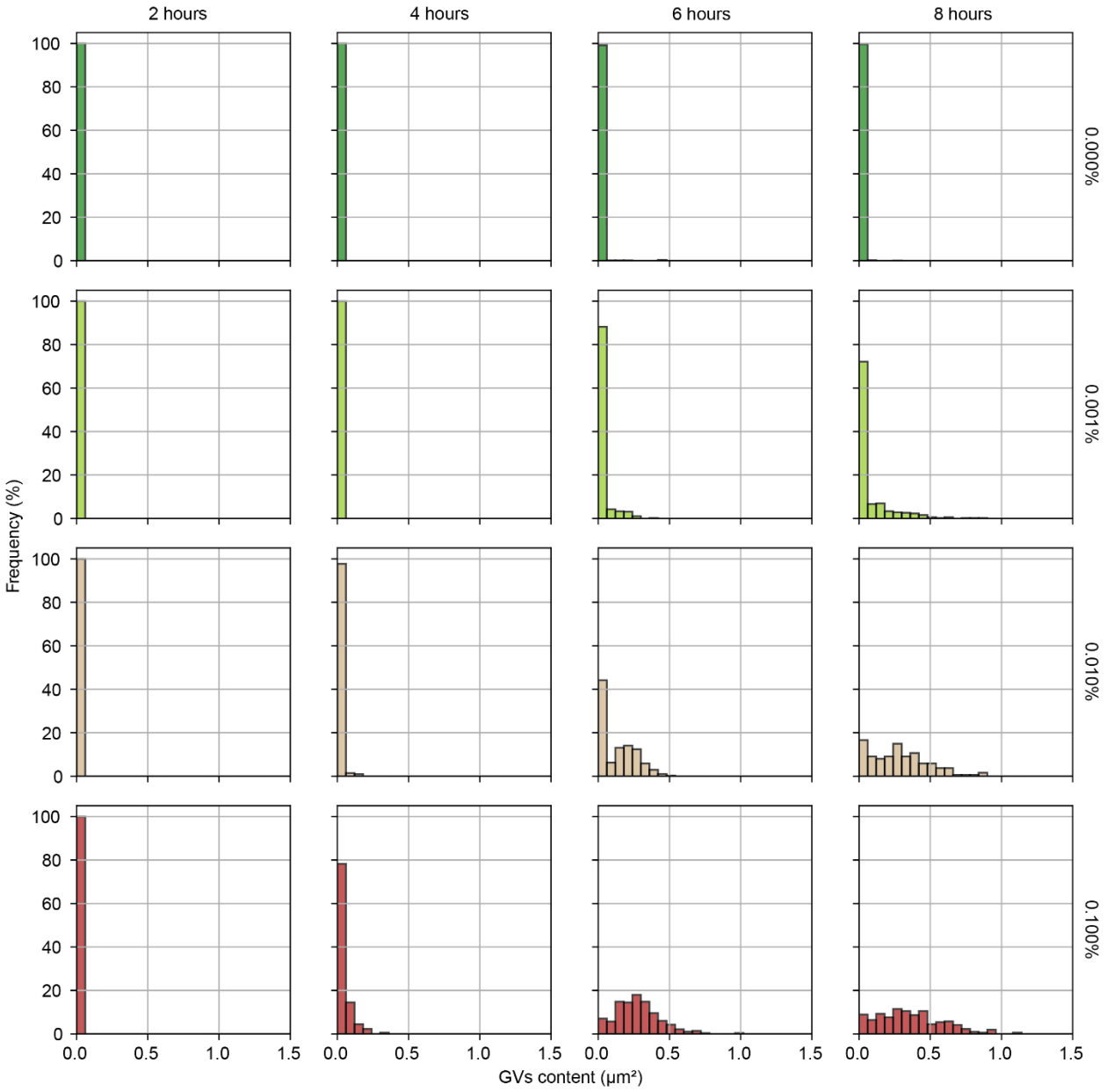

Supplementary Figure 2 : Distribution of cell GV content in batch culture experiments. Each histogram represents the distribution of the 3 replications of the batch culture experiments pooled together. Histograms are sorted by time (in column) and induction strength (in rows).

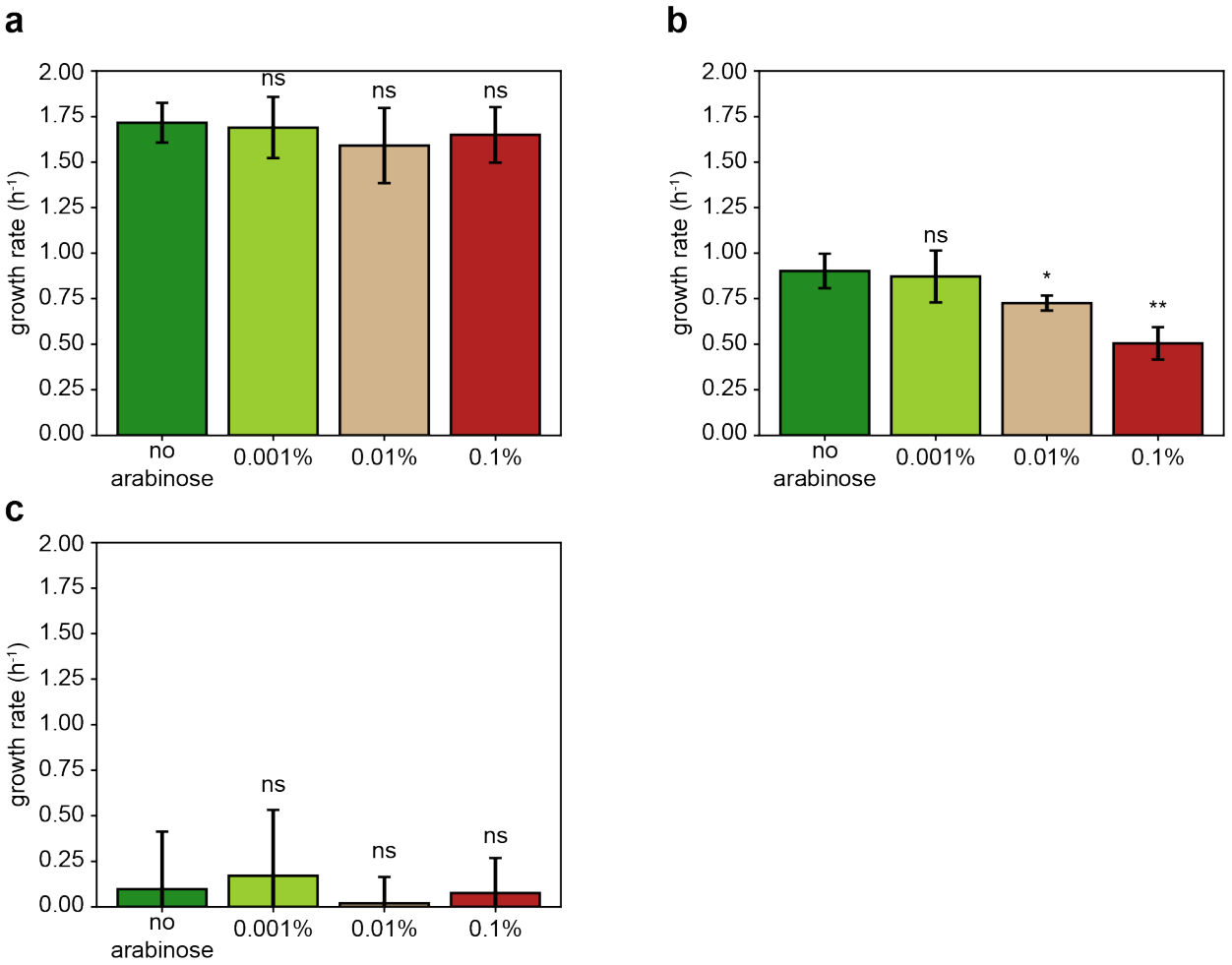

Supplementary Figure 3 : Growth rate in batch culture with arabinose induction. Each bar represents the mean growth rate ± one standard deviation, calculated from the data shown in Fig. 2a, with three independent experiments per condition. Statistical comparisons with the non-induced control were performed using Welch's *t*-test (ns, $p > 0.05$; *, $0.01 < p < 0.05$; **, $0.001 < p < 0.01$; ***, $p < 0.001$). (**a**) Growth rates calculated between 2–4 h. (**b**) Growth rates calculated between 4–6 h. (**c**) Growth rates calculated between 6–8 h.

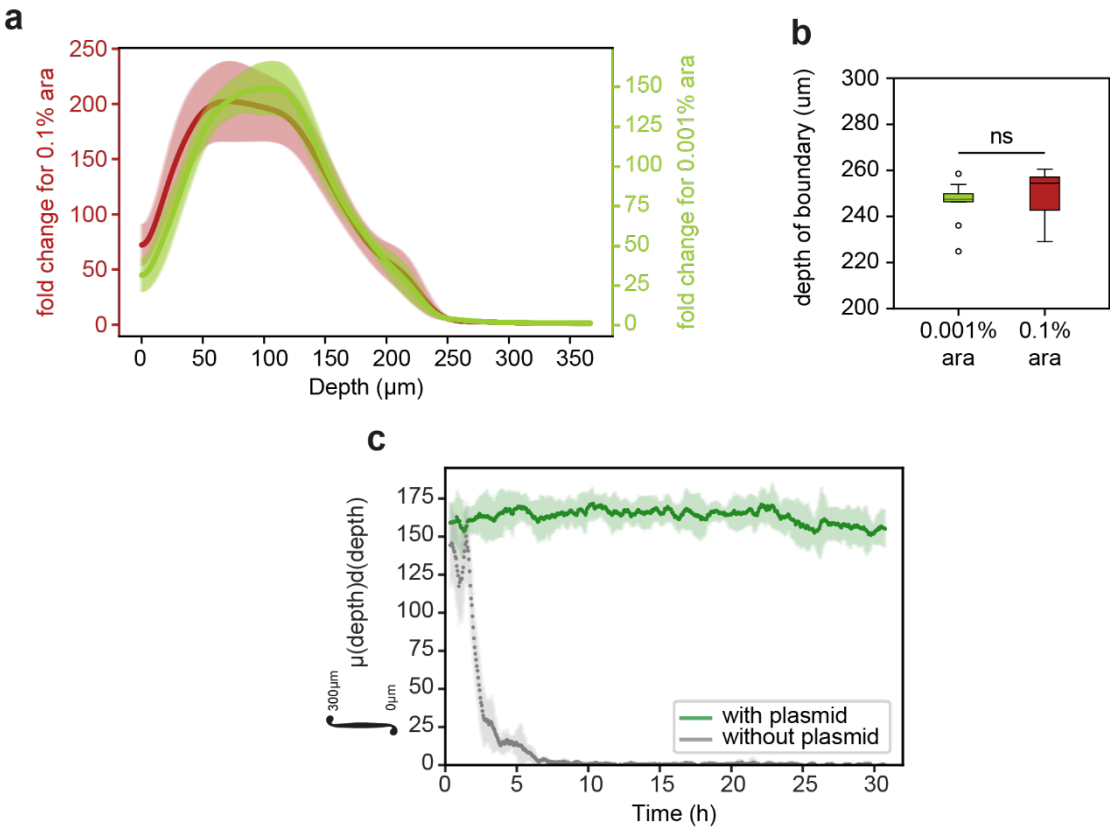

Supplementary Figure 4 : Validation of arabinose and antibiotic diffusion within the microfluidic chamber. (**a**, **b**) To determine whether limited arabinose diffusion could explain the absence of gas vesicle (GV) production in the deeper regions of colonies (as shown in Fig. 4), *E. coli* cells carrying a pBAD-GFP expression plasmid were used as a reporter for arabinose availability. Following chamber loading and filling, cells were exposed to either 0.1% or 0.001% arabinose for 10 hours. Despite the 100-fold difference in inducer concentration, the spatial distribution of GFP expression and the position of the GFP-positive boundary within the colony were nearly identical across conditions, indicating that arabinose diffusion is not a limiting factor for gene expression in the deeper chamber regions. For each condition, 10 replicate chambers were analyzed. In (b), a statistical comparison of the depth of the GFP-positive boundary at both concentrations yielded a non-significant difference (two-tailed t-test, p = 0.520). (**c**) To confirm that the antibiotic concentration remains sufficient throughout the colony depth to maintain plasmid selection, the plasmid-free parental strain bPH_103 was allowed to colonize the chamber. After the chamber was filled, antibiotic was added to the flowing medium at standard working concentrations. The y-axis represents the integrated growth rate across the depth of the chamber, serving as a proxy for total biomass production. Each data point reflects the average of 10 replicates, with color filled area indicating ±1 standard deviation. Without plasmid, the total growth of the colony completely stopped after around 6h, never to restart again, indicating that at every depth of the colony, the plasmid is required to maintain growth.

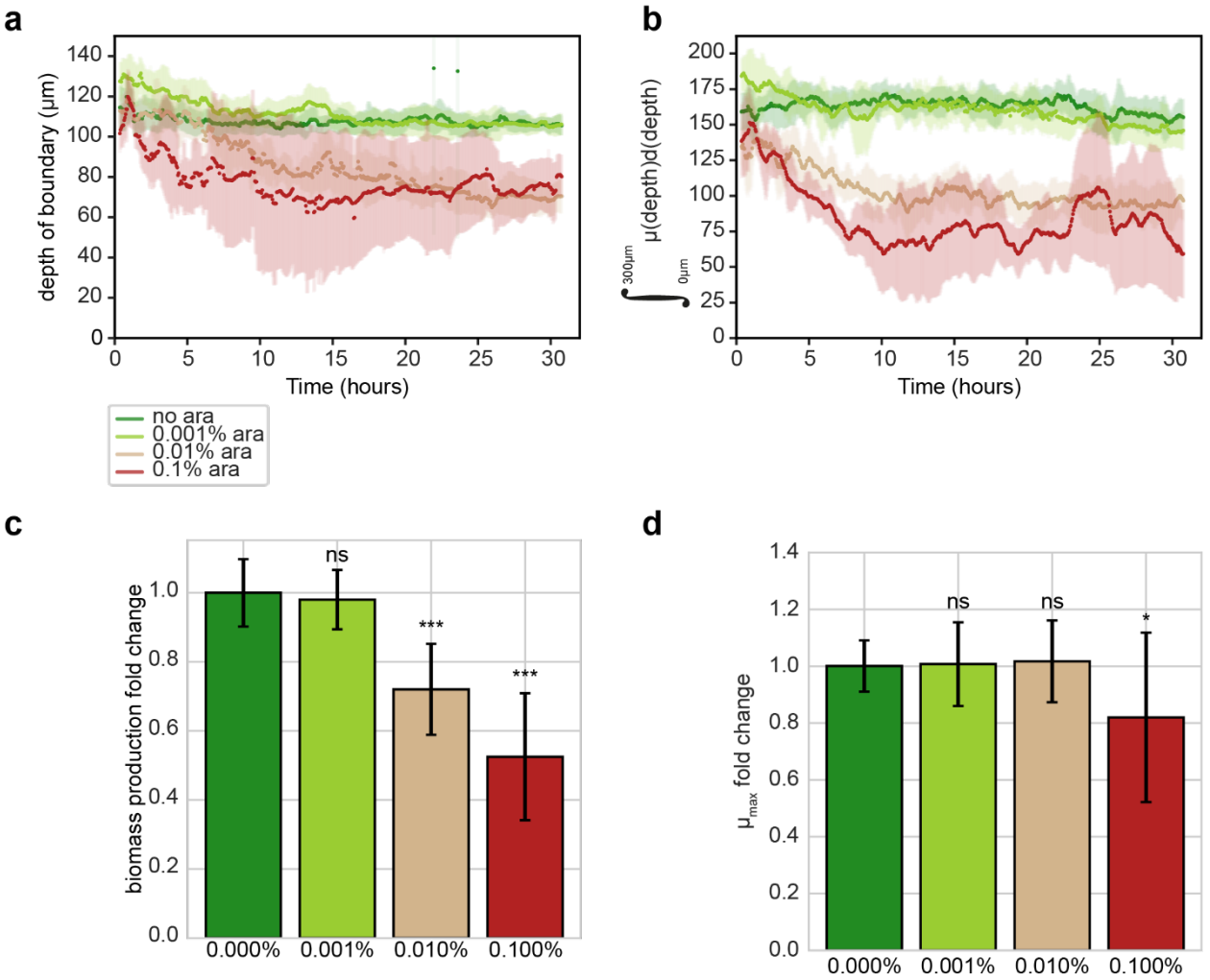

Supplementary Figure 5 : Biomass production in microcolonies following arabinose induction. (**a**) Changes of depth of boundary between growing and non-growing regions of the microcolonies. The boundary depth is determined as the depth beyond which growth is below a threshold corresponding to the mean value + 3 standard deviation of the noise measured in experiments were growth is completely inhibited.

(**b**) Total biomass production over time, calculated as the integral of the local growth rate across the full chamber depth at each time point. For (a) and (b), each data point represents the mean of 26 to 30 replicate chambers pooled from three independent experiments and shaded areas indicate ±1 standard deviation. (**c**) Biomass production yield under different induction conditions, quantified over a stable time window from 10 to 20 hours post-induction. Yields were obtained by integrating the values from panel (b) over this period. Fold changes were calculated relative to the average biomass production of the non-induced control. Bar heights represent the mean across replicates; error bars indicate ±1 standard deviation. (**d**) Maximal growth rate changes across conditions following induction, assessed over the same 9–19 hour window. For each chamber, the fold change in maximal growth rate relative to the initial maximal growth rate (before the start of the induction) was computed. Bar heights represent the mean of these fold changes across replicates; error bars denote ±1 standard deviation. For panels (c) and (d), statistical comparisons with the non-induced control were performed using the Mann–Whitney U test (*ns* : $p > 0.05$; * : $0.01<p<0.05$; ** : $0.001<p<0.01$; *** : $p < 0.001$). Data correspond to the same dataset used in Fig. 4, comprising 26 to 30 replicate chambers from three independent experiments.

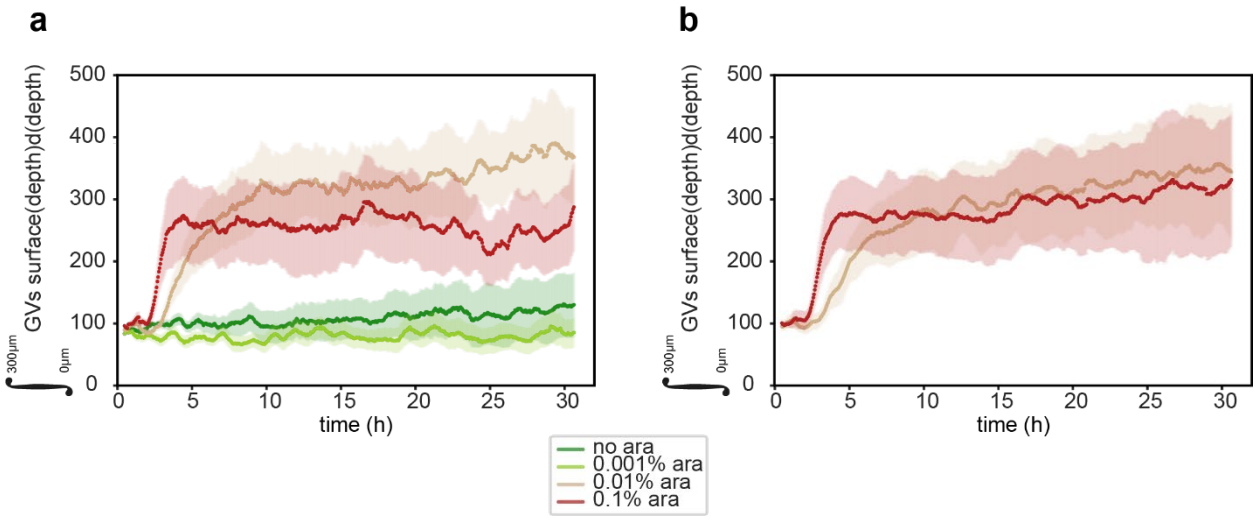

Supplementary Figure 6 : Total GV production over time across microcolony depth. (**a**) Total GV abundance across all induction levels. Data corresponds to the same dataset presented in Fig. 4. (**b**) Total GV abundance for 0.01% and 0.1% arabinose conditions after removing chambers with non-GV-producing population from the time this population spawns to the end of the experiment. For (a) and (b), the *y*-axis represents the total GV abundance at each time point, calculated as the integral of the segmented GV surface area across the full depth of the chamber. Each data point reflects the mean value from 26 to 30 replicate chambers, combined from three independent experiments. Shaded regions indicate ±1 standard deviation.

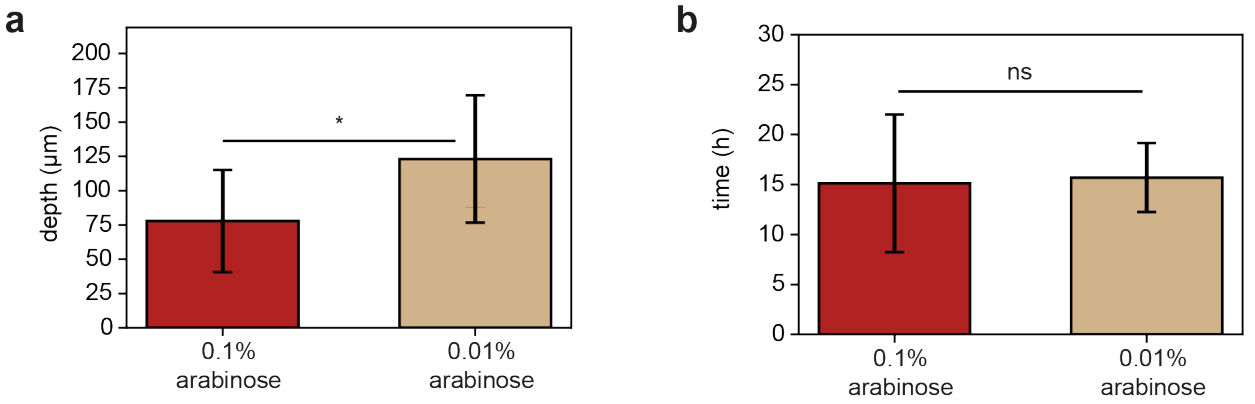

Supplementary Figure 7 : Time and location of non-GV-producing population within the chamber. (**a**) maximum depth (distance to the chamber entry) and (**b**) time of appearance (since the beginning of induction) of non-GV-producing regions under 0.1% and 0.01% arabinose induction. Bar heights represent mean values from the subset of chambers where non-producing regions were observed (20 out of 30 chambers for 0.1% and 7 out of 30 for 0.01% induction). Error bars indicate ±1 standard deviation. Statistical comparisons between induction conditions were performed using the Mann–Whitney U test (ns = $p > 0.1$, * = $p < 0.1$).

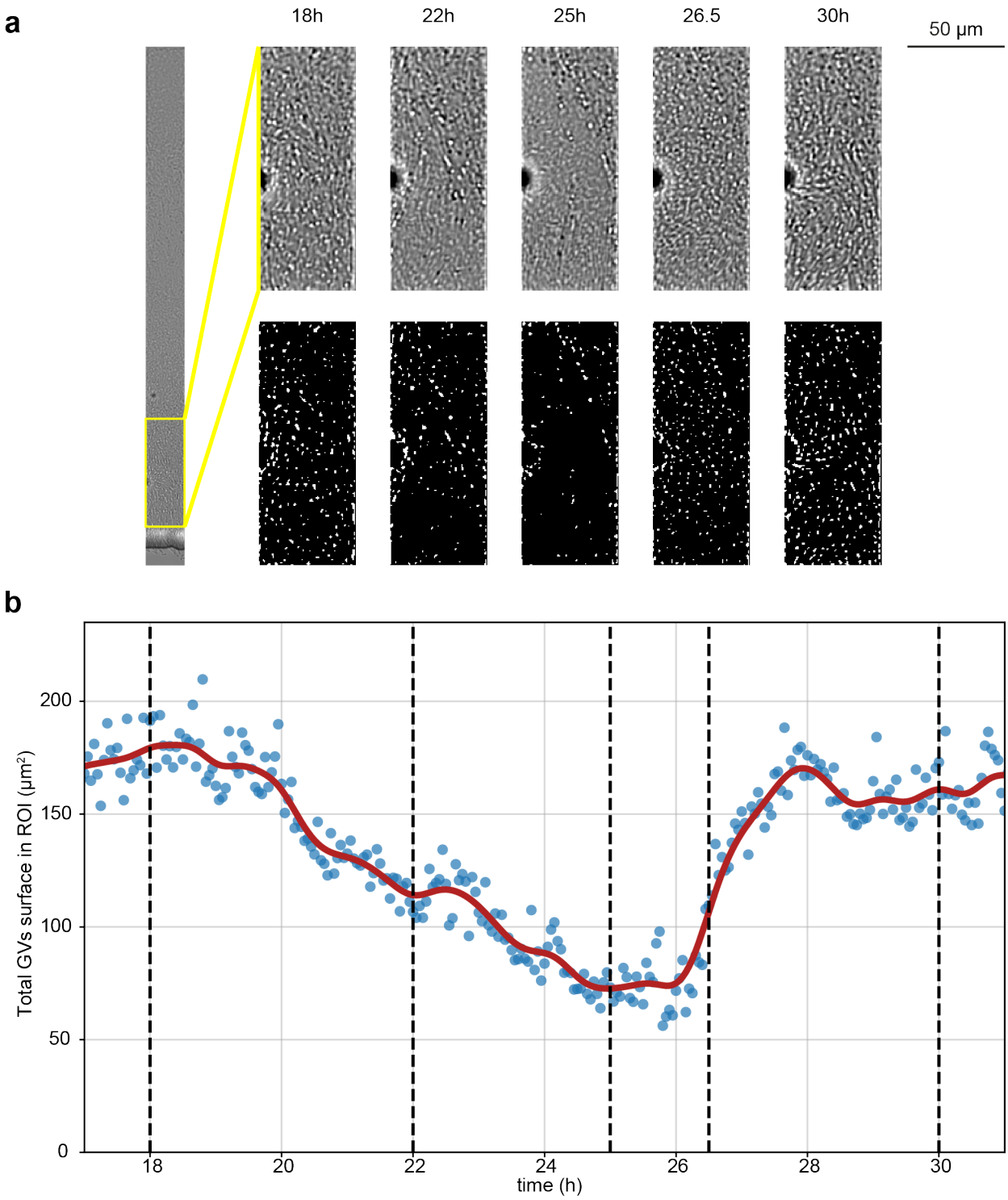

Supplementary Figure 8 : Resumption of GV production in a non-producing subpopulation. In one instance, GV production resumed within a subpopulation that had previously ceased GV expression. (**a**) Representative images of this event. The leftmost image shows the full chamber, with the region of interest (ROI) highlighted by a yellow rectangle. The outlet of the chamber is located at the bottom of the image. The top row presents cropped images of the ROI at selected time points, while the bottom row displays the corresponding segmented GV clusters.

(**b**) Quantification of the total segmented GV surface area within the ROI over time. Blue dots represent individual data points; the red line denotes a smoothed trend obtained using Gaussian smoothing. Vertical black lines indicate the time points corresponding to the images shown in (a).

Chapter II: Increase of cytoplasmic density leads to enhanced bacterial persistence to antibiotics.

Contextual introduction

This chapter focuses on the impact that gas vesicles can have on bacterial persistence to antibiotics. While the connection between these two topics may not seem obvious at first, the origins of this project lie at the crossroads of our team's research history and fortuitous encounter.

Among other research themes, our team has been interested in the phenomenon of cellular persistence to antibiotics, a state in which a subpopulation of cells (including bacteria, yeast, or even cancer cells) can temporarily survive antibiotic exposure without acquiring genetic mutations. This interest led to a collaborative publication in 2019[148], and over the past few years, Céline Cordier, a research engineer in the team, has been studying gene networks potentially involved in persistence in *E. coli*.

At the same time, our team has also been involved in collaborative projects investigating cytoplasmic crowding and its effects on cellular metabolism. One such study resulted in a 2013 publication[149] showing that, in yeast, osmotic shocks can slow down intracellular signaling by increasing molecular crowding. The link between these two areas, cellular crowding and persistence, became apparent when considering that osmotic shocks are also known to increase the proportion of persistent cells. From this, the hypothesis emerged that increased cytoplasmic crowding could contribute to persistence formation.

However, experimentally manipulating cytoplasmic crowding in a stable and sustained way is not trivial. Osmotic shocks, while effective, are transient and often too short-lived to match the timescales of cellular processes such as growth or division. This is where gas vesicles offer an original alternative. As previously discussed (see section Gas vesicles in nature: environment, species and functions), gas vesicles are large intracellular structures that can accumulate in high numbers, occupying a substantial fraction of the cytoplasmic volume and potentially altering the intracellular crowding.

But how can such crowding changes be measured in living cells? A solution came during a 2022 weekly seminar of the UMR 168, when Gilles Tessier from the Institut de la Vision presented his team's work using Quantitative Phase Imaging (QPI), a label-free microscopy technique that enables the measurement of intracellular mass distribution. We reached out to his team to initiate a collaboration aimed at quantifying the volume taken by gas vesicle clusters in cytoplasm, and at investigating whether this correlate with an increased antibiotic persistence.

For this project I worked in close collaboration with Anis Aggoun and Pascal Berto, both working in Gilles Tessier's lab and both experts in QPI microscopy. They dealt with the imaging and image analysis part of the project. I also teamed up with Céline Cordier, who shared her technical knowledge on how to measure persistence in bacteria populations. The product of our work is

presented in the following chapter, written as a paper that will soon be available as preprint on bioRxiv, and is presented in the following chapter in a layout adapted for this PhD thesis.

Supplementary materials associated with this paper are available in Appendix 4. Please note that, as this chapter is written as a standalone paper, it includes its own bibliography, separate from that of the thesis. Accordingly, the reference numbers in the text of this chapter refer to the paper's bibliography.

Article

Increase of cytoplasmic density leads to enhanced bacterial persistence to antibiotics.

Simon Barral[†,1], Anis Aggoun[†,2], Chloé Sasson[3], Céline Cordier[1], Gilles Tessier[2], Jérôme Bonnet[3], Mickael Tanter[4], Pascal Berto[*,2], Pascal Hersen[*,1].

[1] *Physics of Cells and Cancer CNRS UMR168, Sorbonne Université, Institut Curie, 11 Rue Pierre et Marie Curie, 75005 Paris, France.*
[2] *Institut de la Vision, Sorbonne Université, CNRS-UMR 7210, Inserm-UMR S968, Paris 75012, France.*
[3] *Centre de Biologie Structurale CNRS UMR5048 and INSERM* U1054*, University of Montpellier,* 29 Rue de Navacelles, 34090 Montpellier, *France.*
[4] *Physics for Medicine Paris UMR8063, ESPCI Paris, Paris Science Lettres University (PSL), CNRS, 2-10 rue d'Oradour-sur-Glane, 75015 Paris, France.*

[†] *denotes equal contributions.*
* *Correspondence and requests for materials should be addressed to Pascal Berto (pascal.berto@parisdescartes.fr) and/or Pascal Hersen (pascal.hersen@curie.fr).*

Keywords: *bacterial persistence, Quantitative Phase Imaging, Cytoplasmic Crowding, Antibiotic tolerance*

Abstract

Antibiotic persistence is a major threat for public health. Here, we hypothesize that increase in macromolecular crowding driven by cytoplasmic volume reduction can induce bacterial persistence. To address this question, we designed an original method to change the cytoplasmic density and measure the survival rates of bacterial populations over antibiotic stresses. We combined this method with Quantitative Phase Imaging (QPI) to measure accurately the relationships between volume reduction and increase in bacterial persistence using E. Coli as a model bacterium. Our results demonstrate a tight correlation between antibiotic tolerance and cytoplasmic density increase, demonstrating that biophysical properties of the cytoplasm is an important driver of the apparition of persistent cells.

Introduction

The growing threat of antibiotic-resistant bacterial infections is a serious concern for public health, resulting in treatment failures and higher mortality rates[1,2]. Although this issue is commonly linked to the development of genetic resistance, other contributing factors must also be considered. One such factor is bacterial persistence, which is now widely recognized as a significant cause of recurring infections and unsuccessful antibiotic treatments[3–5]. Persistence occurs when a small subset of bacteria temporarily survives antibiotic exposure without undergoing genetic mutations. Unlike resistant bacteria, which continue to multiply in the presence of antibiotics due to genetic adaptations, persistent cells exhibit a temporary, non-inherited tolerance to these drugs. After antibiotic treatment ends, these surviving cells can resume growth, causing the infection to relapse[6,7]. This phenomenon has been observed in various bacterial species, including *Escherichia coli*, *Pseudomonas aeruginosa*, *Mycobacterium tuberculosis*, and *Staphylococcus aureus*, and is believed to be widespread among bacteria[8]. The prevailing explanation for the formation of persistent cells is that certain subpopulations enter a "dormant" state, in which their growth and metabolism slow down almost completely. As a result, antibiotics that target vital cellular processes to cause lethal damage[9] are thought to be less effective against these dormant cells.

In recent years, significant progress has been made in identifying the molecular mechanisms responsible for this dormant state. Several cellular pathways, especially toxin-antitoxin modules[10,11] and (p)ppGpp signaling[12–14], have been proposed as key actors of persistent cell formation. However, the upstream regulatory processes driving these mechanisms remain a topic of debate[15]. Additionally, recent research has revealed that dormancy alone does not fully account for the formation of persistent cells, suggesting that other physiological changes are also involved[16,17].

Importantly, several studies have shown that hyperosmotic shock promotes the persistence of *E. coli* when exposed to ribosome-targeting antibiotics[18–20]. This effect has been attributed either to increased efflux pump expression[20] or to changes in membrane polarization[19]. However, it is also known that hyperosmotic shock alters the cytoplasmic volume[21] and macromolecular crowding within cells[22]. Alterations in crowding are known to impact bacterial metabolism and growth by influencing the diffusion of macromolecules and their biochemical reaction rates[23–26]. Indeed, cells interior is already dense (around 300g/L for bacteria and yeast) and volume reduction can lead to colloidal phase transition and massive reduction of diffusion coefficient with the cytoplasm[27]. Said differently, biophysical modification of the cytoplasm properties could slow down cellular processes, inducing the entry into dormancy and decreasing the potential effect of antibiotics.

The recent development of Quantitative Phase Imaging (QPI) offers a method to probe in live cells the biophysical properties of the cytoplasm with quantitative accuracy. Briefly, and in contrast with epifluorescence or bright field methods, QPI gives a measurement of the optical path across a biological sample, which is then linked to the refractive index of the biological sample being observed and thus gives an estimate of the mass variation and distribution within the biological sample. QPI has been used to observe cytoplasmic heterogeneity in many different cell types and offer a unique, quantitative method to explore the link between the biophysical properties of the cytoplasm and, for instance, bacterial persistence.

Here, we hypothesize that increase in macromolecular crowding driven by cytoplasmic volume reduction can induce bacterial persistence. To address this question, we designed an original

method to change the bacterial cytoplasmic density and measure the survival rates of bacterial populations in response to antibiotic stresses. We combined this method with QPI to measure accurately the relationships between volume reduction and increase in bacterial persistence using *E. coli* as a model bacterium. Our results demonstrate a tight correlation between the persistence in antibiotics and cytoplasmic density increase that was never reported. It indicates that biophysical properties of the cytoplasm can also be important drivers of the apparition of persistent cells and should be included in recent efforts to fight against persistent cells.

Results

Sudden Osmotic stress leads to increased antibiotic tolerance.

We first used sorbitol induced hyper osmotic stress to apply a volume reduction to bacterial cells exposed to antibiotic stress and measured the survivability of these cells (Figure 1). When using *E. coli* cells and ribosome targeting antibiotics (tobramycin and streptomycin) we systematically observed a significant increase of the proportion of persistent cells. This effect was observed even though osmotic stress is also partially detrimental to cell growth and survivability. Importantly, the observed protective effect is massive, with a survivability rate increased by several order of magnitude going from 0.015(+- 0.0036)% for tobramycin and 0.004(+- 0.003)% for streptomycin to virtually all cells surviving the antibiotic exposure in both cases (Figure 1). The cause of this result, that is supported by the literature[18–20], can however be disputed in the sense that hyperosmotic stress also leads to a global stress response that may be responsible for the observed effect. Alson, the resulting volume changes obtained by hyperosmotic stress are temporary, as cells can recover from within several minutes to several hours, depending on the magnitude of the osmotic challenge[21]. Therefore, another method to change the cytoplasmic density is needed to test the relationship between the physical properties of the cell interior and the enhanced persistence of bacteria.

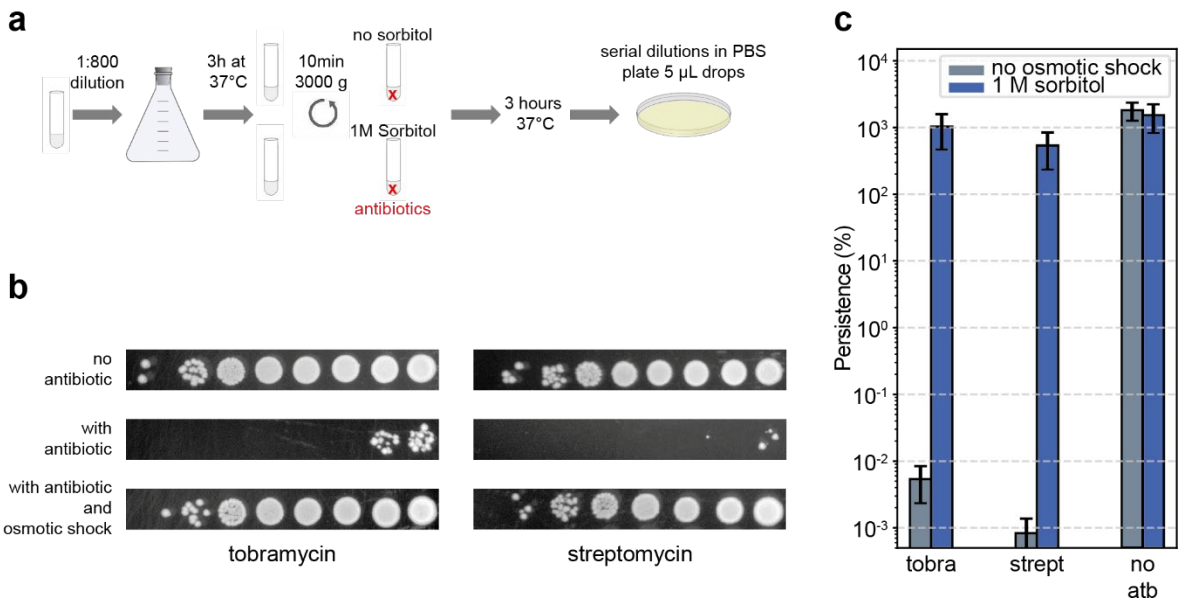

Figure 1 : Hyperosmotic shock induces bacteria persistence in aminoglycosides antibiotics (**a**) Diagram of the protocol used to evaluate the fraction of persistent cells within a population exposed to antibiotics and osmotic shock (**b**) Representatives images of the colonies produced by serial dilution drops, from highest cells concentration (right) to the lowest (left). (**c**) Quantifications of persistence changes induced by 1 M sorbitol hyperosmotic shock concomitant with exposure to antibiotics in *E.coli*. "Persistence (%)" represents the CFU after treatment divided by CFU before treatment (See Supplementary information). For tobramycin and no antibiotics conditions, N=3, for streptomycin N=4. Error bars represent one standard deviation.

Cytoplasmic density can be increased by GV bacterial production

An alternative to cell volume compression would be to increase protein production to densify the cytoplasm. Yet, the resulting effect on crowding will depend on the nature of the protein and can lead to additional effects, such as the formation of biocondensates and heterogeneous density maps which will make it difficult to estimate the change of density within the cytoplasm at the cellular level. We therefore decided to test a different route involving the production of Gas Vesicles (GVs) by bacteria (Figure 2). GVs are intracellular, proteinaceous structures filled with gas that self-assemble within cells. They are naturally produced by various species of aquatic microorganisms, likely to regulate cell buoyancy[28,29] in the wild. Individual GV are rod-shaped with conical ends, ranging from 200 to 800 nm in length and about 100 nm in width, and they typically form clusters inside the cells, forming what is sometimes referred to as "gas vacuoles"[28,29]. In 2023, Hurt and colleagues engineered plasmids that allow for the controlled production of GVs in any *E. coli* strain upon arabinose induction, originally designed for acoustic imaging of bacteria[30]. Because of their unique interactions with ultrasound, GVs provide an excellent system to explore how acoustic imaging and acoustic forces can be used to probe biological processes. In our study, we aimed to use GVs to increase cytoplasmic crowding. These structures are stable over time and occupy cytoplasmic volume by filling it with gas. As a result, part of the cytoplasm becomes inaccessible to macromolecules, increasing crowding in the remaining space. This effect can be thought of as inflating a balloon inside

the cell, which partitions the interior into two distinct regions: GV-occupied zones and active cytoplasmic zones. We built *E. Coli* strains able to produce GVs upon arabinose induction (Figure 2) and obtained cells that were expressing different levels of Gas Vesicles depending on arabinose concentrations (Figure 2). Cells also had a plasmid to express GFP in the cytoplasm to facilitate image analysis. To produce GVs in a controllable manner, *E. coli* cells were transformed with an arabinose-inducible plasmid expressing the proteins necessary for GVs production (Figure 2a). GVs production was confirmed using electron microscopy, which revealed the presence of GVs in the cytoplasm after induction. In bright-field microscopy, clusters of GVs were observed after 2 to 6 hours of induction with arabinose concentrations ranging from 0.001% to 0.1% (w/w) as bright spots due to light diffraction by gas vesicles (Figure 2d). Our results demonstrated that the volume of GVs within the cytoplasm increased with increasing arabinose concentrations and induction time, therefore giving us an alternative method to vary the cell interior density.

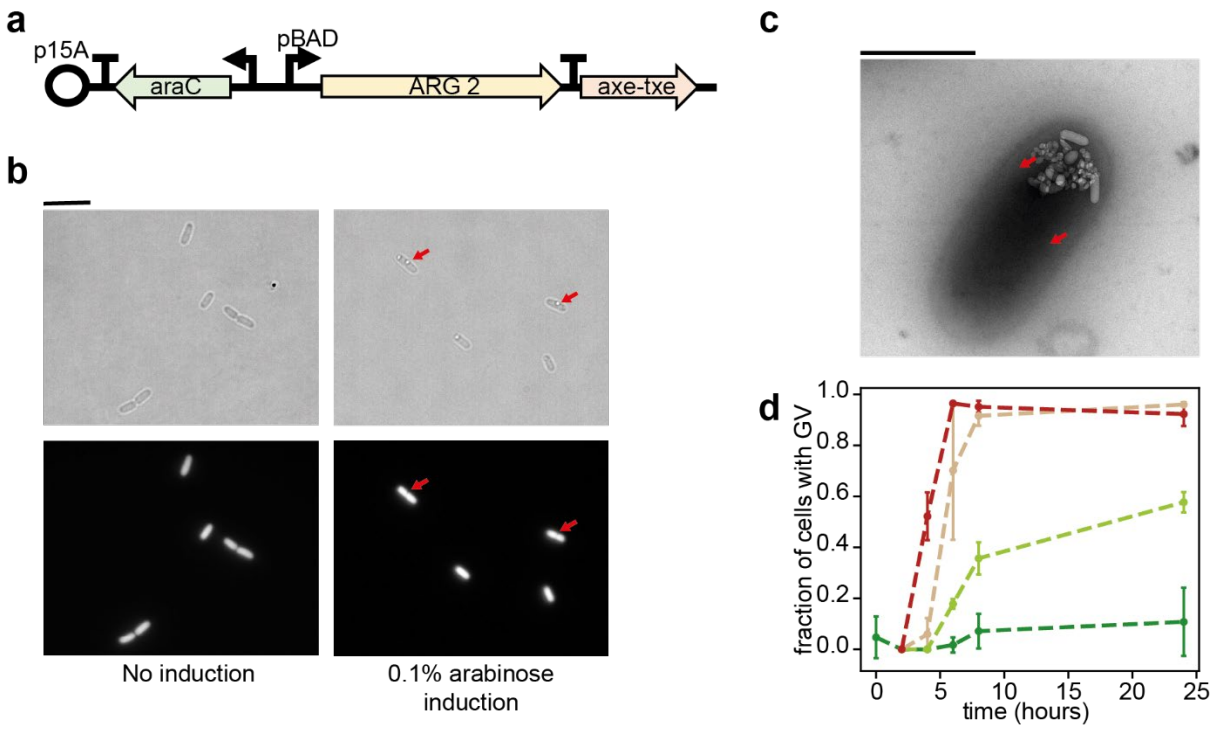

Figure 2 : GVs production in *E. coli*. (**a**) Diagram of the arabinose-inducible plasmid used to produce Gas Vesicles. ARG2 (for Acoustic Gene Reporter 2[30]) represents the operon containing all the necessary genes for GVs production. (**b**) Bright-field (top) and fluorescence microscopy (bottom) images of *E. coli* with (right) and without (left) arabinose induction of GVs production. Red arrows indicate GVs clusters within the cells. Scale bar represents 3 µm. (**c**) Transmission Electron Microscopy image of an *E. coli* cell containing Gas Vesicles. Some individual Gas Vesicles are indicated by red arrows. Scale bar represents 1 µm. (**d**) Fraction of cells containing Gas Vesicles clusters visible in bright field microscopy over time upon various induction strength (red = 0.1%, orange = 0.01%, light green = 0.001% and green = 0% arabinose (w/w)) Error bars represent one standard deviation. N=3.

Cells producing GVs show an increased persistence in antibiotics

Cells were cultivated in varying arabinose concentrations (0–0.1%). After 6 h of induction, when GVs had accumulated, the proportion of persistent cells was assessed by exposing cultures to tobramycin for 3 h and then measuring survival. The number of surviving cells was determined as before by counting colony-forming units (CFU) on agar plates before and after antibiotic exposure (Figure 3). A positive correlation was observed between the level of arabinose induction and the proportion of persistent cells (Figure 3b). Under non-induced conditions, 7.5×10^{-5} % (± 2.6×10^{-6}) of the cells were persistent, whereas this proportion increased to 0.076% (± 0.018) under the strongest induction condition. This means that producing and accumulating GVs conferred a 10,000-fold increase in the number of persistent cells. For comparison, this is, as for our previous hyperosmotic compression experiments, a massive increase compared to the observed persistence in "high persistence" Hip7A mutant strains reported in the literature[31,32], which could reach up to 1000 fold increase. This result confirmed our hypothesis and is a first demonstration that GVs can have a different role than buoyancy regulation.

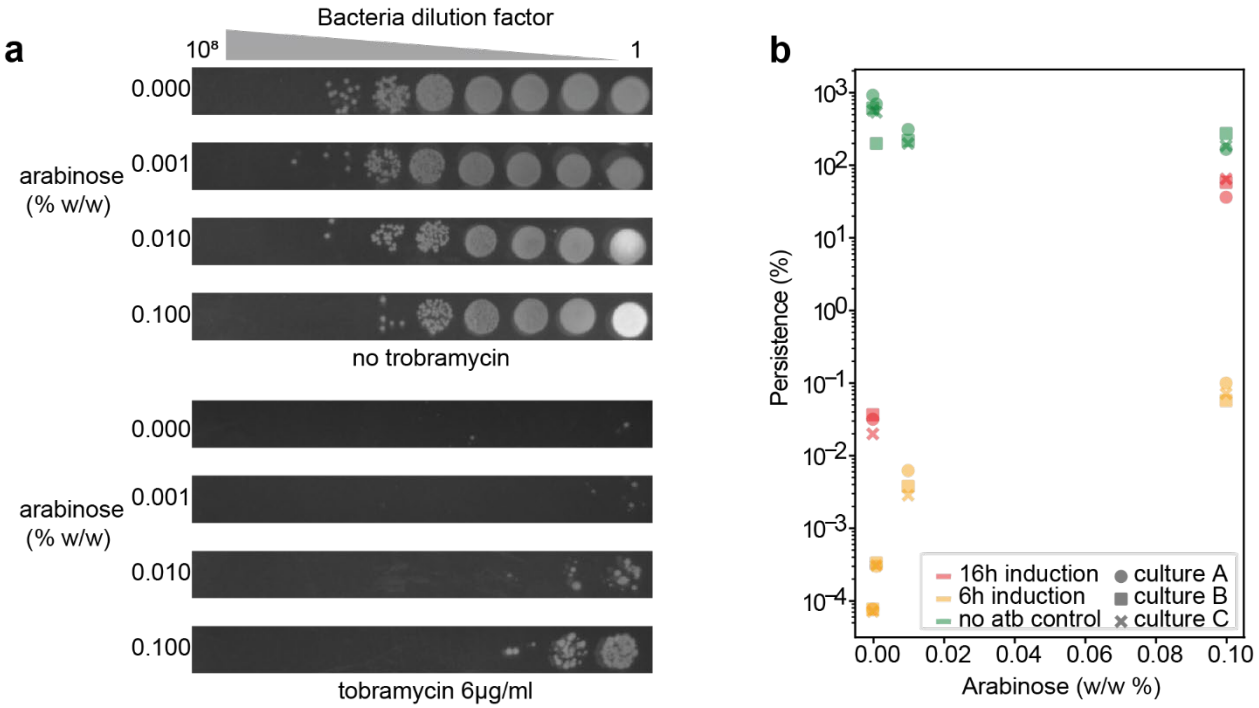

Figure 3 : Measure of GVs impact on bacteria persistence. (**a**) Representative images of persistence measurement readout: colonies on agar plates after serial dilution drops of cells grown with various arabinose concentrations, after exposure to tobramycin (bottom) or without exposure to tobramycin (top). (**b**) Persistence of 3 biological replicates for various arabinose concentrations. Each color corresponds to a culture condition. Each marker shape indicates a biological replica.

We can measure cell volume occupied by gas with Quantitative Phase Imaging

To investigate the relationship between total GV volume within cells and persistence, we employed QPI. QPI measures the phase shift of light as it passes through a transparent specimen, such as a bacterium. This phase shift arises due to the slower propagation of light through materials with higher refractive indices than water. In biological samples, a higher concentration of macromolecules corresponds to a higher refractive index and, consequently, a greater phase shift. Thus, the measured phase shift is directly proportional to the dry mass content of the sample, enabling label-free, indirect quantification of cellular mass and visualization of its spatial distribution in microscopy[33]. To achieve this, we utilized a wavefront sensing setup incorporating a thin diffuser, as described in previous work[34] (Figure 4a). Because the refractive index of gas (n_a) is substantially lower than that of the cytoplasm (n_b), regions of the cell containing GVs exhibit marked differences in Optical Path Difference (OPD), which reflects the integrated refractive index contrast relative to the surrounding medium (Figure 4b). This setup enabled OPD mapping of the samples (Figure 4c), in which cytoplasmic regions were segmented using masks generated from fluorescence images (Figure 4d). Assuming that the presence of gas vesicles does not alter the dry mass of the cell and that GV-producing cells retain their rod shape, we estimated the fraction of cytoplasmic volume occupied by GVs (termed “gas occupancy”), as detailed in Supplementary information. By performing these measurements on a large number of cells from the same samples used for persistence assays, we constructed a curve of mean gas occupancy across three biological replicates under varying induction strengths, after 6 hours of induction. This analysis revealed that up to ~6% of the cytoplasmic volume can be occupied by GVs in 6 hours of induction (Figure 4e).

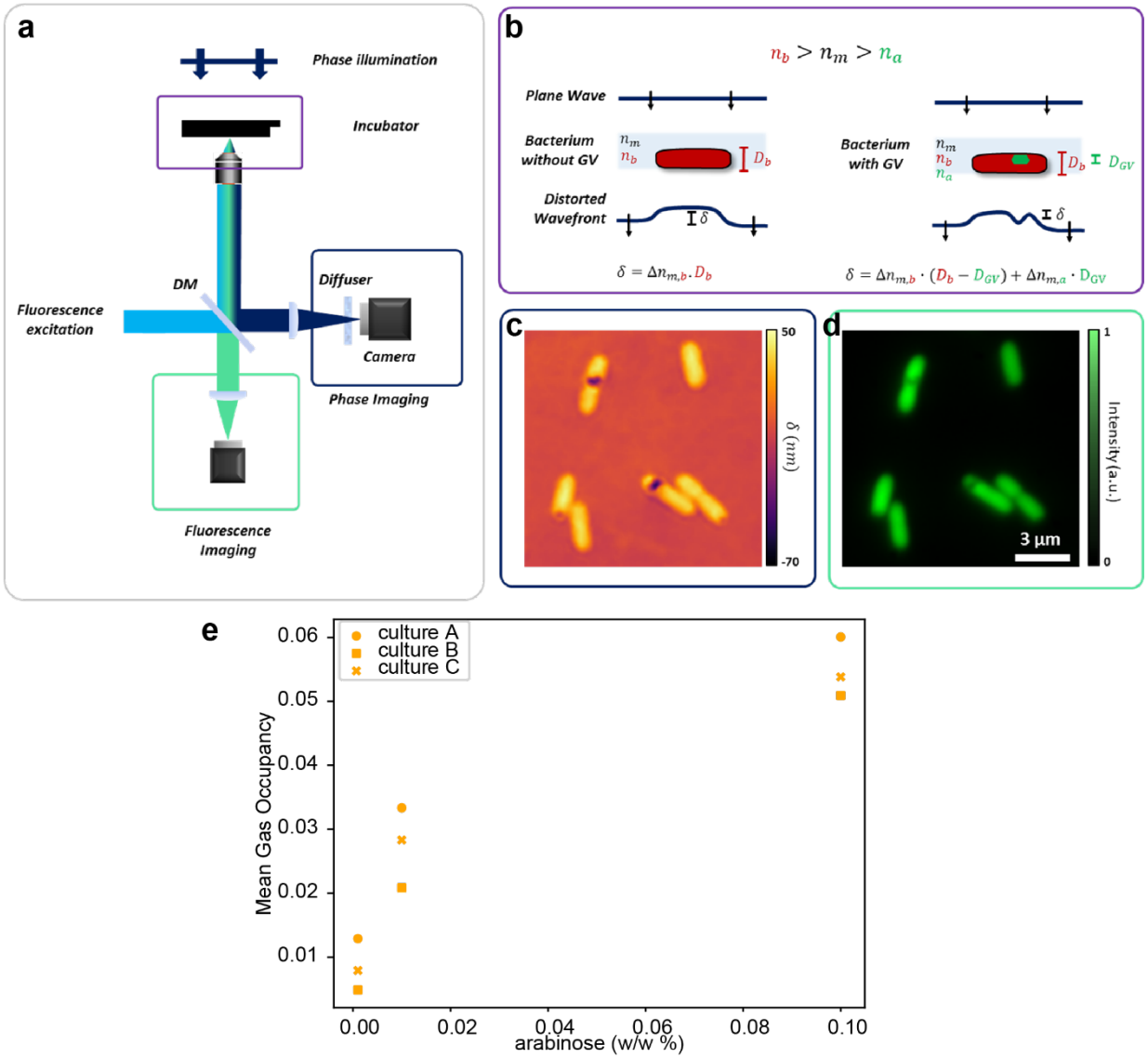

Figure 4 : Setup for Quantitative Phase Imaging of bacteria and measure of GVs mean gas occupancy in cells (**a**) Simplified scheme of the imaging setup. For phase imaging, the sample, located within an incubator at 37°, is illuminated with a collimated beam at λ= 470nm. The transmitted light, bearing the wavefront distortion induced by the sample, is reflected by a dichroic mirror towards a DiPSI wavefront sensor yielding a quantitative phase image of the sample. The fluorescence imaging is performed by illuminating the sample with a light source at \lambda = 485 nm in an epi-configuration. The collected light is then transmitted by the dichroic mirror towards a second camera yielding a fluorescence image of the sample. (**b**) Illustration of the wavefront distortion induced by a bacterium with (Left) and without (Right) gas vesicles. (**c**) Phase and (**d**) fluorescence images of bacteria acquired using the setup described in (**a**). The GVs clusters produced by some of the bacteria is reflected by a dip in the OPD values. (**e**) Mean Gas Occupancy of the GVs in cells calculated from the optical volume difference (OVD) values (see Supplementary information) for various induction strengths. Each marker shape indicates a biological replica.

There is an exponential relationship between the proportion of persistent cells and the intracellular gas volume.

Taken together, we can combine the previous measurements to plot the relationship between the survivability (i.e. the persistence level) of bacteria in function of the relative volume of GVs within the cytoplasm. Strikingly, we observed (Figure 5) that all our data point collapsed on a master curve, showing a sharp increase of the survivability when increasing the cytoplasm density with GV. This master curve suggests strongly that there is a direct, physical relationships between these two quantities. This curve can be fitted by an exponential function. When extending the induction time to 16 hours to achieve higher gas vesicle content, we observed an even greater level of persistence. However, these data points did not collapse onto the same curve as those from the 6-hour induction samples. This discrepancy is likely attributable to the longer culture time, as the 16-hour samples were in the stationary phase, during which persistence is inherently higher than in the exponential phase[35], regardless of gas vesicle presence.

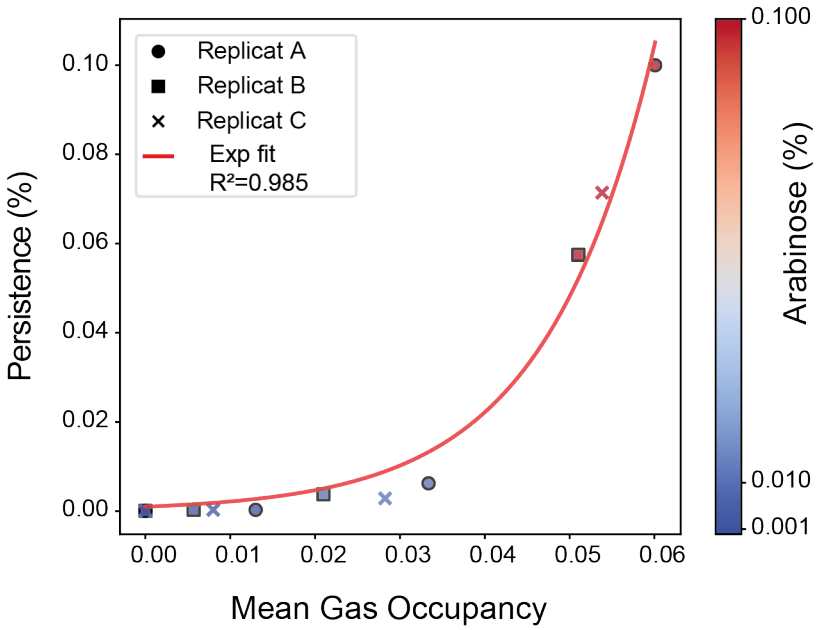

Figure 5 : Exponential relationship between gas occupancy and persistency: Plot of persistence as a function of mean gas occupancy. Colors indicate the strength of induction, and symbols represent biological replicates. The red curve shows the exponential fit with the equation $y = 1.00 \times 10^{-3} \cdot \exp(77.5 \cdot x)$ (R^2=0.985; see Supplementary information).

Discussion

In this study, we confirmed that osmotic shocks enhance the persistence of *E. coli* cells exposed to ribosome-targeting antibiotics (Figure 1), consistent with findings reported in the literature[18–20]. Hyperosmotic shocks are known to compress the cytoplasm, potentially altering intracellular crowding[22,27]. Based on this, we hypothesized that changes in cytoplasmic crowding contribute to the observed increase in persistence following hyperosmotic shock.
To test this hypothesis, we employed a controllable approach to modulate cytoplasmic crowding in bacterial populations and assessed the resulting effects on persistence. While hyperosmotic shocks can transiently alter cytoplasmic crowding, they may also induce other confounding effects that influence persistence. To circumvent this limitation, we engineered an *E. coli* strain capable of producing GVs upon arabinose induction (Figure 2a). GV production provided a robust and tunable means to manipulate intracellular crowding, and we observed a positive correlation between GV production levels and persistence (Figure 3).

Could this phenomenon simply be explained by a slowdown of cell growth due to the burden of producing GVs proteins?
The connection between cell growth and persistence has already been documented in the literature. Indeed, several studies have shown that persistent cells are highly enriched in fractions of the population that are nongrowing or slowly growing in bacteria populations[6,16]. This raises the question of whether the persistence increase observed in our study could simply result from a slowdown in cell growth caused by the burden of producing gas vesicle.
When producing GVs, we observed that the population's growth rate began to slow down approximately six hours after induction (Supplementary Figure 1a), the time point at which persistence measurements were initiated. For the arabinose-inducible promoter used in this study, mRNA production begins within tens of seconds after induction, and proteins are detectable on the timescale of a few minutes[36]. By the time the growth slowdown was observed (six hours post-induction), cells had already been producing GVs proteins for many generations, without any growth rate reduction observed. The observed growth rate reduction after 6h is therefore likely not the consequence of a bottleneck in proteomic or metabolic resources caused by induction of GVs production.

While several underlying mechanisms are likely at play here, it is not unreasonable to wonder whether GV accumulation within the cytoplasm also contributed in the reduction of growth rate. Indeed, as shown in Supplementary Figure 1b, we observed that the average amount of GVs per cell increases over time.

More strikingly, we also observed the effect of GVs on persistence even for cells in stationary phase (after 16h of batch culture), where growth is nearly entirely arrested, irrespective of GV production (Figure 3). Under these conditions, stationary-phase cells without GVs exhibited a roughly 300-fold increase in persistence relative to exponential-phase cells, consistent with previous reported in the litterature[35]. Notably, the presence of GVs in stationary-phase cells further increased persistence by an additional 1000-fold compared to stationary-phase cells without GVs.

These findings suggest that the effect of GV production on persistence is not completely attributable to the metabolic burden of GV proteins production. Instead, accumulation of GVs

is also a likely contributor. But how could GVs accumulation in the cytoplasm change the persistence of cells?

Our hypothesis is that the accumulation of GVs, by occupying intracellular space, increases cytoplasmic crowding. This heightened crowding alters the physical properties of the cytoplasm, ultimately reducing the effectiveness of the antibiotics.
As demonstrated in this work and the litterature[30], stronger induction leads to greater GVs production, logically resulting in a larger intracellular volume occupied by gas and thus a higher molecular crowding.
Cytoplasm, whether in eukaryotes or bacteria, have been shown to exhibit behaviors consistent with those of soft colloids, possessing glass-like properties[27,37,38]. These systems can be broadly modeled as suspensions of small, deformable particles dispersed in a liquid. At low particle crowding, Brownian motion dominates, allowing free diffusion. However, as the crowding, or colloid volume fraction, increases, particle mobility becomes progressively restricted, and viscosity rises dramatically as a function of crowding[39].

Therefore, if cytoplasm behaves as a soft colloid, a direct link between crowding and persistence would imply that both viscosity and persistence scale similarly with colloid volume fraction. As others demonstrated[27,40,41], the viscosity of soft colloids exhibits an exponential divergence as the colloid volume fraction approaches the glass transition. Notably, assuming our Mean Gas Occupency measurements constitutes a proxy to the colloid volume fraction, our data reveal a similar exponential relationship between persistence and colloid volume fraction (Figure 5). This supports our hypothesis that increased macromolecular crowding in the cytoplasm can trigger bacteria persistence in antibiotics.

In living cells, the diffusion of macromolecules within the cytoplasm is a critical parameter for maintaining cellular function[42,43]. Several key metabolic reactions[43], including translation[26], have been shown to be diffusion limited. High cytoplasmic density can also lead to the formation of diffusion barriers[44,45], and it has been suggested that the combination of cell size and macromolecular concentration in both prokaryotes and eukaryotes is optimized to support rapid diffusion[46].
The diffusion coefficient of a molecule is governed by the Stokes–Einstein relationship, which predicts that diffusion scales inversely with viscosity[47]. As discussed earlier, in systems resembling soft colloids, viscosity increases with crowding. Consequently, heightened crowding slows macromolecular diffusion, leading to a global slowdown of cellular processes. Experimental evidence supporting this relationship has been reported in both yeast[27] and bacteria[48], where increased cytoplasmic crowding was shown to reduce diffusion rates and metabolic activity of cells.
In this study, we focused on persistence in the presence of tobramycin. Tobramycin, like other aminoglycosides, is a bactericidal antibiotic that relies on active cellular processes to exert its effects. It irreversibly binds to the 30S subunit of the ribosome, disrupting translation and leading to the production of aberrant, non-functional proteins. These proteins accumulate and interfere with cellular processes, ultimately causing cell death[49]. Crucially, the efficacy of tobramycin depends on active translation.

If GV accumulation increases cytoplasmic crowding to the point of reducing translation rates, it is unsurprising that this could enhance persistence against aminoglycosides.

Taken together, these findings reveal that crowding is another, previously unexplored physiological parameter contributing to the formation of persistent cells. Understanding the mechanisms underlying persistent formation is crucial for addressing relapsing infections. Notably, the crowding effect on persistence is not limited to a single organism, as the soft colloid behavior of the cytoplasm is broadly conserved across species[50]. Increased crowding has been shown to affect metabolism in both eukaryotes[27,51] and prokaryotes[48]. Although eukaryotic cytoplasm is generally less crowded than that of prokaryotes, it responds in a similar way to further crowding, highlighting the universality of this property[48]. These observations suggest that cytoplasmic crowding may represent a fundamental parameter contributing to persistence across diverse organisms. Indeed, persistence is not limited to bacterial cells; it has for exemple also been observed in *Candida albicans* biofilms exposed to antifungal drugs[52]. In cancer, persistent cells are a major driver of deadly tumor relapses following treatment. Similar to bacteria, these cells often exhibit slow growth and an overall reduction in metabolic activity. Whether this metabolic slowdown is a cause of persistence or a consequence of the treatment remains unclear[53]. However, based on our results, we speculate that increased cytoplasmic crowding could also contribute to driving persistence, particularly given the densely packed nature of cells within the tumor microenvironment.

Materials and Methods

Strain, plasmids and culture conditions.

pBAD-bARGSer-AxeTxe plasmid (Addgene #192473) encoding for the GV production upon arabinose induction was transformed with heat shock transformation into *E.coli* K12 BW25113 ΔfliA Δ(araD-araB), from the Keio collection. The Δ(araD-araB) deletion makes it unable to consume arabinose, ensuring that induction level remain stable overtime in batch culture. The resulting transformed strain was subsequently transformed with heat shock with a plasmid for constitutive sfGFP production in cytoplasm. The resulting strain was named bPH_669.

To culture it, Luria-Bertani (LB) Miller medium was used. It was prepared by adding 10g Bacto™ Tryptone (Gibco) with 10g Sodium Chloride (Sigma Aldrich) and 5g yeast extract (Sigma Aldrich) per liter of miliQ water, mixing and autoclaving it.

For experiments, bPH_669 was plated from glycerol stock onto LB Miller agar plate with chloramphenicol and kanamycin and incubated at 37°C overnight. Pre-cultures were then started from single colonies in 5ml of LB Miller with chloramphenicol and kanamycin and incubated overnight at 37°C with 270 rpm agitation. For each replicate, pre-cultures were started from different isolated colonies. 50ul of pre-cultures were then added to 5ml of fresh LB Miller with chloramphenicol and kanamycin. L-Arabinose (Thermo Scientific ref 365180250) was added from a 40% (w/w) stock solution to a final concentration between 0 and 0.1% (w/w). Cultures were then incubated at 37°C with 270 rpm agitation for 6h to produce GVs. For conditions with the maximum GV production, incubation lasted for 16h with 0.1 % arabinose.

Measurement of persistence in tobramycin

Isolated colonies of bPH_669 were used to start cultures in 5 ml of LB Miller broth containing chloramphenicol and kanamycin. These cultures were incubated overnight at 37°C with shaking.

After overnight incubation, the cultures were diluted 1:100 in fresh LB Miller with chloramphenicol, kanamycin, and arabinose at the appropriate concentration. They were then incubated for 6 or 16 hours at 37°C with shaking. After incubation, the cell concentration (cells/ml) in each culture was measured either by optical density or by counting with a Helber counting chamber (Hawksley Z30000) under a Olympus IX83 microscope with a UPlanSApo 100×/1.40 objective. All samples were then adjusted to approximately 3.5 × 10^7 cells/mL. Next, a 10-fold serial dilution of each sample was prepared, and 5 µl of each dilution was spotted onto LB Miller agar plates (1% agar). The plates were incubated overnight at 37°C to determine the 'T0' value, representing the number of live cells in each sample before antibiotic exposure.

For persistence experiments with GVs, tobramycin was added to the adjusted samples at a final concentration of 6 µg/mL. For persistence experiments with osmotic shock, the cells were centrifuged and resuspended in fresh LB Miller with chloramphenicol, kanamycin, and either 0 or 0.5 M sorbitol (Sigma) (corresponding to a 1 Osmol/kg shock), along with 6 µg/mL tobramycin. These samples were incubated for 3 hours at 37°C with shaking. After 3 hours, 10-fold serial dilutions were made in 96-well plates, and 5 µL drops of each dilution were plated on LB Miller agar (1% agar). The plates were incubated overnight at 37°C to determine the number of live cells after antibiotic exposure ('Tatb'). Finally, the number of surviving cells in each sample was estimated by counting the colonies at the lowest dilution where well-separated colonies were visible. Persistence for each sample was calculated using the formula: (Tatb/T0) × 100.

Sample preparation for QPI imaging

For QPI imaging, the same bacterial cultures used for the persistence measurements were employed. Agar pads were prepared in Fluorodish FD35-100 (WPI) by placing a drop of melted LB + 1% agarose solution between two coverslips separated by a layer of tape. Once the gel had solidified, one of the coverslips was removed, leaving the agar pad on the remaining coverslip. These pads were allowed to dry for a few minutes before 1 µL of the bacterial culture was added and allowed to dry again. The resulting pads were then hermetically sealed into the Fluorodish using valap (a mixture of lanolin, Vaseline, and paraffin), ensuring that the agar was in contact with the bottom of the well. The wells were then filled with Milli-Q water before placing them under the microscope.

QPI imaging

To quantify the relative cytoplasmic volume occupied by GVs, we employed Quantitative Phase Imaging (QPI), which measures the optical path difference (OPD) caused by variations in refractive index within cells. The total OPD over a cell's area yields the Optical Volume Difference (OVD), which normally correlates with cellular dry mass. However, in the presence of GVs, which contain gas with a much lower refractive index than the surrounding cytoplasm, the OVD is reduced due to the negative contribution of gas. This allows estimation of GV volume (V_G) relative to the total cell volume (V_B)

To extract the mean gas occupancy (V_G / V_B), we compared OVD and volume-normalized OVD across induced and control populations. Based on the assumptions that GV production does not alter cellular dry mass or volume distribution, we derived occupancy from statistical differences in QPI signals between the two populations. Cell geometry was estimated from phase images, and cross-sectional area was used to calculate V_B. By imaging large numbers of cells with and without GV induction under identical conditions, we estimated the average fractional gas content per cell.

Additional details, including full derivations and equations, are provided in the supplementary information.

Supplementary Information

Supplementary_material.pdf contains detailed information on protocols and image analysis used in this work.

All data used to generate the figures and associated scripts are also provided.

Supplementary Figures

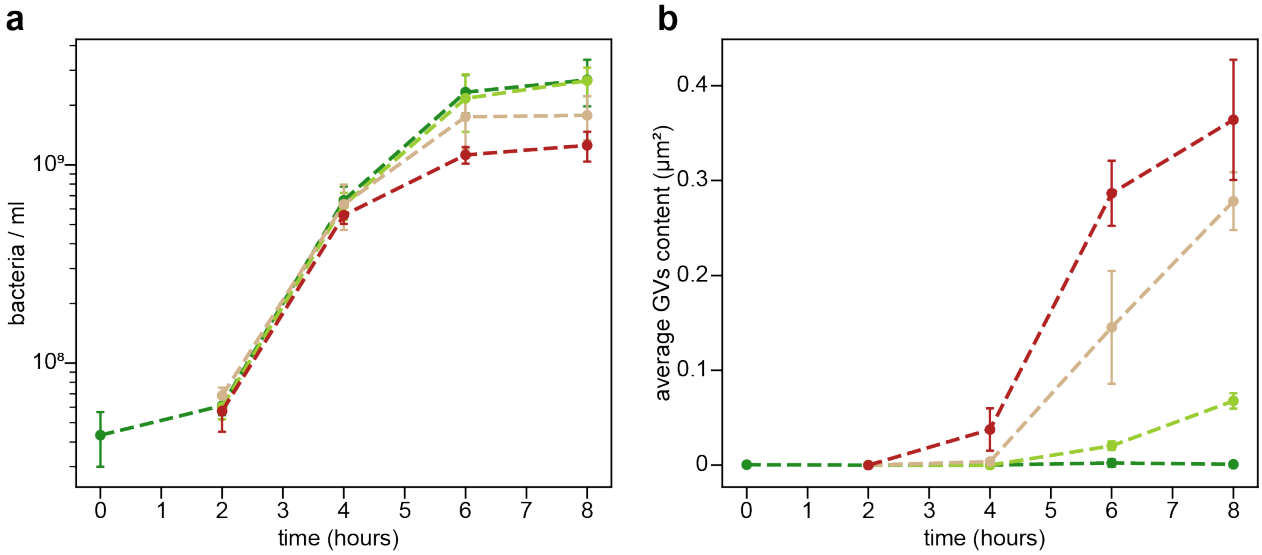

Supplementary Figure 1 : Growth and GV production in batch culture over time. (**a**) Growth curve (in log scale) of bPH_669 under various induction strength for GV production. (**b**) Average GVs content per cell for cells that contain GV clusters over time for various induction strength. GV content is measured in bright field microscopy as the surface of of the cell for which pixel value is above a GV detection threshold, as described in Supplementary material. Points represent the mean of the average values for at least 50 cells for 3 independent experiments. Error bars represent one standard deviation. Red curve : 0.1% arabinose, Orange curve : 0.01% arabinose, Light green curve : 0.001% arabinose, Dark green curve : no arabinose.

References

1. Antimicrobial resistance: global report on surveillance. https://www.who.int/publications/i/item/9789241564748.
2. Livermore, D. M. Has the era of untreatable infections arrived? *J. Antimicrob. Chemother.* **64 Suppl 1**, i29-36 (2009).
3. Levin, B. R. & Rozen, D. E. Non-inherited antibiotic resistance. *Nat. Rev. Microbiol.* **4**, 556–562 (2006).
4. Balaban, N. Q., Gerdes, K., Lewis, K. & McKinney, J. D. A problem of persistence: still more questions than answers? *Nat. Rev. Microbiol.* **11**, 587–591 (2013).
5. Fauvart, M., De Groote, V. N. & Michiels, J. Role of persister cells in chronic infections: clinical relevance and perspectives on anti-persister therapies. *J. Med. Microbiol.* **60**, 699–709 (2011).
6. Balaban, N. Q., Merrin, J., Chait, R., Kowalik, L. & Leibler, S. Bacterial persistence as a phenotypic switch. *Science* **305**, 1622–1625 (2004).
7. Lewis, K. Persister cells. *Annu. Rev. Microbiol.* **64**, 357–372 (2010).
8. Fisher, R., Gollan, B. & Helaine, S. Persistent bacterial infections and persister cells | Nature Reviews Microbiology. https://www.nature.com/articles/nrmicro.2017.42.
9. Kohanski, M. A., Dwyer, D. J. & Collins, J. J. How antibiotics kill bacteria: from targets to networks. *Nat. Rev. Microbiol.* **8**, 423–435 (2010).
10. Wang, X. & Wood, T. K. Toxin-Antitoxin Systems Influence Biofilm and Persister Cell Formation and the General Stress Response ▿ . *Appl. Environ. Microbiol.* **77**, 5577–5583 (2011).
11. Ronneau, S. & Helaine, S. Clarifying the Link between Toxin–Antitoxin Modules and Bacterial Persistence. *J. Mol. Biol.* **431**, 3462–3471 (2019).
12. Maisonneuve, E., Castro-Camargo, M. & Gerdes, K. (p)ppGpp controls bacterial persistence by stochastic induction of toxin-antitoxin activity. *Cell* **154**, 1140–1150 (2013).
13. Fung, D. K. C., Chan, E. W. C., Chin, M. L. & Chan, R. C. Y. Delineation of a bacterial starvation stress response network which can mediate antibiotic tolerance development. *Antimicrob. Agents Chemother.* **54**, 1082–1093 (2010).
14. Nguyen, D. *et al.* Active starvation responses mediate antibiotic tolerance in biofilms and nutrient-limited bacteria. *Science* **334**, 982–986 (2011).
15. Harms, A., Maisonneuve, E. & Gerdes, K. Mechanisms of bacterial persistence during stress and antibiotic exposure. *Science* **354**, aaf4268 (2016).
16. Orman, M. A. & Brynildsen, M. P. Dormancy Is Not Necessary or Sufficient for Bacterial Persistence. *Antimicrob. Agents Chemother.* **57**, 3230–3239 (2013).
17. Zou, J., Peng, B., Qu, J. & Zheng, J. Are Bacterial Persisters Dormant Cells Only? *Front. Microbiol.* **12**, (2022).
18. Zhang, P. *et al.* Nanoparticles Promote Bacterial Antibiotic Tolerance via Inducing Hyperosmotic Stress Response. *Small* **18**, 2105525 (2022).
19. Morawska, L. P. & Kuipers, O. P. Antibiotic tolerance in environmentally stressed Bacillus subtilis: physical barriers and induction of a viable but nonculturable state. *microLife* **3**, uqac010 (2022).
20. Zhu, M. & Dai, X. High Salt Cross-Protects Escherichia coli from Antibiotic Treatment through Increasing Efflux Pump Expression. *mSphere* **3**, e00095-18 (2018).
21. Pilizota, T. & Shaevitz, J. W. Fast, Multiphase Volume Adaptation to Hyperosmotic Shock by Escherichia coli. *PLOS ONE* **7**, e35205 (2012).
22. Mika, J. T., Van Den Bogaart, G., Veenhoff, L., Krasnikov, V. & Poolman, B. Molecular sieving properties of the cytoplasm of Escherichia coli and consequences of osmotic stress. *Mol. Microbiol.* **77**, 200–207 (2010).

23. Minton, A. P. The Influence of Macromolecular Crowding and Macromolecular Confinement on Biochemical Reactions in Physiological Media *. *J. Biol. Chem.* **276**, 10577–10580 (2001).
24. Cayley, S. & Record, M. T. Large changes in cytoplasmic biopolymer concentration with osmolality indicate that macromolecular crowding may regulate protein-DNA interactions and growth rate in osmotically stressed Escherichia coli K-12. *J. Mol. Recognit. JMR* **17**, 488–496 (2004).
25. Zimmerman, S. B. & Minton, A. P. Macromolecular crowding: biochemical, biophysical, and physiological consequences. *Annu. Rev. Biophys. Biomol. Struct.* **22**, 27–65 (1993).
26. Klumpp, S., Scott, M., Pedersen, S. & Hwa, T. Molecular crowding limits translation and cell growth. *Proc. Natl. Acad. Sci. U. S. A.* **110**, 16754–16759 (2013).
27. Miermont, A. *et al.* Severe osmotic compression triggers a slowdown of intracellular signaling, which can be explained by molecular crowding. *Proc. Natl. Acad. Sci.* **110**, 5725–5730 (2013).
28. Walsby, A. E. Gas Vesicles. *Microbiol. Rev.* **58**, 94–144 (1994).
29. Pfeifer, F. Distribution, formation and regulation of gas vesicles. *Nat. Rev. Microbiol.* **10**, 705–715 (2012).
30. Hurt, R. C. *et al.* Genomically Mined Acoustic Reporter Genes Enable On- Demand In Vivo Monitoring of Tumor-Homing Bacteria.
31. Moyed, H. S. & Bertrand, K. P. hipA, a newly recognized gene of Escherichia coli K-12 that affects frequency of persistence after inhibition of murein synthesis. *J. Bacteriol.* **155**, 768–775 (1983).
32. Korch, S. B., Henderson, T. A. & Hill, T. M. Characterization of the hipA7 allele of Escherichia coli and evidence that high persistence is governed by (p)ppGpp synthesis. *Mol. Microbiol.* **50**, 1199–1213 (2003).
33. Nguyen, T. L. *et al.* Quantitative Phase Imaging: Recent Advances and Expanding Potential in Biomedicine. *ACS Nano* **16**, 11516–11544 (2022).
34. Berto, P., Rigneault, H. & Guillon, M. Wavefront sensing with a thin diffuser. *Opt. Lett.* **42**, 5117–5120 (2017).
35. Dewachter, L. *et al.* The Dynamic Transition of Persistence toward the Viable but Nonculturable State during Stationary Phase Is Driven by Protein Aggregation. *mBio* **12**, e00703-21.
36. Johnson, C. M. & Schleif, R. F. In vivo induction kinetics of the arabinose promoters in Escherichia coli. *J. Bacteriol.* **177**, 3438–3442 (1995).
37. Parry, B. R. *et al.* The bacterial cytoplasm has glass-like properties and is fluidized by metabolic activity. *Cell* **156**, 183–194 (2014).
38. Zhou, E. H. *et al.* Universal behavior of the osmotically compressed cell and its analogy to the colloidal glass transition. *Proc. Natl. Acad. Sci.* **106**, 10632–10637 (2009).
39. Weeks, E. R. Introduction to the Colloidal Glass Transition. *ACS Macro Lett.* **6**, 27–34 (2017).
40. Mattsson, J. *et al.* Soft colloids make strong glasses. *Nature* **462**, 83–86 (2009).
41. Jamali, S., Boromand, A., Wagner, N. & Maia, J. Microstructure and rheology of soft to rigid shear-thickening colloidal suspensions. *J. Rheol.* **59**, 1377–1395 (2015).
42. Mika, J. T. & Poolman, B. Macromolecule diffusion and confinement in prokaryotic cells. *Curr. Opin. Biotechnol.* **22**, 117–126 (2011).
43. Schavemaker, P. E., Boersma, A. J. & Poolman, B. How Important Is Protein Diffusion in Prokaryotes? *Front. Mol. Biosci.* **5**, 93 (2018).
44. Konopka, M. C., Shkel, I. A., Cayley, S., Record, M. T. & Weisshaar, J. C. Crowding and confinement effects on protein diffusion in vivo. *J. Bacteriol.* **188**, 6115–6123 (2006).

45. Konopka, M. C. *et al*. Cytoplasmic Protein Mobility in Osmotically Stressed Escherichia coli. *J. Bacteriol.* **191**, 231–237 (2009).
46. Soh, S., Banaszak, M., Kandere-Grzybowska, K. & Grzybowski, B. A. Why Cells are Microscopic: A Transport-Time Perspective. *J. Phys. Chem. Lett.* **4**, 861–865 (2013).
47. Einstein, A. Zur Theorie der Brownschen Bewegung. *Ann. Phys.* **324**, 371–381 (1906).
48. Cayley, S., Lewis, B. A., Guttman, H. J. & Record, M. T. Characterization of the cytoplasm of *Escherichia coli* K-12 as a function of external osmolarity. *J. Mol. Biol.* **222**, 281–300 (1991).
49. Reyhanoglu, G. & Reddivari, A. K. R. Tobramycin. in *StatPearls* (StatPearls Publishing, Treasure Island (FL), 2024).
50. Nishizawa, K. *et al*. Universal glass-forming behavior of in vitro and living cytoplasm. *Sci. Rep.* **7**, 15143 (2017).
51. Vazquez, A., Menezes, M. A. de, Barabási, A.-L. & Oltvai, Z. N. Impact of Limited Solvent Capacity on Metabolic Rate, Enzyme Activities, and Metabolite Concentrations of S. cerevisiae Glycolysis. *PLOS Comput. Biol.* **4**, e1000195 (2008).
52. LaFleur, M. D., Kumamoto, C. A. & Lewis, K. Candida albicans Biofilms Produce Antifungal-Tolerant Persister Cells. *Antimicrob. Agents Chemother.* **50**, 3839–3846 (2006).
53. Shen, S., Vagner, S. & Robert, C. Persistent Cancer Cells: The Deadly Survivors. *Cell* **183**, 860–874 (2020).

Chapter III: Side projects

Forword

As mentioned in the objectives section of the introduction, while most of my work was dedicated to the projects described in Chapter I and Chapter II, I also worked on other "side projects," so to speak. Two such projects will be described here, both aimed at expanding the methodological toolkit for studying gas vesicles and related topics.

Before presenting these, I would like to briefly mention a study recently published by Mickael Tanter's team at ESPCI, to which I contributed. In this work, I provided some of the purified gas vesicles used and collaborated with Mathis Vert, a PhD student in Mickael Tanter's team, to establish the protocol for encapsulating gas vesicles in a phantom gel without introducing additional bubbles, a task that proved more challenging than it might seem for two inexperienced PhD students ! This clean embedding method allowed high-quality acoustic imaging.

The paper introduces a new ultrasound imaging method, called nonlinear singular value decomposition (SVD) beamforming, designed to improve gas vesicle imaging. As discussed earlier, existing techniques like cross amplitude modulation (xAM) and amplitude modulation (AM) have limitations: they typically require many pulse transmissions, produce long signals that limit imaging depth, and can be difficult to calibrate while balancing performance and safety. The idea behind nonlinear SVD beamforming is to send ultrasound pulses at different pressure levels and then apply SVD (a mathematical technique that breaks down complex signals into simpler components or patterns) to separate the gas vesicle signal from the tissue background. By analyzing how the signal varies with pressure, the method isolates the nonlinear contribution of gas vesicles more effectively. The paper is available in Appendix 7.

Spheroids as *in vitro* tumor models and their infection with bacteria

Context

One of the motivating factors behind our interest in gas vesicles was their potential application in bacterial cancer therapy. In such therapeutic strategies, engineered bacteria are administered systemically or locally to colonize tumors and elicit anti-tumor effects, either through the secretion of therapeutic payloads or by stimulating host immune responses. Over the past decade, a growing body of proof-of-concept studies has demonstrated the promise of synthetic biology in this context. For instance, in a landmark 2016 study, Din *et al.*[150] engineered *Salmonella enterica* to harbour a synchronized lysis circuit, enabling population-level periodic self-lysis once a bacteria population threshold was reached. Cells were also engineered to produce the pore-forming toxin Haemolysin E which was released by the lysis into the tumor microenvironment, while a subpopulation of surviving bacteria repopulated the tumour, establishing a pulsatile delivery cycle. In murine models of colorectal cancer, this strategy led to a significant reduction in tumor growth. This is one illustrative example among many recent synthetic biology-based strategies, several of which have been reviewed elsewhere[151,152].

As synthetic biology applications in cancer therapy advance, there is increasing interest in physiologically relevant *in vitro* models that can bridge the gap between 2D cultures and animal models. Three-dimensional spheroids, formed by culturing mammalian cells under non-adherent or low-attachment conditions, provide a valuable platform for such investigations. Indeed, spheroids recapitulate key features of the tumor microenvironment, including gradients of oxygen, nutrients, and metabolites, as well as cell–cell interactions[153,154]. They are also relatively straightforward to generate, even high-throughput formats, from various cell lines, making them suitable for screening applications[155]. In 2019, Harimoto *et al.*[156] described a methodology for generating spheroids and infecting them with bacteria, enabling investigation of bacterial colonization dynamics and activity of synthetic circuit activity within a 3D tumor-like context. Given our lab's focus on synthetic biology and cancer, we were naturally drawn to this approach and sought to reproduce the method in-house, with the goal of integrating it into future therapeutic bacteria research projects. For example, we had the idea of infecting spheroids from various cells lines with *E.coli* producing gas vesicles to better characterize their behavior in different tumor models. At the time, no one in our team had prior experience with 3D mammalian cell culture. Given the alignment with my PhD focus on bacterial therapies for cancer, I took the initiative to learn these techniques and introduce this platform into our laboratory toolkit.

To this end, I contributed by learning how to produce spheroids, how to infect them and how to check whether the infection worked in 2D microscopy. I then developed a protocol to visualize bacteria colonies distribution within the tumor in 3D.

Generating spheroids and infecting them

To implement this model in our laboratory, I undertook training in the generation and infection of spheroids. While I had prior experience with mammalian cell culture, I had never worked with 3D systems. To address this, I collaborated closely with Habib Hani, a research engineer in Jérôme Bonnet's group at the Centre de Biologie Structural, to learn the techniques necessary for spheroid culture and infection.

To generate spheroids, we used the ultra-low attachment plate method. This involves seeding a defined number of cells in suspension into hydrophilic polymer-coated U-bottom wells. The coating prevents cell adhesion to the well, causing the cells to aggregate as they settle to the bottom and adhere to one another. Over the course of a few days, this aggregation leads to the formation of a compact spheroid. When maintained under appropriate culture conditions, these spheroids continue to grow over time. Such well plates are commonly referred to as "ultra-low attachment plates".

To test spheroid infections, I chose to work with *Escherichia coli* Nissle 1917, whereas Harimoto's work had primarily used *Salmonella Typhimurium*. *E. coli* Nissle 1917 is widely used as a candidate for therapeutic bacteria in cancer applications[157–159]. Being a strain of *E. coli*, it is easy to handle in the lab, particularly for genetic engineering, and we already had a large collection of plasmids optimized for this host. To detect bacterial colonies within the spheroids, I introduced a plasmid encoding constitutive expression of GFP, making the bacteria fluorescent. This engineered strain was then used to infect spheroids.

To infect the spheroids, I followed the approach described by Harimoto et al.[156]. The engineered *E. coli* Nissle 1917 strain was added to ultra-low attachment wells containing pre-formed, four-day-old spheroids and incubated for four hours in nutrient-rich mammalian cell culture medium to allow bacterial colonization. After incubation, the spheroids were thoroughly washed and transferred to fresh wells containing medium supplemented with gentamicin. Since this bacterial strain is not resistant to gentamicin, the antibiotic eliminates any remaining bacteria. However, due to its poor permeability across eukaryotic membranes[160], gentamicin does not effectively penetrate the spheroids. As a result, only bacteria that successfully infiltrated the spheroid during the incubation period are able to survive and replicate, while external bacteria are killed. This step ensures that bacterial growth is restricted to the spheroid interior, preventing uncontrolled colonization of the surrounding medium (Figure 9a). Detailed protocols for spheroid generation and infection are provided in Spheroids preparation, infection and clearing.

Finally, to assess the outcome of the infection, I imaged the spheroids using both brightfield and fluorescence microscopy, which revealed the presence and distribution of GFP-expressing bacterial colonies within the spheroid structure (Figure 9b), similar to what was reported in Harimoto work. This confirmed that I was able to replicate their method. I added the protocols to common protocol base of the team and taught it to several team members, making it part of our toolkit.

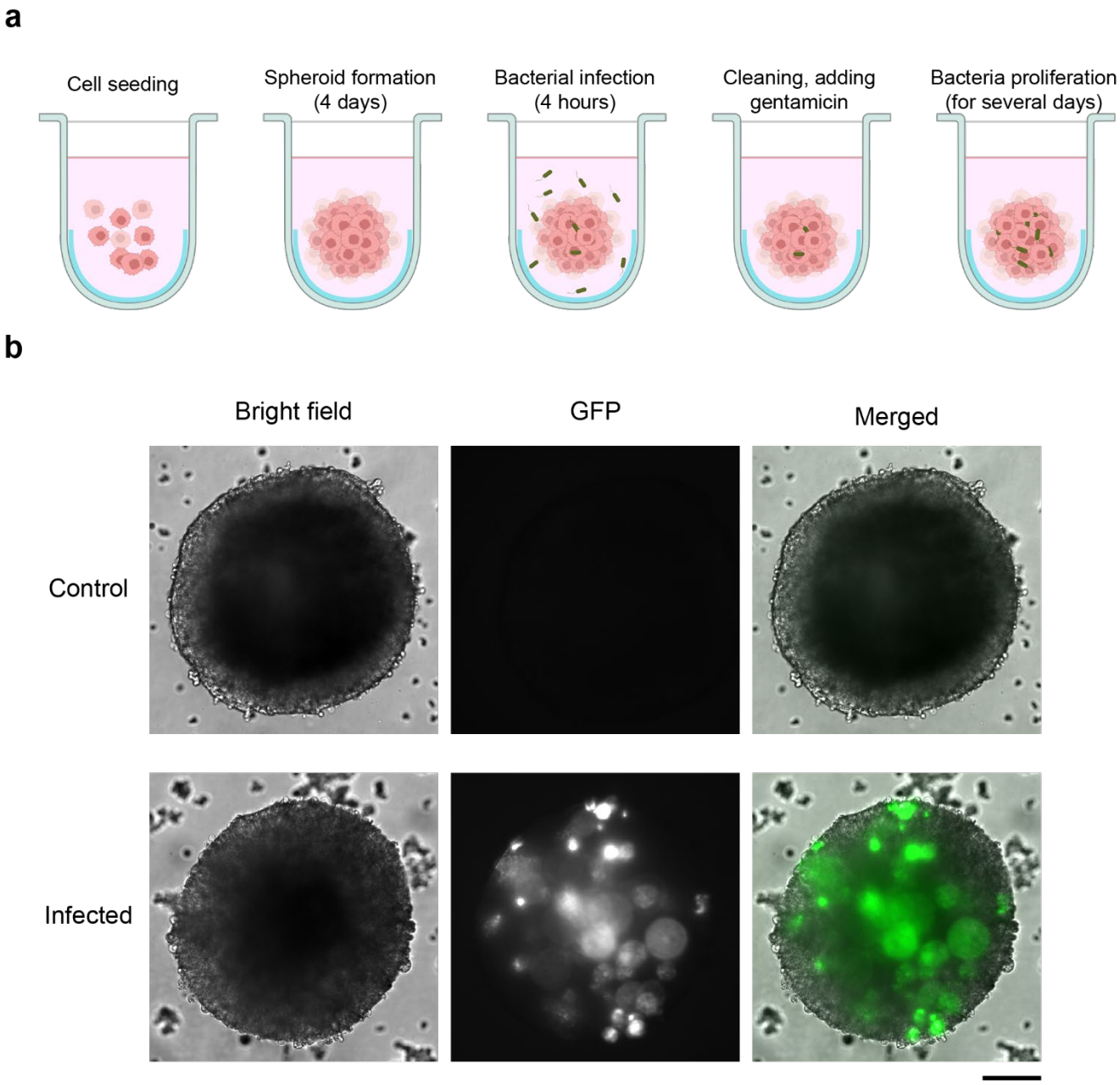

Figure 9 : Generation and infection of spheroids with engineered bacteria.(**a**) Schematic representation of the protocol used to generate spheroids in ultra-low attachment plates and infect them with bacteria. (**b**) HEK 293 cell spheroids imaged three days post-infection, shown without (top) and with (bottom) bacterial infection. Identical image acquisition settings and contrast adjustments were applied to both conditions. Scale bar: 50 μm.

3D imaging of bacteria distribution

While images as those presented in Figure 9b reveal the presence of bacteria and can potentially provide their relative quantification, they do not offer accurate information on the spatial distribution of bacterial microcolonies within the spheroid. Indeed, the images are two-dimensional, whereas spheroids are three-dimensional structures. As a result, they only provide information about the location of bacterial microcolonies in the x and y axes, but offer little insight into their z position (depth), and therefore how deep inside the spheroid bacteria are. Yet, this information is important. As mentioned earlier, one of the key features of spheroids is their ability to mimic gradients found in solid tumors. For example, oxygen concentration is typically lower at the center of the spheroid than at its edges, and such gradients can strongly influence bacterial proliferation and distribution.

A possible solution for obtaining 3D localization would be to use confocal microscopy or spinning disk systems to acquire optical sections through the spheroid. However, since spheroids are dense structures, light penetration is limited, making it difficult to detect signals from bacteria located deep inside or on the side opposite the objective. This limitation may lead to an underestimation of bacterial colonization. An alternative approach could involve cryosectioning the spheroids into thin slices, imaging each section, and reconstructing the spheroid digitally. However, this method is laborious, and the slicing process can introduce artefacts that compromise accurate reconstruction of the original 3D structure.

Therefore, to observe the spheroids in greater depth, I decided to try a different approach and work with tissue clearing. Tissue clearing refers to a set of chemical techniques used to render tissues transparent. While many different solutions can be used, they typically rely on the same underlying principle. Tissues are opaque mainly due to mismatches between the refractive index (RI) of their aqueous environment and the cellular components, leading to light scattering. The goal of tissue clearing is to place the sample in a solution with a matching RI either by altering the sample's RI (for example, through lipid removal), by adjusting the surrounding solution's RI to match that of the sample, or by a combination of both. Although tissue clearing techniques have been known for over a century[161], significant progress has been made in recent decades, making it relatively straightforward to render whole organs transparent (see Figure 10a for a nice example)[162–164]. Once a tissue is transparent, it can be imaged entirely using confocal microscopy to generate 3D reconstructions. While tissue clearing is mostly applied to imaging the brain or other organs, I decided to use it to observe the infected spheroids.

For this, I used a commercially available, ready-to-use glycerol-based solution called RapiClear, with a refractive index adjusted to 1.49. The protocol I followed for spheroid tissue clearing is described in Spheroids preparation, infection and clearing. Briefly, spheroids were washed in phosphate-buffered saline (PBS), fixed in 4% paraformaldehyde, permeabilized with Triton solution, and stained with 4',6-diamidino-2-phenylindole (DAPI), a blue fluorescent DNA dye, before being washed again in PBS. Most of the PBS was then removed and replaced with RapiClear solution. After a few minutes of incubation, the spheroids became transparent and could be observed with spinning disk microscopy, enabling 3D imaging. Illustrative examples of the results are shown in Figure 10.

Results

My goal with this side project was to adapt these spheroid formation, infection, and imaging methods so that our team could acquire the expertise to implement and use them in our lab. The results I present here illustrate that and provided valuable proof-of-concept insights. The data presented here in Figure 10 should be considered as an illustrative example of the type of information this method can provide, rather than as part of a complete biological study.

First, as shown in Figure 10b, the clearing worked in the sense that I was able to produce a Z-stack covering the entire spheroid from top to bottom, with all cell nuclei clearly visible, including those at the center of the structure. Because the clearing was successful, we can assume that most bacterial colonies within the spheroid could be detected regardless of their depth. This enabled me to perform several measurements on the colonies, shown in Figure 10d and e. I demonstrated that it was possible to quantify the spatial distribution of bacterial colonies, here expressed as the distance between their center of mass and the spheroid border, in a spheroid three days post-infection. These preliminary results indicate that no *E. coli* colony was detected in the core of the spheroid, up to approximately 40 µm around the center. Most colonies (75% of them) were found within the first 80 µm from the spheroid surface. The average distribution was 54 ± 38 µm, indicating a predominance near the surface, which is consistent with expectations for *E. coli*. While I did not measure pH or oxygen concentration in these spheroids, others have established that such 3D cultures typically exhibit decreasing oxygen levels and pH values towards the center[165]. Because *E. coli* is a facultative anaerobe and its optimal growth at 37°C occurs around neutral pH[166,167], it is expected that colonization preferentially occurs near the spheroid surface. This was also suggested by the results of Harimoto et al. [156].

Furthermore, from such Z-stacks, it is also possible to measure the volume of individual bacterial colonies, as shown in Figure 10e. From the colony volume, and assuming the bacteria are tightly packed with a known average volume per bacterium, the number of bacteria per colony can be estimated. This is important for anticipating the microenvironment to which the bacteria are exposed. As discussed in Chapter I of this thesis, gradients rapidly develop within bacterial colonies, influencing both growth and metabolism. The colony size can also impact the behavior of engineered genetic circuits in therapeutic bacteria. For example, as described in the previously mentioned 2016 study by Din et al.[150], the synchronized lysis circuit designed to release a tumor-targeting toxin depends on the accumulation of secreted signaling molecules reaching a threshold concentration to trigger lysis. The size of the colony plays a key role in determining whether, and how quickly, this threshold is achieved. Notably, small colonies ,particularly in environments with fluid flow, may fail to accumulate sufficient signaling molecules to reach the triggering threshold[168]. It is also likely that the typical volume of bacterial colonies varies depending on the tumor (or spheroid) cell type. For example, epithelial cell tumors may provide less intercellular space for bacterial colony development than the mesenchymal ones[165]. Knowing the typical size and distribution of colonies in these contexts is therefore valuable for the rational design of genetic circuits tailored to specific tumor microenvironments. However, the dimensions of bacterial colonies within tumors have remained largely unstudied to date. With the technique I have described here, it would be possible to study the relationship between cell line type and bacterial colony volume. In the example presented in Figure

10, using HEK 293 cell spheroids, I observed that most colonies were fairly small, containing a few hundred bacteria (assuming an average volume of 1.2 μm^3 per bacterium), while a small number of colonies were of much larger colonies containing up to approximately 2.7×10^4 cells. This method therefore offers valuable potential for characterizing bacterial growth and distribution within spheroids.

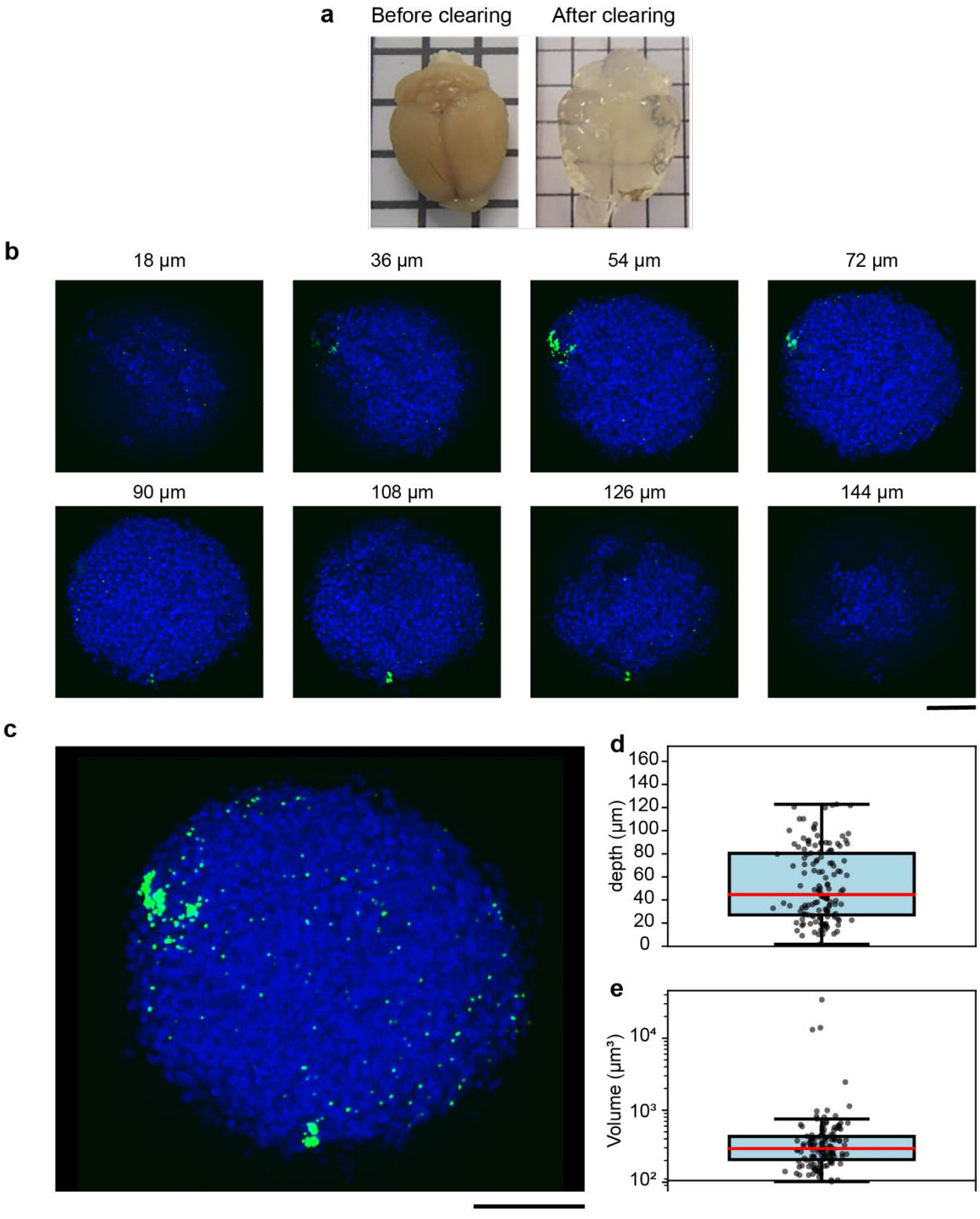

Figure 10 : 3D imaging of bacterial microcolonies within spheroids. (**a**) Example of tissue clearing in whole mice brain, here using sucrose solution to reach the targeted organ refractive index. Adapted from Gómez-Gaviro *et al.* 2020[169]. (**b**) Individual slices at various depth of a Z stack obtain from spinning disk microscopy on a 346 µm-wide HEK 293 cell spheroid, after DAPI labelling and clearing. (**c**) Top view of a

3D projection of the stack shown in (b), making most colonies visible. For (b) and (c), blue indicates DAPI-labelled spheroid cell nuclei; green indicates GFP-expressing *E. coli*, revealing bacterial microcolonies. Scale bars for (b) and for (c) both represents 100 μm. (**d**) Example of the depth distribution of bacterial microcolonies within the spheroid shown in (b) and (c). The y-axis represents the distance between the center of mass of each bacterial colony and the border of the spheroid. (**e**) Example of the volume distribution of bacterial microcolonies within the same spheroid. In (d) and (e), each point represents an individual microcolony, 147 colonies were identified in this example.

GV flash labelling for super resolution imaging

Context

While the uses of gas vesicles described in the introduction mainly rely on detecting them through ultrasound imaging, optical imaging of gas vesicles in microscopy remains important for their study, particularly for observations at the cellular level in living cells, a resolution that cannot be achieved with ultrasound. As I showed in Chapter I, it is possible to image gas vesicles using simple brightfield or phase contrast microscopy, since gas vesicles scatter light. However, this method is not ideal, as it likely only enables detection of clusters of gas vesicles, and key questions such as "how many individual gas vesicles are required to be detected in this way?" remain unanswered. Furthermore, gas vesicles are not the only intracellular structures that can act as refractile bodies in cells, especially in eukaryotic cells. Therefore, to facilitate research on gas vesicles, improved methods for their optical detection would be highly beneficial.

One possible strategy would be to engineer gas vesicle structural proteins (such as GvpA or GvpC) to include fluorescent protein tags. However, fluorescent proteins like GFP are relatively large (27 kDa for GFP) compared to gas vesicle proteins (approximately 7 kDa for GvpA and 20 kDa for GvpC), and such fusions would likely disrupt protein function and impair vesicle assembly. Some studies have reported fusing split-GFP fragments to various gas vesicle proteins[60,170], including GvpA, but this was done solely to map protein–protein interactions, and these studies did not assess whether gas vesicles could still form with split-GFP fragments fused to their components.

An alternative approach that is less likely to disrupt protein function is the insertion of small peptide tags into the gas vesicle protein sequence, which can then serve as binding sites for fluorescent markers. This strategy was used in 2016 by Lakshmanan *et al*[81], who reported adding a 13-amino-acid SpyTag[g] to the C-terminus of GvpC. The modified GvpC retained its ability to bind gas vesicles, similar to the wild-type protein. When the modified gas vesicles were incubated with SpyCatcher (SpyTag partner protein) fused to a fluorescent marker, they could be visualized by fluorescence microscopy. While this technique enabled fluorescent detection of gas vesicles, it required incubation of purified, tagged gas vesicles with SpyCatcher and subsequent removal of excess SpyCatcher, and was never reported for use in intact cells. As a result, no straightforward solution for fluorescent imaging of gas vesicles in living cells is currently available.

In 2022, during my attendance at the ISBUS conference at Caltech (as previously mentioned), I had the opportunity to discuss this challenge over a beer with Erik Schrunk, a PhD student in Shapiro's team who was working on this very issue. His approach involved inserting a six-amino-acid

[g] The SpyTag–SpyCatcher system enables covalent labeling of proteins through a genetically encoded peptide–protein pair. A 13-amino acid peptide (SpyTag) is fused to the protein of interest, while its binding partner, SpyCatcher (a derived protein domain) can be attached to a variety of functional payloads, including fluorescent proteins. Upon contact, the two partners spontaneously form a stable covalent isopeptide bond under physiological conditions, enabling efficient and site-specific labeling using a minimal tag on the protein of interest[171].

tetracysteine (TC) motif at the C-terminus of the GvpA protein. When proteins containing this TC tag come into contact with the biarsenical ligand FlAsH, the ligand binds specifically to the tag and becomes fluorescent[172]. Using TC-tagged GvpA in combination with FlAsH, it was therefore possible to selectively label gas vesicles for fluorescence imaging. At that time, Erik had already demonstrated that the system functioned effectively in mammalian cells and, to a lesser extent, in bacteria. His work was subsequently published in 2024[173]. His work was particularly interesting to me, as developing and implementing new tools and methods for working with gas vesicles, and making them accessible to the community, was one of the goals of my PhD, as explained earlier. In addition, while researching FlAsH labeling, I came across a 2012 paper describing its application in PALM microscopy[174] [h], despite the fact that it was not designed for it. This was especially exciting because FlAsH labeling of GvpA combined with PALM could potentially enable super-resolution imaging of gas vesicle structures. Furthermore, at Institut Curie, we also had access to the CurieCore platform, equipped with several microscopes suitable for PALM microscopy that would allow us to test that. This presented a valuable opportunity to both expand the toolkit available for studying gas vesicles at the cellular level and to establish a collaboration with Shapiro's team. We contacted Michael Shapiro and Erik Schrunk about this project, and they kindly agreed to provide us with plasmids for the production of TC-tagged gas vesicles in *E. coli*, allowing us to begin experiments immediately. The goal was to see if we could image the structure of gas vesicles in super resolution microscopy.

Protocol and results

Before delving into super-resolution imaging, it was essential to verify that gas vesicles could be observed using standard fluorescence microscopy. This initial step relied on a straightforward protocol, adapted from preliminary experiments conducted by Erik Schrunk whose work focused primarily on mammalian cells, with limited testing in bacteria. The approach consisted of incubating cells with FlAsH dye for a few minutes, followed by washing in PBS containing 2,3-Dimercapto-1-propanol (also known as BAL or British anti-Lewisite), prior to imaging.

However, during my initial attempts, I observed that the dye did not appear to penetrate the bacterial cells effectively, even when using elevated FlAsH concentrations and extended incubation times. This challenge is consistent with reports from other studies, which noted that FlAsH struggles to cross the outer membrane of bacteria[176]. To address this limitation, I explored various strategies to transiently

[h] PALM stands for Photoactivated Localization Microscopy. It is a super-resolution imaging technique that enables visualization of cellular structures at the nanometer scale, surpassing the diffraction limit of conventional light microscopy. PALM relies on photoactivatable or photoswitchable fluorescent proteins or dyes that can be stochastically activated and imaged one at a time. In a typical PALM experiment, a fluorescence movie of the sample is recorded in which individual fluorophore molecules will blink, only emitting light for a few frames and producing a point spread function (PSF). From the PSF, the position of the individual fluorophore can then be estimated with high precision (typically via Gaussian fitting), to nanometer accuracy. The final image is reconstructed from the accumulated localizations of many individual fluorophores. PALM achieves a lateral (xy) resolution of roughly 10 to 30 nm depending on the setup and sample conditions. This technique is widely used to study the organization of proteins, organelles, and molecular complexes in fixed or live cells[175].

permeabilize the bacterial envelope and facilitate dye entry. These included heat shock, electroporation, and treatment with low concentrations of lysozyme, an enzyme that partially degrades the cell wall. Among these, lysozyme treatment produced the most promising results. I adapted a protocol previously described by Ignatova and Gierasch[176] for FlAsH labeling of proteins in *E. coli*. The detailed method is provided in Protocols . As illustrated in Figure 11a-c, gas vesicles that are clearly visible by phase-contrast microscopy also exhibit a corresponding fluorescent signal. Nevertheless, some cells lacking visible gas vesicles displayed a strong, homogeneous fluorescence, likely reflecting the presence of unassembled GvpA protein.

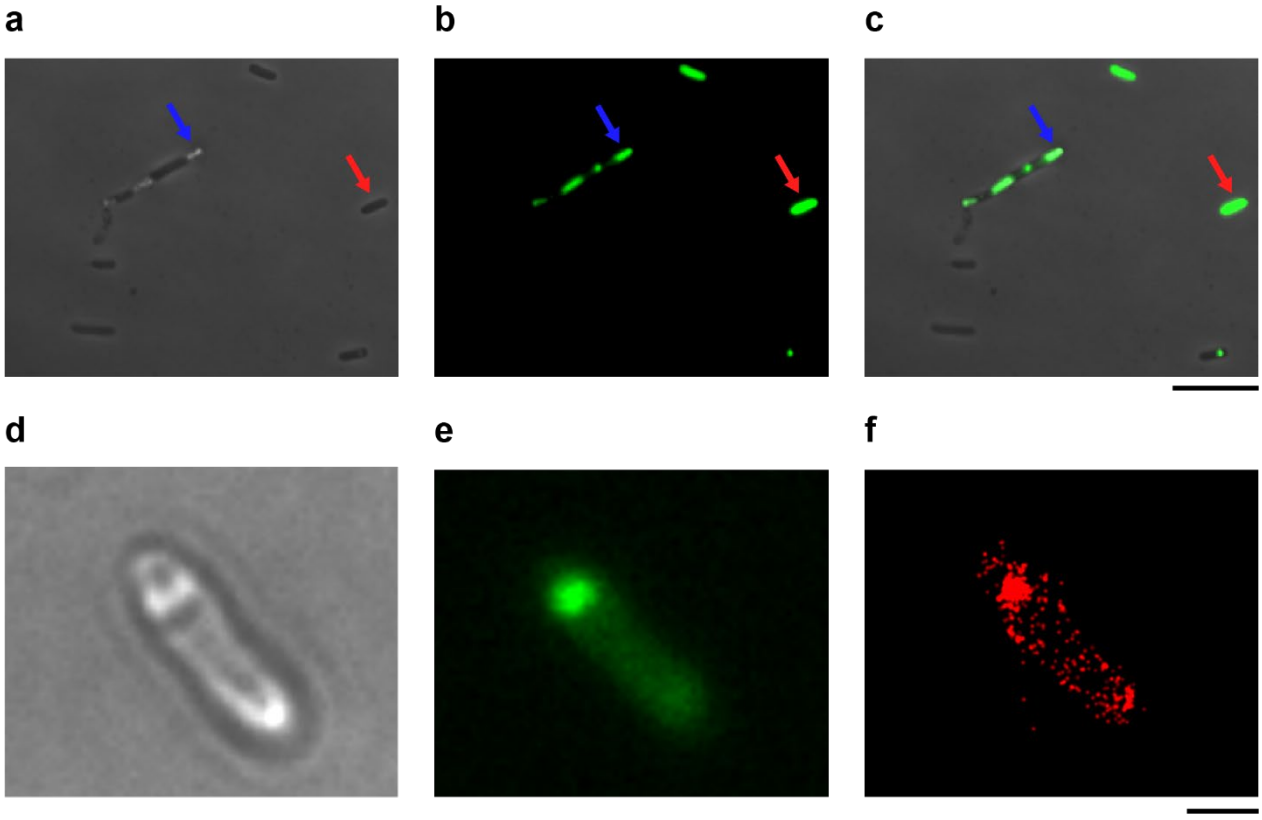

Figure 11 : GvpA labelling with FlAsH in cells. (**a**)(**b**)(**c**) Cells with gas vesicles and GvpA labelling in standard microscopy, respectively in phase contrast in (a), fluorescence in (b) and overlay of (a) and (b) in (c). Gas vesicles clusters appear as bright white spots in phase contrast. Blue arrow indicates localization of a gas vesicles cluster with matching FlAsH labellig, red arrow indicates a case with cell fluorescence despite the absence of detectable gas vesicles clusters in phase contrast. Error bar represents 10 μm. (**d**)(**e**)(**f**) E.coli containing gas vesicles imaged with PALM microscope, with the same cell respectively bright field image in (d), where refractile body can be seen at the top end of the cell, standard fluorescent imaging in (e), captured before triggering the blinking of the dye, and PALM image in (f), where each red dot indicate one GvpA molecule. In places were labeled proteins are closely packed, dots overlap forming clusters as seen on the top end of the cell. Error bar represents 750nm.

Having confirmed the ability to label gas vesicles with FlAsH, I proceeded to explore their visualization using super-resolution microscopy. I began with the protocol described by Lelek *et al.*[174], introducing several adjustments during the course of optimization. This work was done with the help of David Mazaud from the CurieCoreTech Cell and Tissue Imaging platform, who's expert in super resolution microscopy technics. After multiple rounds of refinement, we established a set of parameters that provided the best results. In summary, bacteria containing gas vesicles were labeled with FlAsH and washed with BAL. The bacteria were then immobilized on poly-lysine-coated coverslips, which were mounted on slides with cavities containing a photoswitching buffer. The buffer composition followed standard formulations, with β-mercaptoethanol used as the reducing agent. The sample was first imaged using bright-field and conventional fluorescence microscopy, then photobleached at 488 nm for a few seconds. This was followed by a pulse at 408 nm and continuous excitation at 488 nm. Under these conditions, the FlAsH molecules exhibited blinking, allowing the acquisition of movies that could subsequently be processed to generate super-resolution images.

An illustrative example of the results is shown in Figure 11d-f. These experiments demonstrated that, under suitable conditions, FlAsH does blink and can indeed be used for PALM microscopy. The localization of a large number of GvpA molecules corresponded well with the bright refractile bodies seen in bright-field microscopy, suggesting that FlAsH effectively labeled gas vesicle clusters. In addition, less dense GvpA localizations were observed throughout the cytoplasm, likely representing GvpA not yet assembled into vesicles.

Limitations

Despite achieving blinking of FlAsH-labeled gas vesicles, each blink was of low brightness, that is, the number of photons emitted per event was limited, even when using the excitation laser at full power. In super-resolution microscopy, the precision of molecular localization fundamentally depends on the number of detected photons: fewer photons result in greater positional uncertainty and ultimately lower resolution[175,177]. In our case, the best achievable resolution was approximately 60 nm, which is relatively low compared to the typical 10-30 nm range expected for PALM microscopy. Given the dimensions of gas vesicles (200-1000 nm in length and 45–200 nm in width), this resolution was insufficient for precise structural visualization.

Furthermore, the reconstructed PALM images were generated from more than 20,000 frames, at which point nearly all fluorophores had been photobleached and no further blinking could be detected. These reconstructions therefore represented the maximum point density attainable under our experimental conditions. Although gas vesicle clusters may contain tens of thousands of GvpA monomers[17], we obtained only a few hundred localizations per cell, even in regions where gas vesicle clusters were visible. This suggests that the vast majority of GvpA molecules were either not labeled, did not blink, or both, despite using FlAsH concentrations more than ten times higher than typically recommended for imaging in mammalian cells.

While my goal was to resolve the structure of individual gas vesicles using this technique, this was not achieved. This limitation arose partly from the low brightness and labeling efficiency of the dye, but also from the natural tendency of gas vesicles to cluster within cells. Since our imaging was performed in 2D, overlapping gas vesicles were difficult to distinguish. Even with improved labeling, structural imaging of gas vesicles by PALM would likely require identification of isolated vesicles, which may be challenging to find within the intra cellular context.

Finally, the current protocol is not suited for live cell imaging. Indeed, it involve of many toxic steps for the cells : high concentration of Flash, lysozymes, polylysine, and intense illumination. While I did not tested the impact on cell viability, it would most likely impair cell growth and metabolism, if not stop at all.

In conclusion, while this method did allow us to use PALM to image GvpA and provided somewhat better resolution than standard fluorescence microscopy, it proved suboptimal for imaging gas vesicles at super-resolution or for use in live cells.

This does not mean that imaging gas vesicles with fluorescence in live cells is unattainable. Various works[63,81] showed that the SpyTag–SpyCatcher system could be used to label purified gas vesicles with fluorescent dye, specifically on GvpC and GvpJ. This strategy could potentially be adapted for live-cell imaging by expressing SpyCatcher directly in the cell fused to a fluorescent protein, such as SpyCatcher-sfGFP; ready-to-use plasmids for this are available from Addgene. The SpyCatcher system also offers versatility, as it could be fused to PALM-adapted fluorescent proteins like PA-GFP[178] or mEos2[179], enabling super-resolution microscopy. Considering that editable sites in GvpC and GvpJ have been identified (namely, the C-terminus regions)[63,81], this could be implemented relatively quickly for these proteins. For GvpA, however, inserting the 13-amino-acid SpyTag sequence at a position that does not interfere with gas vesicle formation would be a more challenging task. For super resolution in fixed cells, another solution would be to use antibodies targeting GvpA ribs and/or GvpC, conjugated to fluorophores compatible with super-resolution microscopy. However, such antibodies are not commercially available, and to my knowledge, “homemade” versions of gas vesicles targeting antibodies were only described once over 30 years ago[51]. Producing such antibodies would likely be a demanding and resource-intensive endeavor.

Conclusion

Gas vesicles are gas-filled protein nanostructures that have gained significant attention over the past decade, primarily due to their unique acoustic properties, which make them valuable tools as acoustic reporters. Among the many possible applications of such structures, their **heterologous expression in bacteria**, offering an acoustic analogue to fluorescent proteins, holds great promise for **non-invasive imaging of therapeutic bacteria** in animal models, particularly within tumors or the gastrointestinal tract. However, research in this direction remains at an early, proof-of-concept stage, and the **physiological impact of heterologous gas vesicle production** has so far received little attention.

Therefore, the goal of my PhD was to fill this knowledge gap by identifying and quantifying **the physiological effects that gas vesicle expression may have on host cells**. This is a key step toward bridging the gap between existing preliminary demonstrations and real-world translational applications, especially in the context of microbial therapies and synthetic biology.

To reach this goal, I conducted quantitative measurements of *E. coli* growth following the induction of heterologous gas vesicle expression, both in homogeneous batch cultures and in bacterial microcolonies within a custom-built microfluidic setup. In both systems, I demonstrated that gas vesicle expression imposes a measurable metabolic burden on the host cells. Specifically, induction led to a significant **decrease in biomass yield**, up to twofold depending on induction strength, indicating that fewer cells were produced per unit of available nutrients. I also observed that nutrient **consumption rates** seem to **increase** upon induction, which in the microcolonies resulted in a **contraction of the actively growing zone**.

Additionally, I reported clear signs of **cellular stress** in gas vesicle-producing cells, with nearly one-third of the population exhibiting filamentation after just a few hours of induction. Finaly, I showed that over a longer time, **non-producing subpopulations** emerged within microcolonies. The appearance of these subpopulations correlated with higher induction levels and tended to originate from non-growing or slow-growing regions within the colony suggesting that they could arise from stress-induced mutations, although asymmetric inheritance of gas vesicle clusters during cell division could also play a role here. All of these findings are compiled in a manuscript currently under preparation and soon to be available on bioRxiv.

In parallel, and in collaboration with Gilles Tessier's team at the Institut de la Vision, we quantified the **average cytoplasmic volume fraction occupied by gas vesicles** in *E. coli* using quantitative phase imaging, across various levels of induction. Additionally, I measured the **proportion of persister cells** surviving antibiotic treatment under the same conditions. Interestingly, we observed a strong **exponential correlation** between the cytoplasmic volume occupied by gas vesicles and the fraction of persister cells. We hypothesize that this relationship reflects the impact of increased cytoplasmic crowding caused by gas vesicle accumulation, suggesting that the biophysical state of the cytoplasm may play a critical role in driving bacterial persistence. This insight highlights how crowding changes

can be another factor influencing cell persistence. This work is also compiled in a manuscript currently in preparation and will soon be available on bioRxiv.

Finally, I also dedicated time to smaller **side projects** related to gas vesicles and synthetic biology. Notably, I introduced into our team's toolkit the capacity to work with **spheroids** and **to infect them with bacteria**, which is most useful to work on engineered therapeutic bacteria against cancer. I then explored the use of **tissue clearing** techniques to visualize and make measurements on bacterial microcolonies in three dimensions within *in vitro* tumor models. While the results I produced are still preliminary, they demonstrate the promising potential of this approach to investigate bacterial colonization of tumor-like structures with engineered strains. In parallel, I attempted to take advantage of recent advances in gas vesicle fluorescent labeling to enable **super-resolution imaging**. Specifically, I combined **FlAsH labeling of GvpA**, a technique originally intended for conventional fluorescence microscopy, with **PALM imaging** to observe structure of gas vesicles in bacteria cells. While I did observe some degree of blinking behavior from the FlAsH fluorophores, their low brightness and the sparse density of localizations led to limited resolution. As a result, it was not possible to resolve the structure of individual gas vesicles under these conditions, showing that FlAsH labeling is not suited for super resolution microscopy of gas vesicles in cells.

Perspectives

Gvp stoichiometry optimization

Gas vesicles are promising tools for synthetic biology and, in particular, for bacterial therapies. However, their use remains largely confined to proof-of-concept studies. To bridge the gap to genuine translational applications, further optimization is needed. While much of the literature has focused on improving ultrasound imaging techniques to detect and quantify gas vesicles with increasing sensitivity and precision *in vivo* (see Ultrasound imaging), I believe another aspect deserves more attention: **biological optimization.** My work demonstrated that gas vesicle production impacts host cell growth, which will likely affect the functions these engineered bacteria can perform. Reducing this burden is thus essential to facilitate their broader adoption.

One approach involves **optimizing the stoichiometry of the proteins required for gas vesicle assembly**. Most studies to date have expressed all the genes in the operon from a single promoter, but some results in mammalian cells showed that altering the relative expression of specific genes in the gas vesicle operon can significantly impact gas vesicle yield. For example, increasing the ratio of GvpA relative to other proteins enhanced vesicle production[82], indicating that GvpA availability may be a limiting factor to gas vesicle production in that context. Increasing production of GvpA alone likely imposes a lower metabolic cost than uniformly upregulating all 19 genes in the operon, making it a metabolically cheaper solution to increase gas vesicles production.

Considering the many proteins involved, testing different protein ratios empirically in living systems would however be a massive task, requiring extensive cloning and strain construction. An alternative strategy could be to leverage **cell-free protein synthesis systems**, where protein expression can be driven directly from PCR products or plasmids in a cell lysate or reconstituted transcription-

translation system[180]. Because expression can be achieved from PCR products, this approach bypasses most of the cloning steps and different stoichiometries can be screened simply by adjusting the number of gene copy. Transformations and culturing can also be bypassed with this method. Notably, Antoine Levrier et al.[180] recently demonstrated a workflow for producing entire phages (build from 55 expressed proteins, much more than any gas vesicles) using cell-free systems, enabling rapid screening of mutant phage libraries. Applying a similar workflow to gas vesicle operons could provide an efficient route to identify optimal gene ratios for vesicle production while minimizing the burden on living hosts.

Expending gas vesicles use to other bacteria chassis

So far, all studies employing ARGs for the production of gas vesicles have been conducted **only in *Escherichia coli* strains**. This predominance is unsurprising, given that specific *E. coli* strains (most notably *E. coli* Nissle 1917) have been extensively explored as chassis for bacteria-mediated cancer therapies, owing to their established safety profiles and capacity for tumor colonization[158,181]. More fundamentally, *E. coli* remains the primary workhorse of synthetic biology: its genetic tractability, broad suite of optimized molecular tools, and compatibility with standardized synthetic circuits make it the default host for developing complex genetic systems.

Nevertheless, ***E. coli* is not the sole organism of interest for bacteria-based cancer therapy**. A growing body of work highlights the therapeutic promise of diverse bacterial species, including attenuated *Salmonella*[150,182,183], *Bifidobacterium*[184,185], *Clostridium*[186], *Listeria monocytogenes*[187,188], and various *Lactobacillus* strains[189,190]. Each of these species offers unique advantages, ranging from preferential tumor tropism and deep-tissue colonization to intrinsic immunomodulatory properties, that make them attractive chassis in the toolbox of live cancer therapeutics. To fully realize the potential of gas vesicle-based imaging and diagnostics within this context, it will be therefore **essential to extend ARG expressions beyond *E. coli*** to these alternative hosts.

Achieving this transition will not be trivial, however. Even within *E. coli*, engineering robust gas vesicle production required multiple design iterations, with significant improvements made between first- and second-generation ARG constructs. To establish the second generation of ARGs capable of reliable performance in *E. coli*, Hurt *et al*.[82] conducted an extensive empirical screen of gas vesicle gene clusters derived from 15 different species, selecting those that generated the strongest acoustic signals. Yet, there is no assurance that configurations optimized for *E. coli* will translate seamlessly to other bacterial chassis. Furthermore, translating these systems into alternative hosts will likely pose additional challenges, including species-specific differences in transcriptional regulation, the absence of universal replicons, low transformation efficiencies, codon usage biases, and the frequent necessity for host-adapted promoters.

Although such efforts are technically demanding, advancing ARG technology into these clinically relevant species is essential to establish gas vesicles as a versatile and impactful tool for imaging and monitoring engineered bacteria in cancer therapy.

References

1. Quote Origin: The Most Exciting Phrase in Science Is Not 'Eureka!' But 'That's Funny' – Quote Investigator®. https://quoteinvestigator.com/2015/03/02/eureka-funny/ (2015).
2. Serendipity, Happenstance, and Luck: The Making of a Molecular Tool. *The Scientist* https://www.the-scientist.com/serendipity-happenstance-and-luck-the-making-of-a-molecular-tool-71497.
3. Chalfie, M., Tu, Y., Euskirchen, G., Ward, W. W. & Prasher, D. C. Green fluorescent protein as a marker for gene expression. *Science* **263**, 802–805 (1994).
4. Heim, R., Prasher, D. C. & Tsien, R. Y. Wavelength mutations and posttranslational autoxidation of green fluorescent protein. *Proc. Natl. Acad. Sci.* **91**, 12501–12504 (1994).
5. Tian, F., Xu, G., Zhou, S., Chen, S. & He, D. Principles and applications of green fluorescent protein-based biosensors: a mini-review. *The Analyst* **148**, 2882–2891 (2023).
6. Swaminathan, S. GFP: the green revolution. *Nat. Cell Biol.* **11**, S20–S20 (2009).
7. Romei, M. G. & Boxer, S. G. Split Green Fluorescent Proteins: Scope, Limitations, and Outlook. *Annu. Rev. Biophys.* **48**, 19–44 (2019).
8. The Nobel Prize in Chemistry 2008. *NobelPrize.org* https://www.nobelprize.org/prizes/chemistry/2008/summary/.
9. Weissman, T. A. & Pan, Y. A. Brainbow: New Resources and Emerging Biological Applications for Multicolor Genetic Labeling and Analysis. *Genetics* **199**, 293–306 (2015).
10. Livet, J. *et al.* Transgenic strategies for combinatorial expression of fluorescent proteins in the nervous system. *Nature* **450**, 56–62 (2007).

11. Lauterorn, R. Die sapropelische Lebewelt. Ein Beitrag zur Biologie des Faulschlammes natürlicher Gewässer. *Naturhist-Med* (1915).

12. Fogg, G. E. The Gas-Vacuoles of the Myxophyceae (cyanophyceae). *Biol. Rev.* **16**, 205–217 (1941).

13. Klebahn. Gasvacuolen, ein Bestandtheil der Zellen der wasserbfuthebildenden Phycochromaceen. https://www.algaebase.org/search/species/detail/?species_id=62058 (1895).

14. Walsby, A. E. Structure and function of gas vacuoles. *Bacteriol. Rev.* **36**, 1–32 (1972).

15. Walsby, A. E. The Gas Vacuoles of Blue-Green Algae. *Sci. Am.* **237**, 90–97 (1977).

16. Bowen, C. C. & Jensen, T. E. Blue-Green Algae: Fine Structure of the Gas Vacuoles. *Science* **147**, 1460–1462 (1965).

17. Walsby, A. E. Gas Vesicles. *Microbiol. Rev.* **58**, 94–144 (1994).

18. Hurt, R. C. *et al.* Genomically Mined Acoustic Reporter Genes Enable On- Demand In Vivo Monitoring of Tumor-Homing Bacteria.

19. Pfeifer, F. Distribution, formation and regulation of gas vesicles. *Nat. Rev. Microbiol.* **10**, 705–715 (2012).

20. Oren, A. The Function of Gas Vesicles in Halophilic Archaeaand Bacteria: Theories and Experimental Evidence. *Life Open Access J.* **3**, 1–20 (2012).

21. Gosink, J. J., Irgens, R. L. & Staley, J. T. Vertical distribution of bacteria in arctic sea ice. *FEMS Microbiol. Ecol.* **11**, 85–90 (1993).

22. Gosink, J. J. & Staley, J. T. Biodiversity of gas vacuolate bacteria from Antarctic sea ice and water. *Appl. Environ. Microbiol.* **61**, 3486–3489 (1995).

23. Griffiths, A. E., Walsby, A. E. & Hayes, P. K. The homologies of gas vesicle proteins. *J. Gen. Microbiol.* **138**, 1243–1250 (1992).

24. Oliver, R. L. & Walsby, A. E. Direct evidence for the role of light-mediated gas vesicle collapse in the buoyancy regulation of Anabaena flos-aquae (cyanobacteria). *Limnol. Oceanogr.* **29**, 879–886 (1984).

25. Beard, S. J., Hayes, P. K. & Walsby, A. E. Growth competition between Halobacterium salinarium strain PHH1 and mutants affected in gas vesicle synthesis. *Microbiology* **143**, 467–473 (1997).

26. Simon, R. D. Interactions Between Light and Gas Vacuoles in Halobacterium salinarium Strain 5: Effect of Ultraviolet Light. *Appl. Environ. Microbiol.* **40**, 984–987 (1980).

27. Shear, H. & Walsby, A. E. An investigation into the possible light-shielding role of gas vacuoles in a planktonic blue-green alga. *Br. Phycol. J.* **10**, 241–251 (1975).

28. Ogawa, T., Sekine, T. & Aiba, S. Reappraisal of the so-called light shielding of gas vacuoles in Microcystis aeruginosa. *Arch. Microbiol.* **122**, 57–60 (1979).

29. Li, N. & Cannon, M. C. Gas Vesicle Genes Identified in Bacillus megaterium and Functional Expression in Escherichia coli. *J. Bacteriol.* **180**, 2450–2458 (1998).

30. Keulen, G. van, Hopwood, D. A., Dijkhuizen, L. & Sawers, R. G. Gas vesicles in actinomycetes: old buoys in novel habitats? *Trends Microbiol.* **13**, 350–354 (2005).

31. Dutka, P. *et al.* Structure of Anabaena flos-aquae gas vesicles revealed by cryo-ET. 2022.06.21.496981 Preprint at https://doi.org/10.1101/2022.06.21.496981 (2022).

32. Dutka, P. *et al.* Measuring gas vesicle dimensions by electron microscopy. *Protein Sci. Publ. Protein Soc.* **30**, 1081–1086 (2021).

33. Walsby, A. E. & Bleything, A. The Dimensions of Cyanobacterial Gas Vesicles in Relation to Their Efficiency in Providing Buoyancy and Withstanding Pressure. *Microbiology* **134**, 2635–2645 (1988).

34. Direct evidence for the role of light-mediated gas vesicle collapse in the buoyancy regulation of Anabaena flos-aquae (cyanobacteria)1 - Oliver - 1984 - Limnology and Oceanography - Wiley Online Library. https://aslopubs.onlinelibrary.wiley.com/doi/10.4319/lo.1984.29.4.0879.

35. Walsby, A. E., Simpson, J. H. & Fogg, G. E. Lower limit of the gas permeability coefficient of gas vesicles. *Proc. R. Soc. Lond. B Biol. Sci.* **223**, 177–196 (1984).

36. Walsby, A. E. & Fogg, G. E. The pressure relationships of gas vacuoles. *Proc. R. Soc. Lond. B Biol. Sci.* **178**, 301–326 (1997).

37. Walsby, A. E. The properties and buoyancy-providing role of gas vacuoles in Trichodesmium Ehrenberg. *Br. Phycol. J.* **13**, 103–116 (1978).

38. Hayes, P. K. & Walsby, A. E. The inverse correlation between width and strength of gas vesicles in cyanobacteria. *Br. Phycol. J.* **21**, 191–197 (1986).

39. Windenburg, D. F. & Trilling, C. Collapse by Instability of Thin Cylindrical Shells Under External Pressure. *J. Fluids Eng.* **56**, 819–825 (1934).

40. Walsby, A. E. The Gas Vesicles and Buoyancy of Trichodesmium. in *Marine Pelagic Cyanobacteria: Trichodesmium and other Diazotrophs* (eds. Carpenter, E. J., Capone, D. G. & Rueter, J. G.) 141–161 (Springer Netherlands, Dordrecht, 1992). doi:10.1007/978-94-015-7977-3_9.

41. Konopka, A. E., Staley, J. T. & Lara, J. C. Gas vesicle assembly in Microcyclus aquaticus. *J. Bacteriol.* **122**, 1301 (1975).

42. Gantt, E., Ohki, K. & Fujita, Y. Trichodesmium thiebautii; structure of a nitrogen-fixing marine blue-green alga (Cyanophyta). *Protoplasma* **119**, 188–196 (1984).

43. Walsby, A. E., Van Rijn, J., Cohen, Y. & Fogg, G. E. The biology of a new gas-vacuolate cyanobacterium, Dactylococcopsis salina sp. nov., in Solar Lake. *Proc. R. Soc. Lond. B Biol. Sci.* **217**, 417–447 (1997).

44. Walsby, A. E. & Buckland, B. Isolation and Purification of Intact Gas Vesicles from a Blue–Green Alga. *Nature* **224**, 716–717 (1969).

45. Jones, D. D. & Jost, M. Isolation and chemical characterization of gas-vacuole membranes fromMicrocystis aeruginosa Kuetz. emend. Elenkin. *Arch. Für Mikrobiol.* **70**, 43–64 (1970).

46. Hayes, P. K. & Powell, R. S. ThegvpA/C cluster ofAnabaena flos-aquae has multiple copies of a gene encoding GvpA. *Arch. Microbiol.* **164**, 50–57 (1995).

47. Pfeifer, F. Recent Advances in the Study of Gas Vesicle Proteins and Application of Gas Vesicles in Biomedical Research. *Life* **12**, 1455 (2022).

48. Offner, S., Hofacker, A., Wanner, G. & Pfeifer, F. Eight of Fourteen gvp Genes Are Sufficient for Formation of Gas Vesicles in Halophilic Archaea. *J. Bacteriol.* **182**, 4328–4336 (2000).

49. Monson, R. E., Tashiro, Y. & Salmond, G. P. C. Overproduction of individual gas vesicle proteins perturbs flotation, antibiotic production and cell division in the enterobacterium Serratia sp. ATCC 39006. *Microbiology* **162**, 1595–1607 (2016).

50. Huber, S. T. & Jakobi, A. J. Structural biology of microbial gas vesicles: historical milestones and current knowledge. *Biochem. Soc. Trans.* **52**, 205–215 (2024).

51. Buchholz, B. E. E., Hayes, P. k. & Walsby, A. E. The distribution of the outer gas vesicle protein, GvpC, on the Anabaena gas vesicle, and its ratio to GvpA. *Microbiology* **139**, 2353–2363 (1993).

52. Huber, S. T., Terwiel, D., Evers, W. H., Maresca, D. & Jakobi, A. J. Cryo-EM structure of gas vesicles for buoyancy-controlled motility. *Cell* **186**, 975-986.e13 (2023).

53. Beard, S. J., Hayes, P. K., Pfeifer, F. & Walsby, A. E. The sequence of the major gas vesicle protein, GvpA, influences the width and strength of halobacterial gas vesicles. *FEMS Microbiol. Lett.* **213**, 149–157 (2002).

54. Dunton, P. G., Mawby, W. J., Shaw, V. A. & Walsby, A. E. Analysis of tryptic digests indicates regions of GvpC that bind to gas vesicles of Anabaena flos-aquae. *Microbiol. Read. Engl.* **152**, 1661–1669 (2006).

55. Hayes, P. K., Buchholz, B. & Walsby, A. E. Gas vesicles are strengthened by the outer-surface protein, GvpC. *Arch. Microbiol.* **157**, 229–234 (1992).

56. Kinsman, R., Walsby, A. e. & Hayes, P. k. GvpCs with reduced numbers of repeating sequence elements bind to and strengthen cyanobacterial gas vesicles. *Mol. Microbiol.* **17**, 147–154 (1995).

57. Völkner, K., Jost, A. & Pfeifer, F. Accessory Gvp Proteins Form a Complex During Gas Vesicle Formation of Haloarchaea. *Front. Microbiol.* **11**, (2020).

58. Vasilikis, D. & Karamanos, S. A. Mechanics of Confined Thin-Walled Cylinders Subjected to External Pressure. *Appl. Mech. Rev.* **66**, (2013).

59. gvpC - Gas vesicle protein C - Dolichospermum flosaquae (Anabaena flos-aquae) | UniProtKB | UniProt. https://www.uniprot.org/uniprotkb/P09413/entry.

60. Jost, A. & Pfeifer, F. Interaction of the gas vesicle proteins GvpA, GvpC, GvpN, and GvpO of Halobacterium salinarum. *Front. Microbiol.* **13**, (2022).

61. Zimmermann, P. & Pfeifer, F. Regulation of the expression of gas vesicle genes in Haloferax mediterranei: interaction of the two regulatory proteins GvpD and GvpE. *Mol. Microbiol.* **49**, 783–794 (2003).

62. Cai, K. *et al.* The model cyanobacteria Anabaena sp. PCC 7120 possess an intact but partially degenerated gene cluster encoding gas vesicles. *BMC Microbiol.* **20**, 110 (2020).

63. Ling, B. *et al.* Truly Tiny Acoustic Biomolecules for Ultrasound Imaging and Therapy. *Adv. Mater.* **36**, 2307106 (2024).

64. Li, Z. *et al.* Phase transition of GvpU regulates gas vesicle clustering in bacteria. *Nat. Microbiol.* **9**, 1021–1035 (2024).

65. Salahshoor, H. *et al.* Geometric effects in gas vesicle buckling under ultrasound. *Biophys. J.* **121**, 4221–4228 (2022).

66. Iburg, M. *et al.* Elucidating the assembly of gas vesicles by systematic protein-protein interaction analysis. *EMBO J.* **43**, 4156 (2024).

67. Shapiro, M. G. *et al.* Genetically encoded reporters for hyperpolarized xenon magnetic resonance imaging. *Nat. Chem.* **6**, 629–634 (2014).

68. Walsby, A. E. & Fogg, G. E. The permeability of blue-green algal gas-vacuole membranes to gas. *Proc. R. Soc. Lond. B Biol. Sci.* **173**, 235–255 (1997).

69. Walsby, A. E. Permeability of Gas Vesicles to Perfluorocyclobutane. *Microbiology* **128**, 1679–1684 (1982).

70. Jaffer, F. A. & Weissleder, R. Molecular imaging in the clinical arena. *JAMA* **293**, 855–862 (2005).

71. Pysz, M. A., Gambhir, S. S. & Willmann, J. K. Molecular imaging: current status and emerging strategies. *Clin. Radiol.* **65**, 500–516 (2010).

72. Tsien, R. Y. Imagining imaging's future. *Nat. Rev. Mol. Cell Biol.* **Suppl**, SS16-21 (2003).

73. Demené, C. *et al.* Transcranial ultrafast ultrasound localization microscopy of brain vasculature in patients. *Nat. Biomed. Eng.* **5**, 219–228 (2021).

74. Shapiro, M. G., Atanasijevic, T., Faas, H., Westmeyer, G. G. & Jasanoff, A. Dynamic imaging with MRI contrast agents: quantitative considerations. *Magn. Reson. Imaging* **24**, 449–462 (2006).

75. Gilad, A. A., Winnard, P. T., van Zijl, P. C. M. & Bulte, J. W. M. Developing MR reporter genes: promises and pitfalls. *NMR Biomed.* **20**, 275–290 (2007).

76. Shapiro, M. G. *et al.* Biogenic gas nanostructures as ultrasonic molecular reporters. *Nat. Nanotechnol.* **9**, 311–316 (2014).

77. Appendix A: Typical Acoustic Properties of Tissues. in *Basics of Biomedical Ultrasound for Engineers* 313–314 (John Wiley & Sons, Ltd, 2010). doi:10.1002/9780470561478.app1.

78. Aldrich, J. E. Basic physics of ultrasound imaging. *Crit. Care Med.* **35**, S131 (2007).

79. Singh, A., Gopalakrishnan, P. H. & Panicker, M. R. Ultrasound based Gas Detection: Analyzing Acoustic Impedance for High-Performance and Low-Cost Solutions. *2023 16th Int. Conf. Sens. Technol. ICST* 1–5 (2023) doi:10.1109/ICST59744.2023.10460790.

80. Maresca, D. *et al.* Nonlinear ultrasound imaging of nanoscale acoustic biomolecules. *Appl Phys Lett* (2017).

81. Lakshmanan, A. *et al.* Molecular Engineering of Acoustic Protein Nanostructures. *ACS Nano* **10**, 7314–7322 (2016).

82. Hurt, R. C. *et al.* Genomically mined acoustic reporter genes for real-time in vivo monitoring of tumors and tumor-homing bacteria. *Nat. Biotechnol.* 1–13 (2023) doi:10.1038/s41587-022-01581-y.

83. Sawyer, D. P. *et al.* Ultrasensitive ultrasound imaging of gene expression with signal unmixing. *Nat. Methods* **18**, 945–952 (2021).

84. Burns, P. N. Harmonic imaging with ultrasound contrast agents. *Clin. Radiol.* **51 Suppl 1**, 50–55 (1996).

85. de Jong, N., Bouakaz, A. & Frinking, P. Basic acoustic properties of microbubbles. *Echocardiogr. Mt. Kisco N* **19**, 229–240 (2002).

86. Maresca, D., Sawyer, D. P., Renaud, G., Lee-Gosselin, A. & Shapiro, M. G. Nonlinear X-Wave Ultrasound Imaging of Acoustic Biomolecules. *Phys. Rev. X* **8**, 041002 (2018).

87. Wu, J. & Tong, J. Measurements of the nonlinearity parameter B A of contrast agents. *Ultrasound Med. Biol.* **24**, 153–159 (1998).

88. Nayak, R. *et al.* Harmonic imaging for nonlinear detection of acoustic biomolecules. *bioRxiv* 2024.06.18.599141 (2024) doi:10.1101/2024.06.18.599141.

89. Zhang, G. *et al.* Amplitude-Modulated Singular Value Decomposition for Ultrafast Ultrasound Imaging of Gas Vesicles. *IEEE Trans. Med. Imaging* **PP**, (2025).

90. Dunton, P. G. & Walsby, A. E. The diameter and critical collapse pressure of gas vesicles in Microcystis are correlated with GvpCs of different length. *FEMS Microbiol. Lett.* **247**, 37–43 (2005).

91. Bourdeau, R. W. *et al.* Acoustic reporter genes for noninvasive imaging of microorganisms in mammalian hosts. *Nature* **553**, 86–90 (2018).

92. Hurt, R. C. *et al.* Directed Evolution of Acoustic Reporter Genes Using High-Throughput Acoustic Screening. *ACS Synth. Biol.* **13**, 2215–2226 (2024).

93. Kim, S., Zhang, S. & Yoon, S. Multiplexed Ultrasound Imaging Using Spectral Analysis on Gas Vesicles. *Adv. Healthc. Mater.* **11**, 2200568 (2022).

94. Lakshmanan, A. *et al.* Acoustic biosensors for ultrasound imaging of enzyme activity. *Nat. Chem. Biol.* **16**, 988–996 (2020).

95. Terwiel, D. *et al.* Acoustic pH sensor for dynamic ultrasound imaging of cellular acidification. 2025.01.24.634762 Preprint at https://doi.org/10.1101/2025.01.24.634762 (2025).

96. Szymczak, A. L. & Vignali, D. A. A. Development of 2A peptide-based strategies in the design of multicistronic vectors. *Expert Opin. Biol. Ther.* **5**, 627–638 (2005).

97. Farhadi, A., Ho, G. H., Sawyer, D. P., Bourdeau, R. W. & Shapiro, M. G. Ultrasound imaging of gene expression in mammalian cells. *Science* **365**, 1469–1475 (2019).

98. Mizushima, R. *et al.* Multiplexed 129Xe HyperCEST MRI Detection of Genetically Reconstituted Bacterial Protein Nanoparticles in Human Cancer Cells. *Contrast Media Mol. Imaging* **2020**, 5425934 (2020).

99. Howells, A. R. *et al.* A drug-selectable acoustic reporter gene system for human cell ultrasound imaging. *Bioeng. Transl. Med.* **9**, e10584 (2023).

100. Fournier, L., de La Taille, T. & Chauvierre, C. Microbubbles for human diagnosis and therapy. *Biomaterials* **294**, 122025 (2023).

101. Errico, C. *et al.* Ultrafast ultrasound localization microscopy for deep super-resolution vascular imaging. *Nature* **527**, 499–502 (2015).

102. Tanter, M. & Fink, M. Ultrafast imaging in biomedical ultrasound. *IEEE Trans. Ultrason. Ferroelectr. Freq. Control* **61**, 102–119 (2014).

103. Wang, G. *et al.* Surface-modified GVs as nanosized contrast agents for molecular ultrasound imaging of tumor. *Biomaterials* **236**, 119803 (2020).

104. Le Floc'h, J. *et al.* In vivo Biodistribution of Radiolabeled Acoustic Protein Nanostructures. *Mol. Imaging Biol.* **20**, 230–239 (2018).

105. Nittayacharn, P. *et al.* Efficient ultrasound-mediated drug delivery to orthotopic liver tumors – Direct comparison of doxorubicin-loaded nanobubbles and microbubbles. *J. Control. Release Off. J. Control. Release Soc.* **367**, 135–147 (2024).

106. Hou, X. *et al.* Nanobubble-actuated ultrasound neuromodulation for selectively shaping behavior in mice. *Nat. Commun.* **15**, 2253 (2024).

107. Maresca, D. *et al.* Acoustic biomolecules enhance hemodynamic functional ultrasound imaging of neural activity. *NeuroImage* **209**, 116467 (2020).

108. Pian, Q. *et al.* Multimodal Biomedical Optical Imaging Review: Towards Comprehensive Investigation of Biological Tissues. *Curr. Mol. Imaging* **3**, 72–87 (2014).

109. Brindle, K. M. Gene reporters for magnetic resonance imaging. *Trends Genet.* **38**, 996–998 (2022).

110. Pines, A. Molecular Imaging using a Targeted Magnetic Resonance Hyperpolarized Biosensor. *Science* **314**, (2006).

111. Recombinantly expressed gas vesicles as nanoscale contrast agents for ultrasound and hyperpolarized MRI - Farhadi - 2018 - AIChE Journal - Wiley Online Library. https://aiche.onlinelibrary.wiley.com/doi/epdf/10.1002/aic.16138.

112. Stuart, E. S., Morshed, F., Sremac, M. & DasSarma, S. Antigen presentation using novel particulate organelles from halophilic archaea. *J. Biotechnol.* **88**, 119–128 (2001).

113. Adamiak, N., Krawczyk, K. T., Locht, C. & Kowalewicz-Kulbat, M. Archaeosomes and Gas Vesicles as Tools for Vaccine Development. *Front. Immunol.* **12**, 746235 (2021).

114. Hill, A. M. & Salmond, G. P. C. Microbial gas vesicles as nanotechnology tools: exploiting intracellular organelles for translational utility in biotechnology, medicine and the environment. *Microbiology* **166**, 501–509 (2020).

115. Stuart, E. S., Morshed, F., Sremac, M. & DasSarma, S. Cassette-based presentation of SIV epitopes with recombinant gas vesicles from halophilic archaea. *J. Biotechnol.* **114**, 225–237 (2004).

116. DasSarma, P. *et al.* Haloarchaeal gas vesicle nanoparticles displaying Salmonella antigens as a novel approach to vaccine development. *Procedia Vaccinol.* **9**, 16–23 (2015).

117. Childs, T. S. & Webley, W. C. In vitro assessment of halobacterial gas vesicles as a *Chlamydia* vaccine display and delivery system. *Vaccine* **30**, 5942–5948 (2012).

118. Dutta, S., DasSarma, P., DasSarma, S. & Jarori, G. K. Immunogenicity and protective potential of a Plasmodium spp. enolase peptide displayed on archaeal gas vesicle nanoparticles. *Malar. J.* **14**, 406 (2015).

119. DasSarma, S. & DasSarma, P. Gas Vesicle Nanoparticles for Antigen Display. *Vaccines* **3**, 686–702 (2015).

120. DasSarma, S. *et al.* An improved genetic system for bioengineering buoyant gas vesicle nanoparticles from Haloarchaea. *BMC Biotechnol.* **13**, 112 (2013).

121. Mestas, J. & Hughes, C. C. W. Of Mice and Not Men: Differences between Mouse and Human Immunology. *J. Immunol.* **172**, 2731–2738 (2004).

122. Louisnard, O. & González-García, J. Acoustic Cavitation. in *Ultrasound Technologies for Food and Bioprocessing* (eds. Feng, H., Barbosa-Canovas, G. & Weiss, J.) 13–64 (Springer, New York, NY, 2011). doi:10.1007/978-1-4419-7472-3_2.

123. Ashokkumar, M., Lee, J., Kentish, S. & Grieser, F. Bubbles in an acoustic field: An overview. *Ultrason. Sonochem.* **14**, 470–475 (2007).

124. Wu, J. & Nyborg, W. L. Ultrasound, cavitation bubbles and their interaction with cells. *Adv. Drug Deliv. Rev.* **60**, 1103–1116 (2008).

125. Aryal, M., Arvanitis, C. D., Alexander, P. M. & McDannold, N. Ultrasound-mediated blood-brain barrier disruption for targeted drug delivery in the central nervous system. *Adv. Drug Deliv. Rev.* **0**, 94–109 (2014).

126. Bar-Zion, A. *et al.* Acoustically triggered mechanotherapy using genetically encoded gas vesicles. *Nat. Nanotechnol.* **16**, 1403–1412 (2021).

127. Tayier, B. *et al.* Biosynthetic nanobubbles for targeted gene delivery by focused ultrasound. *Nanoscale* **11**, 14757–14768 (2019).

128. Xie, L., Wang, J., Song, L., Jiang, T. & Yan, F. Cell-cycle dependent nuclear gene delivery enhances the effects of E-cadherin against tumor invasion and metastasis. *Signal Transduct. Target. Ther.* **8**, 1–16 (2023).

129. Zhang, J. *et al*. Biosynthetic Gas Vesicles Combined with Focused Ultrasound for Blood–Brain Barrier Opening. *Int. J. Nanomedicine* **17**, 6759–6772 (2022).

130. Wood, A. K. W. & Sehgal, C. M. A Review of Low-Intensity Ultrasound for Cancer Therapy. *Ultrasound Med. Biol.* **41**, 905–928 (2015).

131. Costley, D. *et al*. Treating cancer with sonodynamic therapy: A review. *Int. J. Hyperthermia* **31**, 107–117 (2015).

132. Song, L. *et al*. Gas-filled protein nanostructures as cavitation nuclei for molecule-specific sonodynamic therapy. *Acta Biomater.* **136**, 533–545 (2021).

133. Blackmore, J., Shrivastava, S., Sallet, J., Butler, C. R. & Cleveland, R. O. Ultrasound Neuromodulation: A Review of Results, Mechanisms and Safety. *Ultrasound Med. Biol.* **45**, 1509–1536 (2019).

134. Li, G. *et al*. Noninvasive Ultrasonic Neuromodulation in Freely Moving Mice. *IEEE Trans. Biomed. Eng.* **66**, 217–224 (2019).

135. Yoo, S.-S. *et al*. Focused ultrasound modulates region-specific brain activity. *NeuroImage* **56**, 1267–1275 (2011).

136. Lee, W. *et al*. Image-Guided Focused Ultrasound-Mediated Regional Brain Stimulation in Sheep. *Ultrasound Med. Biol.* **42**, 459–470 (2016).

137. Verhagen, L. *et al*. Offline impact of transcranial focused ultrasound on cortical activation in primates. *eLife* **8**, e40541 (2019).

138. Beisteiner, R. *et al*. Transcranial Pulse Stimulation with Ultrasound in Alzheimer's Disease-A New Navigated Focal Brain Therapy. *Adv. Sci. Weinh. Baden-Wurtt. Ger.* **7**, 1902583 (2020).

139. Fan, C.-H. *et al*. Sonogenetic-Based Neuromodulation for the Amelioration of Parkinson's Disease. *Nano Lett.* **21**, 5967–5976 (2021).

140. Tsai, S.-J. Transcranial focused ultrasound as a possible treatment for major depression. *Med. Hypotheses* **84**, 381–383 (2015).

141. Ye, P. P., Brown, J. R. & Pauly, K. B. Frequency Dependence of Ultrasound Neurostimulation in the Mouse Brain. *Ultrasound Med. Biol.* **42**, 1512–1530 (2016).

142. Hou, X. *et al.* Precise Ultrasound Neuromodulation in a Deep Brain Region Using Nano Gas Vesicles as Actuators. *Adv. Sci. Weinh. Baden-Wurtt. Ger.* **8**, e2101934 (2021).

143. Yoo, S., Mittelstein, D. R., Hurt, R. C., Lacroix, J. & Shapiro, M. G. Focused ultrasound excites cortical neurons via mechanosensitive calcium accumulation and ion channel amplification. *Nat. Commun.* **13**, 493 (2022).

144. Pouzet, S. *et al.* Optogenetic control of beta-carotene bioproduction in yeast across multiple lab-scales. *Front. Bioeng. Biotechnol.* **11**, (2023).

145. Le Bec, M. *et al.* Optogenetic spatial patterning of cooperation in yeast populations. *Nat. Commun.* **15**, 75 (2024).

146. Lugagne, J.-B. *et al.* Balancing a genetic toggle switch by real-time feedback control and periodic forcing. *Nat. Commun.* **8**, 1671 (2017).

147. Milunov, D. External real time control of E.coli range expansion. (Université Paris Cité, 2023).

148. Windels, E. M. *et al.* Enrichment of persisters enabled by a ß-lactam-induced filamentation method reveals their stochastic single-cell awakening. *Commun. Biol.* **2**, 426 (2019).

149. Miermont, A. *et al.* Severe osmotic compression triggers a slowdown of intracellular signaling, which can be explained by molecular crowding. *Proc. Natl. Acad. Sci.* **110**, 5725–5730 (2013).

150. Din, M. O. *et al.* Synchronized cycles of bacterial lysis for in vivo delivery. *Nature* **536**, 81–85 (2016).

151. Sieow, B. F.-L., Wun, K. S., Yong, W. P., Hwang, I. Y. & Chang, M. W. Tweak to Treat: Reprograming Bacteria for Cancer Treatment. *Trends Cancer* **7**, 447–464 (2021).

152. Liang, S. *et al.* Recent advances in bacteria-mediated cancer therapy. *Front. Bioeng. Biotechnol.* **10**, (2022).

153. Zanoni, M. *et al.* 3D tumor spheroid models for in vitro therapeutic screening: a systematic approach to enhance the biological relevance of data obtained. *Sci. Rep.* **6**, 19103 (2016).

154. Breslin, S. & O'Driscoll, L. The relevance of using 3D cell cultures, in addition to 2D monolayer cultures, when evaluating breast cancer drug sensitivity and resistance. *Oncotarget* **7**, 45745–45756 (2016).

155. Friedrich, J., Seidel, C., Ebner, R. & Kunz-Schughart, L. A. Spheroid-based drug screen: considerations and practical approach. *Nat. Protoc.* **4**, 309–324 (2009).

156. Harimoto, T. *et al.* Rapid screening of engineered microbial therapies in a 3D multicellular model. *Proc. Natl. Acad. Sci.* **116**, 9002–9007 (2019).

157. Zhang, Y. *et al.* Escherichia coli Nissle 1917 Targets and Restrains Mouse B16 Melanoma and 4T1 Breast Tumors through Expression of Azurin Protein. *Appl. Environ. Microbiol.* **78**, 7603–7610 (2012).

158. He, L. *et al.* Intestinal probiotics E. coli Nissle 1917 as a targeted vehicle for delivery of p53 and Tum-5 to solid tumors for cancer therapy. *J. Biol. Eng.* **13**, 58 (2019).

159. He, L. *et al.* Escherichia coli Nissle 1917 engineered to express Tum-5 can restrain murine melanoma growth. *Oncotarget* **8**, 85772–85782 (2017).

160. Elsinghorst, E. A. Measurement of invasion by gentamicin resistance. in *Methods in Enzymology* vol. 236 405–420 (Academic Press, 1994).

161. Spalteholz, W. *Über Das Durchsichtigmachen von Menschlichen Und Tierischen Präparaten Und Seine Theoretischen Bedingungen, Nebst Anhang: Über Knochenfärbung*. (S. Hirzel, Leipzig, 1914).

162. Richardson, D. S. & Lichtman, J. W. Clarifying Tissue Clearing. *Cell* **162**, 246–257 (2015).

163. Richardson, D. S. *et al*. Tissue clearing. *Nat. Rev. Methods Primer* **1**, 84 (2021).

164. Mai, H. & Lu, D. Tissue clearing and its applications in human tissues: A review. *VIEW* **5**, 20230046 (2024).

165. Revokatova, D. P., Koteneva, P. I., Kosheleva, N. V., Shpichka, A. I. & Timashev, P. S. Spheroids from Epithelial and Mesenchymal Cell Phenotypes as Building Blocks in Bioprinting (Review). *Mod. Technol. Med*. **17**, 133–154 (2025).

166. Peleg, M. A New Look at Models of the Combined Effect of Temperature, pH, Water Activity, or Other Factors on Microbial Growth Rate. *Food Eng. Rev.* **14**, 31–44 (2022).

167. Davey, K. R. Modelling the combined effect of temperature and pH on the rate coefficient for bacterial growth. *Int. J. Food Microbiol.* **23**, 295–303 (1994).

168. Danino, T., Mondragón-Palomino, O., Tsimring, L. & Hasty, J. A synchronized quorum of genetic clocks. *Nature* **463**, 326–330 (2010).

169. Gómez-Gaviro, M. V., Sanderson, D., Ripoll, J. & Desco, M. Biomedical Applications of Tissue Clearing and Three-Dimensional Imaging in Health and Disease. *iScience* **23**, (2020).

170. Jost, A., Knitsch, R., Völkner, K. & Pfeifer, F. Effect of Mutations in GvpJ and GvpM on Gas Vesicle Formation of Halobacterium salinarum. *Front. Microbiol.* **12**, (2021).

171. Zakeri, B. *et al*. Peptide tag forming a rapid covalent bond to a protein, through engineering a bacterial adhesin. *Proc. Natl. Acad. Sci. U. S. A.* **109**, E690-697 (2012).

172. Adams, S. R. *et al.* New Biarsenical Ligands and Tetracysteine Motifs for Protein Labeling in Vitro and in Vivo: Synthesis and Biological Applications. *J. Am. Chem. Soc.* **124**, 6063–6076 (2002).

173. Schrunk, E., Dutka, P., Hurt, R. C., Wu, D. & Shapiro, M. G. Bioorthogonal Labeling Enables In Situ Fluorescence Imaging of Expressed Gas Vesicle Nanostructures. *Bioconjug. Chem.* **35**, 333–339 (2024).

174. Lelek, M. *et al.* Superresolution imaging of HIV in infected cells with FlAsH-PALM. *Proc. Natl. Acad. Sci.* **109**, 8564–8569 (2012).

175. Henriques, R., Griffiths, C., Hesper Rego, E. & Mhlanga, M. M. PALM and STORM: Unlocking live-cell super-resolution. *Biopolymers* **95**, 322–331 (2011).

176. Ignatova, Z. & Gierasch, L. M. Monitoring protein stability and aggregation in vivo by real-time fluorescent labeling. *Proc. Natl. Acad. Sci. U. S. A.* **101**, 523–528 (2004).

177. Lelek, M. *et al.* Single-molecule localization microscopy. *Nat. Rev. Methods Primer* **1**, 39 (2021).

178. Patterson, G. H. & Lippincott-Schwartz, J. A photoactivatable GFP for selective photolabeling of proteins and cells. *Science* **297**, 1873–1877 (2002).

179. McKinney, S. A., Murphy, C. S., Hazelwood, K. L., Davidson, M. W. & Looger, L. L. A bright and photostable photoconvertible fluorescent protein. *Nat. Methods* **6**, 131–133 (2009).

180. Lu, Y. Cell-free synthetic biology: Engineering in an open world. *Synth. Syst. Biotechnol.* **2**, 23–27 (2017).

181. Ho, C. L. *et al.* Engineered commensal microbes for diet-mediated colorectal-cancer chemoprevention. *Nat. Biomed. Eng.* **2**, 27–37 (2018).

182. Yoon, W. *et al.* Application of genetically engineered *Salmonella typhimurium* for interferon-gamma–induced therapy against melanoma. *Eur. J. Cancer* **70**, 48–61 (2017).

183. Chen, T. *et al*. Triptolide modulates tumour-colonisation and anti-tumour effect of attenuated Salmonella encoding DNase I. *Appl. Microbiol. Biotechnol.* **103**, 929–939 (2019).

184. Kitagawa, K. *et al*. Development of oral cancer vaccine using recombinant Bifidobacterium displaying Wilms' tumor 1 protein. *Cancer Immunol. Immunother.* **66**, 787–798 (2017).

185. Wei, C. *et al*. Bifidobacteria Expressing Tumstatin Protein for Antitumor Therapy in Tumor-Bearing Mice. *Technol. Cancer Res. Treat.* **15**, 498–508 (2016).

186. Liu, S.-C. *et al*. Optimized Clostridium-Directed Enzyme Prodrug Therapy Improves the Antitumor Activity of the Novel DNA Cross-Linking Agent PR-104. *Cancer Res.* **68**, 7995–8003 (2008).

187. Gunn, G. R. *et al*. Two Listeria monocytogenes Vaccine Vectors That Express Different Molecular Forms of Human Papilloma Virus-16 (HPV-16) E7 Induce Qualitatively Different T Cell Immunity That Correlates with Their Ability to Induce Regression of Established Tumors Immortalized by HPV-161. *J. Immunol.* **167**, 6471–6479 (2001).

188. Liu, Y. *et al*. Intravenous Delivery of Living Listeria monocytogenes Elicits Gasdermin-Dependent Tumor Pyroptosis and Motivates Anti-Tumor Immune Response. *ACS Nano* **16**, 4102–4115 (2022).

189. Mao, L. *et al*. Natural Enzyme-Loaded Polymeric Stealth Coating-Armed Engineered Probiotics by Disrupting Tumor Lactate Homeostasis to Synergistic Metabolism-Immuno-Enzyme Dynamic Therapy. *Adv. Sci.* **12**, 2417172 (2025).

190. Qiu, X., Zou, Z., Lin, T., Guo, C. & Lin, D. Engineered Lactobacillus rhamnosus Producing 3-Hydroxybutyrate: A Dual-Action Therapeutic Strategy for Colon Cancer Cachexia. *Biotechnol. Bioeng.* **122**, 1574–1589 (2025).

Appendixes

Appendix 1 : Phylogenic tree of gas vesicles producing organisms

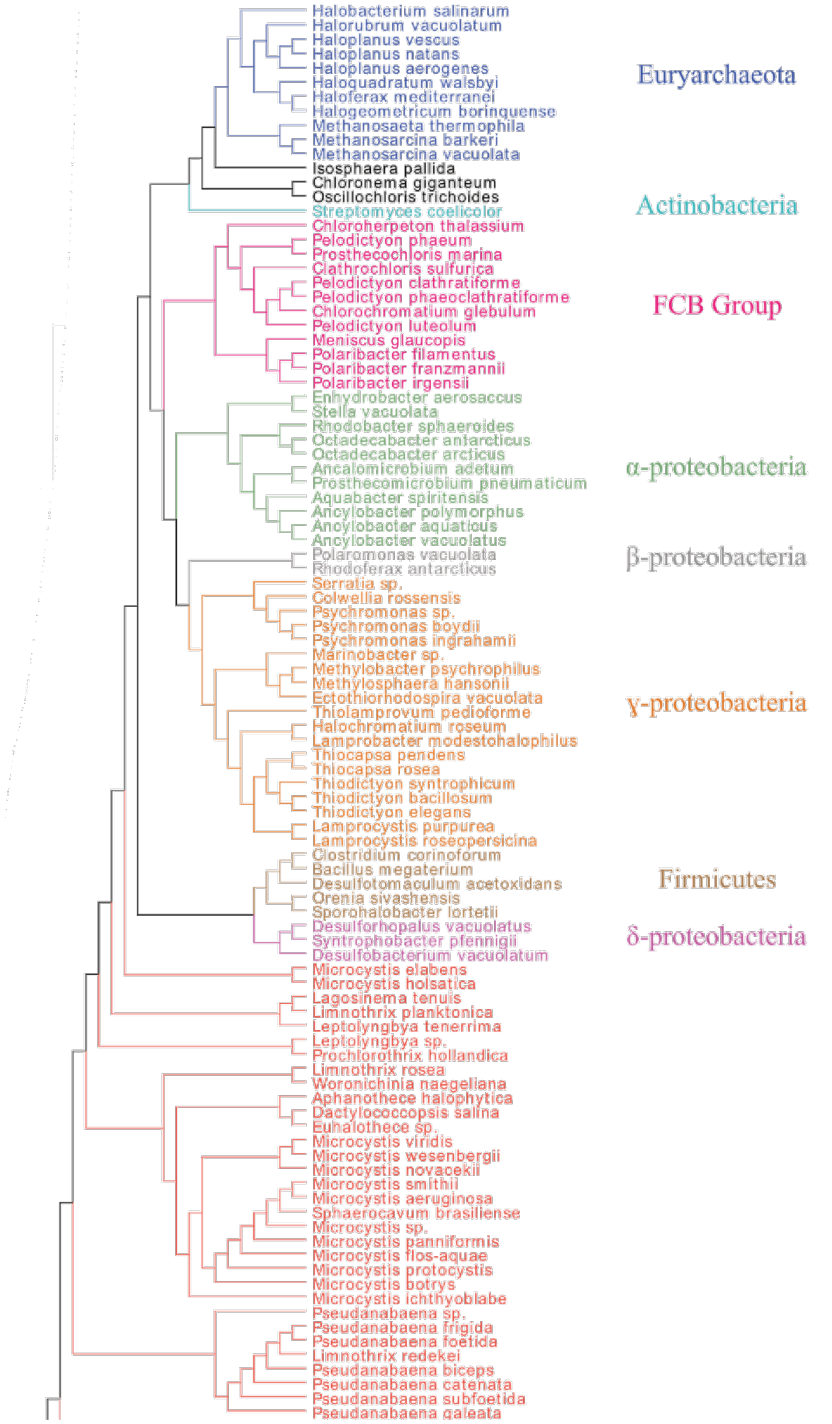

16S phylogenic tree of all known 253 gas vesicles producing organisms (as of 2024), with color indicating different phyla. From Hurt, R. C. *et al.* 2024[18]

Appendix 2 : Modeling gas vesicles efficiency, from Walsby et al[33] :

$$V = \pi r^2 (l + \frac{1}{3} h)$$

$$Vw = \pi \left[l\,(2\,r\,t - t^2) + \left(\frac{2}{3}\right)\left\{ r^2 h - \left(r - \frac{t}{\sin(\alpha)}\right)^2 \left(h - \frac{t}{\sin(\beta)}\right)\right\}\right]$$

$$Vi = V - Vw$$

$$Ratio = Vi/Vw$$

Where *V* represents the total volume of a gas vesicle, *r* is the radius of its cylindrical portion, and *l* is the length of the cylindrical segment. The parameter *h* denotes the height of the conical end caps, which is assumed to be constant across species, with a mean value of 52.8 nm based on measurements from gas vesicles of *Anabaena flos-aquae*. The volume of the vesicle walls is represented by *Vw*, while *t* corresponds to the wall thickness, which is assumed to be equivalent to the thickness of a single GvpA protein, measured at 1.90 nm. The end angle of the conical caps, β, is defined by the equation $2\beta = 2\tan^{-1}(r/h)$, whereas α represents the complementary base angle, given by $\alpha = \tan^{-1}(h/r)$. Finally, *Vi* denotes the internal volume of the vesicle, which corresponds to the volume occupied by gas.

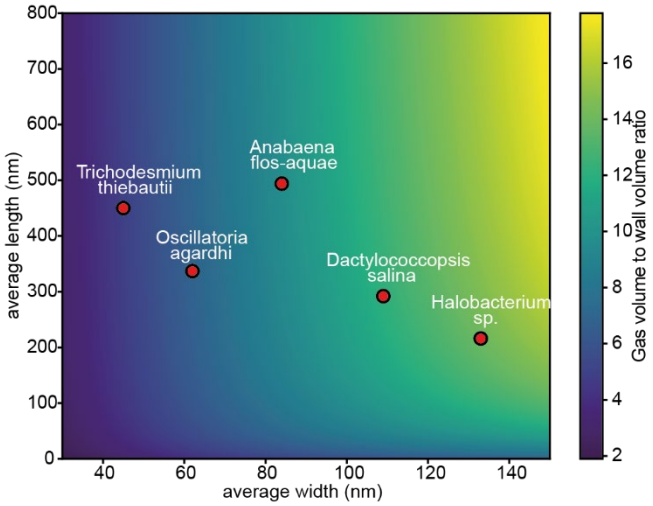

Cost-efficiency of gas vesicles in function of their dimensions, as modeled by Walsby et al.[33] Example species from Table 1 are located as red dots.

Appendix 3 : Supplementary materials from “Heterologous production of Gas Vesicles imposes stress and reduces growth in Escherichia coli in batch culture and microcolonies”

Heterologous production of Gas Vesicles imposes stress and reduces growth in Escherichia coli in batch culture and microcolonies – Supplementary materials

Simon Barral[1], Chloé Sasson[2], Céline Cordier[1], Jessica Riou-Ramon[1], Benoit Sorre[1], Karine Guevorkian[1], Mickael Tanter[3], Jérôme Bonnet[2] , Pascal Hersen*,[1].

[1] *Physics of Cells and Cancer CNRS UMR168, Sorbonne Université, Institut Curie, 11 Rue Pierre et Marie Curie, 75005 Paris, France*.
[2] *Centre de Biologie Structurale CNRS UMR5048 and INSERM* U1054*, University of Montpellier,* 29 Rue de Navacelles, 34090 Montpellier, *France*.
[3]*Physics for Medicine Paris UMR8063, ESPCI Paris, Paris Science Lettres University (PSL), CNRS, 2-10 rue d'Oradour-sur-Glane, 75015 Paris, France*.

[†] *denotes equal contributions*.
* *Correspondence and requests for materials should be addressed to Pascal Hersen (pascal.hersen@curie.fr).*

Strain construction

Background strain

All experiments were made on an E.coli K12 BW25113 ΔfliA strain from Keio collection[1], on which the the kanamycin resistance that was inserted in place of the fliA gene have been removed in previous work[2]. This strain has a deletion of fliA gene preventing it from having any chemotaxis and has the Δ(araD-araB)567 mutation preventing it from degrading arabinose. It will be referred as bPH_103 in this work.

Chemocompetent cells preparation

Chemocompetent bPH_103 cells were prepared using the following protocol. Two days prior to the procedure, colonies of frozen competent cells were streaked onto an LB agar plate without antibiotics and incubated overnight at 37°C. The day before the main experiment, a single colony was inoculated into 5 mL of LB medium (without antibiotics) and grown overnight at 37°C with shaking at 200–250 rpm. Additionally, a box of 200 µL pipette tips and 50 microcentrifuge tubes were placed in a -80°C freezer to pre-chill.
On the day of the experiment, 500 µL of the overnight culture was transferred into 50 mL of fresh LB medium (no antibiotics) in a sterile Erlenmeyer flask. The culture was incubated at 37°C with shaking until it reached an optical density (OD600) between 0.40 and 0.45. Once this OD was

achieved, the entire 50 mL culture was transferred to a pre-chilled 50 mL Falcon tube and incubated on ice for 20 minutes.
The culture was centrifuged at 2500 × g for 10 minutes at 0°C. The supernatant was discarded, and the cell pellet was resuspended in 10 mL of ice-cold 100 mM $CaCl_2$ solution by gentle pipetting. From this step onward, all manipulations were performed on ice to maintain cell competency. The resuspended cells were incubated on ice for 1–2 hours, followed by another centrifugation at 2500 × g for 10 minutes at 0°C. The supernatant was again discarded, and the pellet was resuspended in 2.5 mL of ice-cold $CaCl_2$ solution containing 15% (w/w) glycerol.
Finally, 50 μL aliquots of the competent cell suspension were distributed into pre-chilled microcentrifuge tubes, which were immediately immersed in liquid nitrogen for rapid freezing. Once all tubes were processed, they were transferred to a -80°C freezer for long-term storage.

Plasmids and competent cell transformation

pBAD-bARGSer-AxeTxe plasmid (Addgene #192473) encoding for the GVs production was kindly provided by Sharipo's lab in Caltech. The annotated plasmid map is provided in data/plasmids maps folder. This plasmid will be referred as pPH_576 in this work.

Chemocompetent bPH_103 cells were transformed using a standard heat shock protocol. A frozen aliquot of chemocompetent bPH_103 cells was thawed on ice for 10 minutes. After thawing, 50 ng of plasmid DNA (pPH_576) was added to the tube and gently mixed with a pipette tip. The mixture was incubated on ice for an additional 20 minutes.
Following this incubation, the tube was subjected to a 42°C water bath for 45 seconds to induce heat shock, then immediately returned to ice for 2 minutes. Subsequently, 1 mL of fresh LB Miller medium was added, and the tube was incubated at 37°C with shaking at 270 rpm for 1 hour to allow for recovery and expression of the antibiotic resistance gene.
After recovery, the cells were pelleted by centrifugation at 11,000 × g for 2 minutes and resuspended in 50 μL of LB Miller medium. The resuspended cells were then spread onto an LB agar plate (1%) containing chloramphenicol using sterile glass beads. The plate was incubated at 37°C for 16 hours to allow colony formation.
An isolated colony was selected and inoculated into 5 mL of LB Miller medium supplemented with chloramphenicol. This culture was grown at 37°C with shaking at 270 rpm for 16 hours. The resulting culture was used to prepare glycerol stocks by mixing 500 μL of culture with 500 μL of 50% glycerol solution. The aliquots were then frozen and stored at -80°C for long-term preservation. The resulting strain was named bPH_657.

The pSB4K5-P7-BCD-sfGFP plasmid, used for constitutive production of superfolder GFP (sfGFP), will be referred to as pPH_561 in this study.

Chemocompetent bPH_657 cells were prepared following the previously described protocol. These cells were transformed with the pPH_561 plasmid using the same heat shock procedure as

outlined above. Following transformation, the cells were plated on LB agar containing both chloramphenicol and kanamycin to ensure maintenance of both plasmids within the cells. The resulting strain containing both pPH_576 and pPH_561 was named bPH_669. Similarly, chmocompetent bPH_103 cells were transformed with pPH_561, resulting in strain bPH_670.

The plasmid pBad-sfGFP plasmid (Addgene #85482) can be used to produce GFP upon arabinose induction, using the same promoter as in pPH_635. This plasmid that we named pPH_635, was also inserted into chemocompetent bPH_103 cells, resulting in the bPH_715 strain.

Counting cells and measuring GVs production in batch culture

Culture conditions and sampling

bPH_669 cells from glycerol stocks were streaked onto an LB agar (1%) plate containing chloramphenicol and kanamycin, then incubated at 37°C for 16 hours. Following incubation, an isolated colony was selected and used to inoculate an overnight culture in LB Miller medium supplemented with chloramphenicol and kanamycin. This culture was grown at 37°C with shaking at 270 rpm.
The next morning, a preculture was initiated by inoculating 50 µL of the overnight culture into 5 mL of fresh LB Miller medium containing chloramphenicol and kanamycin. The preculture was grown at 37°C with shaking at 270 rpm for 3 hours. A 100 µL sample of this preculture was collected and stored at 4°C, designated as the time zero (T0) sample for the experiment. Four experimental cultures were then prepared by inoculating 100 µL of the preculture into 5 mL of LB Miller medium containing chloramphenicol, kanamycin, and varying concentrations of arabinose (0%, 0.001%, 0.01%, or 0.1% w/w). These cultures were incubated at 37°C with shaking at 270 rpm for 24 hours.
During the first 8 hours of incubation, 50 µL samples were collected from each culture every 2 hours and stored at 4°C. This entire procedure was repeated three times, with a 24-hour interval between each repetition. For each repetition, cultures were initiated from different colonies originating from the same LB agar plate.

Sample preparation and images capture in bright field microscopy for GVs quantification

Once all samples were collected as described above, they were prepared for assessing the proportion of bacterial populations containing gas vesicle (GV) clusters and for evaluating the size of bright spots observed in bright-field microscopy due to these clusters. Agar pads were prepared for each sample as follows:

A 2% agarose solution in PBS was prepared, autoclaved, and melted prior to use. For pad preparation, a central microscope slide was positioned between two identical slides, each covered

with a layer of electrical tape. A 12 μL drop of the melted PBS-agarose solution was placed onto the central slide. A fourth slide was then gently pressed onto the drop, using the tape-covered slides as guides to apply even pressure. This process flattened the drop, creating an agarose pad with a uniform thickness corresponding to the tape layer. The gel was allowed to cool for 20 seconds before the top slide was removed, and it was then left to dry for 1 minute. Meanwhile, the bacterial sample was thoroughly mixed. For each sample taken after 6 hours of culture, a 10-fold dilution in PBS was performed to ensure isolated cells could be easily segmented during image analysis. A 1 μL drop of this diluted sample was deposited onto the agar pad and allowed to dry for 2 minutes. A coverslip was then gently placed on top of the agar pad and secured to the slide using melted VALAP (a mixture of lanolin, Vaseline, and paraffin). Immediately after preparation, the agar pad was mounted on an Olympus IX83 microscope. The focus was adjusted on the bacteria using a UPlanSApo 100×/1.40 oil objective. Images were captured in both bright-field and GFP fluorescence modes using a Zyla 4.2 sCMOS camera with Metamorph software. For each sample, three images containing at least 26 cells were taken.

Image analysis for GVs quantification

All previously captured images were cropped to retain only the regions unaffected by border artifacts in the GFP channel, where low signal intensity complicates reliable cell segmentation. Bacteria in these images were segmented using TensorFlow with a custom U-Net model trained on GFP images, which outputs segmented cell masks. When necessary, minor corrections to these masks were performed manually in ImageJ to address segmentation errors.
For each segmented cell, the presence and size of GVs clusters were quantified using a custom Python script. Briefly, in each bright-field image, cells were identified using their corresponding segmentation masks. A dynamic threshold was applied within each cell, calculated based on the average background intensity (i.e., non-bacterial regions of the image) multiplied by a constant factor. This adaptive thresholding ensures consistency across different images.
Pixels within the segmented cells that exceeded this threshold were identified and counted as part of the GVs cluster. Concurrently, the total cell surface area, length, and width were also measured. These measurements were repeated for all bacteria in each image, and the mean and standard deviation of all parameters were calculated for each sample. The final reported values represent the mean of three biological replicates for each time point and arabinose concentration.

Sample preparation and image acquisition for counting cells

From the same samples (collected as described in **Culture conditions and sampling**), the number of cells per mL was measured using Helber chamber (Hawksley Z30000).
Prior to cell counting, the engraved chamber was cleaned to remove residual contaminants. The counting area was first rinsed with Milli-Q water using a squeeze bottle, followed by a 70% ethanol wash, and a final rinse with Milli-Q water. To dry the chamber, it was placed on a clean Kimtech tissue, with a second tissue gently pressed onto the counting area. Care was taken not to rub the surface, in order to avoid damaging the etched grid. This drying step was repeated with a fresh

section of tissue until the chamber was completely dry.
A 5 µL drop of the bacterial suspension was carefully pipetted onto the center of the counting area, ensuring that the pipette tip did not make contact with the surface. A clean 22 mm square coverslip was then placed directly on top of the droplet. The liquid spread evenly by capillary action, filling the engraved area and partially extending into the surrounding ring without overflowing it entirely. If liquid extended beyond the ring, this caused unwanted flow across the field of view; such samples were discarded and remounted. Correct loading was confirmed when the coverslip remained firmly in place due to capillary suction, allowing the chamber to be rotated without dislodging the coverslip.
After sample mounting, the loaded chamber was placed on a bright-field microscope equipped with a 20× objective and a 2× optical zoom lens. If the bacterial concentration was too high—evidenced by overlapping cells within the field of view—the sample was diluted 10- or 100-fold in phosphate-buffered saline (PBS) prior to reimaging.
Imaging was performed at four distinct positions within each sample. At each position, *Z*-stacks were acquired in both bright-field and GFP fluorescence channels to capture cells regardless of their axial position. Each *Z*-stack spanned 40 µm in height, using a step size of 2.5 µm, ensuring that all cells within the chamber volume were captured in at least one optical plane.

Image analysis for counting cells

Quantification of cell density was performed by image-based counting within a known chamber volume. The volume of sample above a single engraved square in the counting area is provided by the manufacturer, and the number of squares present in each microscope field of view is predetermined. This allowed direct calculation of the sample volume imaged per field of view, and consequently, the cell density, once the number of cells was known and dilution factors accounted for. Cells can easily be segmented using their GFP signal. This is done using a custom Python script in which, for each *Z*-stack, a maximum intensity projection of the GFP fluorescence channel was generated. Cell segmentation is performed, based on pixel intensity and size thresholding that remains the same for every samples. The number of segmented cells per field was used to compute the cell density in units of bacteria per mL. The final reported value for each sample was obtained by averaging the results from the four *Z*-stacks.

Verifying GVs impact on culture optical density

To verify whether GVs accumulation could impact optical density measurement, we started two cultures, following the same steps as described in ***Culture conditions and sampling*** with bPH_669. In one culture, no arabinose was added. In the other, 0.1% arabinose was added. Both cultures were allowed to grow at 37°C with 225 rpm for 12 hours. After incubation, the number of cells per mL was measured in each sample in Helber chamber, as described in *Sample preparation and image acquisition for counting cells* and *Image analysis for counting cells*. For each sample, 1mL was collected and its cell density was adjusted by adding fresh culture medium to 9E+07 bacteria/ml at room temperature. 200 µl of each adjusted sample were added to wells in transparent 96 well plates,

and 200 µl of fresh medium was used in another well for the blank. Immediately after, OD_{600nm} was measured in a TECAN Spark plate reader after agitation. The OD_{600nm} value for the blank was then subtracted to the OD_{600nm} values for each sample.

Microfluidic experiments

Chip design, mold fabrication and chip preparation

Microfluidic chip design was performed using CelWin5 software. The layout consisted of two photolithographic layers. The first layer, used to define the chamber structures, was 1.4 µm in height and comprised rectangular chambers measuring 375 × 30 µm. The second layer defined the fluidic channels with a height of 30 µm. Each 100 µm-wide channel was aligned with 10 chambers, and each chip included four parallel channels.
Photomasks were printed on plastic substrates for both layers, incorporating alignment crosses to ensure precise overlay during lithography. Standard SU-8 photolithography was carried out on silicon wafers to fabricate the mold. Feature dimensions of the resulting mold were verified using profilometry. To facilitate demolding, the mold surface was silanized to reduce PDMS adhesion. PDMS chips were fabricated by mixing Sylgard 184 silicone elastomer base and curing agent at a 5:1 ratio by weight. The mixture was thoroughly mixed, poured over the mold to a thickness of approximately 1 cm, and degassed under vacuum for 30 minutes to eliminate air bubbles. The mold was then cured overnight at 65 °C. After curing, the PDMS was allowed to cool for 15 minutes before the chips were excised. Inlets and outlets were punched using a biopsy punch, and residual debris was removed using adhesive tape.
For bonding, the PDMS chips and glass coverslips were treated with oxygen plasma for 1.2 minutes and immediately brought into contact. The bonded assemblies were incubated at 65 °C for 30 minutes to enhance adhesion, then cooled to room temperature before use.

Cell culture preparation

E. coli strain bPH_669 (or bPH_670 for antibiotic and bPH_715 for arabinose diffusion experiments both presented in Supplementary Fig. 2) was retrieved from glycerol stocks and streaked onto LB agar plates (1% agar) containing the appropriate selection antibiotics. Plates were incubated at 37 °C for 16 hours. Following incubation, a single colony was picked to inoculate an overnight culture in LB Miller medium supplemented with the corresponding antibiotics. The culture was incubated at 37 °C with shaking at 270 rpm.
The following morning, a preculture was prepared by transferring 50 µL of the overnight culture into 5 mL of fresh LB Miller medium containing selection antibiotics. The preculture was grown at 37 °C with shaking at 270 rpm for 5 hours.

Chip loading and installation

After 5 hours of growth, the preculture was centrifuged at 3000 × *g* for 10 minutes. The resulting cell pellet was resuspended in 250 µL of fresh LB Miller medium supplemented with selection

antibiotics and 5 g/L Pluronic F-127, resulting in an approximate 20× concentration. The concentrated cell suspension was loaded into the microfluidic chip using a syringe fitted with a blunted needle. Both the inlets and outlets were plugged, and the chip was incubated at 37 °C for 30 minutes to allow cells to settle into the chambers.
Following incubation, the chip was affixed to a custom holder using electrical tape and mounted on a preheated Olympus IX83 inverted microscope (set to 37 °C). The plugs were removed, and tubing was connected to each inlet and outlet port. Each channel was connected via tubing to a peristaltic pump on one end (with waste outlet) and to a reservoir containing LB Miller medium supplemented with 5 g/L Pluronic F-127 and selection antibiotics on the other.
Medium flow was initiated at 50 μL/min to flush out any untrapped cells. The chip was then maintained under continuous perfusion (50 μL/min) at 37 °C for 16 hours to allow microcolonies to grow, fully occupy the chamber structures, and establish stable spatial growth gradients.

Recording and medium switch

Time-lapse experiments were conducted using an Olympus IX83 inverted microscope equipped with an Andor Zyla 4.2 sCMOS camera, controlled via MetaMorph software. Imaging was performed with a 20× objective, which allowed simultaneous visualization of all 10 chambers within a single lane of the microfluidic chip in one field of view. Throughout the time-lapse, the chip was maintained at 37 °C under continuous perfusion at 50 μL/min with LB Miller medium supplemented with 5 g/L Pluronic F-127, appropriate selection antibiotics, and the designated arabinose concentration. Images were acquired every 3 minutes in both bright-field and GFP fluorescence channels. Exposure times and illumination intensity were kept constant across all experiments. Up to three independent lanes could be recorded simultaneously. All experiments began with a 1-hour pre-induction phase using medium lacking arabinose to serve as a negative control. Medium switching was performed manually by replacing the reservoir bottle connected to the inlet tubing. The timing of medium replacement accounted for the delay required for the new medium to propagate through the tubing and reach the chamber, which varied depending on tube length. For experiments presented in Supplementary Fig. 2c, in which the efficacy of kanamycin selection within microcolonies was assessed, the switch to kanamycin-containing medium was likewise performed after 1 hour of baseline recording. For each condition, 3 separated experiments were conducted on different days, in which one lane (up to 10 chambers) was imaged.

Images preprocessing

For each field of view, the recordings consisted of a stack of images per channel (bright-field and GFP fluorescence). To correct for mechanical or thermal drift during acquisition, image stacks were first aligned using the SIFT algorithm[3] implemented in Fiji (ImageJ). This alignment step was essential to avoid motion artifacts in downstream optical flow analysis.

From the aligned GFP channel stack, a maximum intensity projection was generated. This projection was used to automatically segment the microfluidic chambers by thresholding, resulting in a binary mask that delineated each chamber. Both alignment and mask generation were performed using a custom Fiji macro. Where necessary, masks were manually refined to ensure accuracy. In addition, the angle required to rotate each field such that chambers were oriented vertically (with flow direction from top to bottom) was determined.

A custom Python script was then used to apply the identified rotation angle to the aligned images. Individual chambers were cropped from the rotated stacks using the corresponding binary masks.

To correct for non-uniform fluorescence intensity across the field of view, the CLASH contrast enhancement method was applied to GFP images. This procedure normalized contrast across the chamber, mitigating signal falloff near the image periphery and ensuring homogeneous intensity profiles for downstream analysis.

Images analysis for growth measurement

For each cropped chamber, optical flow in the vertical direction (y-axis, from the closed end of the chamber toward the inlet) was computed using the Farnebäck algorithm[4], as implemented in OpenCV, from the GFP images. A key parameter in optical flow estimation is the interrogation window size. Smaller windows allow for detection of fine local variations but increase noise, whereas larger windows smooth the signal but are less sensitive to local displacement and more susceptible to boundary artifacts.

After comparing optical flow outputs with manually tracked cell displacements, a 60 × 60 pixel window (19.8 μm) was selected as a trade-off between sensitivity and noise. As a result, the regions within the final 19.8 μm at the top and bottom of each chamber were excluded from downstream analysis due to unreliable y-axis flow estimation.

To generate a one-dimensional velocity profile, the y-component of the flow was averaged along the x-axis at each depth. In time-lapse data, periodic fluctuations in flow were observed—likely resulting from a stick–slip effect due to mechanical or biological instability. To mitigate this, a 10-frame rolling average of the y-flow was applied across time points, resulting in a smoothed representation of flow dynamics over time and depth.

To identify the boundary between growing and non-growing regions, a flow threshold was established based on a negative control were cells cannot grow. Chambers were filled with cells exposed to an antibiotic for which they lacked resistance (see Supplementary Fig. 2c), and the average y-flow and its standard deviation were calculated. The growth threshold was defined as this mean + 3 standard deviations under these non-growing conditions. At each time point, the growth boundary was defined as the first depth position (measured from the chamber end) at which the local y-flow exceeded this threshold.

Since the strains used were non-motile, cell displacement was solely driven by growth. Furthermore, as expansion could occur only in one direction (toward the chamber inlet), cells at the back of the chamber pushes on upstream cells as they divided. Thus, the measured speed at any depth represents the sum of local growth and cumulative growth from deeper regions. To extract the local growth rate, the spatial derivative of the velocity profile was computed along the depth of the chamber. This yielded a depth-resolved profile of instantaneous growth rates. Similar flow-based methods for spatial growth rate estimation have been reported previously[5–7].

Images analysis for GVs measurements

GV clusters were identified and quantified from bright-field microscopy images, where they appear as highly refractile, bright white regions. Segmentation of GV clusters was performed by thresholding pixel intensity values in bright-field images, with pixels above a chamber-specific threshold classified as part of a GV cluster.

Because GV production is only induced after one hour of recording, the initial frames do not contain GV clusters and were used to define the segmentation threshold. Specifically, for each chamber, the threshold was computed as the average intensity value below which 99% of the pixels fell, calculated across the first five time points. This approach allowed for automatic, chamber-specific threshold calibration.

The resulting binary masks were used to segment GV-positive pixels. To construct a depth-resolved GV content profile, the number of segmented pixels was summed within a sliding window spanning the full chamber width (x-axis) and a 50-pixel (16.5 μm) height in the y-axis. The window was centered at each depth to generate a one-dimensional profile of GV abundance across the vertical axis of the chamber.

To mitigate temporal noise and enhance signal stability, a 10-frame rolling average was applied to the GV profiles over time, following the same approach as in the flow-based growth rate analysis (see "*Images analysis for growth measurement*").

Estimation of non-GV-producing spawn probability

To calculate the probability that a cell division leads to the emergence of a non-GV-producing mutant, we counted how many times such populations appeared in each condition, for each experiment, across up to 10 chambers per condition. In total, 20 such events were observed in the 0.1% arabinose condition, and 7 in the 0.01% arabinose condition. Assuming that each observed population originates from a single mutant cell, the probability can be calculated as:

$$p = \frac{M}{d}$$

Where p is the probability that a single cell division gives rise to a non-GV-producing mutant, M is the total number of non-GV-producing populations counted for a given condition in one experiment, and d is the total number of cell divisions that occurred across all chambers

throughout the duration of the experiment.
The total number of divisions d can be estimated as follows:

$$d = \frac{S_{total}}{S_{bact}}$$

Where S_{total} (in μm²) is the total surface area of newly produced bacteria across all chambers for a given condition over the 31-hour duration of the experiment, and $S_{bact}$is the average surface area of a single bacterium. Based on the values reported in Supplementary Figure 1, we used S_{bact} = 3.15 μm².
S_{total} can be calculated as follows:

$$S_{total} = \sum_{c=1}^{N_c} \sum_{f=1}^{N_f} V_{max}^{(c,f)} \times w$$

Where $V_{max}^{(c,f)}$ is the maximum vertical flow speed (μm/frame) in chamber c at frame t, obtained from optical flow analysis (see *Images analysis for growth measurement)*, w is the width of the chamber, set at $w = 30$μm, N_c is the total number of chambers in the experiment for the condition and N_f is the total number of frames in the experiments.

We could also make estimations of the mutation rate per base pair per division from these results as follows :

$$t_{mut} = \frac{M}{(bp \times S_{total})}$$

Where t_{mut} is the mutation rate per nucleotide and bp is the number of base pairs whose mutation lead to non-GV producing phenotype.

Assuming that any base pair mutation within the entire ARG operon and its promoter region (totaling 17,284 base pairs) can lead to the non-GV-producing phenotype, this yields an estimated t_{mut} of $1.0 \times 10^{-12} \pm 2.1 \times 10^{-12}$ for the 0.1% arabinose condition and $2.4 \times 10^{-12} \pm 2.3 \times 10^{-12}$ for the 0.01% condition. However, this likely represents a substantial underestimation of the true mutation rate. It is improbable that any mutation across the entire operon would eliminate GV production. Although the mutational tolerance of each gene in the ARG cluster has not been comprehensively assessed, previous studies have shown that certain regions of *gvpC* and *gvpA* can be mutated without impairing GV formation[8,9]. Moreover, both *gvpC* and *gvpN* can be entirely deleted without abolishing GV formation, though these deletions do alter the acoustic properties of the resulting vesicles[10]. Therefore, mutations in these genes may not manifest as phenotypic changes detectable in our assay. Definitive quantification of the mutation rate would require sequencing-based studies.

Supplementary tables

Supplementary Table 3 : List of plasmids used in this work.

Plasmid number	Plasmid name	Addgene ref	Expressed gene	Induction	Maker	Size (bp)
pPH_576	pBAD-bARGSer-AxeTxe	#192473	$bARG_{ser}$	arabinose	Chloramphenicol	23202
pPH_561	pSB4K5-P7-BCD-sfGFP	Nan	sfGFP	constitutive	Kanamycin	4647
pPH_635	pBAD-sfGFP	#85482	sfGFP	arabinose	Ampicillin	4900

Supplementary Table 4 : list of E.coli strains used in this work.

Strain number	Genotype	Plasmids
bPH_103	E.coli K12 BW25113 ΔfliA Δ(araD-araB)567	None
bPH_657	E.coli K12 BW25113 ΔfliA Δ(araD-araB)567	pPH_576
bPH_670	E.coli K12 BW25113 ΔfliA Δ(araD-araB)567	pPH_561
bPH_669	E.coli K12 BW25113 ΔfliA Δ(araD-araB)567	pPH_576, pPH_561
bPH_715	E.coli K12 BW25113 ΔfliA Δ(araD-araB)567	pPH_635

Supplementary Table 5 : Number of cells included during batch experiments (Figure 2) for each condition for measurements of GVs content, and cell size. "Replicas" represent biological replicas : separated experiments started from different colonies of the bPH_669 strain.

Time (hours)	Arabinose concentration (w/w %)	Replica 1	Replica 2	Replica 3	Total
0	0.000	186	167	191	**544**
2	0.000	21	194	13	**228**
	0.001	61	45	21	**127**
	0.010	27	30	20	**77**
	0.100	43	22	18	**83**
4	0.000	106	64	164	**334**
	0.001	131	158	99	**388**
	0.01	158	79	191	**428**
	0.1	37	57	85	**179**

6	0.000	197	157	194	**548**
	0.001	180	153	249	**582**
	0.010	70	79	157	**306**
	0.100	69	70	144	**283**
8	0.000	237	298	372	**907**
	0.001	133	145	296	**574**
	0.010	51	65	71	**187**
	0.100	60	144	109	**313**

References

1. Baba, T. *et al.* Construction of Escherichia coli K-12 in-frame, single-gene knockout mutants: the Keio collection. *Mol. Syst. Biol.* **2**, 2006.0008 (2006).
2. Lugagne, J.-B. Real-time control of a genetic toggle switch. (Sorbonne Paris Cité, 2016).
3. Lowe, D. G. Distinctive Image Features from Scale-Invariant Keypoints. *Int. J. Comput. Vis.* **60**, 91–110 (2004).
4. Farnebäck, G. Two-Frame Motion Estimation Based on Polynomial Expansion. in *Image Analysis* (eds. Bigun, J. & Gustavsson, T.) 363–370 (Springer, Berlin, Heidelberg, 2003). doi:10.1007/3-540-45103-X_50.
5. Milunov, D. External real time control of E.coli range expansion. (Université Paris Cité, 2023).
6. Dal Co, A., van Vliet, S. & Ackermann, M. Emergent microscale gradients give rise to metabolic cross-feeding and antibiotic tolerance in clonal bacterial populations. *Philos. Trans. R. Soc. B Biol. Sci.* **374**, 20190080 (2019).
7. Stevanovic, M. *et al.* Nutrient Gradients Mediate Complex Colony-Level Antibiotic Responses in Structured Microbial Populations. *Front. Microbiol.* **13**, 740259 (2022).
8. Huber, S. T., Terwiel, D., Evers, W. H., Maresca, D. & Jakobi, A. J. Cryo-EM structure of gas vesicles for buoyancy-controlled motility. *Cell* **186**, 975-986.e13 (2023).
9. Dutka, P. *et al.* Structure of *Anabaena flos-aquae* gas vesicles revealed by cryo-ET. *Structure* **31**, 518-528.e6 (2023).
10. Ling, B. *et al.* Truly Tiny Acoustic Biomolecules for Ultrasound Imaging and Therapy. *Adv. Mater.* **36**, 2307106 (2024).

Appendix 4 : Supplementary materials from “Increase of cytoplasmic density leads to enhanced bacterial persistence to antibiotics”

Increase of cytoplasmic density leads to enhanced bacterial persistence to antibiotics – supplementary materials

Simon Barral[†,1], Anis Aggoun[†,2], Chloé Sasson[3], Céline Cordier[1], Gilles Tessier[2], Jérôme Bonnet[3], Mickael Tanter[4], Pascal Berto[*,2], Pascal Hersen[*,1].

[1] *Physics of Cells and Cancer CNRS UMR168, Sorbonne Université, Institut Curie, 11 Rue Pierre et Marie Curie, 75005 Paris, France.*
[2] *Institut de la Vision, Sorbonne Université, CNRS-UMR 7210, Inserm-UMR S968, Paris 75012, France.*
[3] *Centre de Biologie Structurale CNRS UMR5048 and INSERM* U1054*, University of Montpellier,* 29 Rue de Navacelles, 34090 Montpellier, *France.*
[4] *Physics for Medicine Paris UMR8063, ESPCI Paris, Paris Science Lettres University (PSL), CNRS, 2-10 rue d'Oradour-sur-Glane, 75015 Paris, France.*

[†] *denotes equal contributions.*
* *Correspondence and requests for materials should be addressed to Pascal Berto (pascal.berto@parisdescartes.fr) and/or Pascal Hersen (pascal.hersen@curie.fr).*

Keywords: *bacterial persistence, Quantitative Phase Imaging, Cytoplasmic Crowding, Antibiotic tolerance*

Strain construction

Background strain

All experiments were made on an E.coli BW25113 ΔfliA strain from Keio collection[1], on which the the kanamycin resistance that was inserted in place of the fliA gene have been removed in previous work[2]. This strain has a deletion of fliA gene preventing it from having any chemotaxis and has the Δ(araD-araB)567 mutation preventing it from degrading arabinose. It will be referred as bPH_103 in this work.

Chemocompetent cells preparation

Chemocompetent bPH_103 cells were prepared using the following protocol. Two days prior to the procedure, colonies of frozen competent cells were streaked onto an LB agar plate without antibiotics

and incubated overnight at 37°C. The day before the main experiment, a single colony was inoculated into 5 mL of LB medium (without antibiotics) and grown overnight at 37°C with shaking at 200–250 rpm. Additionally, a box of 200 µL pipette tips and 50 microcentrifuge tubes were placed in a -80°C freezer to pre-chill.
On the day of the experiment, 500 µL of the overnight culture was transferred into 50 mL of fresh LB medium (no antibiotics) in a sterile Erlenmeyer flask. The culture was incubated at 37°C with shaking until it reached an optical density (OD600) between 0.40 and 0.45. Once this OD was achieved, the entire 50 mL culture was transferred to a pre-chilled 50 mL Falcon tube and incubated on ice for 20 minutes.
The culture was centrifuged at 2500 × g for 10 minutes at 0°C. The supernatant was discarded, and the cell pellet was resuspended in 10 mL of ice-cold 100 mM $CaCl_2$ solution by gentle pipetting. From this step onward, all manipulations were performed on ice to maintain cell competency. The resuspended cells were incubated on ice for 1–2 hours, followed by another centrifugation at 2500 × g for 10 minutes at 0°C. The supernatant was again discarded, and the pellet was resuspended in 2.5 mL of ice-cold $CaCl_2$ solution containing 15% (w/w) glycerol.
Finally, 50 µL aliquots of the competent cell suspension were distributed into pre-chilled microcentrifuge tubes, which were immediately immersed in liquid nitrogen for rapid freezing. Once all tubes were processed, they were transferred to a -80°C freezer for long-term storage.

Plasmids and competent cells transformations

pBAD-bARGSer-AxeTxe plasmid (Addgene #192473) encoding for the GVs production was kindly provided by Sharipo's lab in Caltech. The annotated plasmid map is provided in data/plasmids maps folder. This plasmid will be referred as pPH_576 in this work.

Chemocompetent bPH_103 cells were transformed using a standard heat shock protocol. A frozen aliquot of chemocompetent bPH_103 cells was thawed on ice for 10 minutes. After thawing, 50 ng of plasmid DNA (pPH_576) was added to the tube and gently mixed with a pipette tip. The mixture was incubated on ice for an additional 20 minutes.
Following this incubation, the tube was subjected to a 42°C water bath for 45 seconds to induce heat shock, then immediately returned to ice for 2 minutes. Subsequently, 1 mL of fresh LB Miller medium was added, and the tube was incubated at 37°C with shaking at 270 rpm for 1 hour to allow for recovery and expression of the antibiotic resistance gene.
After recovery, the cells were pelleted by centrifugation at 11,000 × g for 2 minutes and resuspended in 50 µL of LB Miller medium. The resuspended cells were then spread onto an LB agar plate (1%) containing chloramphenicol using sterile glass beads. The plate was incubated at 37°C for 16 hours to allow colony formation.
An isolated colony was selected and inoculated into 5 mL of LB Miller medium supplemented with chloramphenicol. This culture was grown at 37°C with shaking at 270 rpm for 16 hours. The resulting culture was used to prepare glycerol stocks by mixing 500 µL of culture with 500 µL of 50% glycerol solution. The aliquots were then frozen and stored at -80°C for long-term preservation. The resulting strain was named bPH_657.

The pSB4K5-P7-BCD-sfGFP plasmid, used for constitutive production of superfolder GFP (sfGFP), will be referred to as pPH_561 in this study. An annotated plasmid map is provided in data/plasmids maps folder.

Chemocompetent bPH_657 cells were prepared following the previously described protocol. These cells were transformed with the pPH_561 plasmid using the same heat shock procedure as outlined above. Following transformation, the cells were plated on LB agar containing both chloramphenicol and kanamycin to ensure maintenance of both plasmids within the cells.
The resulting strain containing both pPH_576 and pPH_561 was named bPH_669.

Measuring GVs production in batch culture

Culture conditions and sampling

bPH_669 cells from glycerol stocks were streaked onto an LB agar (1%) plate containing chloramphenicol and kanamycin, then incubated at 37°C for 16 hours. Following incubation, an isolated colony was selected and used to inoculate an overnight culture in LB Miller medium supplemented with chloramphenicol and kanamycin. This culture was grown at 37°C with shaking at 270 rpm.
The next morning, a preculture was initiated by inoculating 50 µL of the overnight culture into 5 mL of fresh LB Miller medium containing chloramphenicol and kanamycin. The preculture was grown at 37°C with shaking at 270 rpm for 3 hours. A 100 µL sample of this preculture was collected and stored at 4°C, designated as the time zero (T0) sample for the experiment.
Four experimental cultures were then prepared by inoculating 100 µL of the preculture into 5 mL of LB Miller medium containing chloramphenicol, kanamycin, and varying concentrations of arabinose (0%, 0.001%, 0.01%, or 0.1% w/w). These cultures were incubated at 37°C with shaking at 270 rpm for 24 hours.
During the first 8 hours of incubation, 100 µL samples were collected from each culture every 2 hours and stored at 4°C. A final sample was taken at the 24-hour time point. This entire procedure was repeated three times, with a 24-hour interval between each repetition. For each repetition, cultures were initiated from different colonies originating from the same LB agar plate.

Sample preparation and images capture in bright field microscopy

Once all samples were collected as described above, they were prepared for assessing the proportion of bacterial populations containing gas vesicle (GV) clusters and for evaluating the size of bright spots observed in bright-field microscopy due to these clusters. Agar pads were prepared for each sample as follows:

A 2% agarose solution in PBS was prepared, autoclaved, and melted prior to use. For pad preparation, a central microscope slide was positioned between two identical slides, each covered with a layer of electrical tape. A 12 µL drop of the melted PBS-agarose solution was placed onto the central slide. A

fourth slide was then gently pressed onto the drop, using the tape-covered slides as guides to apply even pressure. This process flattened the drop, creating an agarose pad with a uniform thickness corresponding to the tape layer. The gel was allowed to cool for 20 seconds before the top slide was removed, and it was then left to dry for 1 minute.
Meanwhile, the bacterial sample was thoroughly mixed. For each sample taken after 6 hours of culture, a 10-fold dilution in PBS was performed to ensure isolated cells could be easily segmented during image analysis. A 1 µL drop of this diluted sample was deposited onto the agar pad and allowed to dry for 2 minutes. A coverslip was then gently placed on top of the agar pad and secured to the slide using melted VALAP (a mixture of lanolin, Vaseline, and paraffin).
Immediately after preparation, the agar pad was mounted on an Olympus IX83 microscope. The focus was adjusted on the bacteria using a UPlanSApo 100×/1.40 oil objective. Images were captured in both bright-field and GFP fluorescence modes using a Zyla 4.2 sCMOS camera with Metamorph software. For each sample, three images containing at least 26 cells were taken.

Image analysis

All previously captured images were cropped to retain only the regions unaffected by border artifacts in the GFP channel, where low signal intensity complicates reliable cell segmentation. Bacteria in these images were segmented using TensorFlow with a custom U-Net model trained on GFP images, which outputs segmented cell masks. When necessary, minor corrections to these masks were performed manually in ImageJ to address segmentation errors.
For each segmented cell, the presence and size of GVs clusters were quantified using a custom Python script. Briefly, in each bright-field image, cells were identified using their corresponding segmentation masks. A dynamic threshold was applied within each cell, calculated based on the average background intensity (i.e., non-bacterial regions of the image) multiplied by a constant factor. This adaptive thresholding ensures consistency across different images.
Pixels within the segmented cells that exceeded this threshold were identified and counted as part of the GVs cluster. Concurrently, the total cell surface area, length, and width were also measured. These measurements were repeated for all bacteria in each image, and the mean and standard deviation of all parameters were calculated for each sample. The final reported values represent the mean of three biological replicates for each time point and arabinose concentration.

Persistence measurement

Culture conditions and sample preparation

bPH_669 cells from glycerol stocks were streaked onto LB agar (1%) plates containing chloramphenicol and kanamycin and incubated at 37°C for 16 hours. After incubation, three isolated colonies were selected to initiate three independent cultures in 5 mL of LB Miller medium supplemented with kanamycin and chloramphenicol, representing three biological replicates. These cultures were grown for 16 hours at 37°C with 270 rpm agitation.
Subsequently, 50 µL from each replicate culture was used to inoculate 5 mL of fresh LB Miller medium with kanamycin and chloramphenicol, generating three precultures. After 3 hours of incubation under the same conditions, experimental cultures were initiated by inoculating 100 µL of each preculture

into 5 mL of fresh LB Miller medium containing kanamycin, chloramphenicol, and arabinose at final concentrations of 0%, 0.001%, 0.01%, or 0.1% (w/w). These experimental cultures were incubated for 6 hours at 37°C with 270 rpm agitation, a timepoint at which bacterial growth remains in the exponential phase and GVs begin to accumulate.
For each experimental culture, 1 mL was transferred to an Eppendorf tube for preparation and imaging via quantitative phase imaging (QPI; see "QPI Measurement"). The remaining culture was adjusted to a cell density of ~3.5×10^7 cells/mL in LB Miller with chloramphenicol and kanamycin. Cell density was measured either via optical density at 600 nm (OD600) or direct bacterial counts using a Helber counting chamber (Hawksley, SKU: Z30000) for samples containing GVs. GVs, being highly refractive, were expected to affect OD measurements. Samples with adjusted cell numbers were stored at 4°C until further processing, including antibiotic exposure and plating, performed 16 hours later.
The same protocol was applied to a subset of experimental cultures with incubation extended to 16 hours instead of 6 hours, focusing on two conditions: 0% arabinose and 0.1% (w/w) arabinose. This extended incubation enabled the cells to reach the maximum possible GV concentration. Additionally, to obtain a population enriched for GVs, an alternative protocol was employed under the 16-hour induction condition with 0.1% arabinose. Before cell density equilibration, samples were centrifuged at 600×g for 30 minutes. This process leveraged the altered buoyancy of GV-containing cells, which float due to their gas-filled vesicles. Centrifugation accelerated the flotation, resulting in a floating layer enriched in GV-containing cells. This floating layer was carefully separated from the non-floating fraction by removing most of the medium below with a syringe and needle. The floating layer was resuspended in fresh LB Miller medium supplemented with chloramphenicol and kanamycin. Its cell density was then equilibrated as for the other samples at around ~3.5×10^7 cells/mL and stored at 4°C until further processing.

Antibiotic exposure and plating

Large squared plates of LB Miller with 1% agar with no antibiotics where prepared. Each equilibrated samples were then split in two parts. A 8 steps 10x serial dilution was prepared from one part in a sterile 96 well plate in fresh LB Miller containing chloramphenicol and kanamycin. For each of these series of dilutions, 5 µL were then dropped onto a plate, allowed to dry for 2 minutes and incubated at 37°C for 16 hours. This serial dilution will be used to calculate the "T0" CFU of the culture condition, corresponding the CFU of the sample before antibiotic exposure.
For the remaining part of the samples, 1mL was transferred into a sterile 6 well plate, 6 µM final of tobramycin were added and the sample was incubated for 3 hours at 37°C with 230 rpm agitation. After incubation, as for the T0 samples before, a 8 step 10x serial dilution was prepared and 5 µL of each dilution of the series were dropped onto an LB agar plate, allowed to dry and incubated for 16 hours at 37°C. These series provide experimental results later referred to as "Test" and will be used to evaluate the proportion of the population that was able to restart growth after antibiotic expose once the antibiotic is removed.
The exact same protocol was also applied to another 1 mL of the same samples, but no tobramycin was added before incubation, providing a negative control referred as "Neg".

Persistence quantification

After 16 hours of incubation, plates were removed from the incubator, and images were captured using a Bio-Rad Gel reader. All plate images are available in provided data/persistence folder (. Colony counts were performed manually for each sample at the most concentrated dilution in the serial dilution series where distinct, isolated colonies were clearly identifiable. For each sample, the number of colonies and the corresponding dilution factor were recorded in a .csv file with the prefix "counting" in the filename. All counting .csv files are available in data/persistence folder. The counting data were processed using a custom Python script (the environment and script are available in data/persistence folder) to calculate the persistence for each sample. Briefly, the Colony Forming Units (CFU) for each sample in each condition ("T0," "Test," and "Neg") were determined using the formula:

$$CFU = N_{col} \times 10^{dil - 1}$$

where N_{col} is the number of counted colonies, dil is the dilution factor at which the colonies were counted, and CFU represents the number of Colony Forming Units in the undiluted sample drop. Persistence for each sample was then calculated using the formula:

$$Persistence\ (\%) = \left(\frac{CFU_{test}}{CFU_{T0}}\right) \times 100$$

Where CFU_{test} is the CFU for the "Test" series (antibiotic-exposed samples), and CFU_{T0} is the CFU for the "T0" series (samples before antibiotic exposure). $Persistence\ (\%)$ represents the percentage of the original population (T0) that survived and regrew after antibiotic exposure. These calculations were performed for each biological replicate (labelled A, B, and C) and the results were plotted.

Gas volume measurement

Agar pad preparation

For all samples used for persistence measurements, gas volume (GV) measurements via quantitative phase imaging (QPI) were also performed. Consequently, the culture conditions and sample preparation followed the same protocol described in the section "Persistence Measurement - Culture Conditions and Sample Preparation."
Agar pads were prepared on 35-mm glass-bottom Fluorodishes. First, a sterile PBS solution containing 1% agarose was prepared and melted. Then, 10 µL of the melted gel was deposited onto a round 18-mm coverslip, whose edges were taped with a single layer of laboratory tape. A second clean coverslip was gently pressed onto the gel for a few seconds until the agarose solidified. Once polymerized, the top coverslip and the tape layer were carefully removed, and the agar pad was allowed to dry for 2 minutes.
Bacterial samples were thoroughly shaken to ensure a homogenous suspension with well-separated cells, facilitating subsequent cell segmentation. A 1-µL aliquot of the bacterial culture was then deposited onto the agar pad and left to absorb for 1 minute. The bottom coverslip containing the agar pad was inverted and carefully placed into the Fluorodish, ensuring the side with the cells was in direct contact with the dish's glass bottom. The coverslip was hermetically sealed to the dish using

molten VALAP. Finally, MilliQ water was added inside the Fluorodish to fully covet the attached coverslip, preventing agar pad drying.

Mean Gas Occupancy measurement

Traditional phase imaging techniques, such as Phase Contrast Microscopy or Differential Interference Contrast Microscopy offer an enhanced contrast when imaging transparent samples such as bacteria, but only provide qualitative information: the formed image is an entangled mix of phase and intensity contributions. Quantitative Phase Imaging (QPI) methods allow for a precise measurement of the phase shift, or retardance, undergone by light as it propagates through the sample. This retardance is directly related to the optical properties of the sample, specifically, its refractive index distribution $n(x, y, z)$. That is because light travels at different speeds depending on the refractive index of the medium. The higher the refractive index, the slower the light travels, causing an accumulation of retardance as light propagates through regions in the sample with different refractive indices. This retardance can be quantified as an optical path difference (OPD), which takes into account both the physical distance and the refractive index variations in the sample. This quantity, which we refer to as δ can be expressed as :

EQ 1 $$\delta(x, y) = \int_0^L (n(x, y, z) - n_m)\, dz$$

Where n_m is the refractive index of the medium surrounding the sample and L the thickness of the sample along the z direction for a given region of coordinates (x, y).

Another key quantity is the optical volume difference (OVD). It represents the cumulative optical path length differences that light experiences as it passes through the entire sample. Mathematically, the OVD can be expressed as the integral of the optical path differences over the surface S occupied by the sample in the image :

EQ 2 $$OVD = \int_V (n(x, y, z) - n_m) dV = \int_S \delta(x, y) dS$$

The refractive index of the sample is linked to its mass density. When imaging biological specimens immerged in aqueous media ($n_m \simeq 1.33$), the OVD reflects the total retardance of light introduced by the various non-aqueous components present in the sample (proteins, lipids, ADN etc.). The total mass of these components, referred to as the dry mass m, can be linked to the OVD by the following relation:

EQ 3 $$OVD = \gamma m$$

With γ the refractive index increment which lies between 0.18 et $0.21\ \mu m^3/pg$ for the majority of cells.

In this work, EQ 3 doesn't hold true in the case of GVs production by the bacteria and needs to be adjusted to account for the fact that the OVD can bear a negative contribution attributed to the presence of gas. We adjust the expression of the OVD as follows:

EQ 4 $$OVD = \gamma m + \Delta n V_G$$

Where V_G is the total volume of gas contained in the bacterium and $\Delta n = -0.33$ the difference of refractive index between gas and the aqueous medium. Note that Δn is considered large compared to the difference of refractive index between the bacterium and the medium. Therefore, even a small quantity of gas can introduce a non-negligeable contribution to the measured OVD.

In order to quantify the molecular crowding in a bacterium of volume V_B, we can define the gas occupancy $\frac{V_G}{V_B}$ which reflects the relative volume occupied by the gas in the bacterium. We can derive an expression for this quantity by reorganizing EQ 4 and dividing both terms by V_B :

EQ 5 $$\frac{V_G}{V_B} = \frac{1}{\Delta n}\left(\frac{OVD}{V_B} - \frac{\gamma m}{V_B}\right)$$

A single measurement of the OVD induced by a bacterium containing gas cannot yield an estimation for $\frac{V_G}{V_B}$. That is because γm, the OVD induced by dry matter, cannot be measured independently from the contribution of air $\Delta n V_G$. Neither can we proceed by imaging a bacterium before and after GVs production because the process takes several hours, during which bacteria continue to grow and divide, making direct comparisons between the two conditions challenging. To address this, we adopted a statistical approach based on three hypothesis:

(i) The presence of gas vesicles does not affect the dry mass contained in a cell. If we consider two cells of the same shape and volume, one that produced GVs and one that did not, the total amount of dry matter contained in each cell is considered equal.

(ii) The distribution of the volume of cells, for a given population, is independent of the quantity of gas produced. Therefore, we consider that GVs production does not alter the shape and average volume of cells across the population.

(iii) We approximate the rod shape of a bacterium by a cylindrical body with rounded, hemispherical caps at both ends.

Let us write :

EQ 6 $$< \frac{V_G}{V_B} >= \frac{1}{\Delta n}\left(< \frac{OVD}{V_B} > - < \frac{\gamma m}{V_B} >\right)$$

Where the operator $<\cdot>$ denotes the statistical average across the population. If we know V_B, $< \frac{OVD}{V_B} >$ can be estimated by imaging a large number of cells from a population for which the gas occupancy $< \frac{V_G}{V_B} >$ is to be estimated. Hyp (i, ii) allow us to estimate $< \frac{\gamma m}{V_B} >$ similarly, but from a control population of cells that did not produce GVs.

V_B can be expressed as the product of the median cross-section S_b and the average height of a bacterium $\overline{h_B}$. Given hyp. (iii), and considering L the total length of the bacterium and r its radius we can write :

EQ 5 $$V_B = \pi r^2 (L - \frac{2}{3} r)$$

EQ 6 $$S_B = r[(\pi - 4)r + 2L]$$

EQ 7 $$\overline{h_B} = \frac{V_B}{S_B} = \frac{\pi r\,(L - \frac{2}{3} r)}{(\pi - 4)r + 2L}$$

Therefore, given that S_b is obtained through segmentation, and can yield L and r, one can estimate V_B using EQ 7.In practise, a bacterial culture is split into two conditions: one where GV production is induced by adding arabinose to the culture medium, and another that serves as control without arabinose. Both cultures get incubated at 37°C for a few hours during which gas vesicles are produced. After incubation a large number of individual bacteria from each condition are imaged yielding measurements for $< \frac{OVD}{V_B} >$ and $< \frac{\gamma m}{V_B} >$.§

References

1. Baba, T. *et al*. Construction of Escherichia coli K-12 in-frame, single-gene knockout mutants: the Keio collection. *Mol. Syst. Biol.* **2**, 2006.0008 (2006).
2. Lugagne, J.-B. Real-time control of a genetic toggle switch. (Sorbonne Paris Cité, 2016).

Appendix 5 : Protocols

Bacteria Stain construction

Chemocompetent E.coli preparation

Material

For 50 50ul aliquots :

- 50 sterile 1.5ml Eppendorf tubes
- 10ml of CaCl2 solution (100mM)
- 2.5ml of CaCl2 100mM + 15% glycerol solution
- 1 Erlenmeyer Flask 250ml
- 55ml of LB
- A bucket of liquid nitrogene OR a bath of absolute ethanol with dry ice
- A 50mL Flacon Tube

Method

Two days before :

- Grow colonies of frozen competent cells on a LB plate (no atb)

The day before :

- Start an overnight culture with a colony in 5ml of LB (no atb), 37°C with shaking
- Put a box of 200uL tips, and 50 Eppendorf tubes in the-80°C freezer

The D day :

Step 1 : In the sterile Erlenmeyer, put 500ul of overnight culture in 50ml of LB (no atb) and let it grow at 37°C with shaking until you reach and OD between 0.40 and 0.45 (measure OD every hours, it takes about 3 hours to reach it).

In the meantime, put the CaCl2 bottle in ice so it cools down to ice temperature and set the 50mL Falcon centrifuge (BMBC, floor 3) at 0°C, close it and let it cool down. Put one 10mL pipette and one 5mL pipette in the freezer to cool down.

Step 2 : When the OD is reached, transfer all 50mL of liquid media in a 50mL Falcon tube. Leave it on ice for 20 minutes.

Step 3 : Centrifuge the tube at 4000rpm (2500rcf) for 10minutes in the cold centrifuge. Discard supernatant and resupend in 10mL of ice cold CaCl2 solution (using the cold pipette) by pipetting up and down. **From now on, everything should be done on ice.**

Step 4 : Put the tube on ice for 1 to 2 hours.

Step 5 : Centrifuge the tube in the 0°C centrifuge (4000 rpm (2500rcf) for 10 minutes). In the mean time go get some liquid nitrogene or prepare the dry ice + ethanol bath.

Step 6 : Discard supernatant and resupend in 2.5mL of cold CaCl2 + glycerol solution by pipetting up and down.

Step 7 : Distribute 50uL of liquid culture in each Eppendorf Tube. Throw them in liquid nitrogene (or dry ice + ethanol bath) one by one and leave it here until all tubes are done. **Don't put your hands in the liquid nitrogene (it's very cold, it can burn you).**

Step 8 : Store in -80°C freezer.

Heat shock E.coli transformation

Materials & Equipment

- Home-made competent *E. coli*. Thaw on ice.
- LB + antibiotic plates. Pre-heat them in the 37°C incubator to avoid heat shocks when you streak them.
- liquid LB medium (made from Sigma-Aldrich/ref: L3022-1KG)
- Plasmids you want to transform
- Water bath at 42°C
- Shaking incubator at 37°C
- Stationary incubator at 37°C
- sterile glass beads or Pasteur pipettes to spread cells on plates

Protocol

First step (T = 0)

- Let the cells melt 10 minutes on ice.
- Add between 10 pg to 100 ng (usually 50 ng works well) of your plasmids DNA into the tube. Do not leave them out of the ice for too long or touch the bottom of the tube with your fingers in order to avoid heat shocks. Put the cells back on the ice for about 20 minutes.
- Put the tubes into the water bath at 42°C for 45 seconds (= heat shock).
- Put tubes back on ice for 2 minutes to reduce damage to the E.coli cells.
- Feed cells with 250-1000 µL sterile LB (with no antibiotic added).
- Incubate tubes for 1 hour at 37°C under agitation.

Second step (T += 1h)

- Because after one hour of incubation you are not sure how concentrated your cells will be in the LB, you will have to streak two different concentrations on your plates to ensure that you get single colonies:
- Drop 25-150 µl of cells on a first plate (1X plate) and spread on the whole plate.
- Centrifuge the rest of the cells 30s at 13000rpm. Remove supernatant, and re-suspend in the remaining LB. (After you quickly got rid of the supernatant, about 25-50µl of LB should remain in the eppendorf tube)
- Drop 25 - 150 µl of concentrated cells on another plate (10X plate) and spread on the whole plate.
- Incubate at 37°C for 12 to 15 hours

- Once you see colonies, do not leave them for too long at 37°C to avoid the development of satellite colonies

Third step (T += 12-15h)

Once your cells have grown into single colonies, you can pick them and grow them in 5 mL LB. Put 5mL LB + 5µL antibiotic in a 14mL round-bottom tube. Pick one isolated colony with the tip of your pipette cone and drop the cone in the tube (Do not forget to rinse the tip of your pipette with EtOH beforehand). Put them in the shaker at 37°C for ~12hrs.

Fourth step (T += 8-15h)

Once the cells have grown in the tubes, you can make glycerol stocks or start miniprep.

Microfluidic experiments

Mold fabrication

Material (in white room)

- 3' silica wafer
- Acetone
- SU8 2002 and 2015 (KAYAKU)
- Laser lithography machine (Heidelberg µPG101) (for layer 1)
- Optical lithography with mask aligner (MJB4) (for a layer 2)
- poly-glycidyl methacrylate (PGMA)
- Isopropyl alcohol (IPA)
- Spin coater

Method

Layer 1 (small layer)

- Clean new wafer in acetone bath, rince with water and dry it.
- Preheat it at 200°C for 5-10 minutes
- Let it cool down 2 minutes
- Put on Spincoater and spread some SU8 2002 on it
- Spincoat at 750rpm 30s (can require adjustments depending on temperature and humidity)
- Pre exposure bake 65°C for 1 minute and 95°C for 2 minutes
- In the meantime, prepare Micropg lythography machine : load the design design, make sure to have the 4mm head loaded, choose 65W laser power and 35%, set the pins for 3' wafer size.
- Let it cool down for 2 minutes

- Load the wafer in Micropg lithography machine, activate vacuum, find plate focus and center
- Start exposure (press “Expose in left corner window)
- PostExposure bake 1 minute at 65°C, 2 minutes at 95°C
- Let it cool down for 2 minutes
- Development : 15sec in PGMA 100 rpm fully submerged, wash with IPA 15sec 100 rpm fully submerged
- Dry and watch under lens if structure are formed
- Hard bake 200°C 5 minutes
- Let cool down

Layer 2 (high layer)

- Preheat it at 200°C for 5-10 minutes
- Let it cool down 2 minutes
- Place in spincoater, turn on vacuum
- Spread SU8 2015 on it
- Spincoat at 2000rpm 30 seconds
- Pre exposure bake 65°C for 1 minute and 95°C for 2 minutes
- In the meantime load mask into the MJB4 and set up parameters
- Let cool down for 2 minutes
- Install wafer in MJB4, align crosses on mask and expose at 140 mJ/cm^2
- Post Exposure back 3 minutes at 95°C
- Let it cool down for 2 minutes
- Development : 2min in PGMA 150 rpm fully submerged, wash with IPA 2min 150 rpm fully submerged
- Dry with air blower
- Hard bake 200°C 5 minutes
- Let cool down

SILANIZATION

- Inside the fume hood, in the vacuum bell, use 2 drops (use plastic pipette) of the silanizing agent in an aluminum foil cap smaller than the wafer size.
- Put wafer in vacuum bell and start vacuum for 15 minutes
- Stop the pump and leave the wafer in the vacuum for an additional 30 minutes
- Remove wafer from vacuum and heat at 150°C for 5 minutes to evaporate excess silane

Preparing chip

Molding

- Get the molds
- Clean them with compressed air thing
- The molds are made in the white chamber - training to be taken
- Prepare PDMS: 10 g/mold + 2/10 (2 g/mold) of hardener: mix
- Use the little cups just underneath the PDMS bench
- stir vigorously till it becomes whitish (1 minute)
- Pour liquid PDMS/ hardener in the mold
- just enough to cover the chip area + border
- Put under vacuum for 1 hour (removes the bubbles)
- Put mold in the bowl
- close it
- Plug tube for small vacuum pump
- launch pump
- let for one hour
- stop the pump
- Let solidify: 4 hours (or O/N) at 65°C

Extraction

- Let cool down at RT
- Cut the chip out of the mold
- Use the spatula to help get it out
- Pierce through appropriate puncher for inlet and outlet
- Transport in an empty petri dish

Mounting

- Get 24 mm x 60 mm slide and the chip: briefly clean with compressed air
- Use tape to further clean the chip
- Slide your fingers on the tape to make sure to capture all dust
- Place chip + slide in the plasma cleaner - the side facing upward will be the one to be sticked to mount the chip (chip up side is the one that contains the circuit).
- Use plasma cleaner / activate surfaces for sticking
- Put slide and chip in (surfaces to be sticked together facing upwards)
- Close the door (make sure to close it well)
- Turn ON vacuum pump
- Prepare time for 1min10sec
- Turn to HI on control knob
- Turn Power ON the plasma cleaner
- When purple light inside, start timer for 1min10sec.
- Turn Power OFF
- Control knob back to OFF
- Unscrew door
- Turn OFF vacuum pump

- Let air enter and open the door
- Get the chip and slice out
- Stick both upward surfaces together - very gently push (preferentially on the sides) to make it stick
- Let stick for 10min at 65C.
- Get out, let cool down at RT.

Loading chip and starting experiments

Material

- Freshly prepared chip
- Homemade sterile LB miller (10g Bacto™ Tryptone (Gibco) + 10g Sodium Chloride (Sigma Aldrich) + 5g yeast extract (Sigma Aldrich) in 1L of miliQ water, mixed and autoclaved)
- Appropriate antibiotics
- Fresh bacteria plate with isolated colonies
- Pluronic f127 (Sigma Aldrich)
- Centrifuge
- MiliQ Water
- Ethanol 70%
- Clean tubings
- Peristatic pump
- Plugs matching your tubings
- 1mL syringe
- Dr Who microscope (Olympus IX83 invert with Andor Zyla 4.2 sCMOS camera, controlled via MetaMorph software)

Day 0 :

- Launch bacteria culture in LB Miller with appropriate antibiotics from isolated colony (5ml)

Day 1 :

- When you arrive in the morning, immediately dilute your overnight culture 1/100 in 5ml of fresh medium. Let it grow at 37°C with agitation for 5-6 hours, so that it is at the very end of the exp phase : you will have plenty of cell, still in good shape !
- Prepare your culture medium : It must be filtered LB Miller and contains 5g/l of f-127 pluronics. After loading you will form the gradient in the chip overnight with a flow of 50ul/min so calculate the volume to prepare accordingly.
- Prepare the microscope and tubings. Turn one the microscope, turn on the heater at 37°C. Wash your tubings with MiliQ water - Ethanol 70° - MiliQ water. Fill the tubings with the medium you prepared.
- After 5-6 h of incubation centrifuge the tube at max speed (3000 rpm) on the big centrifuge for 7 minutes. Remove supernatant and resuspend in 250ul of fresh filtered medium with pluronics (prepared earlier). This way you will have a small amont of **very concentrated** bacteria suspension. Load this suspension into the channels of your chip using clean

beveled pink needle. **Wait ! Not so fast !** Don't push on the piston of the syringe, the channels are not very large, it would build up a lot of pressure, might damage the PDMS and project bacteria everywhere ! Instead turn gently the piston like if you were screwing it into the syringe so liquid is pushed very slowly.

- Bubbles can be stuck into the chambers, which make it unusable. To prevent that, insert a plug in the inlet and outlet of each loaded channel and push on it gently, this will increase the pressure inside the channel and chambers, forcing bubbles to dissolve.
- Attache the chip to an adapter for the microscope using electric tape. Install it under the microscope. Here we will assume you work with Dr Who in 20x. Take a first look at your chambers : Do they contains at least a few bacteria each ? No : repeat the loading step - Yes : good job ! Do they contains bubbles ? No : good job ! Yes : Repeat the plug step
- Connect the chip to your tubings. DO NOT DO IT ABOVE THE MICROSCOPE OBJECTIVE so you don't risk dropping medium on it !
- Put back the chip above the objective. Focus by eye and switch to Metamorph. In 20x you can have one position per channel with all 10 chambers. Prepare imaging parameters. Typical imaging parameters are :
    - 1 frame per 3 minutes, 621 frames total for 31 hours recording
    - 20x objective
    - GFP filters : excitation 470/40nm, 525/50nm (Chroma cube 49002)
    - Exposure : bright field 75ms, GFP 25ms
    - Constant autofocus activated

- It is important to have the chip flat (not tilted) for each position. Using the crosses on the chip you can see tilte easily. The aspect of the crosses changes with the focus, so if it is tilted crosses on the right and left (or top and bot) will not be the same. See table below to see what is acceptable and what is not (for bf, especially for GV experiments. To fix a tilt you can add a layer of electric tape on the side of the adapter that is too low, in the place that is in contact to the platine, to compensate for the tilt. Yous should then make the focus so that the most centered cross is at the optimal focus. Ideally all crosses should be in the acceptable range.

Optimal focus (0um)	Acceptable focus (-1um)	Acceptable focus (+1um)	Too low (here -2um)	Too high (here +2um)
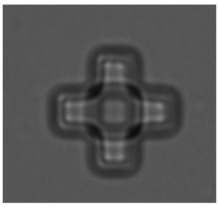	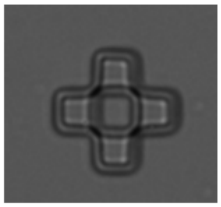	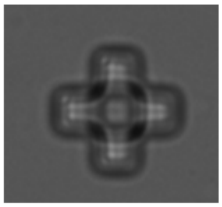		

- Good job, you can now turn of the light of the microscope, go home, have a beer and come back tomorrow once the bacteria filled the chambers and the gradient is stable.

Day 2 :

- The next morning, check that your chambers are filled. They should all be almost completely filled by bacteria. If there are chambers where the bottom part (near the channel) is not completely filled, this might indicate a leak and bubbles flowing from time to time in the channel.
- For channels that are ok, you can set again the positions for the MDA as you did the day before. Check once more all the parameters of the MDA.
- Now you can start recording, switch medium when/if necessary

Images processing

Images preprocessing was done with the Fiji (ImageJ) macro script, it makes stack alignment to correct any drifting in the time lapse and make a binary mask of the chambers.

Image processing was done the Python script.. What does it do ?

- Correct the orientation of the images so that chambers are aligned vertically, with channel at the bottom
- crop each chamber
- adjust with fixed parameters the contrast of the GFP images
- Applie Farnebäck algorithm with OpenCV on GFP images to extract optical flow in the vertical direction
- Calculate a 10-frame rolling average of the y-flow was applied across time points, smoothing the flow
- Calculate local growth rates from optical flow with spatial derivative of the velocity profile computed along the depth of the chamber
- Establish binary masks identifying Gas vesicles from bright field image via automatic thresholding

Batch culture experiments

Bacteria culture conditions

Streaking and Colony Preparation

- Retrieve cells from glycerol stocks.
- Streak cells onto an LB agar (1%) plate supplemented with chloramphenicol and kanamycin.
- Incubate the plate at 37 °C for 16 hours.

Overnight Culture

- Select a single isolated colony.

- Inoculate it into LB Miller medium containing chloramphenicol and kanamycin.
- Grow the culture overnight at 37 °C with shaking at 270 rpm.

Preculture Preparation

- Inoculate 50 µL of the overnight culture into 5 mL of fresh LB Miller medium containing chloramphenicol and kanamycin.
- Grow the preculture at 37 °C with shaking at 270 rpm for 3 hours.
- Collect 100 µL of the preculture and store at 4 °C as the time zero (T0) sample.

Experimental Cultures preparation

- Prepare four experimental cultures by inoculating 100 µL of the preculture into 5 mL of LB Miller medium supplemented with chloramphenicol, kanamycin, and different arabinose concentrations:
    - 0% (control)
    - 0.001% (w/w)
    - 0.01% (w/w)
    - 0.1% (w/w)
- Incubate the cultures at 37 °C with shaking at 270 rpm for 24 hours.

Sampling During Incubation

- For the first 8 hours, collect 50 µL samples from each culture every 2 hours.
- Store all samples at 4 °C until further analysis.

Images capture for GVs quantification

Agar Pad Preparation

- Prepare a 2% agarose solution in PBS, autoclave, and melt before use.
- Position a central microscope slide between two identical slides, each covered with a layer of electrical tape (serving as spacers).
- Place a 12 µL drop of melted PBS-agarose solution on the central slide.
- Gently press a fourth slide onto the drop, using the tape-covered slides as guides to create a uniform pad thickness.
- Allow the agar pad to cool for 20 seconds, remove the top slide, and let the pad dry for 1 minute.

Sample Preparation

- Thoroughly mix the bacterial sample.
- For all samples collected after 6 hours of culture, perform a 10-fold dilution in PBS to ensure individual cells can be easily segmented during image analysis.
- Deposit 1 µL of the diluted sample onto the agar pad and allow it to dry for 2 minutes.

- Place a coverslip gently on top of the pad and seal it to the slide using melted VALAP (a mixture of lanolin, Vaseline, and paraffin).

Microscopy

- Immediately mount the prepared agar pad on an Olympus IX83 microscope.
- Focus on bacterial cells using a UPlanSApo 100×/1.40 oil objective.
- Capture images in both bright-field and GFP fluorescence (excitation 470/40nm, 525/50nm (Chroma cube 49002)) modes using a Zyla 4.2 sCMOS camera with Metamorph software.
- For each sample, take three images, each containing at least several 10s of cells.

Counting cells

Chamber Cleaning and Preparation

- Clean the engraved Helber chamber (Hawksley Z30000) before use:
  - Rinse the counting area thoroughly with Milli-Q water using a squeeze bottle.
  - Wash with 70% ethanol.
  - Rinse again with Milli-Q water.
- Dry the chamber by placing it on a clean Kimtech tissue and gently pressing a second tissue onto the counting area (without rubbing).
- Repeat the drying process with a fresh section of tissue until the chamber is completely dry.

Sample Loading

- Pipette a 5 µL drop of the bacterial suspension onto the center of the counting area.
- Avoid touching the chamber surface with the pipette tip.
- Place a clean 22 mm square coverslip on top of the droplet.
- Allow the liquid to spread by capillary action so it fills the engraved grid and extends slightly into the surrounding ring without overflowing.
- If the liquid extends beyond the ring and causes unwanted flow across the field of view, discard the sample and reload.
- Confirm correct loading when the coverslip remains fixed by capillary suction, allowing the chamber to be rotated without dislodgement.

Microscopy Setup and Imaging

- Place the loaded chamber on a bright-field microscope with 20x objective
- If cell concentration is too high (cells overlapping in the field of view), dilute the sample 10× or 100× in PBS and reload.
- Acquire images at four distinct positions per sample.
- At each position, capture Z-stacks in both bright-field and GFP fluorescence channels ((excitation 470/40nm, 525/50nm (Chroma cube 49002))):
  - Each stack spans 40 µm in height.
  - Use a 2.5 µm step size to ensure all cells are captured in at least one optical plane.

Image-Based Cell Counting

- Determine cell density using image analysis within the known chamber volume:
  - The volume above a single engraved square is specified by the chamber manufacturer.
  - The number of squares per field of view is predetermined, depending on magnification, you can easily count them on BF images if in doubt.
- Segment cells based on their GFP fluorescence using a custom Python script :
  - Generate a maximum intensity projection of each Z-stack (GFP channel).
  - Apply consistent pixel intensity and size thresholds across all samples to segment cells.
- Count the number of segmented cells per field and calculate the cell density (bacteria per mL), adjusting for dilution factors.

Measuring persistence in antibiotics

Culture and sampling

Initial Cultures and Biological Replicates

- Retrieve cells from glycerol stocks.
- Streak onto LB agar (1%) plates supplemented with chloramphenicol and kanamycin.
- Incubate plates at 37 °C for 16 hours.
- Select three isolated colonies and use each to inoculate 5 mL of LB Miller medium supplemented with chloramphenicol and kanamycin (three biological replicates).
- Grow overnight cultures at 37 °C with 270 rpm agitation for 16 hours.

Preculture Preparation

- Inoculate 50 µL from each overnight culture into 5 mL of fresh LB Miller medium with chloramphenicol and kanamycin (one preculture per replicate).
- Grow precultures at 37 °C with 270 rpm shaking for 3 hours.

Experimental Cultures

- Inoculate 100 µL of each preculture into 5 mL of fresh LB Miller medium supplemented with chloramphenicol, kanamycin, and arabinose at final concentrations of 0%, 0.001%, 0.01%, or 0.1% (w/w).
- Incubate cultures at 37 °C with 270 rpm agitation for 6 hours, ensuring cells remain in exponential phase as GVs begin to accumulate.

Sampling

- After 6 or 16hours, transfer 1 mL of each culture to an Eppendorf tube for later quantitative phase imaging.

- Adjust the remaining culture to a cell density of ~3.5×10^7 cells/mL in LB Miller with chloramphenicol and kanamycin. To do so, measure cell density by OD_{600} or by direct counts with a Helber chamber
- Store adjusted samples at 4 °C until further processing

Antibiotic Exposure and Plating

Preparation of T0 (Baseline) CFU Counts

- Prepare large square LB Miller agar plates (1% agar, no antibiotics).
- Split each equilibrated culture into two parts: one for T0 and one for testing.
- For the T0 sample (no antibiotic exposure):
  - Perform an 8-step, 10× serial dilution in fresh LB Miller with chloramphenicol and kanamycin (in a sterile 96-well plate).
  - Spot 5 µL of each dilution onto LB agar plates.
  - Allow spots to dry for 2 minutes.
  - Incubate at 37 °C for 16 hours.
  - These plates provide the baseline CFU (T0) prior to antibiotic treatment.

Tobramycin Treatment (Test Samples)

- Transfer 1 mL of each remaining sample into a sterile 6-well plate.
- Add tobramycin to a final concentration of 6 µM.
- Incubate for 3 hours at 37 °C with 230 rpm agitation.
- After incubation, perform the same 8-step, 10× serial dilution and spot plating procedure as above (5 µL per dilution on LB agar).
- Incubate plates at 37 °C for 16 hours.
- These series provide the “Test” CFU counts, representing the fraction of cells able to resume growth after antibiotic exposure and removal.

Negative Control (No Tobramycin)

- Apply the exact same protocol as for “test” to another 1 mL of the same samples, but omit tobramycin.
- These plates serve as the negative control (“Neg”), representing cells handled identically but without antibiotic stress.

Colony counting and persistence calculation

Plate Imaging and Colony Counting

- After 16 hours of incubation, remove all LB agar plates from the incubator.

- Capture images of each plate using a Bio-Rad Gel reader.
- For each sample, identify the most concentrated dilution in the serial dilution series where distinct, isolated colonies are clearly visible.
- Manually count the colonies for each sample at this dilution.
- Record for each sample the number of colonies (Ncol) and the corresponding dilution factor (dil)
- CFU can be calculated as :

$$CFU = N_{col} \times 10^{dil-1}$$

- Persistence can be calculated as :

$$Persistence\ (\%) = \left(\frac{CFU_{test}}{CFU_{T0}}\right) \times 100$$

Sample preparation for QPI imaging

- Use the same samples prepared for persistence measurements.
- Prepare a sterile 1% agarose solution in PBS and melt it.
- Place a round 18-mm coverslip on a flat surface and line its edges with a single layer of laboratory tape (serving as spacers).
- Deposit 10 µL of the melted agarose onto the center of the coverslip.
- Gently press a second clean coverslip onto the gel for several seconds until the agarose solidifies.
- After polymerization, carefully remove the top coverslip and the tape layer.
- Allow the agar pad to dry for 2 minutes.
- Thoroughly shake the bacterial sample to ensure a homogeneous suspension with well-separated cells (to facilitate segmentation during analysis).
- Deposit a 1 µL aliquot of the bacterial culture onto the agar pad and allow it to absorb for 1 minute.
- Invert the coverslip containing the agar pad and place it into a 35-mm glass-bottom Fluorodish, ensuring that the side with the cells is in direct contact with the glass bottom.
- Seal the coverslip hermetically to the dish using molten VALAP (lanolin, Vaseline, paraffin mixture).
- Add Milli-Q water inside the Fluorodish to fully cover the attached coverslip, preventing the agar pad from drying during imaging.
- Install the Fluorodish on a microscope equipped with quantitative phase imaging setup with 100x objective and image cells in phase and GFP channels.

Spheroids preparation, infection and clearing

Preparation

Materials

- Confluent cell culture flask (T25 is enough)
- Nunclon™ Sphera™ 96-Well U-Shaped-Bottom Microplate (ref thermo : 174925)
- Culture medium if possible, without Phenol red
- Trypsin solution

Protocol

- Remove culture media from your confluent culture flask and wash your cells gently with sterile PBS.
- Remove the PBS and add trypsin (0.5ml for a T25 flask for example). Incubate the flask between 1 and 2 minutes at 37°C.
- Detach the cells by tapping on the side of the flask and look at them under a microscope to make sure they are well detached. Inactivate the trypsin by adding 10 times its volume of fresh culture medium (5ml media for 0.5ml trypsin).
- Transfer to a 50ml Falcon tube and measure cell concentration.
- You will have to put a precise number of cells in a Nunclon sphera well to form spheroids. The more cells you put, the bigger spheroids you will get. For example, with 2500 Hela cells in a well you will get a 800 um large spheroid after 4 days. Determine the number of cells you want (x) and calculate the dilution you need to have x cells in 200ul (the volume of a well).
- Do your dilution in fresh culture medium.
- Add 200ul per well of your dilution without touching the bottom of wells with your pipette tip.
- Incubate at 37°C with 5%CO2. After a day your cells should start to form a spheroid.

Infection

- Streak bacteria on a plate and let them grow overnight.
- Inoculate one colony into liquid medium and grow at 37°C with shaking until OD reaches about 0.1 (approximately 2*10^7 bacteria/ml).
- Take your spheroid plate to the hood. Wash each spheroid once with fresh culture medium (without antibiotics, without phenol red) by removing 170ul from the well without touching the spheroid and then adding 170ul of fresh medium. Do not pipette too strongly, or you might break the spheroid.
- After the last cleaning, remove 10ul from each well and add 10ul of your bacterial solution. This way, you will have 10^6 bacteria/well.
- Incubate at 37°C with 5% CO2 for 4 hours.

- After incubation, wash the spheroids 3 times in fresh culture medium with 5 ug/ml of gentamicin (without phenol red). Ensure to remove bacterial pellets by pipetting up and down in the well before removing the medium.
- Incubate overnight at 37°C with 5% CO2.
- After washing, transfer your spheroids from their original well to a new, unused well containing 200ul of fresh culture medium with 5 ug/ml of gentamicin (without phenol red).
- Wash the spheroids once with fresh culture medium with 10 ug/ml of gentamicin (without phenol red).
- Incubate at 37°C with 5% CO2 for as long as needed. You can observe E. coli colonization nicely 4 days after infection, for example. Wash with fresh culture medium with 10 ug/ml of gentamicin (without phenol red) every 3 days.

Clearing

Materials

- Infected spheroids to image
- PBS
- Paraformaldehyde, 4% in PBS (Thermo Scientific Chemicals)
- Triton x-100 (Sigma Aldrich)
- Bovine Serum Albumin (Thermo scientific)
- 4',6-diamidino-2-phenylindole (DAPI) (Invitrogen)
- RapiClear 1.49 (SunJin Lab)

Protocol

- Wash your spheroid three times in 200ul PBS
- Remove PBS and add 100ul of PFA 4% in PBS for fixation (at 4°C in the fridge, PFA should only be manipulated under chemical hood)
- Incubate 30 minutes at room temperature
- Wash three times in 200ul PBS
- Remove PBS and add 100ul of Triton solution (2% Triton X-100 + 2% BSA in PBS)
- Wash four times in 200ul PBS + 2% BSA
- Incubate at least 2h (the more the better) at 35°C with 60rpm agitation (in small bacteria incubator)
- If you need to label with antibodies or DAPI, it is now !
- DAPI labeling : Remove PBS, add 100ul of DAPI working solution (1ug/ml in PBS, or 1/1000 of the frozen stock solution) and incubate overnight at 4°C with gentle shaking in the dark. Then wash four times in 200ul PBS + 2% BSA
- Remove PBS and add 100ul of RapiClear 1.49
- Incubate 20 minutes in the dark

- Your spheroid is now transparent as long as it stays in RapiClear solution. It can now be imaged in spinning disk microscopy.

Gas Vesicles Flash labeling and super resolution imaging

Bacteria preparation

- E. coli BW25113 cells were transformed via heat shock with the pARA-GVserFlash-AxeTxe plasmid, and transformed clones were selected on LB-Chlo plates after overnight incubation at 37°C.
- A positive clone was then chosen and streaked onto an LB-Chlo 0.1% arabinose plate, followed by overnight incubation at 37°C.
- The following day, the four most opaque/white colonies were selected and resuspended together in 500 µL of LB.
- Lysozyme (Thermo Scientific 90082) was added to achieve a final concentration of 200 ng/mL, and the sample was kept on ice for 15 minutes. Subsequently, Flash EDT2 (Bertin Bioreagent 20704) was added to reach a final concentration of 150 µM and left on ice for an additional 30 minutes in the dark.
- Cells were then centrifuged for 15 minutes at 1000g at 4°C, and the pellet was resuspended in 500 µL of PBS with 250 µM of BAL (Sigma-Aldrich 64046).
- Cells were centrifuged again for 15 minutes at 1000g at 4°C and resuspended in fresh PBS. This washing step was repeated two more times.
- The sample was stored at 4°C in the dark until it was used.

Phase contrast and standard fluorescence microscopy on agar pad

- A gel was prepared by mixing and melting PBS (Phosphate-Buffered Saline) and 1% agarose (D5-C euromedex).
- VALAP wax was prepared by mixing petroleum jelly, lanolin, and paraffin in a 1:1:1 ratio (w/w/w) and melting the mixture.
- To create the agar pad, a microscope slide was sandwiched between two other slides (one on the left and one on the right), both of which had a 100 µm thick tape attached to them. Then, 10 µL of melted PBS gel was dispensed onto the central slide, and another slide was pressed onto the tape of the lateral slide over the gel drop for 30 seconds. This process resulted in the formation of a 100 µm thick agar pad.
- The agar pad was allowed to air-dry at room temperature for 2 minutes. Subsequently, 2 µL of the prepared bacterial sample were carefully applied to the agar pad and left to dry for an additional 2 minutes. After this, a cover slip was placed on the agar pad and sealed using VALAP.
- The agar pad was then mounted on an Olympus IX81 microscope and observed with a 100X objective under phase contrast. Images were captured using a Photometrix Evolve512 CCD camera. For fluorescence imaging, blue light (470nm) was provided by a CoolLED pE4000, and emitted light was filtered at 525nm, with an exposure time of 100ms.

Super resolution microscopy

- Homemade photoswitching buffer was prepared by mixing a phosphate-buffered saline (PBS, pH 7.4) with an oxygen scavenger buffer (0.5 mg/mL glucose oxidase (Sigma), 40 mg/mL catalase (Roche Applied Science), 10 % w/v glucose) and 50 mM of ß-mercaptoethanol in PBS.
- Poly-L-lysine coated cover slip was prepared by dropping and spreading 25ul of 0.1 % Poly-L-lysine solution (Sigma-Aldrich P 8920) and letting it dry for 5 minutes at 37°C. After removing the exedent, 5ul of bacteria preparation was dropped on the Poly-L-lysine coated coverslip.
- After incubating for 10 minutes at 37°C in the dark, the excess bacterial solution was removed. The cavity of a microscope slide with cavities (Marienfeld) was filled with the photoswitching buffer, and the cover slip was carefully placed on it and sealed with dental glue.
- The sample was then mounted under a Nikon TiE2 microscope equipped with an Abbelight SAFe 360 add-on. It was observed using a 100X/1.49NA oil objective and an sCMOS Hamamatsu FusionBT C15440-20UP camera. Bright-field images were captured using only ambient room light to minimize the amount of light exposure to the sample. For standard fluorescence imaging, the sample was excited at 488 nm, and emitted light was filtered at 525 nm, with an exposure time of 100 ms.
- For super-resolution imaging, the sample was initially photobleached for a few seconds at 488 nm at maximum intensity. Subsequently, the sample was exposed to 10 ms pulses of UV at 408 nm at maximum intensity every 90 ms while continuously being excited at 488 nm at maximum intensity. A total of 20,000 images were acquired, each with an exposure time of 100 ms, and the emitted light was filtered at 525 nm.
- Image reconstructions from the acquired movies were performed using Abbelight SAFe Software.

Appendix 6 : Résumé substantiel en français

Impacts des rapporteurs acoustiques codés génétiquement sur la physiologie d'Escherichia coli

Mots-clés : Biologie synthétique, vésicule gazeuse, sonogénétique, contrainte métabolique, microfluidique, ultrasons, encombrement moléculaire, *E.coli*, sphéroïdes

Depuis une quinzaine d'années, les vésicules de gaz suscitent un intérêt croissant au sein de la communauté scientifique en tant qu'outils prometteurs pour l'imagerie acoustique et la biologie synthétique. Mais que sont exactement les vésicules de gaz ?

Découvertes en 1895 par le microbiologiste allemand Heinrich Klebahn, puis observées pour la première fois en microscopie électronique par Bowen et Jensen en 1965, les vésicules de gaz sont des structures intracellulaires présentes chez de nombreuses espèces de bactéries et d'archébactéries aquatiques. Elles se présentent sous forme de cylindres creux aux extrémités coniques, mesurant de 200 à 1000 nm de long pour 45 à 200 nm de large. Leurs parois, épaisses de seulement 2 nm, sont constituées exclusivement de protéines et renferment un espace rempli de gaz. Lorsqu'elles sont produites, elles tendent à s'assembler en larges agrégats appelés « vacuoles de gaz ». À ce jour, environ 250 espèces de micro-organismes aquatiques producteurs de vésicules ont été identifiées. La plupart utilisent ces structures pour ajuster leur flottabilité et se déplacer verticalement dans la colonne d'eau afin d'atteindre des conditions de croissance optimales. Des études phylogénétiques suggèrent que leur apparition est antérieure à la séparation entre bactéries et archébactéries.

Les vésicules de gaz sont produites par l'expression d'opérons comprenant une quinzaine de gènes dont la composition et la régulation varient selon les espèces. Pourtant, elles ne sont constituées que de deux protéines structurales majeures : GvpA et GvpC. GvpA constitue l'élément principal des parois, formées par l'assemblage de ses monomères, qui comportent des pores permettant aux gaz dissous de circuler librement. GvpC, non indispensable à la formation, renforce néanmoins la structure en se fixant à la surface externe et améliore ainsi la tolérance aux pressions élevées. Au cours de la dernière décennie, les vésicules de gaz ont émergé comme des outils polyvalents en recherche biologique. Elles possèdent en effet des propriétés acoustiques similaires à celles des microbulles couramment utilisées en imagerie médicale comme agents de contraste : elles génèrent de forts échos, notamment dans les harmoniques, permettant une détection spécifique in vivo. Elles présentent toutefois plusieurs avantages supplémentaires. Entièrement protéiques, elles peuvent être modifiées génétiquement pour ajuster leurs propriétés acoustiques et peuvent être produites par différents organismes, tels que des espèces bactériennes, des levures et des cellules mammifères. Leur structure rigide leur confère par ailleurs une stabilité prolongée, leur permettant de se maintenir pendant des heures, voire des jours, en conditions in vivo. Enfin, une fois isolées, leur petite taille leur permet de diffuser hors de la circulation sanguine et à l'intérieur de tumeurs solides. Ces caractéristiques ouvrent la voie à un large éventail d'applications : agent de contraste en

imagerie acoustique, cavitation induite par ultrasons in vivo, porteur d'antigène pour la vaccination, neuromodulation par ultrasons, etc. Parmi celles-ci, l'une des plus prometteuses est leur utilisation comme agents de contraste échographiques génétiquement encodés, véritables équivalents acoustiques des protéines fluorescentes telles que la GFP. Cette approche peut permettre de localiser des cellules modifiées ou de suivre l'expression de leurs gènes même lorsqu'elles sont dans un environnement ne permettant pas d'utiliser la fluorescence ou la bioluminescence, comme c'est le cas en profondeur dans les tissus d'un animal. Cela est particulièrement intéressant pour le suivi de bactéries thérapeutiques génétiquement modifiées, que ce soit dans le traitement du cancer ou dans l'étude du microbiote intestinal.

Toutefois, l'impact de leur production hétérologue sur la physiologie de l'hôte demeure peu étudié, alors même que de nombreuses applications reposent sur leur expression dans des organismes non natifs.

L'objectif de ma thèse a été de combler cette lacune en étudiant les impacts physiologiques de ces rapporteurs acoustiques génétiquement encodés chez *Escherichia coli*, un hôte particulièrement pertinent dans le contexte des thérapies bactériennes anticancéreuses et de la biologie synthétique. J'ai principalement examiné deux aspects : l'effet sur la croissance et les conséquences de l'encombrement moléculaire lié à l'accumulation cytoplasmique de vésicules. Ce manuscrit est organisé en trois chapitres, les deux premiers étant rédigés sous la forme d'articles de recherche et visant à être publiés indépendamment.

Dans le premier chapitre, j'ai étudié la croissance de souches d'*E. coli* produisant des vésicules sous induction à l'arabinose. J'ai mesuré leurs courbes de croissance en culture discontinue pour différents niveaux d'induction et, en parallèle, quantifié l'abondance et la taille des agrégats. Parce que les vésicules de gaz diffusent la lumière, leur présence altère les mesures de densité optique habituellement utilisées pour quantifier le nombre de bactéries dans un échantillon. Pour contourner ce problème, j'ai donc compté les bactéries directement dans une chambre de Helber. J'ai pu obtenir une mesure de la proportion des cellules contenant des agrégats de vésicules et mesurer la taille de ces agrégats à partir d'images de microscopie optique à fond clair, dans lesquelles ils apparaissent comme des taches brillantes dans la cellule. Ces expériences ont révélé plusieurs effets majeurs. D'abord, le nombre final de cellules est inversement corrélé au degré d'induction et à la quantité de vésicules produites, révélant une baisse du rendement de production de biomasse pour une quantité de nutriments donnée. De plus, le taux de croissance diminue avec l'induction de la production de vésicules de gaz, mais uniquement aux plus forts niveaux d'induction et après plus de six heures de culture. Enfin, les bactéries produisant des vésicules sont anormalement longues, signe d'un stress important de la cellule. Ces résultats mettent en évidence un effet délétère de la production de vésicules sur la croissance. Cependant, ils pourraient ne pas refléter fidèlement les dynamiques présentes dans des environnements in vivo plus complexes, comme le microbiote intestinal ou les tumeurs solides, où les bactéries se développent en colonies et non en culture liquide homogène. Pour affiner cette analyse, j'ai donc développé une puce microfluidique permettant la croissance de colonies bactériennes bidimensionnelles alimentées en continu par un milieu de culture frais. Ce dispositif reproduit les gradients émergeant spontanément dans les colonies bactériennes. J'y ai

suivi la croissance et la production de vésicules et de biomasse pendant jusqu'à 31 heures, avec différents degrés d'induction. Mes expériences montrent que la production de vésicules réduit la vitesse de croissance et le rendement en biomasse pour une quantité donnée de nutriments, et favorise l'apparition de sous-populations de cellules ne produisant plus de vésicules. Tous ces effets sont proportionnels au degré d'induction. Ainsi, mes résultats confirment que, bien que les vésicules de gaz soient de puissants outils pour l'imagerie acoustique, leur production impose une charge importante aux cellules hôtes, ce qui n'avait jamais été quantifié jusqu'à présent. Ces observations soulignent la nécessité d'optimiser les systèmes d'expression hétérologues et de concevoir de nouveaux circuits de biologie synthétique afin de réduire cette charge, notamment pour les applications nécessitant viabilité et stabilité cellulaire à long terme.

Dans le deuxième chapitre, j'ai étudié un autre aspect de l'impact des vésicules : la persistance face aux antibiotiques. La persistance chez les bactéries est définie comme la capacité d'une partie d'une population bactérienne, sans mutation génétique, à survivre à une exposition à un antibiotique et à reprendre la croissance une fois que celui-ci n'est plus présent. J'ai montré que les cellules produisant et accumulant des vésicules étaient plus persistantes face à des traitements à la tobramycine, avec jusqu'à 10 000 fois plus de cellules persistantes chez les populations avec l'induction la plus forte par rapport à celles sans induction. À l'échelle de la bactérie, les vésicules de gaz sont volumineuses et des dizaines peuvent s'accumuler en une seule cellule, affectant l'encombrement moléculaire dans le cytoplasme. Or, l'augmentation de l'encombrement moléculaire du cytoplasme peut induire des changements physiologiques. J'ai donc émis l'hypothèse que cette accumulation pouvait expliquer l'augmentation de persistance en induisant une augmentation de l'encombrement moléculaire du cytoplasme qui, à terme, affecte la physiologie de la cellule. En utilisant de la microscopie de phase quantitative, j'ai quantifié le volume cellulaire occupé par les agrégats de vésicules de gaz et mis en évidence une forte corrélation entre le volume moyen de gaz par cellule dans une population et la proportion de cellules persistantes dans la tobramycine. De façon intéressante, cette relation est exponentielle, suggérant une possible transition de phase colloïdale du cytoplasme, un phénomène observé lors de l'augmentation de l'encombrement moléculaire. Ces résultats indiquent donc que l'accumulation de vésicules, en augmentant l'encombrement moléculaire du cytoplasme, peut contribuer à l'émergence de cellules persistantes. Ils démontrent ainsi que les propriétés biophysiques du cytoplasme peuvent constituer un facteur clé dans ce phénomène.

Enfin, dans un dernier chapitre, je présente deux projets méthodologiques parallèles visant à élargir les outils disponibles pour l'étude des vésicules. J'ai, d'une part, établi au sein de l'équipe de recherche des méthodes pour travailler avec des sphéroïdes et les faire coloniser par des bactéries, notamment en vue d'applications pour travailler sur des bactéries thérapeutiques contre le cancer. J'ai aussi développé une méthode, utilisant la transparisation des sphéroïdes et la microscopie confocale, permettant la localisation et la quantification des microcolonies bactériennes au sein de ces sphéroïdes. Cela offre par exemple la possibilité d'étudier la pénétration de différentes souches bactériennes dans différents types de tumeurs in vitro en trois dimensions. D'autre part, j'ai aussi développé une méthode pour observer des vésicules de gaz *in cellulo* par microscopie de super-

résolution (PALM). Pour cela, j'ai utilisé un plasmide encodant la production de vésicules de gaz dont la protéine GvpA est modifiée pour pouvoir se lier à FlAsH, un marqueur fluorescent. En me basant sur d'autres travaux ayant utilisé FlAsH en microscopie de super-résolution, j'ai appliqué et optimisé le protocole pour pouvoir observer les vésicules de gaz ayant des GvpA marquées. Bien que le signal obtenu se soit révélé trop faible pour distinguer la structure fine des vésicules, ce travail ouvre des perspectives sur l'observation optique de ces rapporteurs acoustiques, afin d'en faciliter l'étude et le développement.

Dans son ensemble, ce travail met en évidence les effets de l'expression recombinante de vésicules de gaz chez *E. coli*. Il apporte aussi des mesures quantitatives de ces effets ce qui n'avait jusqu'à présent pas été fait dans la littérature. Il constitue une étape clé pour passer de simples preuves de concept à des applications translationnelles concrètes, en particulier in vivo. Le manuscrit se conclut par des réflexions sur les perspectives visant à favoriser le développement et l'utilisation des vésicules de gaz en biologie synthétique et comme rapporteurs acoustiques génétiquement encodés.

Les annexes fournissent les protocoles détaillés de l'ensemble des expériences menées ainsi qu'un article de recherche, publié durant ma thèse et auquel j'ai participé en collaboration avec l'équipe de Mikael Tanter, portant sur la description d'une nouvelle technique d'imagerie acoustique pour les vésicules de gaz in vivo.

Appendix 7 : Amplitude-Modulated Singular Value Decomposition for Ultrafast Ultrasound Imaging of Gas Vesicles

Nonlinear Singular Value Decomposition Beamforming for Ultrasound Imaging of Gas Vesicles

Ge Zhang[1, ‡], Mathis Vert[1,2, ‡], Mohamed Nouhoum[1,2], Esteban Rivera[2], Nabil Haidour[1], Anatole Jimenez[1], Thomas Deffieux[1], Simon Barral[3], Pascal Hersen[3], Claire Rabut[4] , Mikhail G. Shapiro[4,5,6], Mickael Tanter[1,*]

[1] Physics for Medicine Paris, INSERM U1273, ESPCI Paris, PSL University, CNRS, Paris, France

[2] Iconeus, Paris, France

[3] Institut Curie, Université PSL, Sorbonne Université, CNRS UMR168, Laboratoire Physico Chimie Curie, Paris, France

[4] Division of Chemistry and Chemical Engineering, California Institute of Technology, Pasadena, USA

[5]Andrew and Peggy Cherng Department of Medical Engineering, California Institute of Technology, Pasadena, USA

[6] Howard Hughes Medical Institute, California Institute of Technology, Pasadena, USA

[‡] These authors have contributed equally to this study

[*] Correspondence: Mickael Tanter

Abstract

Ultrasound imaging holds significant promise for the observation of molecular and cellular phenomena through the utilization of acoustic contrast agents and acoustic reporter genes. Optimizing imaging methodologies for enhanced detection represents an imperative advancement in this field. Most advanced techniques relying on amplitude modulation schemes such as cross amplitude modulation (xAM) and ultrafast amplitude modulation (uAM) combined with Hadamard encoded multiplane wave transmissions have shown efficacy in capturing the acoustic signals of gas vesicles (GVs). Nonetheless, uAM sequence requires odd- or even-element transmissions leading to imprecise amplitude modulation emitting scheme, and the complex multiplane wave transmission scheme inherently yields overlong pulse durations. xAM sequence is limited in terms of field of view and imaging depth. To overcome these limitations, we introduce an innovative ultrafast imaging sequence called nonlinear singular value decomposition (SVD) beamforming. Our method demonstrates a contrast imaging sensitivity comparable to the current gold-standard xAM and uAM, while requiring 4.8 times fewer pulse transmissions. With a similar number of transmit pulses, nonlinear SVD beamforming outperforms xAM and uAM in terms of an improvement in signal-to-background ratio of + 4.78 ± 0.35 dB and + 8.29 ± 3.52 dB, respectively. Additionally, our method provides a higher flexibility in terms of the selection of acoustic pressure amplitude compared to the other methods. Furthermore, Nonlinear SVD imaging is envisioned to be applicable for the detection of slow moving microbubbles in ultrasound localization microscopy (ULM).

Keywords: Singular value decomposition; Gas vesicles; Ultrasound nonlinear imaging.

1. Introduction

Ultrasound plays a pivotal role in biomedical imaging, providing non-invasive, real-time visualization with high spatial and temporal resolution [1]. The recent development of acoustic reporter genes has significantly expanded the capabilities of ultrasound imaging for observing cellular processes and molecular interactions

[2, 3]. Acoustic biomolecular contrast agents, commonly known as gas vesicles (GVs), have demonstrated substantial potential in a wide range of biomedical applications [4]. These GVs are typically filled with air and encapsulated by a 2-nm-thick protein shell [5-7], possessing respective diameter and length of approximately 85 nm and 500 nm [8]. Previous studies have revealed that certain types of GVs exhibit a strongly nonlinear response to acoustic pressure (e.g. 0.2 – 0.6 MPa), resulting in nonlinear backscattering of ultrasound waves [9, 10]. This nonlinear behavior enables enhanced detection sensitivity and specificity of acoustic contrast agents, such as GVs, utilizing various nonlinear ultrasound imaging paradigms like amplitude modulation [11].

Both the parabolic amplitude modulation (pAM) [12] and cross-propagating amplitude modulation (xAM) [13] pulse sequences entail line-by-line transmissions of the imaging object, requiring three pulses with relative amplitudes of 1/2, 1/2, and 1 to be pre-calibrated in advance and transmitted during imaging [14]. However, both pAM and xAM pulse sequences are constrained by their imaging depth and framerate, limiting their ability for capturing fast nonlinear events and cancelling tissue motion artifacts, especially within deep tissues. In response to these limitations, Rabut et al. introduced ultrafast amplitude modulation (uAM), an imaging technique amalgamating amplitude modulation, multiplane wave transmission, and selective coherent compounding [15]. This innovation enables the acquisition of nonlinear images after successive transmission of tilted, amplitude-modulated plane waves. It has been demonstrated that the uAM method is capable of achieving ultrafast acquisition of larger and deeper fields of view compared to the other existing techniques for imaging GVs. Nevertheless, this method necessitates odd- and even-element transmissions to generate pulses of relative amplitudes 1/2. Additionally, the imaging scheme involving multiplane wave transmission not only amplifies the complexity of transmission and reception but also strongly elevates the spatial peak temporal average intensity (I_{SPTA}) due to prolonged transmit pulses, even at the same mechanical index. Therefore, there is a compelling need to streamline the ultrafast nonlinear imaging scheme to facilitate seamless integration into current ultrasound imaging systems.

To address these challenges, we introduce ultrafast nonlinear singular value decomposition beamforming, a nonlinear imaging paradigm inspired by singular value decomposition beamforming for ultrafast ultrasound imaging [16]. In the last decade, the use of singular value decomposition of ultrasound raw data has been shown to outperform most conventional filtering approaches for the improvement of ultrasound images. First, in linear acoustics, it was shown to discriminate tissue motion from blood flow in ultrafast ultrasound datasets based on spatio-temporal coherence [17] leading to ultrasensitive Doppler imaging. Then, singular value decomposition (SVD) processing of ultrafast compounded plane wave acquisitions was also shown able to improve ultrasound B-mode image quality in the presence of aberrations by estimating the optimal aberration correction law required to produce ultrasound images similar with different plane wave transmit angles [16] or different diverging waves transmissions [18]. Finally, SVD beamforming was applied successfully to retrieve sound speed estimates in ultrasound data and applied successfully in the framework of liver steatosis [19, 20]. SVD beamforming can also be applied to recombine ultrasound images acquired with distinct probes [21, 22]. In the field of nonlinear imaging, higher-order SVD of ultrasonic signals acquired at different pressure levels and different temporal acquisitions was recently proposed to detect moving microbubbles [23]. However, it still relies on the flowing contrast signals. Here, we propose a new nonlinear SVD beamforming approach that does not require any assumption on the motion of contrast agents or GVs. This imaging sequence acquires frames across various acoustic pressure levels. Subsequently, all the frames acquired at the selected pressure levels are concatenated in a Casorati matrix form for SVD processing. Specific modes of the corresponding singular vectors are then selected to reconstruct the final image with high-contrast signals.

The objective of this study is to develop an ultrafast nonlinear SVD beamforming technique that is anticipated to significantly streamline the transmission pulse sequence while achieving better contrast imaging sensitivity and significantly lower acoustic transmission energy compared to the state-of-the-art uAM and xAM imaging schemes. In this study, simulations based on a simple model of backscattered ultrasonic signals in the presence of GVs, speckle noise and background noise were firstly conducted to demonstrate the limitations of the amplitude modulation scheme and the feasibility of utilizing SVD for nonlinear imaging. Subsequently, an *in vitro* gas vesicle phantom was fabricated to validate the pulse sequence and the corresponding post-processing strategies. Signal-to-background ratio (SBR) were employed as image evaluation metric to assess the contrast signal in comparison to the uAM and xAM methods.

2. Materials and Methods

2.1. Simulation

The phantom was simulated using Matlab (Matworks, USA), as depicted in Figure 1. The final simulated in-phase quadrature (IQ) data, is basically comprised of three matrices describing the spatial distribution of tissue signal, S_{Tissue}, gas vesicle signals, $\mathrm{S_{GV}}$, and random noise signals, $\mathrm{S_{Noise}}$, respectively. The backscattering amplitudes of GVs, $\mathrm{B_{GV}}$, and tissue signals, $\mathrm{B_{Tissue}}$, were simulated with respect to the pressure amplitudes, p . Thus, the IQ data can be mathematically expressed as function of spatial and pressure variables:

$$\mathrm{IQ(x,z,p)} = \mathrm{A_{Tissue}} \times \mathrm{B_{Tissue}(p)} \times S_{Tissue}(\mathrm{x,z}) + \mathrm{A_{GV}} \times \mathrm{B_{GV}(p)} \times \mathrm{S_{GV}(x,z)} + \mathrm{A_{Noise}} \times \mathrm{S_{Noise}(x,z)}$$

where $\mathrm{A_{Tissue}}$, $\mathrm{A_{GV}}$, and $\mathrm{A_{Noise}}$ are the scalars which represent the amplitude values of tissue, gas vesicle, and noise components, respectively. $\mathrm{B_{Tissue}}$ and $\mathrm{B_{GV}}$ are the amplitude responses to pressure ramp along the curves which demonstrated the relationship between backscattering amplitude and pressure amplitude as shown in Figure 1(e). It has been noted in prior research that tissue may exhibit a nonlinear signal due to the nonlinear propagation of ultrasound waves within tissues [24].

The backscattering amplitude of gas vesicle signal, as well as both linear and nonlinear tissue signals, were simulated against various acoustic pressure amplitudes. The response from amplitude modulation at the acoustic pressure amplitude, p can be mathematically expressed as:

$$\mathrm{AM(x,z,p)} = \mathrm{IQ(x,z,p)} - 2 \times \mathrm{IQ(x,z,p/2)}$$

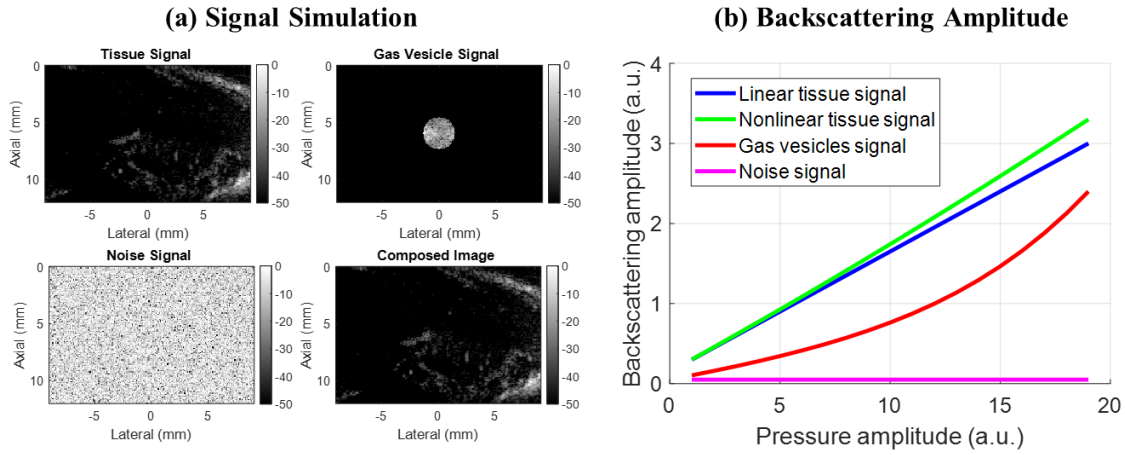

Figure 1. Simulation of ultrasound image composed of tissue, gas vesicle, and noise signals; (b) Backscattering amplitude of tissue signal and gas vesicle signal with respect to pressure amplitude.

2.2. Experimental Setup

Nonlinear GVs were prepared following the methodology outlined in Rabut et al. [15]. In brief, GVs were extracted from buoyant Anabaena flos-aquae cells through hypertonic lysis and subsequently purified by repeated centrifugally assisted flotation and resuspension. The outer GvpC layer of the GVs was then removed through treatment with 6M urea, followed by additional round of centrifugally assisted flotation, dialysis in 1x PBS and resuspension to remove residual GvpC and urea [2].

A tissue-mimicking gas vesicle phantom for imaging was fabricated by casting 1% (w/v) agarose in PBS supplemented with 0.2% (w/v) Al_2O_3. For static imaging, a custom 3D-printed mold was employed to create a cylindrical well with a 2 mm diameter. GVs were incubated at 60 °C for 1 minute, mixed in a 1:1 ratio with molten agarose, resulting in a final gas vesicle concentration equivalent to 3 OD500nm, and loaded into the phantom. The Al_2O_3 concentration was carefully selected to match the scattering echogenicity of the gas vesicle well. This well was precisely centered at a depth of 6 mm. The schematic diagram for *in vitro* setup can be seen in Fig. 2(a).

2.3. Data Acquisition

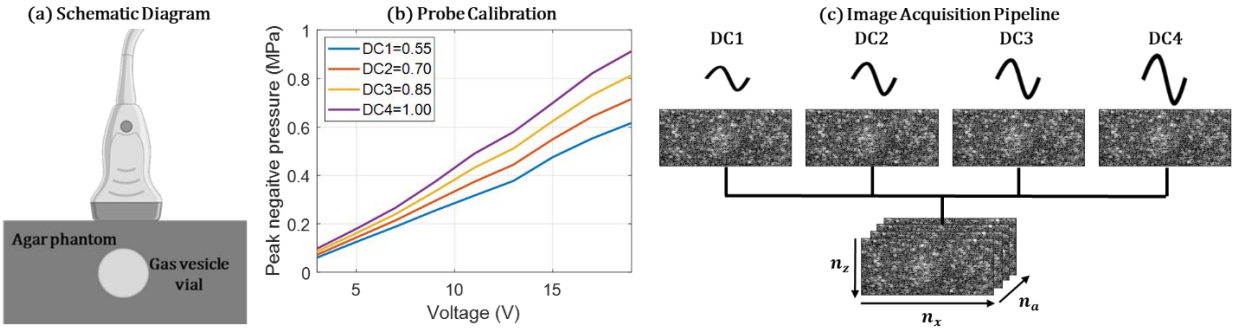

Figure 2. (a) Schematic diagram of the *in vitro* experimental setup; (b) Experimental calibration of the probe used for transmitting pulses with four different duty cycles used for the definition of the transmit signal; (c) Schematic diagram of pulse sequence applied for the image acquisition. Four images acquired with four different duty cycles were used for further image processing.

For image acquisition, ultrasound sequences were implemented and executed on a research ultrasound system (Verasonics, USA) driving a linear ultrasound transducer (128 elements, 15.625 MHz central frequency and a 67% bandwidth at -6 dB). All acquisition scripts and processing codes were developed in Matlab (Matworks, USA). The peak-negative-pressure was increased from 0.1 to 0.8 MPa for the transmission pulses based on the calibration result displayed in in Fig. 2(b).

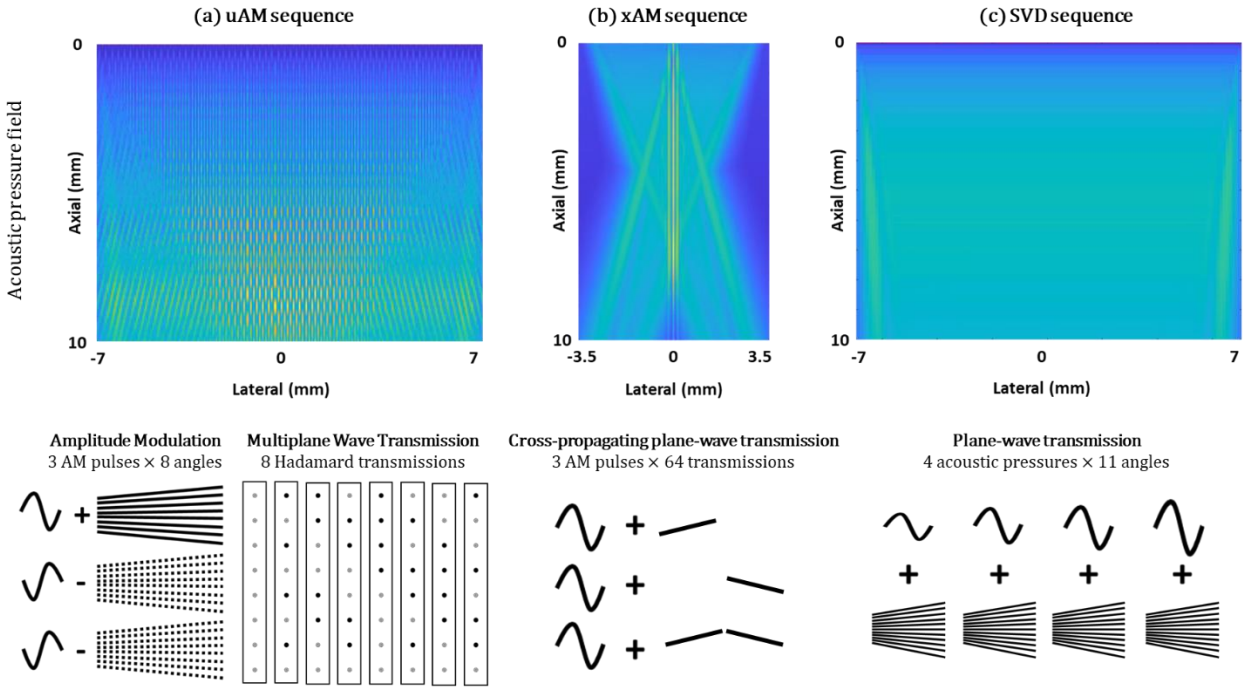

Figure 3. Illustration of (a) uAM pulse sequence, (b) xAM pulse sequence, and (c) nonlinear SVD beamforming pulse sequence, respectively.

xAM and uAM pulse sequences utilized in this study for comparison with nonlinear SVD beamforming have been visually represented in Figure 3. The number of pulses and transmissions between three different imaging sequences were compared and demonstrated in Table 1.

In the uAM pulse sequence as shown in Figure 3(a), eight successive tilted plane waves with a transmission frequency of 15.625 MHz were repeated three times with modulated amplitude: two pulses at half amplitude (achieved by silencing the odd and even elements of the transducer, respectively) and one pulse at full amplitude. These sets of modulated pulses were then reiterated eight times. For each repetition, the polarities of the successive plane waves were determined by the column of the Hadamard matrix of order eight.

In the xAM pulse sequence as shown in Figure 3(b), the xAM splits all the 128 elements into two sub-apertures, the first half sub-aperture (element 1-64) and the second sub-aperture (element 65-128). First, the first sub-aperture was used to transmit a tilted plane wave with a transmission frequency of 15.625 MHz at an angle of 19.5° with respect to the array which was optimized in the previous study [13]. Then the second sub-aperture was used to transmit a symmetric plane wave at the same angle with respect to the array. Finally, the two previous two plane waves were transmitted simultaneously.

In the nonlinear SVD beamforming pulse sequence as shown in Figure 3(c), single-cycle plane waves were transmitted at a frequency of 15.625 MHz, with 11 compounded angles for each pulse with an angle range from -10° to +10°. Then the pulses were repeated for 4 different duty cycles as previously calibrated and shown in Figure 2(b).

After the acquisition of ultrasonic raw data using these three imaging sequences, the radio frequency data were offline beamformed using a delay-and-sum beamformer on GPU, utilizing a resolution grid with a spacing of 0.5λ, resulting in the generation of IQ data.

Table 1. Comparison of the number of pulses and transmissions between different pulse sequences. N represents the number of pressure amplitude utilized in nonlinear SVD beamforming.

Sequence type	Number of waveforms	Number of transmissions	Number of pressure amplitude	Hadamard Encoding	Number of pulses
SVD (N=4)	1	11	4	0	44
SVD (N=16)	1	11	16	0	176
uAM	3	8	1	8	192
xAM	3	64	1	0	192

2.4. Nonlinear Singular Value Decomposition Beamforming

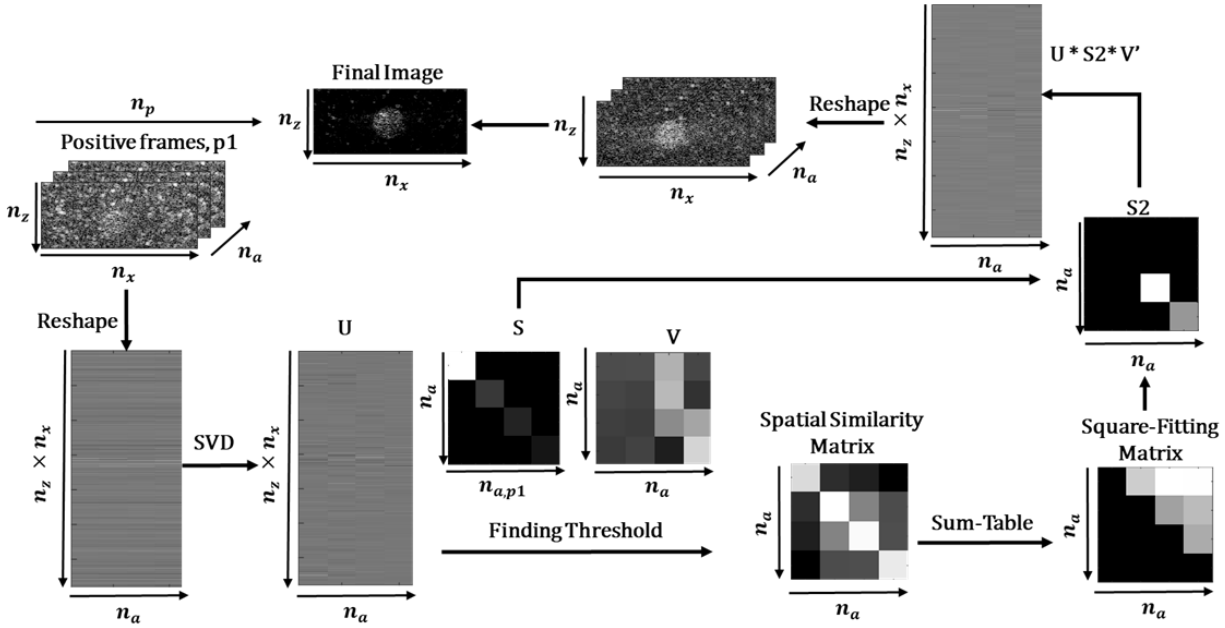

Figure 4. Processing pipeline of the nonlinear singular value decomposition beamforming.

The processing pipeline of the nonlinear SVD beamforming technique was developed and evaluated in this study. The acquired beamformed image series, IQ, in-phase/quadrature (IQ) data can be rearranged by concatenation of IQ image stacks as $IQ(x,z,a)$, where $IQ(x,z,a)$ represents the concatenated IQ data acquired at the different acoustic pressure amplitudes. x represents the lateral dimension, z represents the axial dimension, a represents the number of acoustic pressure amplitudes.

The singular value decomposition beamforming was performed to decompose the reshaped data of frames into a weighted, ordered sum of separable spatio-pressure modes expressed by U, S, and V as:

$$IQ(x,z,a) = \sum_{t1}^{t2} U S V'$$

where U and V are the corresponding matrices and S is the weighting matrix. U represent the spatial modes of the acquisition. V represent the pressure modes in this study.

The spatial matrix, U, was used to perform the threshold selection to generate the spatial similarity matrix and square-fitting matrix, respectively, to determine the values of t1 and t2 used in SVD processing as described in the previous study [25]. Briefly, the spatial similarity matrix is obtained from the covariance of modules of the spatial singular vectors, U. Two square-like domains are demonstrated along the diagonal of the spatial similarity matrix, representing the tissue background and the contrast signal subspaces in our study. Then, a square-fitting matrix was converted from the spatial similarity matrix to determine the SVD threshold t1 and t2. Then t1 and t2 were used to filter the weighting matrix, S, to generate a new weighting matrix, S2.

The original S matrix was replaced by the new matrix S2, to generate the SVD-filtered dataset, $g(x,z,a)$, which filtered out the tissue background signals:

$$g(x,z,a) = \sum_{t1}^{t2} U\,S2\,V'$$

The final image, $g(x,z)$ was generated by incoherently summing all the images at different acoustic pressure amplitudes as below:

$$g(x,z) = \sum_{a1}^{a1} |g(x,z,a)|$$

The detailed post-processing pipeline can be seen in Figure 4.

2.5. Optimal Selection of Acoustic Pressure

To fairly compare the performance of xAM, uAM, and SVD sequences, each method required to be performed under its optimum imaging pressure. In order to select the corresponding optimum imaging pressure, each sequence was repeated 100 times per second for the data acquisition at a single pressure level. Then the acoustic pressure amplitude was increased progressively from 0.15 to 0.80 MPa to determine when the GVs were destructed for three methods respectively. All the other imaging conditions were kept the same as previously described in the section 2.3. At the end, the optimal acoustic pressure for each sequence (without significant GV destruction) was used for imaging the same GV phantom to evaluate the performance of each sequence.

2.6. Image Evaluation

The parameter used for the evaluation of the image quality was signal-to-background ratio (SBR) evaluating the GV contrast as previously described in the literature [14]:

$$SBR = 20log_{10}\left(\frac{A_{Signal}}{A_{Background}}\right)$$

A_{Signal} is the mean amplitude of signal within the contrast region; $A_{Background}$ is the mean amplitude of signal within the tissue region.

3. Results

3.1. Simulation Results

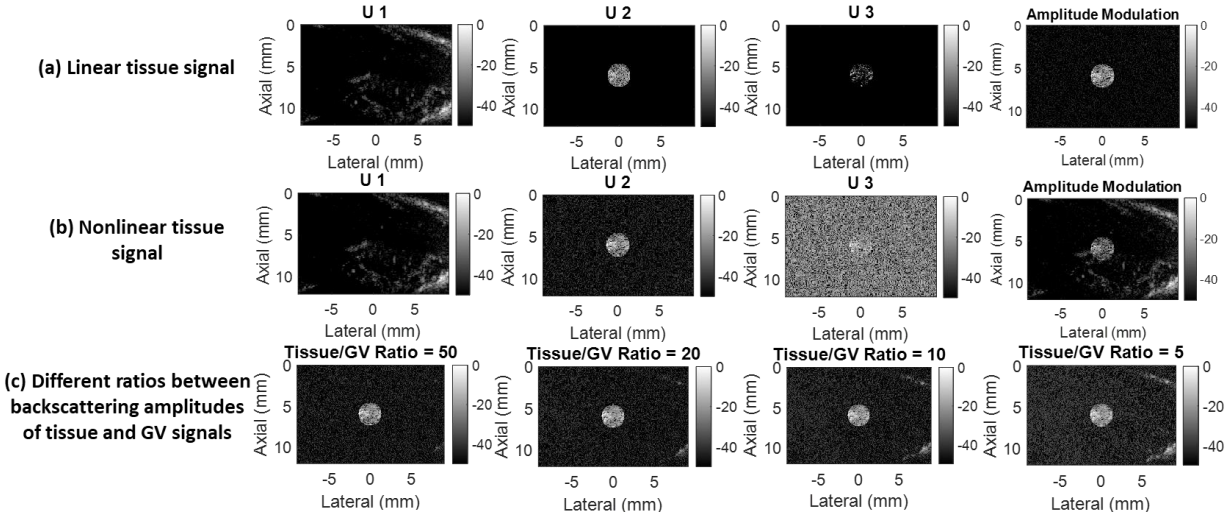

Figure 5. Simulation of nonlinear SVD beamforming on gas vesicle phantom and the first three spatial singular vectors and the corresponding amplitude modulation imaging. (a) when the tissue response is linear to the pressure; (b) when the tissue response becomes nonlinear. (c) The second spatial singular vectors when the ratios between backscattering amplitudes of tissue and GV signals are different.

The simulation results presented in Fig.5 show the comparison between the linear and nonlinear tissue signals. It can be seen that the conventional amplitude modulation method cannot completely remove the tissue signal when the tissue exhibits a nonlinear behavior. For the proposed SVD beamforming method, the tissue signals can be significantly removed in both cases of linear and nonlinear tissue behaviors. Fig. 5(c) presents the images obtained by nonlinear SVD beamforming for different ratios between backscattering amplitudes of tissue and GV signals. It can be seen that, the nonlinear SVD beamforming method can better extract the GV signal and suppress tissue signal at a higher ratio between backscattering amplitude of tissue and GV signals.

3.2. In Vitro Demonstration of nonlinear SVD beamforming

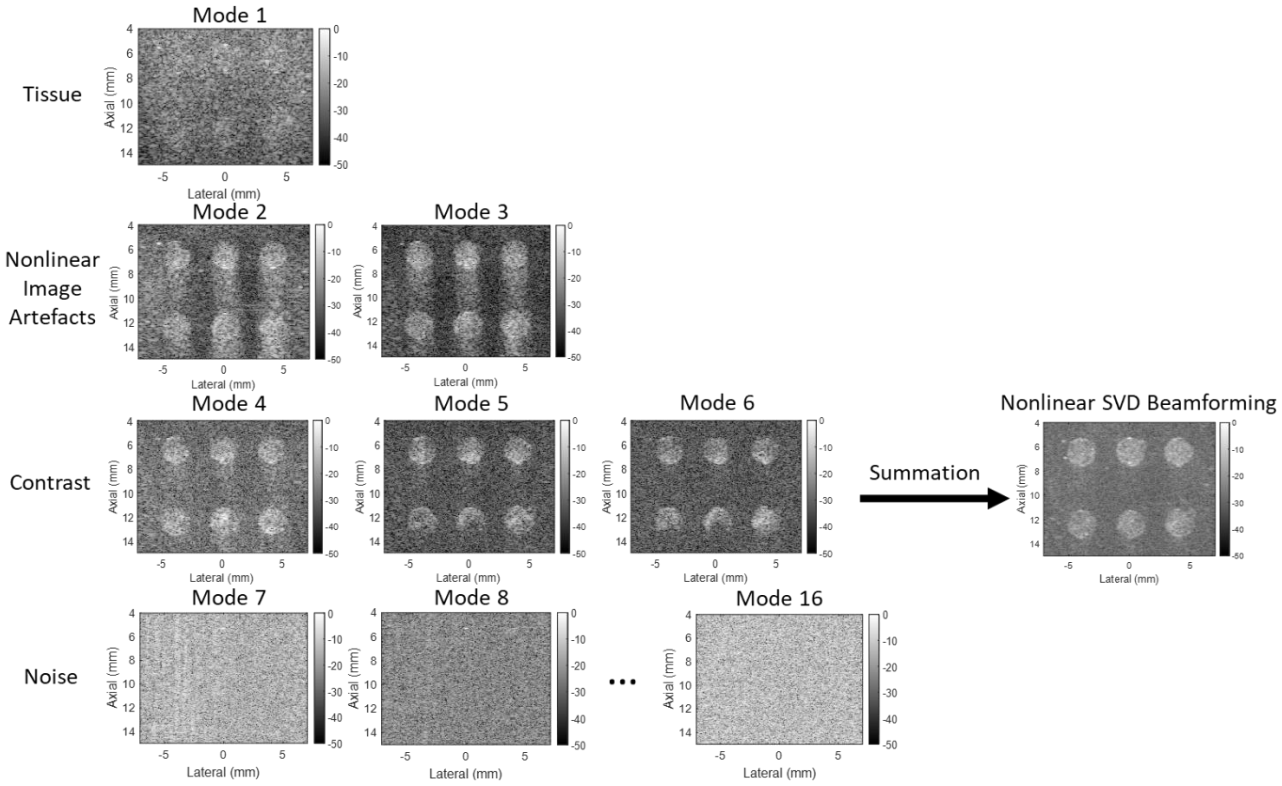

Figure 6. Visualization of the spatial matrix, U for each mode presented in nonlinear singular value decomposition beamforming. Nonlinear SVD beamforming is able to classify the modes into tissue, nonlinear image artefact, contrast, and noise signals. All the images are displayed with a dynamic range of -50 dB.

As can been seen from Figure 6, during the processing of nonlinear SVD beamforming, the input data was decomposed into various modes of spatial matrices, U_i. Each SVD mode contains different acoustic information which was derived from the original input data. It can be seen that mode 1 represents the tissue signal, i.e. the signal corresponding to highly similar data at different amplitudes. The image obtained in the following modes highlight the nonlinear response and thus the presence of GV inclusions and the nonlinear image artefacts appeared on the modes 2 and 3. In the modes 4 to 6, mainly the GV contrast signals were included. The noise signals are shown in the remaining modes.

3.3. Dependence on Number of Pressure Levels

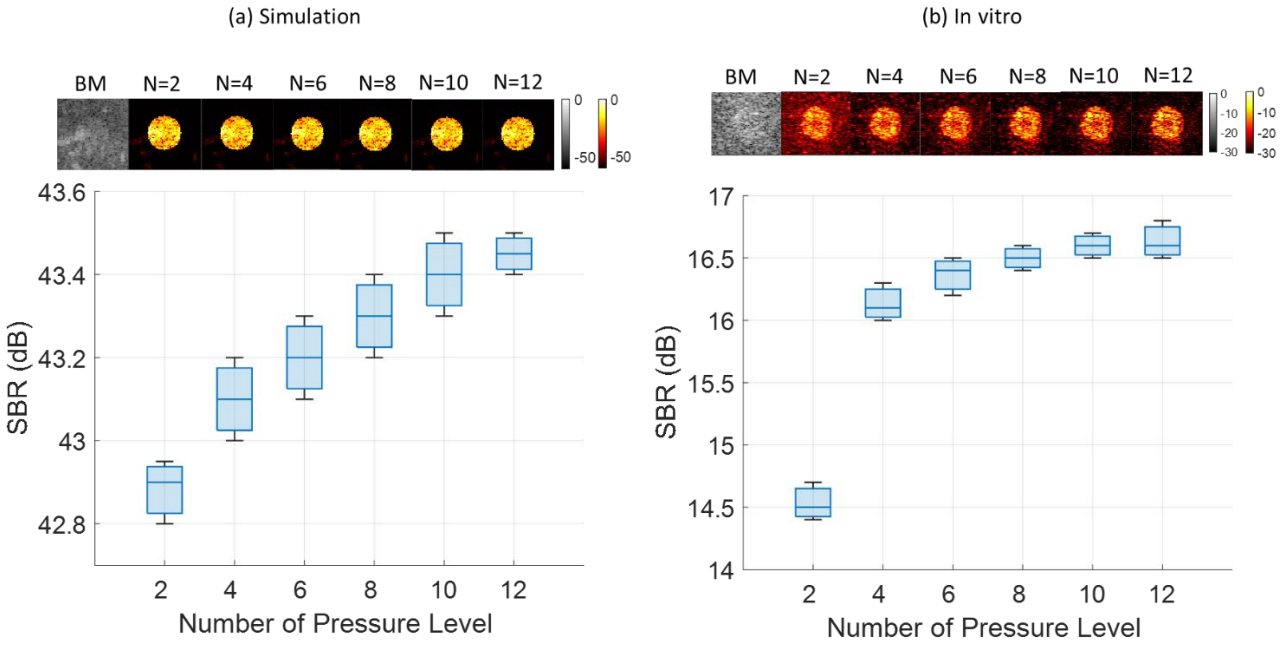

Figure 7. Effect of the number of pressure levels used in the nonlinear SVD beamforming. (a) Simulation images for different numbers of pressure levels; (b) *In vitro* images for different numbers of pressure levels; (c) Image quantification for simulation; (d) Image quantification for *in vitro* experiments.

As can be seen in Figure 7, SBR increased for the simulation results with respect to the number of pressure levels. For the *in vitro* experiments, the SBR level also increases with the number of pressure levels used for the acquisition. Experimental SBR tends to rapidly saturate for pressure levels larger than 4. A N=4 number of pressure levels was used in our further studies as it demonstrates a good contrast imaging sensitivity while it requires a smaller number of transmit pulses.

3.4. Optimal Selection of Acoustic Pressure

In order to select the corresponding optimum imaging pressure, each sequence was repeated 100 times per second for the data acquisition at a single pressure level. Then the acoustic pressure amplitude was increased progressively from 0.15 to 0.80 MPa to determine when the GVs were destructed for three methods respectively, which enabled a fair comparison by searching the optimal conditions for each technique. Then the value of SBR was quantified for each sequence at each pressure level along with the visualization of GV contrast.

(a) SVD Sequence

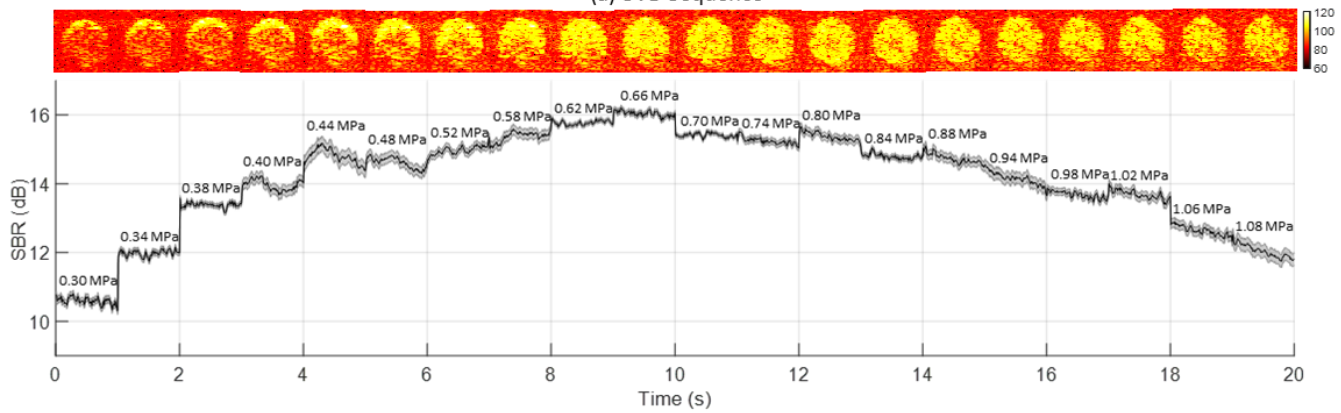

(b) uAM Sequence

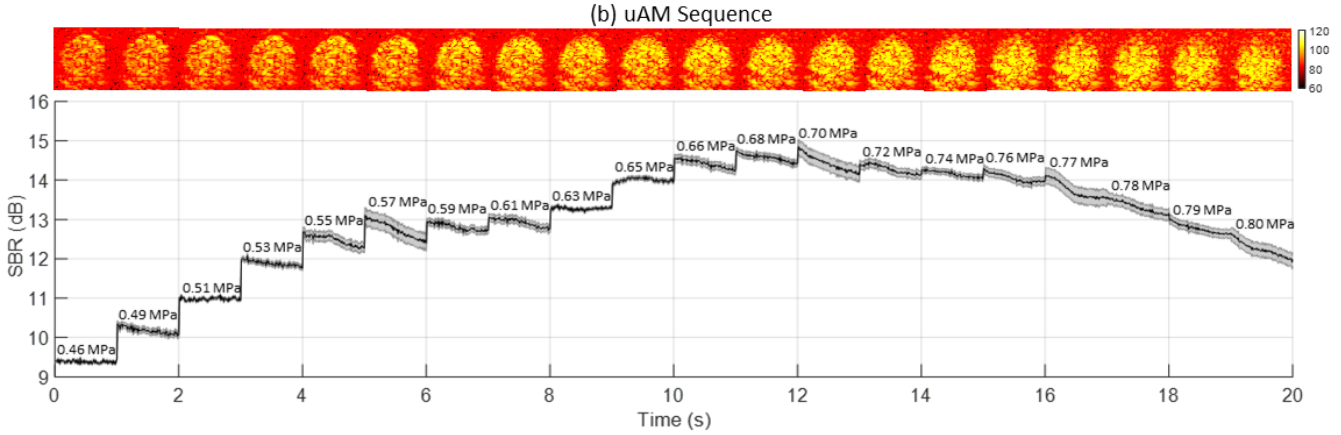

(c) xAM Sequence

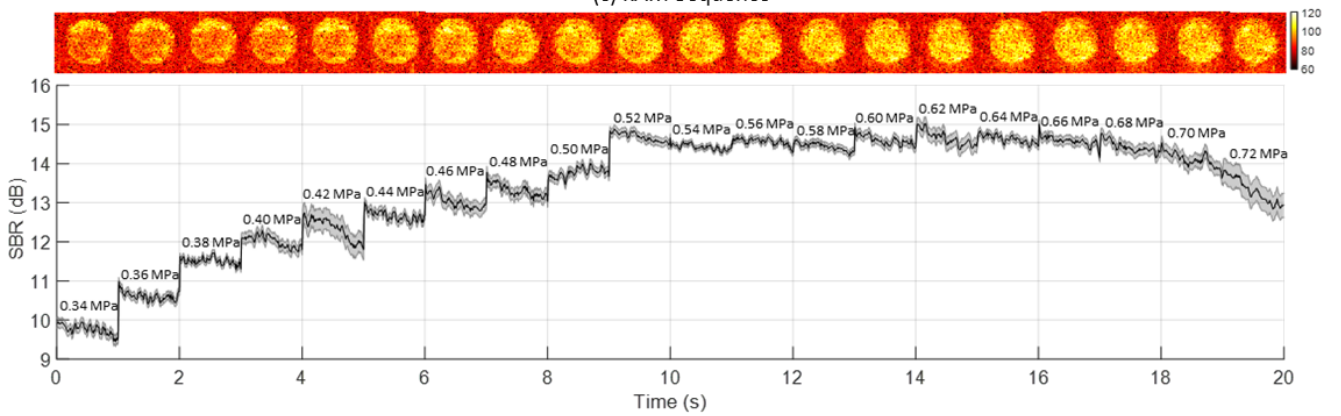

(d) SBR against maximum pressure

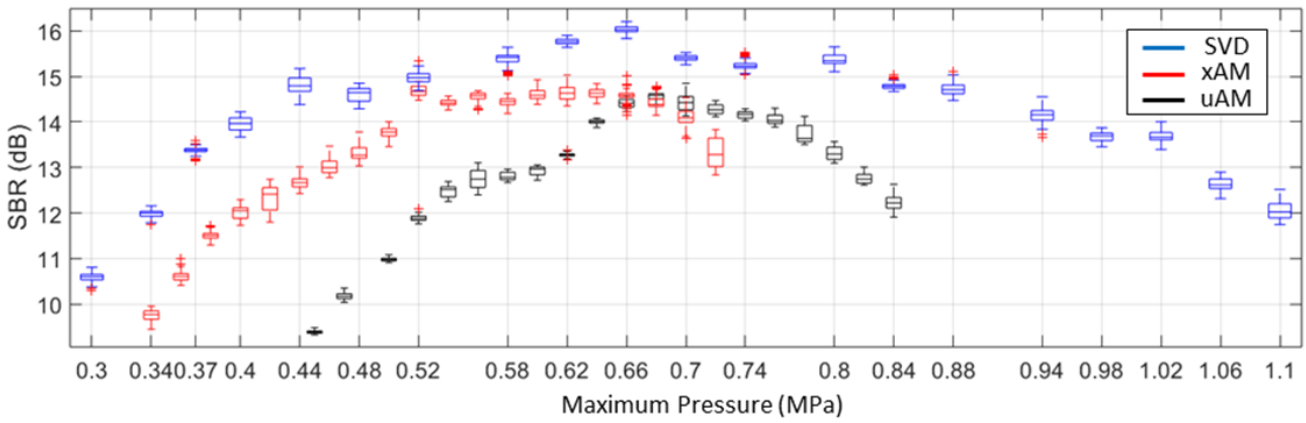

Figure 8. Quantification of signal-to-background ratio (SBR) and visualization of using (a) xAM, (b) uAM, and (c) nonlinear SVD beamforming techniques across the increasing acoustic pressures. The solid line and shaded error bar represent the mean and standard deviation values of SBR correspondingly. All the images are displayed with a dynamic range of -40 dB.(d) SBR across peak-negative-pressure ranged from 0.15 MPa to 0.80 MPa for the comparison of three imaging methods. Red, black, and blue box plots represent for xAM, uAM, and nonlinear SVD beamforming sequences respectively.

Figure 8 shows the images the corresponding SBR quantification of the three methods by progressively increasing the acoustic transmit pressures. At each pressure level, the acquisition was repeated for 100 times in 1 second in order to evaluate the potential loss of signal due to GVs progressive disruption. It can be seen that the optimum acoustic pressure required for nonlinear SVD beamforming to obtain the higher SBR is around 0.66 MPa. The SBR value remains high for nonlinear SVD beamforming on a wide range of transmit pressures (0.40-0.94 MPa above 14 dB) compared to uAM (0.65-0.77 MPa above 14 dB) and xAM (0.52-070 MPa above 14 dB). Additionally, the maximal SBR peaks for uAM and xAM appeared to be around 15 dB while our proposed method demonstrated a maximal SBR peak at 16 dB when only four different pressure levels were used.

3.5. Global Comparison between uAM, xAM and SVD sequences at optimal pressure

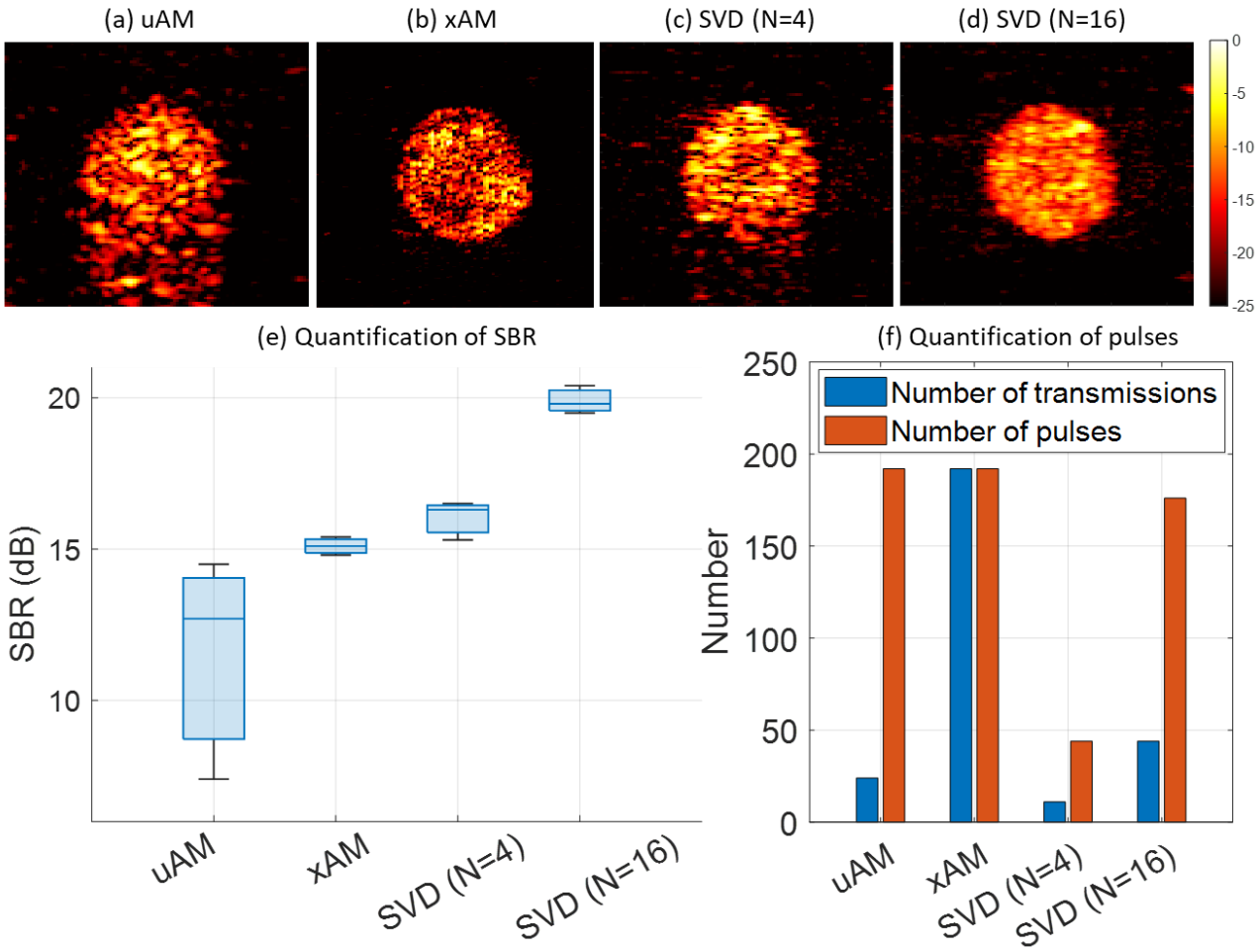

Figure 9. Comparison of *in vitro* GV phantom between uAM, xAM, and our proposed nonlinear SVD beamforming methods. (a) uAM image; (b) xAM image; (c) our proposed nonlinear SVD beamforming method using the number of pressure level of 4; (d) our proposed nonlinear SVD beamforming method using the number of pressure level of 16. All the images were displayed with a dynamic range of -25 dB. (e) Quantification of SBR between different methods. (f) Quantification of the number of transmissions and pulses used for each imaging acquisition.

The results shown in Figure 9 summarize the experimental comparison between xAM, uAM, and nonlinear SVD beamforming methods to extract the GV signals. The optimal acoustic pressures for each imaging methods were found out in Figure 8 and applied for a fair comparison. It can be seen that, uAM image demonstrates a good tissue background suppression capability and a good contrast enhancement of GV signals. However, strong nonlinear imaging artefacts remain present below the GV inclusion. The xAM image demonstrates better axial and lateral resolution and boundary detection of the GV contrast. The nonlinear SVD beamforming method exhibits a higher SBR compared to uAM and xAM methods when the number of pressure level is equal to 4 (Fig 9.c, d, e). For this number of pressure levels, our nonlinear SVD beamforming method required 4.4 times less number of pulses (respectively xx and xx transmits) to achieve such a performance. When a higher number of pressure levels (N=16) was used for nonlinear SVD beamforming in order to reach comparable numbers of transmit pulses, the resulting images were further optimized and provided higher contrast and more tissue background suppression compared to uAM and xAM. The detailed comparison of the number of pulses and transmissions for each method can be seen in Figure 9(f).

4. Discussion

In this study, we introduce a new nonlinear ultrasound imaging method exploiting the singular value decomposition of ultrafast plane wave compounded data acquired at different pressure amplitude levels. The SVD processing applied to these backscattered ultrasound signals comprising the nonlinear signature of GVs and nonlinear propagation in surrounding tissues extracts independent images, each exhibiting a different nonlinear dependence with respect to the transmit amplitude. The cancellation of high-order singular value component permits to filter the signals backscattered by tissues and select the nonlinear signals originating from GVs. It is anticipated that our proposed nonlinear SVD beamforming technique will enhance contrast detection and suppress tissue background signals, particularly in scenarios involving strong nonlinear tissue signals and the absence of motion of GVs or microbubbles. The outcomes of both simulations and *in vitro* experiments demonstrate the better contrast detection capabilities of the proposed method while requiring 4.4 times less pulse transmissions or I_{spta} compared to the state-of-art uAM and xAM imaging techniques.

Furthermore, the nonlinear SVD beamforming method helps to remove the nonlinear imaging artefacts which have been previously reported in AM images in the literature [13, 15, 26]. These nonlinear imaging artefacts are inevitable for images based on conventional AM schemes. These artefacts are due to suboptimal ability of AM schemes based on odd/even transmits to cancel linear components of the propagation. It can be seen from Figure 6 that the SVD decomposition process decomposes the spatial modes into four different categories, which are tissue background signals, nonlinear imaging artefacts, GV contrast, and noise. As tissue signals, nonlinear imaging artefacts, and GV contrast signals exhibit different degrees of nonlinearity, SVD processing is able to decompose and rearrange the spatial matrices according to their different degrees of nonlinearity.

In order to provide sufficient sensitivity, the uAM method requires to implement the multiplane wave Hadamard encoding technique for gas vesicle imaging. It involves a notably larger number of pulses and transmissions within the imaging protocol. A prior study demonstrated that, this approach yields a higher spatial peak temporal average intensity (I_{SPTA}) owing to the longer transmit pulses [27]. Additionally, it can be seen from Figure 8 that uAM required significantly higher peak-negative-pressure (PNP) to obtain the highest SBR, which may affect its performance *in vivo* when there will be more attenuation of the transmission pressure.

The xAM method exploits the cross propagation of plane waves tilted at a certain angle with respect to the transducer array. Although the xAM image demonstrated a superior image resolution and the boundary detection of GV contrast due to the nature of its focused-shape transmission, its imaging depth, lateral field of view and frame rate are also limited by the intrinsic nature of its transmission scheme. As can be seen from Figure 3(b), the maximum imaging depth is limited at around 8 mm as the angle of sub-aperture plane wave transmission with respect to the transducer array was set as 19.5° as optimized in the previous study [13]. The lateral field of view is limited to the 64 central lines of the ultrasonic B-mode image.

One major advantage of nonlinear SVD beamforming compared to the other conventional AM schemes stands in the fact that the exact transmit pressure amplitude levels do not require to be precisely known and calibrated. Nonlinear SVD beamforming extracts this information without prior knowledge. It is a strong advantage compared to conventional AM transmission schemes that require an exact ½ amplitude transmission. For uAM, the subtraction step faces another additional drawback. The use of odd and even elements transmission in conventional nonlinear ultrasound creates a background noise as the subtraction of odd and event backscattered signals does not reach zero for the linear propagation content.

In this study, a total of four pressure levels were found sufficient to reach high quality images and employed for most data acquisitions as shown in figure 6. Firstly, it demonstrated the highest SBR value among the group. Secondly, it required the fewest number of pulses and transmissions when compared to all the other larger pressure levels and can be achieved at ultrafast frame rates. If sensitivity is favored compared to frame rate, the number of transmit amplitudes can be increased. As shown with 16 transmit amplitudes corresponding to a similar number of transmit pulses compared to xAM and uAM, the imaging sensitivity of nonlinear SVD beamforming is further improved reach even higher image quality (+6 dB compared to AM schemes).

As can be observed in Figure 8 that, the SBR value remains high for nonlinear SVD beamforming on a wide range of maximal transmit pressures (0.40-0.94 MPa above 14 dB) compared to uAM (0.65-0.77 MPa above 14 dB) and xAM (0.52-070 MPa above 14 dB). This demonstrates that nonlinear SVD beamforming is much less sensitive to a non-optimal selection of transmission amplitude. Thus, it provides more flexibility in terms of the selection of transmission amplitude. Additionally, for one selected transmission amplitude, the amplitude will strongly vary *in vivo* due to tissue attenuation in depth. Nonlinear SVD beamforming method will be less sensible to this issue than the other two methods.

The nonlinear SVD beamforming method proposed exploits here the concept of coherence in a new way. The acquisitions and processing permits to discriminate the pixels of the image exhibiting the same dependence with respect to transmit amplitude. Compared to former exploitation of temporal coherence for tissue/blood discrimination [17] and angular coherence for aberration correction [16], the current approach relies of the coherence with respect to transmit amplitude. Our method does not rely on temporal information, therefore it further enables to effectively capture contrast signals of slowly-moving/non-moving GVs either present in tissues or flowing in very small vessels. However, it may also reveal

significant promise in the domain of ultrasound localization microscopy [1], poised to enhance the detection of ultrasonic signatures originating from slowly moving contrast agents.

This work has been focused on the development of nonlinear ultrasound imaging of non-disrupting GVs. Further work could adapt and extend this nonlinear SVD beamforming concept to the imaging of GVs disruption. In particular, the exploitation ultrafast data acquired during the fast dissolution curve of GVs just after disruption may be discriminated. Future works will also investigate the in vivo validation of nonlinear SVD beamforming in rodents.

5. Conclusions

Our study underscores the potential of ultrafast nonlinear SVD imaging leveraging the capabilities of acoustic reporter genes. The long-lasting pursuit of improved imaging methodologies for *in vivo* detection of contrast agents has driven significant advancements in contrast Ultrasound. This ultrafast nonlinear SVD beamforming technique, utilizing the information from spatial and pressure domains, exhibits compelling performance as demonstrated across simulated and *in vitro* experiments. Nonlinear SVD beamforming technique outperforms other conventional amplitude modulation sequences, even in the complex context of nonlinear tissue responses, while preserving fast frame rate capabilities. Further in vivo studies in rodents should demonstrate the interest of this technique in the context of ultrasound molecular and cellular imaging using acoustic reporter genes.

Acknowledgement

This work was supported by Inserm research accelerator (Inserm ART) in Biomedical Ultrasound and by the French national research agency (ANR) under ANR-21-CE19-0050 program (Project SonoGT). MGS is an investigator of the Howard Hughes Medical Institute.

References

1. Errico, C., et al., *Ultrafast ultrasound localization microscopy for deep super-resolution vascular imaging.* Nature, 2015. **527**(7579): p. 499-502.
2. Lakshmanan, A., et al., *Preparation of biogenic gas vesicle nanostructures for use as contrast agents for ultrasound and MRI.* Nature Protocols, 2017. **12**(10): p. 2050-2080.
3. Shapiro, M.G., et al., *Biogenic gas nanostructures as ultrasonic molecular reporters.* Nature Nanotechnology, 2014. **9**(4): p. 311-316.
4. Zhang, G., et al., *Ultrasound Molecular Imaging and Its Applications in Cancer Diagnosis and Therapy.* ACS Sensors, 2022. **7**(10): p. 2857-2864.
5. Dutka, P., et al., *Measuring gas vesicle dimensions by electron microscopy.* 2021. **30**(5): p. 1081-1086.
6. Huber, S.T., et al., *Cryo-EM structure of gas vesicles for buoyancy-controlled motility.* Cell, 2023. **186**(5): p. 975-986.e13.
7. Dutka, P., et al., *Structure of Anabaena flos-aquae gas vesicles revealed by cryo-ET.* Structure, 2023. **31**(5): p. 518-528.e6.
8. Bar-Zion, A., et al., *Acoustically triggered mechanotherapy using genetically encoded gas vesicles.* Nature Nanotechnology, 2021. **16**(12): p. 1403-1412.

9. Shapiro, M.G., et al., *Biogenic gas nanostructures as ultrasonic molecular reporters.* Nat Nanotechnol, 2014. **9**(4): p. 311-6.
10. Maresca, D., et al., *Nonlinear ultrasound imaging of nanoscale acoustic biomolecules.* Applied Physics Letters, 2017. **110**(7).
11. Eckersley, R.J., C.T. Chin, and P.N. Burns, *Optimising phase and amplitude modulation schemes for imaging microbubble contrast agents at low acoustic power.* Ultrasound Med Biol, 2005. **31**(2): p. 213-9.
12. Maresca, D., et al., *Nonlinear ultrasound imaging of nanoscale acoustic biomolecules.* Appl Phys Lett, 2017. **110**(7): p. 073704.
13. Maresca, D., et al., *Nonlinear X-Wave Ultrasound Imaging of Acoustic Biomolecules.* Physical Review X, 2018. **8**(4): p. 041002.
14. Hurt, R.C., et al., *Genomically mined acoustic reporter genes for real-time in vivo monitoring of tumors and tumor-homing bacteria.* Nature Biotechnology, 2023. **41**(7): p. 919-931.
15. Rabut, C., et al., *Ultrafast amplitude modulation for molecular and hemodynamic ultrasound imaging.* Applied Physics Letters, 2021. **118**(24).
16. Bendjador, H., T. Deffieux, and M. Tanter, *The SVD Beamformer: Physical Principles and Application to Ultrafast Adaptive Ultrasound.* IEEE Transactions on Medical Imaging, 2020. **39**(10): p. 3100-3112.
17. Demené, C., et al., *Spatiotemporal Clutter Filtering of Ultrafast Ultrasound Data Highly Increases Doppler and fUltrasound Sensitivity.* IEEE Trans Med Imaging, 2015. **34**(11): p. 2271-85.
18. Bendjador, H., et al., *The SVD beamformer with diverging waves: a proof-of-concept for fast aberration correction.* Physics in Medicine & Biology, 2021. **66**(18): p. 18LT01.
19. Imbault, M., et al., *Ultrasonic fat fraction quantification using in vivo adaptive sound speed estimation.* Phys Med Biol, 2018. **63**(21): p. 215013.
20. Imbault, M., et al., *Robust sound speed estimation for ultrasound-based hepatic steatosis assessment.* Phys Med Biol, 2017. **62**(9): p. 3582-3598.
21. Foiret, J., et al., *Improving plane wave ultrasound imaging through real-time beamformation across multiple arrays.* Scientific Reports, 2022. **12**(1): p. 13386.
22. Park, E.Y., et al., *Fast volumetric ultrasound facilitates high-resolution 3D mapping of tissue compartments.* Sci Adv, 2023. **9**(22): p. eadg8176.
23. Wahyulaksana, G., et al., *Higher Order Singular Value Decomposition Filter for Contrast Echocardiography.* IEEE Trans Ultrason Ferroelectr Freq Control, 2023. **70**(11): p. 1371-1383.
24. Salahshoor, H., et al., *Geometric effects in gas vesicle buckling under ultrasound.* Biophysical Journal, 2022. **121**(21): p. 4221-4228.
25. Baranger, J., J. Aguet, and O. Villemain, *Fast Thresholding of SVD Clutter Filter Using the Spatial Similarity Matrix and a Sum-Table Algorithm.* IEEE Trans Ultrason Ferroelectr Freq Control, 2023. **70**(8): p. 821-830.
26. Matalliotakis, A., et al., *Impact of wavefront shape on nonlinear ultrasound imaging of monodisperse microbubbles.* arXiv, 2024.
27. Gong, P., P. Song, and S. Chen, *Hadamard-Encoded Multipulses for Contrast-Enhanced Ultrasound Imaging.* IEEE Trans Ultrason Ferroelectr Freq Control, 2017. **64**(11): p. 1674-1683.